Radiation Damage in Nanocrystalline Iron

A Thesis

Submitted to the Faculty

of

Drexel University

by

Gregory Alan Vetterick

in partial fulfillment of the

requirements for the degree

of

Doctor of Philosophy

May 2014

DEDICATION

To my late mother, Dale Elaine Vetterick. Thank you for everything.

ACKNOWLEDGEMENTS

I must begin by expressing my gratitude to Professor Mitra L. Taheri for her tireless effort to create opportunities for me and the rest of our research group. Without her this project would not have gotten off the ground, nor would I have been introduced to all of the following people who helped shape not just my project but my future as a scientist, engineer, and person.

Among those people to whom I was introduced over the course of these four years, there are many who I could not have done without. Foremost amongst them are Dr. Amit Misra, Dr. Mark Kirk, and Dr. Khalid Hattar whom I cannot thank enough for their patience and guidance. Their willingness to work with me and to provide access to invaluable resources was essential to the success of the project and my growth as a scientist.

Thank you to Mr. Kevin Baldwin for not knowing when to say no. Without the seemingly inexhaustible supply of sputtered films coming from Los Alamos I would have gotten nowhere. Similarly for Mr. Pete Baldo at Argonne National Laboratory. Thanks for staying those extra hours to get just a few more irradiation runs in and for the engaging conversations that made those hours fly by.

A great thank you to everyone in my research group for putting up with me these last few years, and never failing to lend a hand when I needed it. Thank you especially to Mr. Matthew Hartshorne and Mr. Christopher Barr for all the help you have given me over the past few years, and to Mr. Asher Leff for the Nye tensor map calculations.

Of course I cannot leave out those who have me lent their time and wisdom; Dr. Garritt Tucker and Jacob Gruber of Drexel University, Dr. David Srolovitz and Jian Han of the University of Pennsylvania, Dr. Craig Johnson in the Centralized Research Facilities at Drexel University, Dr. Fei Gao of Pacific Northwest National Laboratory, Dr. Raymond Unocic of Oak

Ridge National Laboratory, Dr. Michael J. Demkowicz of Massachusetts Institute of Technology, Dr. Roger Stoller and Dr. Haixuan Xu of Oak Ridge National Laboratory, and Dr. Michel Barsoum at Drexel University.

Finally, I have to thank my friends and family who stuck with me through the last few years. In particular, I am eternally grateful for the endless patience, love, and support of my beautiful fiancée Emily, who gave me the motivation to finish.

TABLE OF CONTENTS

LIST OF FIGURES

LIST OF TABLES

ABSTRACT

There is strong evidence that grain boundaries act as recombination sites for interstitials and vacancies in a polycrystalline material. The prevailing theory is that grain boundaries act to absorb freely mobile interstitials and vacancies as well as sub-microscopic defect clusters, thereby depleting the region adjacent to the grain boundary of sufficient point defects to produce visible defect structures (e.g. stacking fault tetrahedra, voids, and dislocation loops). This theory is the basis for the design of radiation tolerant materials engineered to remove the large non-equilibrium point defect concentration created in cascades under irradiation by high energy particles by introducing a large number of grain boundary sinks.

This thesis presents direct experimental evidence for a number of mechanisms operating to remove radiation damage at grain boundaries by *in-situ* transmission electron microscopy of free standing nanocrystalline iron films. It was found that the size of dislocation loops found in irradiated iron decreases with smaller grain size until a minimum cluster size is reached (about 2-5nm). The number density of defect clusters appears less affected by the presence of a high number of grain boundary sinks, but does vary strongly with the sink strength of the particular boundaries. If a small grain is defined by grain boundaries are capable of producing a very strong denuded zone, the cluster density can be very small. Therefore, the magnitude of this effect is dependent on the grain boundary character well into the nanocrystalline grain size regime.

This work also shows that, in addition to the ability of a grain boundary to absorb sub-microscopic defects, the mobility and absorption of microscopic defect structures (i.e. defect clusters and dislocation loops) at grain boundaries has a strong influence on the response of a material to irradiation. Using *in-situ* TEM we examined the behavior of these microscopic DCs in nanocrystalline iron. The one-dimensional loop hop of **b**=1/2<111> DCs was found to

transport DCs to close proximity to GBs where they could annihilate, suggesting a contribution to the long range flux of interstitials to GB sinks. This process had marked effects on the morphology of the irradiated microstructure in nanocrystalline iron, limiting the length of DC strings and reducing the coalescence of DCs into larger defect loops.

Furthermore, the research presented in this thesis showed that when large dislocation loops are able to form they may just as easily be lost to grain boundaries: a process which enhances the effect that grain boundary sinks have on the microstructure of the irradiated material. *In-situ* TEM irradiations in nanocrystalline iron at temperatures from 50K to 773K show that as the temperature of the specimen is increased from cryogenic temperatures (e.g. 50K), the mobility of first **b**=1/2<111> defect clusters, then **b**=1/2<111> dislocation loops, and finally **b**=<100> dislocation loops reaches sufficient levels to enable climb to grain boundaries resulting in absorption. In nanocrystalline materials with a high density of grain boundary sinks this activity results in a small downward shift in the transition temperature between a **b**=1/2<111> dominated microstructure and one that consists primarily of **b**=<100> dislocation loops. At 773K, the microstructure is largely free of any dislocation loops in nanocrystalline iron, a stark change from previous work in microcrystalline iron where the **b**=<100> loops remain stable. The shift in the transition temperature agrees well with initial hypotheses in literature that the nature of the loops remaining in irradiated iron depends on the relative stabilities of the dislocation loops arising due to the elastic anisotropy of iron from thermal magnetic fluctuations, and the high mobility of **b**=½<111> dislocation loops compared to **b**=<100> dislocation loops.

Using in-situ transmission electron microscopy, the activity of dislocation loops in nanocrystalline iron were directly observed and analyzed using orientation mapping. By comparing *in-situ* TEM results to molecular dynamics simulations, the process of absorption was elucidated for microscopic defect clusters, **b**=1/2<111> dislocation loops, and **b**=<100> dislocation loops.

CHAPTER 1. OVERVIEW

1.1 Introduction

Worldwide electrical power generation demands are expected to grow by 56% by the year 2040 [1]. In order to meet this demand, new infrastructure will be needed and the current focus on climate change and domestic dependence of energy is driving a resurgence of research into zero-carbon alternatives to coal and oil. In fact, nuclear power and renewable energy are both the world's fastest-growing energy sources, each increasing by 2.5% per year [1]. Nuclear energy already represents the largest amount (16%) of the world's electricity produced by any nongreenhouse-gas-emitting source [2]. As of 2014, the International Atomic Energy Agency lists 437 operational nuclear power reactors in 31 countries around the world, including 104 in the United States.

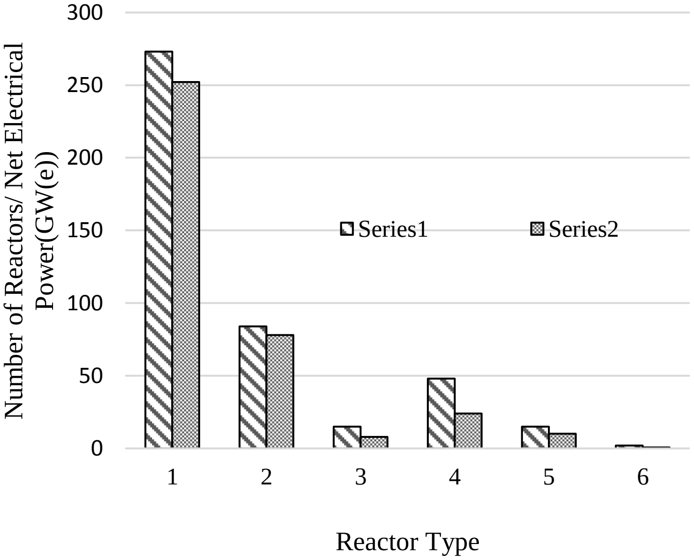

Figure 1. Number of operational nuclear reactors by type and net electrical power as of December 31, 2012 (PWR=pressurized water reactor, BWR=boiling water reactor,

GCR=gas cooled reactor, PHWR=pressurized heavy water reactor, LWGR=light water graphite reactor, FBR=fast breeder reactor) [3].

In the United States, 100 of the 104 reactors are currently operating and together produce 19.4% of the electricity in the country. Almost half of the 104 operational nuclear plants are more than 24 years old, and the last nuclear reactor entered service in 1996. The picture is similar around the world as shown in Figure 2, although worldwide there are reactors still being built. Since the last reactor was brought online in the United States, reactors have been connected to the grid in Brazil (1), China (14), Czech Rep (2), France (4), India (10), Iran (1), Japan (8), Korea (10), Pakistan (2), Romania (2), Russia (4), Slovakia (2), and Ukraine (2) [3].

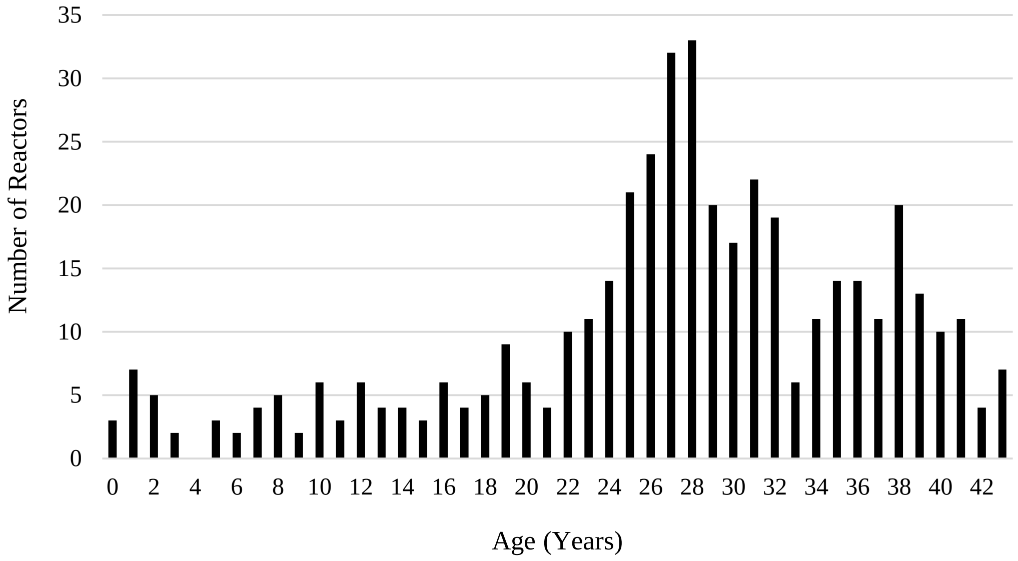

Figure 2. Worldwide number of reactors in operation by age as of December 31, 2012 [3].

Around the world there are another 72 reactors under construction, but there is only one under construction in the United States - the Tennessee Valley Authority (TVA) Watts Bar 2 which is scheduled to being operation in December 2015. In order to keep up with demand for electricity, U.S. utility companies have increased the capacity factor of the reactors from 55.9% in 1975, to 66% in 1990, to 90.3% in 2002, and have maintained a level at around 90% until present day [4]. In addition, aging nuclear power plants are being kept online beyond their original licensed lifetime. Originally, most reactors in the United States were issued licenses to operate for 30-40 years. The original operating license length was based on anti-trust considerations, not technical limitations, so many operators are applying for 20 year lifetime extensions in order to keep the reactors running during the period of low construction [5].

As of 2011, 69 of the reactors in the United States have been granted lifetime extensions of 20 years [5]. The extension of current reactor lifetimes from 40 years to 60 years improves the return on initial investment and buys time for the development of future nuclear reactors. Many plants are already looking at an additional 20 year extension out to 80 years of operation as there is no limit on the number of extensions that can be applied for. It has been estimated that it would cost ~$500B to replace the current fleet of reactors, and 4-8 reactors per year would have to be built to maintain current growth levels as the current fleet begins shutdown, even with 20-40 year lifetime extensions [5]. There is, therefore, a critical need to keep the existing fleet of reactors running, and finalize the technology necessary to build new reactors that provide worthwhile improvements to existing designs.

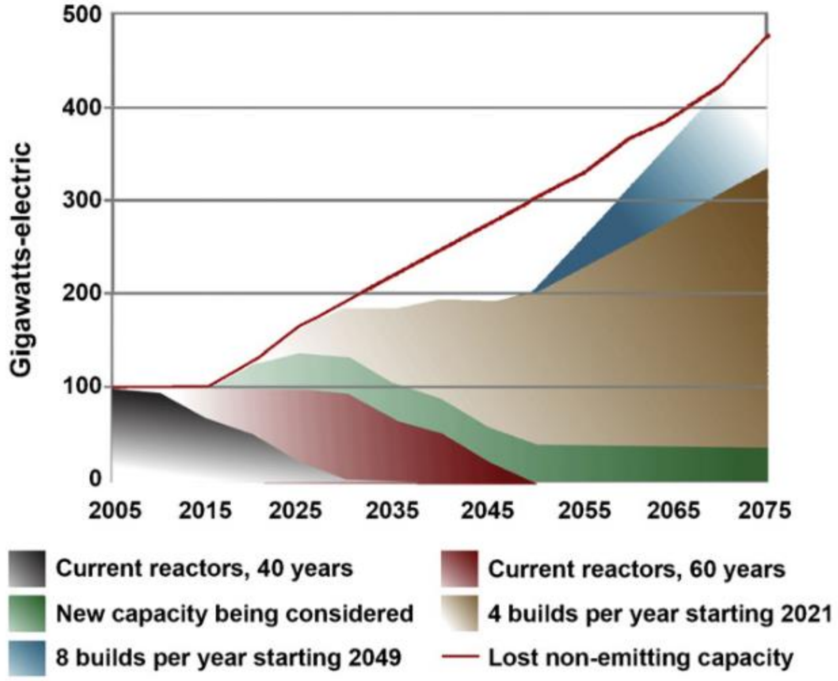

Figure 3. Total generating capacity of current and planned U.S.A. nuclear power plants as a function of time. Unshaded area under red line represents lost capacity if plants are decommissioned after 60 years. From Kenik et al. [5].

1.2 Motivation

The downside of extending the operating lifetimes of nuclear reactors to 60, 80, or even more years is that the material degradation issues that are a part of every reactor design are compounded. The industry invests about $7.5 billion per year in maintenance and upgrades of these older reactors as they reach the end of their licensed lifetimes. This damage occurs in large part due to the flux of neutrons generated by the nuclear fission reaction. Over a 40 year lifetime, structural components in the core of a boiling water reactor (BWR) will be impacted by 10^{22} neutrons/cm^2 (~7dpa) or 10^{23} n/cm^2 (~70dpa) in a pressurized water reactor (PWR) [6]. Each neutron initiates a cascade of atoms that results in a non-equilibrium concentration of interstitial and vacancy point defects. Point defect interaction in the material leads to significant changes in chemistry, mechanical properties, and physical dimensions leading to enhanced corrosion, premature fatigue and fracture, and out of tolerance components, respectively.

As the operating life of existing reactors have been extended, new materials (along with new design features and operating practices) have been in continual development to improve the safety, decrease the operating costs, and increase the performance and efficiency of the current fleet of nuclear reactors. In addition to retrofitting the old but still running Generation II reactors, these improvements were used for Generation III reactors built in the 1990s outside the United States. More advanced Generation III+ designs build upon these evolutionary improvements and will be the designs of choice for reactors built through 2030. Future Generation IV reactors are considered revolutionary designs and feature altogether different operating principles that promise to provide (1) manageable nuclear waste, effective fuel utilization, and increased environmental benefits, (2) competitive economics, (3) recognized safety performance, and (4) secure nuclear energy systems and nuclear materials for a lower risk of proliferation [2].

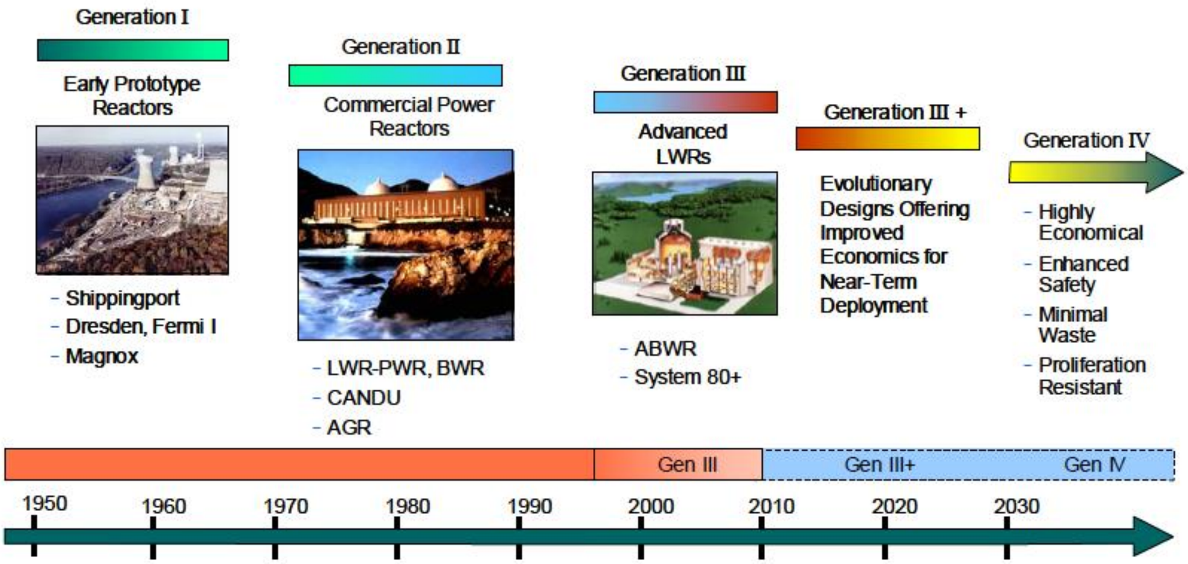

Figure 4. The generations of nuclear reactor designs. From the U.S. Department of Energy [2].

Lifetime extensions of current reactors in the United States will play a key role of bridging the gap before the Generation IV nuclear reactors can be built. Unfortunately, the design of new reactor concepts has outpaced the development of materials that can withstand the operating environments required by the concepts. Therefore, there exists a critical need for new materials that can extend the lifetime of currently operational reactors and better withstand the predicted operating environment of the future Generation IV reactors. This generation of nuclear reactors actually encompasses a number of different designs including the Gas-Cooled Fast Reactor System, Lead-Cooled Fast Reactor System, Molten Salt Reactor System, Sodium-Cooled Fast Reactor System, Supercritical-Water-Cooled Reactor System, and Very-High-Temperature Reactor System [2]. The operating conditions of fission and fusion reactor are characterized by combinations of high temperatures, large time-varying stresses, chemically reactive environments, and intense neutron radiation fields [7]. The operating conditions and material requirements for Generation IV reactors have been described in detail [8-16]. All of these reactor designs share a common theme, higher operating temperatures, faster fuel burn, and longer lifetimes. Materials in the primary side of the reactor will experience up to 200 dpa (i.e. atoms will be displaced from their lattice positions up to 200 times) at temperatures up to 1000°C. As a result, large excess concentrations of vacancy and self-interstitial atom (SIA) defects will be created leading to many detrimental effects.

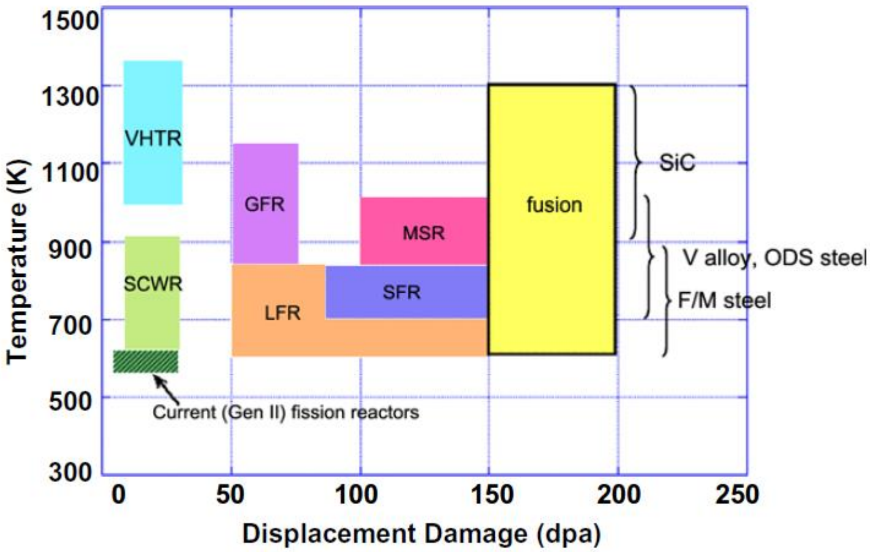

Figure 5. Overview of operating temperatures and displacement damage dose regimes for structural materials in current (generation II) and proposed future (Generation IV) fission and fusion energy systems. The six Gen IV fission systems are Very High Temperature Reactor (VHTR), Super Critical Water Reactor (SCWR), Lead Fast Reactor (LFR), Gas Fast Reactor (GFR), Sodium Fast Reactor (SFR), and Molten Salt Reactor (MSR) [17].

Candidate materials for advanced reactors, especially Generation IV designs, must meet rather demanding criteria. They should provide (from Murty et al. [14]): (1) Excellent dimensional stability against thermal and irradiation creep, void swelling, etc., (2) Favorable mechanical properties such as strength, ductility, creep rupture, fatigue, creep–fatigue interactions, etc., (3) Acceptable resistance to radiation damage (irradiation hardening and embrittlement) under high neutron doses (10–150 dpa or displacements per atom), helium embrittlement, etc., and (4) High degree of chemical compatibility between the structural materials and the coolant as well as with the fuel, including resistance to irradiation-assisted stress corrosion cracking (IASCC).

Steel is one of the primary materials used for the construction of Gen II-III+ nuclear reactors in both the primary reactor side and secondary electricity generation side water circuits. Some of the largest components in the reactor are made of low alloy or stainless steel including the pressure vessel (309SS clad low alloy), core support structure (304SS), fuel supports (SS), control rods (304/316SS), steam separator (304SS), and steam piping (low alloy). Many of the materials used in today's reactors (e.g. Zircalloy and low alloy steels) are unlike to be suitable for use in Generation IV reactors. Ferrous metals will also be critical for the development of Generation IV reactor designs. Advanced ferritic, body centered cubic steels are being developed to handle the requirements of future fusion and advanced fission reactors. Examples of these materials include reduced activation ferritic/martensitic (RAFM) steels with a nominal composition of Fe-9Cr-1Ti-1W, and oxide dispersion strengthened (ODS) steels with some variation of the composition Fe-14Cr-1Ti-0.3Y_2O_3 [18, 19]. These alloys are promising because they show low activation due to the replacement Nb, Mo and Ni with Ta and W, improved high temperature strength, admirable corrosion resistance (on par with AISI 316 in the case of the ODS alloys), and superior swelling resistance because of their BCC structure high dislocation and precipitate density [20].

The reliable performance of advanced radiation tolerant materials are essential to the safe operation of advanced nuclear reactors over their extended operational lifetime. Despite extensive study, there is no comprehensive understanding of the fundamental principles that drive radiation hardening, swelling, and radiation induced segregation (RIS) which arise due to the interactions of point defects created by neutron collisions with the microstructure. This is particularly true in advanced ferritic alloys such as RAFM and ODS steels because of their complex microstructure and chemistry. The combination of ultrafine grain size, solid solution hardening, precipitates, and high dislocation density give these alloys excellent high temperature mechanical properties and, almost as a byproduct, enhanced radiation resistance.

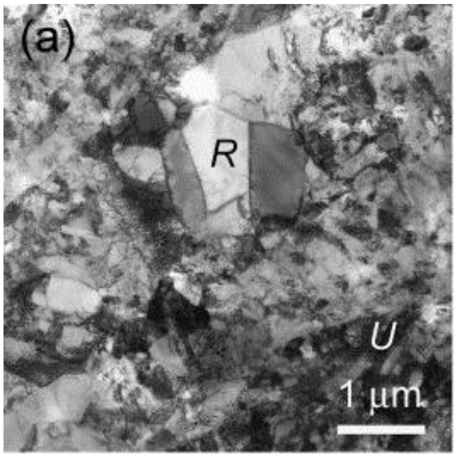

Figure 6. Effect of heat treatment on the grain microstructure of an ODS Fe–12Cr alloy annealed at 1023 K for 4 hours. R and U mark recovered and unrecovered regions, respectively [20].

1.3 Problem Statement

Microstructural features (i.e. grain boundaries, precipitates, and dislocations) that dominate nanostructured ferritic alloys are considered to be effective sites for the annihilation of interstitials and vacancies, therefore making them excellent sinks for defect in a material produced by irradiation. NFA steels generally have ultrafine grain size, which means they have a large number of grain boundaries. A number of authors have reported observing regions of material with reduced populations of defect clusters or smaller defect clusters along grain boundaries in a number of materials including ferrous alloys [21-27]. This phenomenon has subsequently generated significant interest as a means to control radiation damage [28, 29], in particular for materials in which the grain size is very small, such as in nanocrystalline materials. By decreasing the grain size of a material to the nanocrystalline range, a high density of grain boundaries are introduced to act as defect sinks and therefore reduce the amount of damage occurring from interstitial and vacancy clustering. The effect has already been shown in several materials including $MgGa_2O_4$ [24], and TiNi [30]. ZrO_2 [31], Pd [31], Cu–0.5A_2O_3 [32], and Ni[32, 33], but there has been no work in structural materials such as iron even though grain boundaries in ferritic/martensitic steels have shown evidence of denuded zones [21, 22].

When nanocrystalline materials are designed based on this theory, a large number of grain boundaries are introduced, usually with no regard to the type of grain boundary. This is in spite of the fact that radiation phenomena such as the formation of denuded zones and radiation induced segregation have been shown to be affected by the nature of the grain boundary. In addition, there have been no studies examining the mechanisms for radiation tolerance in nanocrystalline materials. The theory and study of denuded zones has focused exclusively on SIA and vacancy diffusion, and largely ignores the contributions from defect clusters that must arise due to production bias [34]. There has been very little work looking specifically at grain boundaries under irradiation. For example, a significant portion of research to systematically study the irradiation behavior of ferritic steels has been performed in low dislocation density, large grained pure iron. As a consequence, there is limited knowledge of the effect of individual microstructural features (e.g. grain boundaries) on radiation damage in iron.

In order to design more radiation tolerant microstructures for nuclear reactor structural materials, it is critical to understand in a comprehensive manner how the interplay between grain size, grain boundary character, and the mechanisms for the action of a grain boundary sink contribute to the radiation tolerance of a material.

The objective of the research presented in this thesis was to attempt to answer four critical questions:

1. What is the influence of grain boundary density (grain size) on radiation damage in BCC iron?
2. What is the grain boundary character effect on radiation damage accumulation near GBs?
3. What is the influence of defect mobility on point defect loss at GBs in BCC iron?
4. At what grain size do GBC and defect mobility effects break down?

To answer these questions, transmission electron microscopy (TEM) and related advanced characterization techniques (e.g. precession OIM, STEM/EDS, and eels) were used to study model ferritic iron alloys (i.e. Fe and Fe-9Cr). TEM samples prepared from thin films and bulk materials were be irradiated *in-situ*, allowing for dynamic observation of the behavior of the alloy under ion irradiation.

Experimental observations of radiation damage generally only allow for study of point defect cluster structure (e.g. interstitial or vacancy nature, 2D or 3D structure, and dislocation habit planes) and the kinetics of their formation and movement above a resolvable size of about 3nm. Therefore, simulation techniques such as molecular dynamics were used in an attempt to elicit the mechanisms of the observed behaviors.

1.4 Organization of Work

This thesis is organized into several chapters outlining the synthesis, characterization, irradiation, and mechanical testing of nanocrystalline iron thin films. It begins with an overview of radiation damage mechanisms from the production of both free point defects and clusters in the cascade through their effect on the microstructure of materials, with an emphasis on how grain boundaries affect irradiation behavior. It will continue with the current state of understanding of irradiation damage in iron and the framework in which this investigation resides. The methodology is presented with special considerations to working in thin films including the substantiation of several techniques utilized for this study. The results cover the deposition of iron thin films, annealing the films to achieve varied grain size, the effects of that grain size on radiation damage and the mechanisms for that behavior, and finally the mechanical behavior of nanocrystalline films. These sections are then summarized and the need for future work is outlined.

CHAPTER 2. REVIEW OF LITERATURE

2.1 Radiation Damage in Materials

The collision of a neutron with a crystal lattice produces cascade events resulting in the creation of interstitials and vacancies at values far in excess of equilibrium. The defects may be present as single defects or as small clusters, either of which are free to diffuse to sinks such as grain boundaries and free surfaces. The thermodynamic and kinetic stability of these point defects determines how the material responds to the radiation. In metallic alloys used in light water reactors (LWRs), the manifestation of defect production is excessive hardening, swelling, amorphization, and irradiation assisted stress corrosion cracking (IASCC) due to radiation induced segregation (RIS). The following section details how point defects (interstitials and vacancies) are created, how they interact, and how this leads to damage phenomena and ultimately failure. Understanding these correlations from the atomic scale through the mesoscale is the quintessential goal in the study of radiation's effects in materials.

2.1.1 Origin of Point Defects

Over their 40 year lifetime, structural components in the core of a boiling water reactor (BWR) will be impacted by 10^{22} neutrons/cm^2 (~7dpa) or 10^{23} n/cm^2 (~70dpa) in a pressurized water reactor (PWR) [6]. About 77% of these neutrons are thermal in nature and possess less than 1MeV of energy [8]. Each impact of a neutron with the core components transfers energy from the incident particle to the lattice in what is called a radiation damage event [35]. Radiation damage events can be broken down into four stages: collision, thermal spike, quenching, and annealing. The collision stage encompasses the energy transfer from the neutron to the primary knock-on atom (PKA) which creates a cascade of additional knock on atoms before the PKA terminates as an interstitial. A limited volume is formed in which the majority of atoms are energetic and temporarily in motion, leaving vacant lattice sites [35, 36]. Lattice vibrations are produced by the excess energy, resulting in a thermal spike on the order of 10^4 K [37]. The heat is dissipated into the surrounding atoms until thermodynamic equilibrium is reached, during which time point defects spontaneously combine and annihilate, form stable Frenkel pairs (single interstitial atoms (SIA) and vacancies), or form defect clusters [35, 36]. The result is a highly damaged volume of material which is composed of a core of vacancies or vacancy clusters surrounded by a shell of SIAs [38].

Cascade collapse has been studied experimentally by irradiating pure metals with heavy ions (e.g. Mo [39], Cu [40, 41], Ag [42, 43], Au [44], Ni [45-47], Fe [48], W [49], Co [50], Ru [51], Cu_3Au [52, 53]). These studies were focused on measuring the dose required to form microscopically (TEM) visible defect clusters for different ion species and energies. This is because initial point defect production via the displacement cascade occurs on too short a time scale (10^{-18} to 10^{-8} seconds) to be observed experimentally. For more in-depth understanding of cascades, computer simulations using molecular dynamics (MD) are required. MD enables the researcher to study phenomena on the order of 10–15 ps, including the cascade as well as point defect production and interaction [54-62].

Vacancies in metal lattices are considered to be simply a missing atom on the lattice with the nearest neighbors relaxing inward accounting for a small relaxation volume. They have low formation energies (< 2eV) and high migration energy (>0.5eV) leading to a low mobility [35]. The basic picture of an interstitial is similar, as an extra atom placed in one of the energetically favorable free volume sites in the crystal lattice (i.e. the octahedral and tetrahedral sites in cubic metals). In reality the lowest energy configuration for an interstitial is when two atoms share a single lattice site. This arrangement, called the dumbbell or split-interstitial configuration, wherein the atoms form a doublet with an axis along the (100) direction for FCC metals and the (110) for the BCC lattice [35, 63]. Unlike vacancies, interstitials have a high formation energy (>2.0eV), a large relaxation volume ($\sim 2\Omega$) and a low migration energy (< 0.15eV) leading to a high mobility [35].

Beyond the split interstitial configuration, multiple interstitials may agglomerate as they have a relatively high binding energy around 1eV. After formation, large clusters of interstitials are unlikely to dissociate because the energy needed to dissociate an interstitial rises to 2–4eV. Although vacancy clusters are less favorable with small binding energies around 0.1eV, they are also still seen in irradiated metals. An important consequence of point defect clustering is the formation of dislocation loops, which have a direct effect on the development of the irradiated microstructure. As interstitials or vacancies reach a critical cluster size, the most stable formation becomes a planar defect known as a prismatic or Frank loop. These can be envisioned as the insertion or removal (interstitial and vacancy, respectively) of a disk of atoms from a close packed plane, creating an intrinsic stacking fault. Kinetic Monte Carlo (KMC) simulations can be used to study the evolution of the point defects into experimentally resolvable features [37]. KMC follows migration, emission, coalescence, and sink interactions over timescales on the order of tens of years [37]. The interactions of point defect loops, stacking fault tetrahedron, voids, and other dislocations arising from point defect clustering are responsible for radiation hardening and swelling in irradiated metals.

2.1.2 The Production Bias

While interstitials and vacancies are always produced in equal numbers, they are not necessarily formed in the cascade as individual interstitials and vacancies as envisioned in the classic Frenkel pair. Figure 7, while by no means comprehensive, shows the potential forms of interstitials and vacancies created in the cascade. The important point is that large numbers of defects are known to gather together to form small defect clusters. The formation energies of various clusters (e.g. interstitial vs. vacancy of different Burgers vectors) are different, as is the mobility of each cluster type. This phenomenon, known as the production bias [34, 64, 65], has extensive consequences on the irradiation behavior of a material.

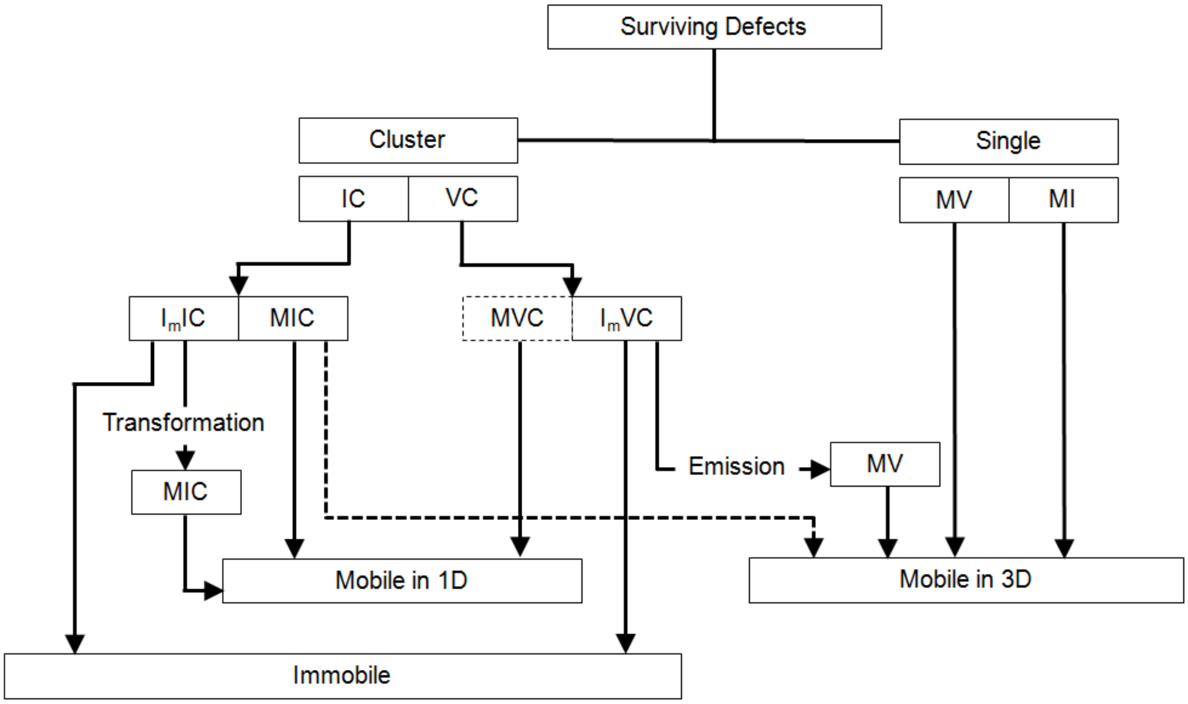

Figure 7. A schematic of the defect production in a cascade. Modified from [64] and [65].

One of the primary effects is an increase in displacement efficiency. Displacement efficiency is a measure of the fraction of point defects that survive the cascade quench, a value which is critical to the development of the irradiated microstructure. The spontaneous formation of defect clusters in a cascade reduces the likelihood of recombination. This effect is enhanced by the fact that many of the defect clusters are glissile, so they may move away from the cascade region. The importance of clustering contributes to the higher defect survival rate in FCC materials compared to BCC metals [66]. Beyond the initial defect production, the production bias has important consequences on the formation of the irradiated microstructure. For example, the high mobility of interstitial clusters formed in cascades is thought to permit them to drift to defect sinks, enabling excess vacancies to form microscopic voids [67]. Conversely, the formation of immobile interstitial clusters enables the formation of interstitial dislocation loops by the aggregation of interstitials that would otherwise be very mobile and lost to grain boundaries. This has been used as an explanation [68] for the formation of large interstitial loops in irradiated iron [69].

2.1.3 Denuded Zones

It is clear that a full description of the fundamentals of radiation damage must incorporate a complete understanding of the numbers and size distribution of the defect clusters arising from the cascade. This requires knowledge of the initial spatial distribution of the point defects created in a cascade (including the formation of defect clusters), their mobility in the cascade, and point defect losses caused by mutual recombination. While the Production Bias Model has been proposed, there remains a large amount of work before these details are discerned and the results can be used to predict radiation damage phenomena. For now, many radiation damage effects are described using theories based on the motion of individual point defects, often termed freely migrating defects (FMDs) [35].

The classic example of a situation where FMDs are used to describe a phenomenon that occurs in materials under irradiation is in the description of denuded zones. A denuded zone is a region near a defect sink (a microstructural feature where point defects can be annihilated) where a lower population or a size decrease of defect clusters such as dislocation loops is observed. Two examples of denuded zones are shown in Figure 8, highlighting the fact that they may form for both interstitial clusters [24] and voids [70]. Similar denuded zones have also been observed at grain boundaries in many materials [25, 71-74].

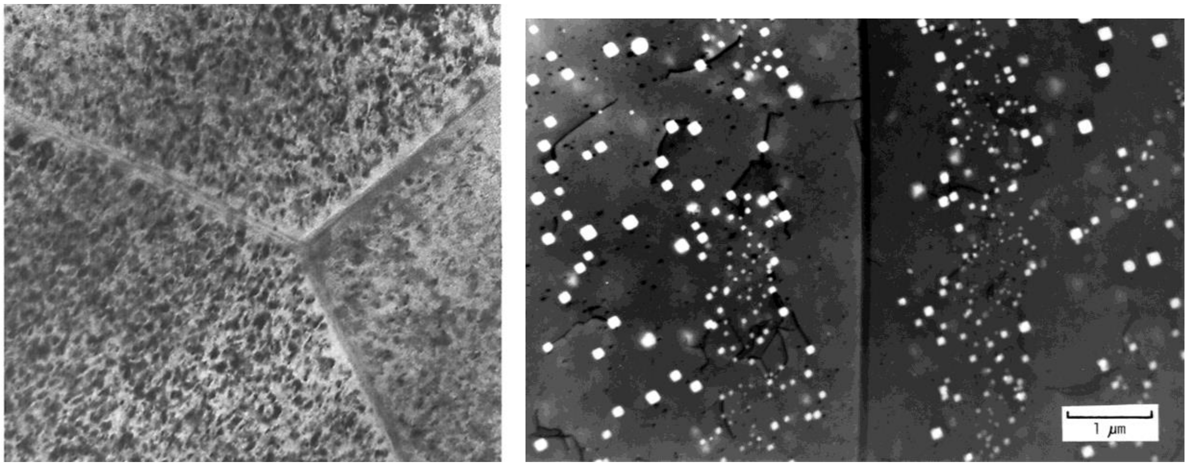

Figure 8. (left) Grain boundary denuded zones in MgAl2O4 [24], and (right) Void-free regions in Cu irradiated in fission reactor (1 dpa) at 350°C [70].

Denuded zones form because grain boundaries are effective sites for the annihilation of point defects. This effect can occur very early in the damage formation process (i.e. during the cascade event), where the grain boundary effectively reduces the cascade efficiency. This type of behavior has been explored using molecular dynamics simulations that are able to track individual interstitials and vacancies formed during the cascade. The Cascade events that occur at or near a grain boundary lose a large fraction of the interstitials formed during the cascade due to spontaneous recombination with the boundary event [75-79]. Samaras et al. [80] showed that the highly mobile interstitials are attracted to regions of high tensile pressure along the grain boundary and migrate toward these regions by 1D and 3D glide. The process of interstitial migration is shown in Figure 9, where the paths of the interstitials are shown as black lines.

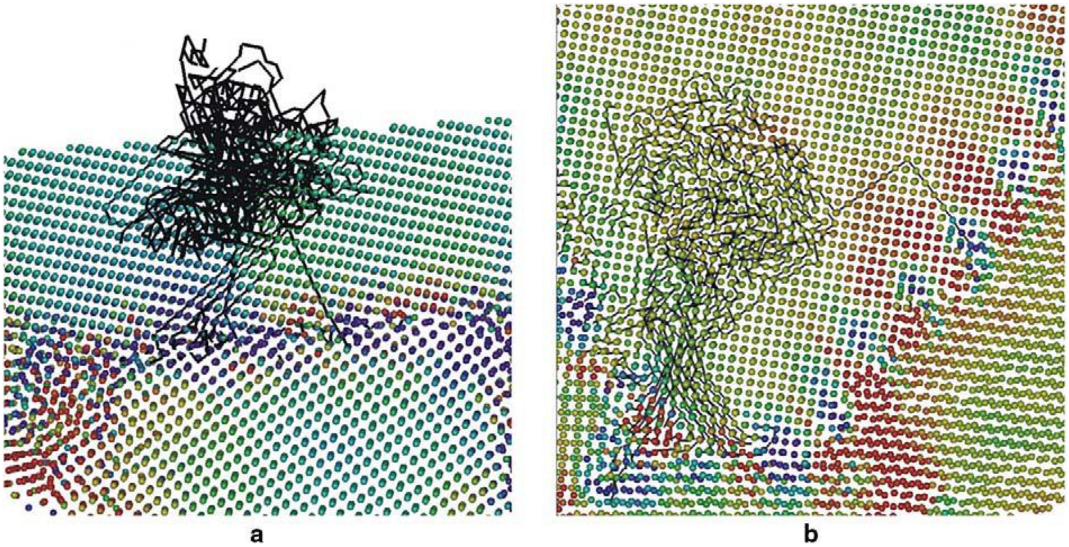

Figure 9. Black lines indicate the movement of atoms during the displacement cascade in (a) bcc Fe and (b) fcc Ni on a backdrop of the pressure present in the relaxed sample. The interstitials move to the nearby GB structure at high tensile pressure [80].

Once the interstitials reach the boundary they annihilate with the free volume present in the grain boundary. Figure 10 shows this process in detail from MD simulations of radiation cascades in nanocrystalline nickel. The figure shows the positions of atoms 7.35 ps after the primary knock-on atom is introduced. The atoms are in the middle of two simultaneous replacement collision sequences (RCSs) that are directed toward the grain boundary. The lines extending from each atom represent the atomic displacement vectors from (red=7.35-8.95 ps and black=8.95-14.15 ps after the PKA is introduced). The RCSs continue into the grain boundary until the damage in accommodated by free volume (marked in yellow). Structural relaxation of the grain boundary permits it to accommodate the atomic transport and ultimately the extra point defects.

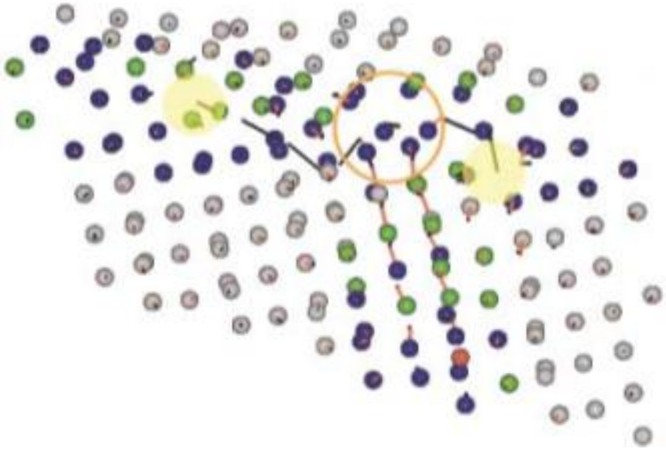

Figure 10. Displacement vectors (>1.5 Å) of Ni atoms at a GB showing how the GBs acts as an interstitial sink, by the annihilation of interstitials with free volume in the GB (marked in yellow) [76].

The immediate result of the annihilation of interstitials at the grain boundary is a higher survival rate for vacancies following the cascade [75, 81]. Figure 11 shows a case where the grain boundary accommodates the interstitial atoms by adding an extra atomic plane on one of the grains, effectively causing grain boundary migration. The vacancies remain in the matrix, which has the potential to enable the formation of large vacancy structures. However, these observations were made with traditional molecular dynamics simulations which are not able to be performed on long enough time scales to visualize the diffusion of vacancies.

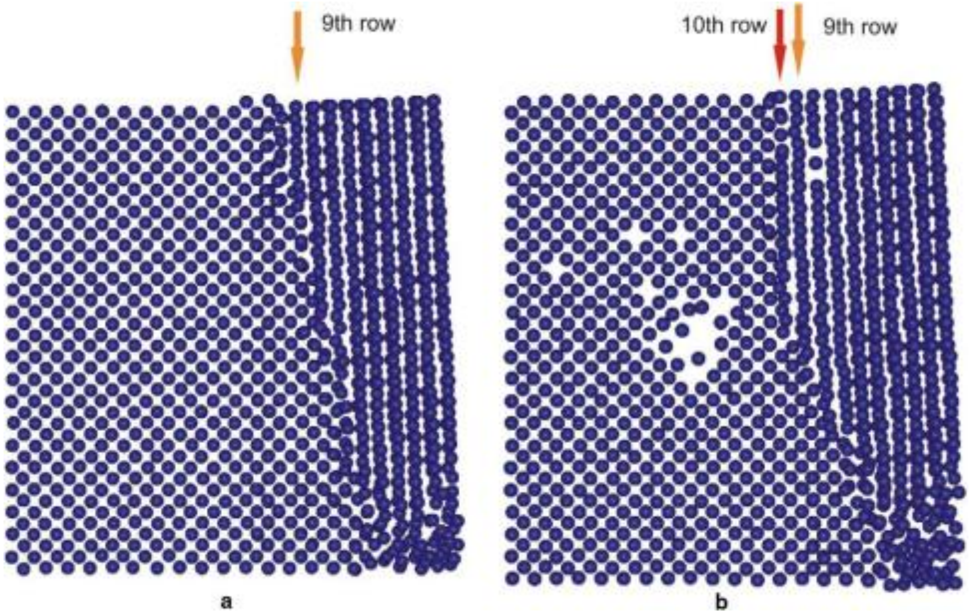

Figure 11. Section of the relaxed bcc Fe sample with GB. (b) Same section after a 20 keV PKA displacement cascade, with vacancy defect clusters present [77].

Although the diffusion of vacancies occurs on timescales that are too long for molecular dynamics simulations, there are processes that may act to remove vacancies from the region adjacent to the grain boundary through a non-diffusive mechanism. Bai et al. [81] proposed a mechanism wherein the interstitials that are loaded into the boundary by the process described above may then annihilate vacancies remaining in the grain through a non-diffusive process, reducing the residual concentration [81]. Figure 12 outlines this process with representative snapshots from a temperature accelerated molecular dynamics simulation of a collision cascade near a grain boundary at 300 K. The figure shows the locations of nondefective atoms (black spheres), interstitials (larger green spheres), and vacancies (smaller blue spheres) along with the motion vector (purple lines) for atoms that move more than 1 Å between frames. In (A) the initial damage structure produced by MD is shown, and the GB region is enclosed by two dashed lines. Frame (B) shows the five vacancies below the GB form a cluster after 21.3 ns. (C and D) At 23.0 ns, three interstitials emit from the GB with a barrier of 0.17 eV to annihilate three vacancies. Note that (C) shows how atoms move during this transition, and (D) shows the final configuration after the event is completed. (E and F) Configurations before and after another interstitial emission event at 23.5 ns. (G and H) Configurations before and after the last interstitial emission event at 23.8 ns. (I) At 348.0ns, the two vacancies above the GB diffuse to the GB via the slower conventional hopping mechanism.

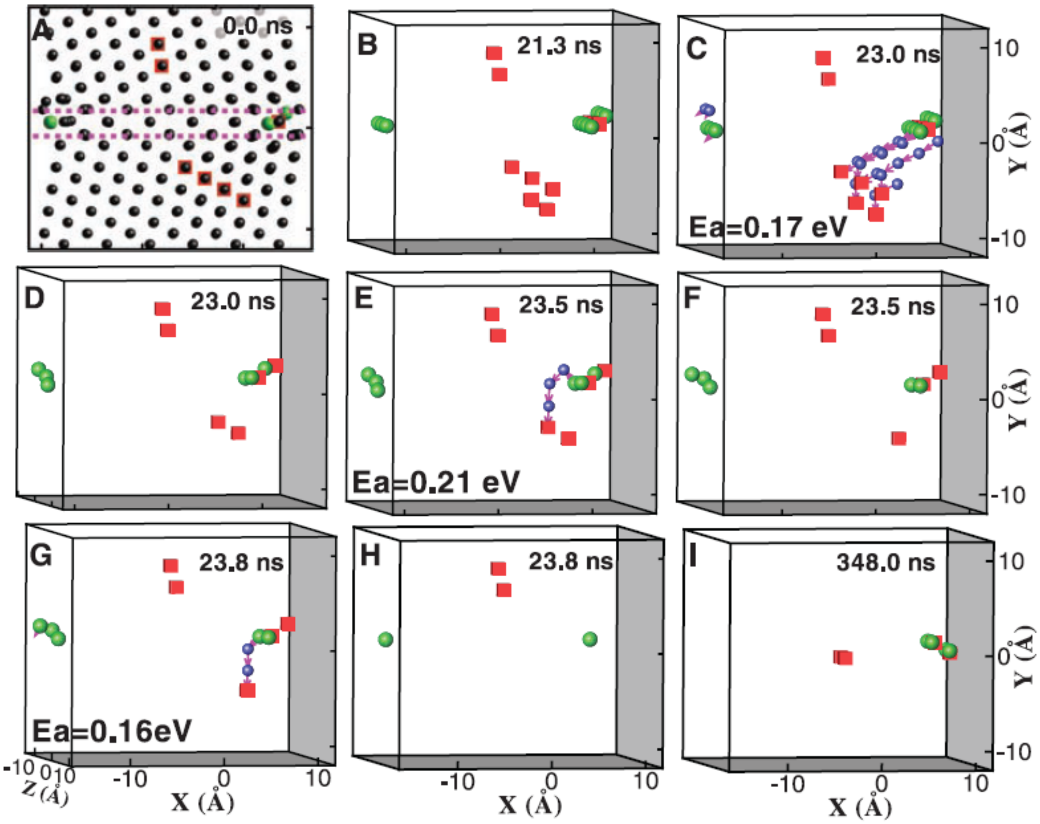

Figure 12. Snapshots from temperature accelerated dynamics (TAD) simulation showing process of vacancy annihilation near GBs [81].

The annihilation of interstitials at grain boundaries, combined with the mechanism proposed by Bai et al. provides a reasonable explanation for the action of a grain boundary as a denuded zone, but these processes act only a few angstroms (~1.5nm) into the matrix. Many denuded zones are on the order of tens of nanometers in width to a few microns in width in polycrystalline materials [21, 22, 27], which suggests contributions from diffusion must be present in order to account for the movement of point defects over longer length scales. These point defect annihilation processes at grain boundaries create a concentration gradient, driving the diffusion of freely mobile interstitials and vacancies to the boundary [23, 26, 82].

The concentration profile created by irradiation-assisted diffusion of point defects has long been accounted for in irradiated materials [72, 73]. In the case of Mansur [72], a model was derived for the point defect profiles in the presence of a one-dimensional sink (i.e. a free surface) to understand the lack of voids near the sample surface. A similar explanation was given by Zinkle [23] to explain the defect free region near the surface of ion irradiated $MgAl_2O_4$. Figure 13 shows the Depth-dependent microstructure of an $MgAl_2O_4$ specimen irradiated with MeV Al^+ ions to a fluence of 5 X 10^{20} ions/m^2 or about 14dpa. Zinkle noted that in some cases there was a low density of very large dislocation loops in the denuded region near the surface, suggesting that the absence of defect clusters was due to suppressed loop nucleation instead of a reduction of defect production. The author used the work of others to develop a simple schematic describing the concentration profile of interstitials near the free surface (Figure 13, bottom). It was postulated that dislocation loop nucleation would be suppressed in a wide region adjacent to the defect sink due to the low interstitial supersaturation.

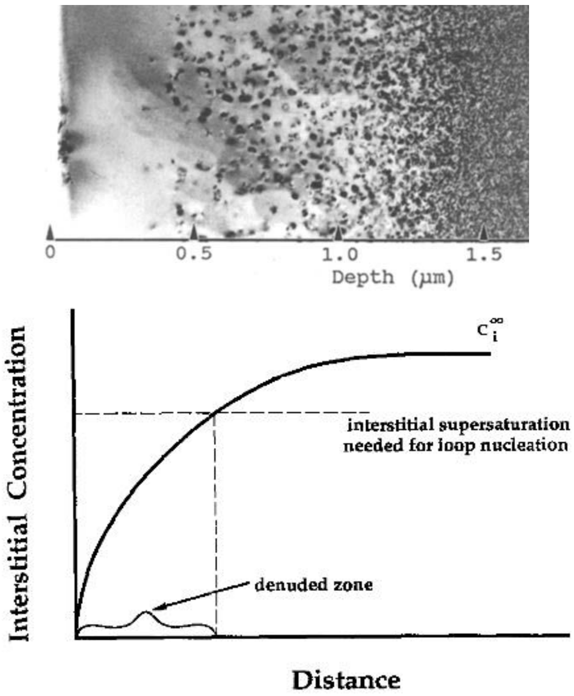

Figure 13. Denuded zone in $MgAl_2O_4$ [23].

Dislocation loops were prevented from forming in the region near the sink where the interstitial supersaturation was below a critical value needed for loop nucleation. The so-called denuded zone has a width proportional to $\sqrt{\boldsymbol{C_i^\infty D_i/P}}$ where $\boldsymbol{D_i}$ is the interstitial diffusion rate, P is the damage rate, and $\boldsymbol{C_i^\infty}$ is the nonequilibrium interstitial concentration away from the sink. $\boldsymbol{C_i^\infty}$ is dependent on the survival of point defects and $\boldsymbol{D_i}$ such that $\boldsymbol{C_i^\infty} \propto \sqrt{\boldsymbol{PD_v/D_i}}$.

Therefore, at defect sinks such as dislocations, grain boundaries, or free surfaces a concentration gradient arises with the non-equilibrium concentrations of point defects in the material giving rise to diffusion of point defects to sinks. As a result, the production of point defects by cascade events does not proceed with full impunity, but instead a competition arises between the production of defects and the recombination or annihilation of interstitials and vacancies at defect sinks. The graphic solution the diffusion equations for a low sink density pure metal during low temperature irradiation are shown in Figure 14 [35]. During linear buildup, the concentration of interstitials and vacancies are too low for recombination or sinks to play a role. In the quasi-steady state regime, the buildup of point defects levels off as recombination balances the defect production rate. The effect of diffusion becomes apparent as true steady state is reached. Because the interstitials diffuse much more readily than vacancies, their relative equilibrium concentration is much lower. Interstitial loss to the sink also decreases the recombination rate, thereby increasing the vacancy concentration above that found in the quasi-steady state.

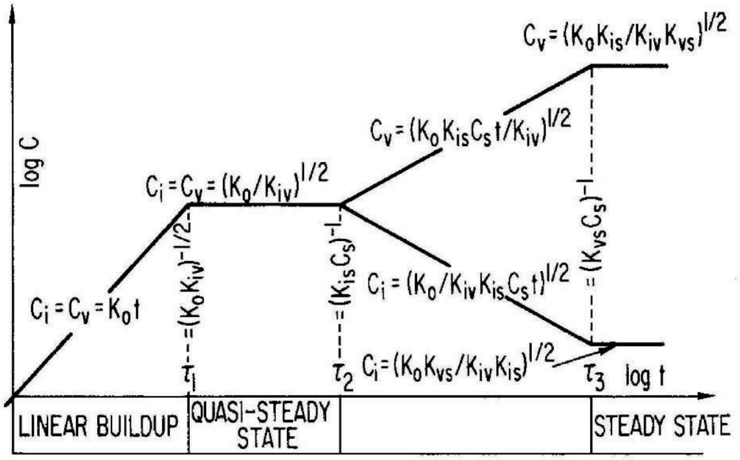

Figure 14. Point defect concentrations in a low temp, low sink density irradiation [35].

Irradiation-induced diffusion has implications beyond the increase in diffusion rate from radiation-enhanced diffusion coefficients. If solute atoms in the matrix have a preferential association with either the interstitial or vacancy defect flux, they may segregate within the material. If the sink is a grain boundary, it will be enriched by atoms diffusing as interstitials and depleted of atoms that exchange preferentially with vacancies. This mechanism is referred to as radiation induced segregation and is responsible for changes in grain boundary chemistry in many multicomponent alloys including: Cu-Li and AI-Li [83]; Mo-Re [84]; Ni-Cu [85]; and perhaps most important to nuclear reactor applications, Fe-Ni-Cr [86-88]. Most of the theory for radiation induced segregation has been focused in the Fe-Cr-Ni alloy system, including austenitic stainless steels (AISI 304L, 316L) and nickel based alloys. The primary proposed mechanism is the inverse Kirkendall effect where interstitials preferentially migrate by one atom type while vacancies exchange preferentially with another atom type. Evidence for this mechanism is found in the fact that $d_{Cr}^{V} > d_{Fe}^{V} > d_{Ni}^{V}$ in austenitic alloys implies there will be a preferential coupling even if it is assumed that $d_{Cr}^{I} = d_{Fe}^{I} = d_{Ni}^{I}$, which must be assumed since the relative diffusion coefficients for atom-interstitial diffusion are not known [35].

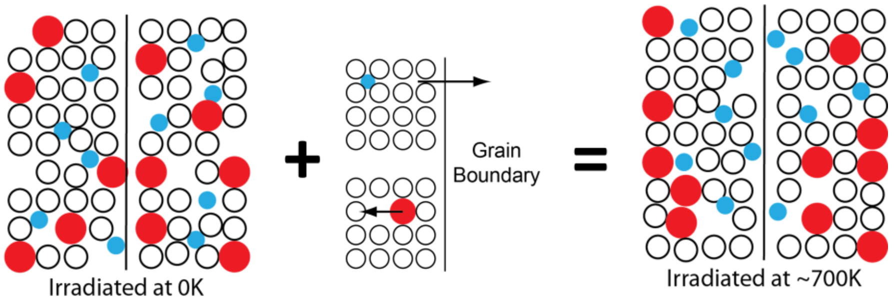

Figure 15. Simplified schematic of radiation induced segregation (RIS).

Extensive experimental work has been done to measure the effects of radiation induced segregation at grain boundaries in the Fe-Cr-Ni alloy system as a function of temperature, irradiation dose, and composition [89-97]. Of primary interest is the chromium content which can drop several percent at the grain boundary, sensitizing the material to intergranular corrosion. While the composition profile is normally recorded as a V-shape drop in Cr content (Figure 16), an interesting feature sometimes appears in the 5-10nm wide segregation profile for chromium - a characteristic W-shape consisting of a peak concentration at the boundary bounded on either side by a depleted zone which has a chromium concentration below that of the bulk. The leading theory for this profile is that chromium is first enriched at the grain boundary through thermal segregation before being depleted by RIS. Thermal segregation in FCC Fe-Cr-Ni consists of the formation of $M_{23}C_6$ carbides at the boundary and an adjacent depleted zone at high temperature. Support for this theory is that a high purity AISI 304L steel is less likely to display the W-shaped composition profile, which agrees with previous observations of thermal segregation [94].

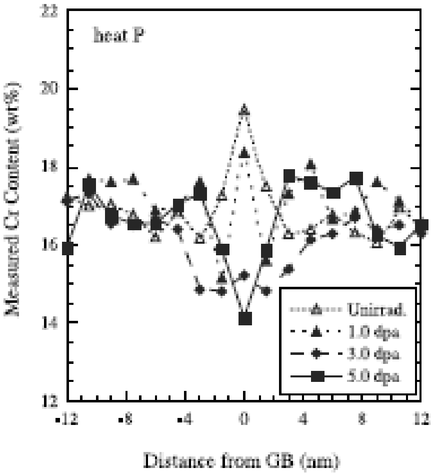

Figure 16. STEM-EDS of a GB in 304L [95].

2.1.4 Defect Clusters and Denuded Zones

Although the production bias model has gained considerable attention, and is required to explain some observations in irradiated materials, the motion of individual point defects is still by and large the most commonly used way to describe the motion of defects to grain boundaries. Very limited experimental work [33, 98] has been performed to explore the contribution of defect clusters to the flux of interstitials and vacancies to the grain boundary, but this work has indicated that point defects bound in interstitial clusters and dislocation loops may also be transported to the boundary by mobile dislocation clusters and loops, or through pipe diffusion along immobile frank loops that have grown close to the boundary by climb. Figure 17 shows the absorption of a small defect cluster by a grain boundary in nanocrystalline nickel. The loop, indicated by an arrow, diffused toward the GB accompanied by continuous reduction of its diameter before being fully absorbed and annihilated by the grain boundary.

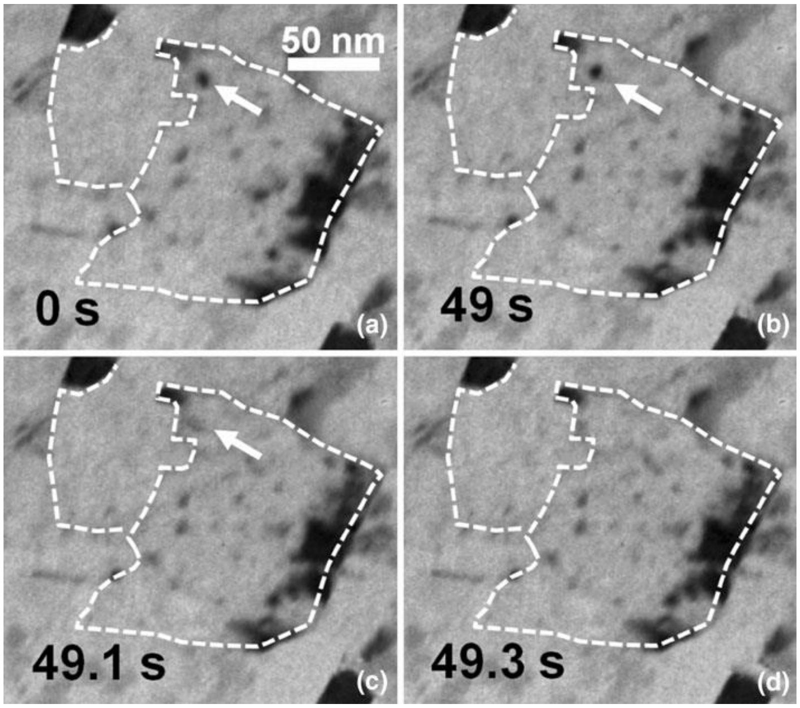

Figure 17. ***In-situ* TEM of a defect cluster being absorbed by a grain boundary in nanocrystalline Ni [33].**

A second mechanism has also been proposed for irradiation induced segregation based on the formation of mobile defect-solute complexes. Solute atoms may bind with a point defect cluster (i.e. vacancy or interstitial loop) so that if the defect complex diffuses to a sink, the solute is dragged along with it. Mobile defect-solute complexes have been shown to be important in segregation in dilute alloys [99] but it is more difficult to define a defect-solute complex in concentrated alloys. Predictions of grain boundary segregation by this mechanism in concentrated Fe-Cr-Ni alloys tend to over predict the effects, whereas the Kirkendall effect can be made to fit experimental data rather well [35]. The theory may still be applicable to dilute solutes such as silicon in concentrated Fe-Cr-Ni alloys. Figure 18 shows a reconstruction of atom probe tomography data [100] wherein nickel and silicon rich precipitates (bound to loops) are seen to be denuded from the region near the grain boundary leaving the boundary itself enriched.

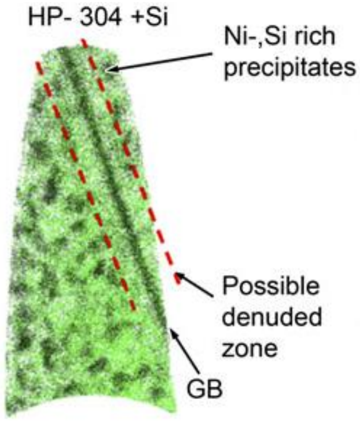

Figure 18. APT of a 304L GB [100].

2.1.5 Grain Boundary Character Dependence

Identifying the nature of a grain boundary in a polycrystalline material requires defining the degree of misorientation between the two grains and the orientation of the grain boundary plane. Therefore, to distinguish one boundary from another five macroscopic degrees of freedom are required (i.e. boundaries can be described using Brandon's criterion [101]). Defining the grain boundary character is important because significant property variations can exist depending on structure of grain boundary. Figure 19 shows three examples of boundary structures that form by rotating one crystal about a single axis (twist). Panel A shows a Σ3 {112} coherent twin boundary. The Σ notation denotes a special type of grain boundary known as a coincident site lattice (CSL) boundary which have misorientations such that 1/Σ of the lattice points coincide, creating a regular and ordered configuration with low energy. The boundary with the highest coincidence is the Σ3 coherent twin boundary where one in three atoms sits on a coincident site. This type of boundary has a very low configurational energy, low stress, and low free volume. Rotating slightly off of the Σ3 {112} orientation creates a semicoherent grain boundary (Panel B). In this case, the energy of the boundary has increased significantly. The boundary has large stress fields that extend into the lattice, but still has relatively low free volume. Further rotation of the grains with respect to one another can result in an incoherent or random high angle boundary where the free volume is very high but the stress is relatively low (although not as low as the coherent boundary). The work by Samaras et al. [76, 77] showed that the interstitials are attracted to regions of high tensile stress and accommodated by the free volume, indicating that both of these features are required in the boundary for it to act as an efficient sink. Therefore it is important to study radiation damage as a function of grain boundary character as these boundaries may exhibit strongly different behavior.

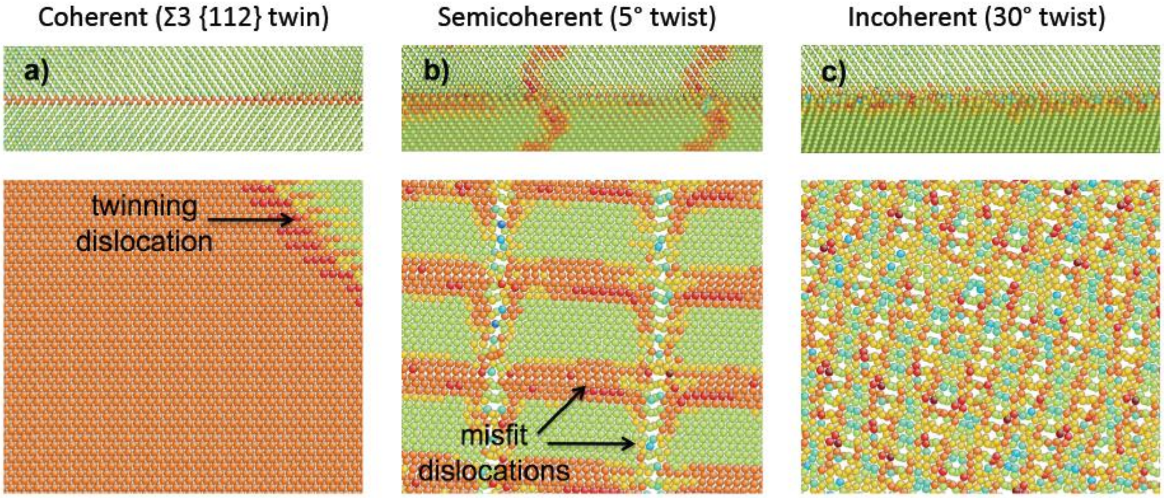

Figure 19. Example grain boundary structures (Dr. Mike Demkowicz, MIT).

Although the studies in the previous sections noted an influence of grain boundaries on radiation damage (e.g. the denuded zone), no particular attention was paid to the structure of the grain boundary. Very few studies have taken into account boundary structure when examining the presence of denuded zones in a material. Figure 20, taken from a paper by Griffith et al. [27] was used to discuss the effect of interstitial vs. vacancy mobility on defect cluster formation; however, it can also be noted from the image that each of the boundaries shown in the micrographs denuded zones that are distinctly different in width.

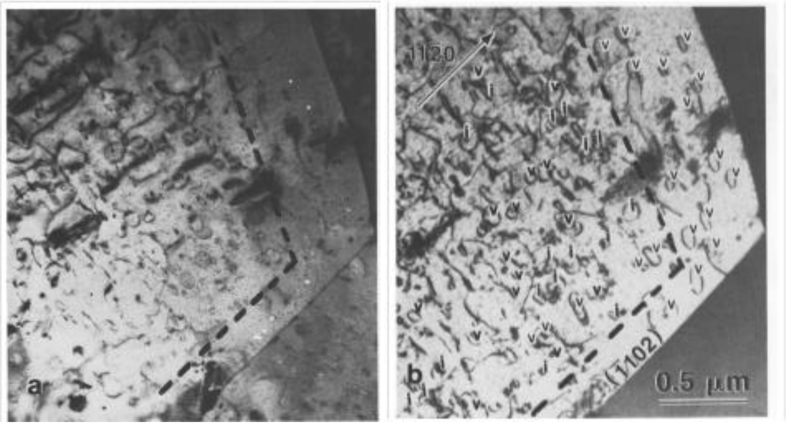

Figure 20. Grain boundary denuded zones in Zr alloys [27].

Some studies have attempted to experimentally determine the dependence of grain boundary denuded zones on grain boundary character. A recent paper by Han et al. [26] studied the dependence of the width of void-denuded zones on grain boundary characters in Cu irradiated with He ions at elevated temperature using transmission electron microscopy correlated with GB misorientations and normal planes determined by electron back-scatter diffraction. They found that the void denuded zone widths at Σ3 <110> tilt grain boundaries ranged from 0 to 24 nm and increased with the grain boundary plane inclination angle. For non-Σ3 GBs, VDZ widths were much wider, ranging from 40 to 70 nm and generally increased with misorientation angle.

While general trends were observed in the denuded zone widths as a function of grain boundary character, there were indications that more factors were at play than simply the boundary structure. The authors found considerable scatter in the data, indicating that the remaining crystallographic parameters may also play a role in determining the sink efficiencies. Additionally, the width of the void denuded zone was often different on each side of the same grain boundary in the case of some asymmetrical boundary. Voids were also observed within GB planes and their density and radius also appeared to depend on GB character.

In addition to having an effect on defect clustering, grain boundary character is thought to play a significant role in radiation induced segregation. Scientific investigation of the specific influence of grain boundary structure on radiation damage has been limited to a few studies [102, 103]. Sakaguchi et al. has shown that radiation induced segregation is indeed dependent on grain boundary character in proton irradiated stainless steel (Figure 21).

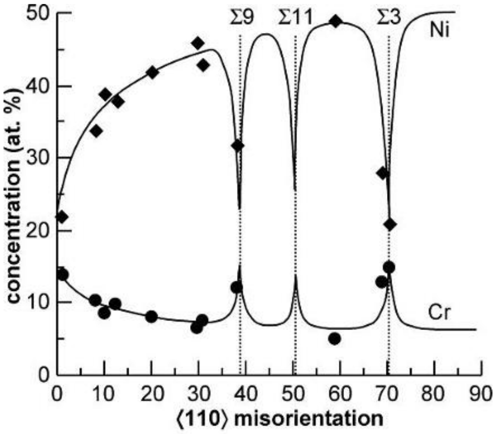

Figure 21. Cr segregation with misorientation [103].

2.1.6 Defect Mobility Effects on the Denuded Zone

Another interesting feature in Figure 20 is that the denuded zone for interstitial loops is much wider than that of vacancy clusters. Both vacancy loops (marked with a "V") and voids (white circles in the underfocused image at left) are found within the region denuded of interstitial dislocation loops (indicated with the letter "I"). The micrographs of the denuded zone are evidence of the relative mobilities of the point defect species. The higher mobility of interstitials leads to a wider denuded zone, and additional vacancies are able to cluster to form voids because vacancy recombination with interstitials is reduced in the denuded region.

2.2 Defect Formation in Iron

Since the focus of this thesis is on the radiation behavior of iron, it is important to outline the current understanding of radiation damage in ferrous metals. The behavior of iron under irradiation is quite unique. It is not only different from HCP and FCC materials, but also presents a significant deviation from even other BCC metals such as Mo and W. The effects of neutron and ion irradiation in iron have been studied experimentally in detail. The first studies were indirect, involving measurements of changes in mechanical properties, electrical resistivity, and diffusivity. It was understood that irradiation produced point defects affected these properties, but direct observation of the microstructure was not attempted until the late 1950's. The first attempts in iron were unsuccessful [104, 105], but were quickly followed by Eyre in 1962 [106, 107] who was the first to image point defect clusters in iron. Although iron has been the subject of a vast number of studies, the fundamental processes driving the formation of microstructural features (e.g. dislocation loops and voids) are still under much debate. In the following sections, the culmination of 50 years of research of irradiation in iron is presented amounting to the current state of knowledge.

2.2.1 Microstructure of Irradiated Iron

The microstructure of irradiated iron (Figure 22) consists primarily of two types of dislocation loops - one having a Burgers vector **b**=1/2<111> and the other **b**=<100>. Among the first to be observed were dislocation loops comprised of pure <100> edge dislocations with **b**=<100> lying on the {100} plane in pure iron irradiated at 500-600°C [108]. This type of dislocation loop is unique to iron amongst the BCC metals, and its mechanism of formation is still unknown. Dislocation loops with a Burgers vector of **b**=1/2<111> were first seen by Dr. Ian Robertson in his Ph.D. work [109]. The formation mechanism of the **b**=1/2<111> type loops is fairly well understood, but the habit plane is still not fully known. Robertson determined the shape of the loop was consistent with a circular loop lying within about 10° of the $(1\bar{1}1)$ plane and identified them as pure-edge or close to pure-edge in character [109]. Arakawa found that the habit plane of the **b**=1/2<111> loops appeared to range from approximately {110} to {111}[110]. Similarly, Hernández-Mayoral et al found that dislocation loops with **b**=1/2$[\bar{1}11]$

appeared to lie on the (111) plane and not the $(\bar{1}11)$ plane, and were therefore not of pure edge type.

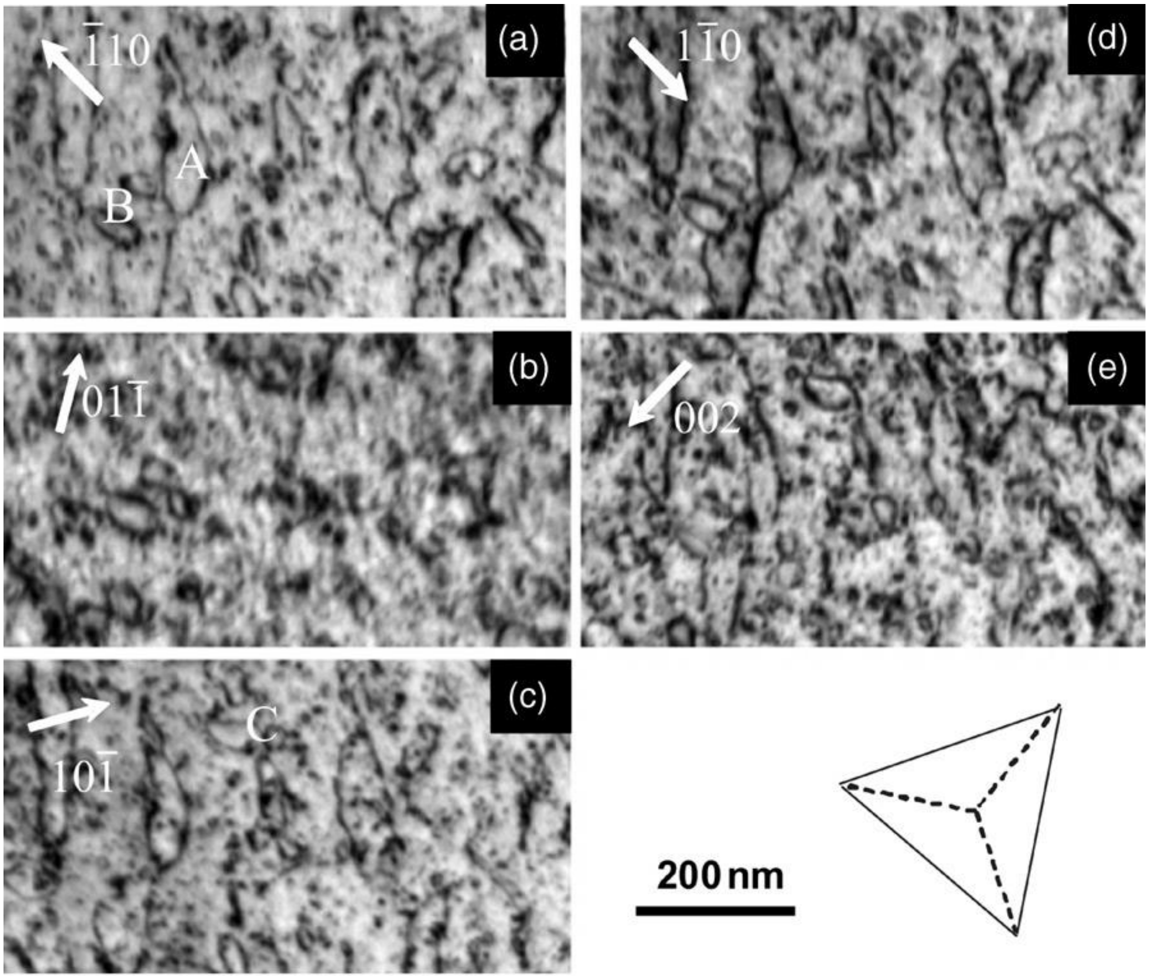

Figure 22. A series of TEM micrographs using different reflections to show dislocation loops in UHP Fe irradiated with 150 keV Fe+ ions to a dose of 1.6x1019 ions cm-2 (~10 dpa) at 300°C. The large loops have ½<111> Burgers vectors [69].

Due to the difficulty of the microscopy needed to identify the nature of the dislocation loops [109, 111], the structure of the dislocation loops is often ambiguous. Loops with

b=1/2<111> and **b**=<100> have been identified both as interstitial in nature [21, 69, 109, 110, 112-114] and vacancy in nature [48, 69, 115]. Vacancies are also known to form micro-voids or loose vacancy sponges, which are detectable by positron annihilation experiments [116] but not by TEM until very high doses [69]. Electron microscopy of irradiated defects relies on the interactions of electrons with the long-range strain fields associated with prismatic dislocation loops (i.e. closed vacancy loops) [49, 69, 115]. Voids, however, do not have a large strain field and are more difficult to see in the TEM until they reach several hundred vacancies (1-3nm) in size so that they create Fresnel contrast [117]. The formation of microvoids is far preferential to the formation of vacancy dislocation loops in iron [117].

2.2.2 Defect Production

The formation of the irradiated microstructure is the result of the survival rate of the defects from the cascade, the form those defects take, and the mobility of the interstitials and vacancies created. The production of defects in iron from a cascade follows the principles of the production bias model [34, 64, 65]. The short timescale of cascade events makes direct experimental observation difficult if not impossible using even today's advanced characterization techniques. Indeed the first studies of the cascade damage in iron were performed using calculations of classical equations of motion in high-speed computer in 1964 [55]. This model was able to show that the result of the primary knock on collision was a chain of displacements that favor <111> and <100> directions. Atoms displaced in this way required 17eV for the <100>, 34eV for the <110>, and 38eV for the <111> directions. It also showed that interstitials favored a dumbbell configuration along the <110> direction.

More advanced computational simulations have been the main focus of study for cascade events in iron since the initial study by Erginsoy. Molecular Dynamics became the method of choice after work by Calder and Bacon [57, 118], who modified the MOLDY code by Finnis [119]. This work became the basis of many more MD simulations which have become more sophisticated as computation hardware advances [58, 59, 120-122].

Molecular dynamics has shown that, for α-Fe, the most stable configuration of small clusters (< 10 SIAs) is a set of <111> crowdions [35]. Next in stability is the <110> crowdion. These crowdions also may act as nuclei for the formation of perfect interstitial dislocation loops with Burgers vector 1/2<111> or <100>, respectively. A significant portion of the interstitials produced during the cascade are clustered together. Malerba [122] summarized the predictions for the production of interstitial clusters based on several different potentials. The results show that up to three quarters of the interstitials produced in the cascade are in the form of clusters, which has significant impact on the formation of the irradiated microstructure.

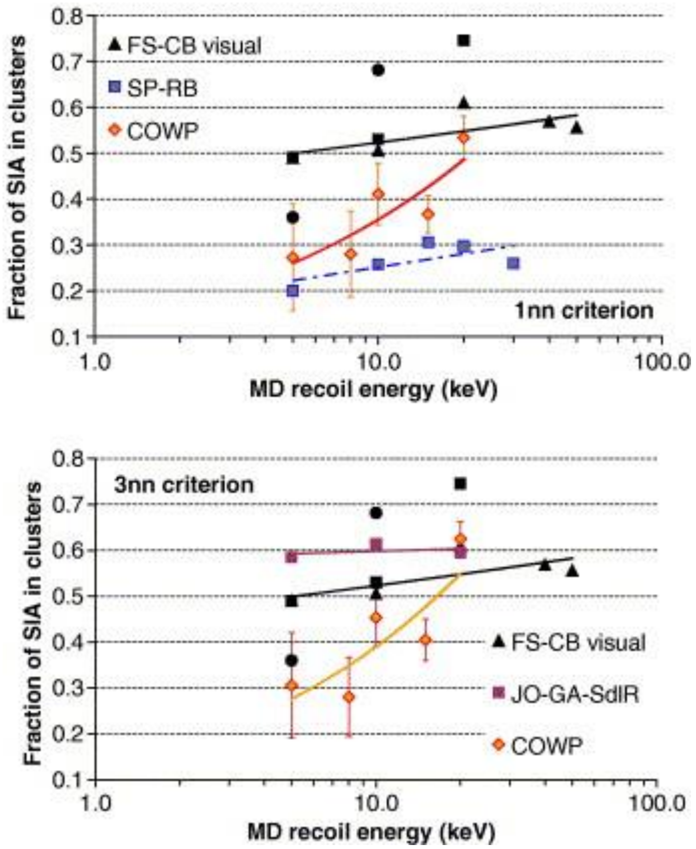

Figure 23. SIA clustered fraction obtained from different potentials using 1 nn (above) and 3 nn (below) criteria for the analysis [122].

The interstitial clusters produced in the cascade are highly glissile, which contributes to a number of damage phenomena found in iron (the mobility will be discussed in a following section). For example, the high mobility of interstitial clusters formed in cascades is thought to permit them to drift to defect sinks, enabling excess vacancies to form microscopic voids [67].

The stability of vacancy clusters is low relative to interstitial clusters, as can be seen in Figure 24 that is based on MD simulations of cascades in iron. One of the most stable configurations for vacancy clusters in iron are either a set of di-vacancies concentrated on two adjacent {100} planes which results in a perfect dislocation loop with Burgers vector <100>

after growth. Another is a set of first nearest neighbor vacancies on a {110} plane that unfaults into a perfect loop with Burgers vector 1/2<111>. Vacancy loops can also exist in the faulted configuration. The loops will generally unfault to form perfect loops when the number of vacancies reaches about 40 [12]. However in all cases the formation of microvoids is far preferential to the formation of vacancy dislocation loops in iron [117].

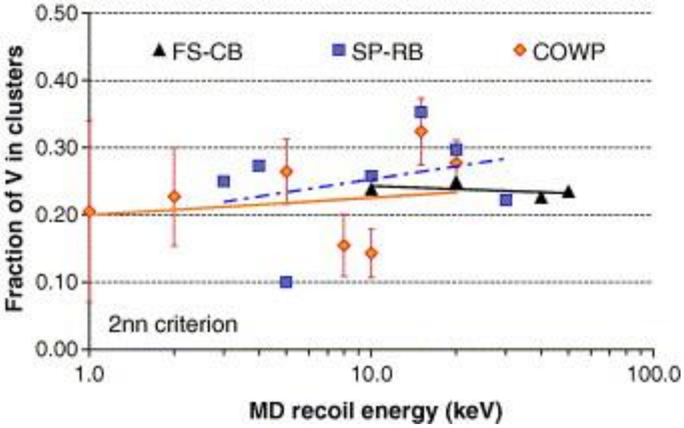

Figure 24. Vacancy clustered fraction obtained from different potentials using 2 nn criterion for the analysis [122].

Cascade events in iron were first experimentally studied by Jenkins et al. in 1978, who explored the impact of low-dose heavy-ion irradiation by studying α-iron irradiated at room temperature to doses of ≤$5x10^{12}$ ions cm^{-2} with heavy ions (Fe^+, Ge^+, Kr^+, Xe^+ and W^+) at energy between 40keV and 240 keV [48]. It was found that self-ion irradiation with any energy did not produce radiation damage, indicating that displacement cascades in a-iron produced by self-ions do not collapse to dislocation loops at room temperature. This is in strong contrast to the results from self-ion irradiation, in the same energy range, of both FCC and BCC metals of similar atomic weight such as Cu, Ni and Cr, where vacancy loops appeared to form from the center of each cascade. They were able to show, however, that the defect yield increased with ion mass (Figure 25). They showed that this effect was driven primarily by the size of the cascade volume, not the number of displacements created by the collision. The larger volume meant that longer diffusion was required for recombination, leaving more point defects available to form clusters.

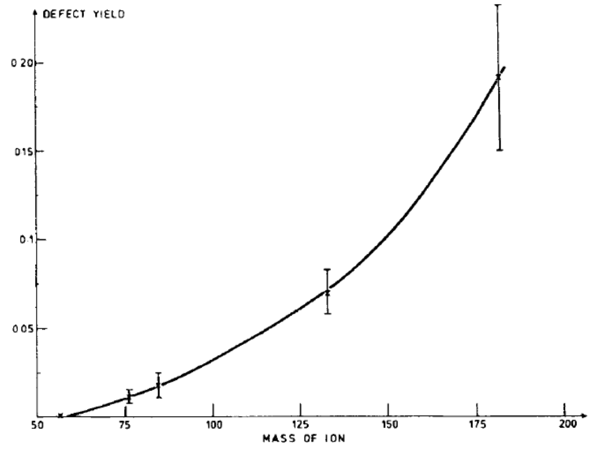

Figure 25. Defect yield from a cascade as a function of ion mass [48].

The very high mobility of interstitial clusters makes it questionable why large interstitial loops have been observed in TEM investigations of irradiated iron [69]. An explanation for this phenomenon can be found in the work by Terentyev et al. [68]. Their molecular dynamics simulations showed that small interstitial defect clusters with complex structure and very low mobilities can be formed by nonparallel <110> dumbbells. These clusters could act as trapping sites for other interstitial clusters and serve as a nucleation site for larger interstitial loops.

"The growth of microscopic voids during the irradiation of metals is due to the preferential drift of interstitials to dislocations, thus allowing the excess vacancies to accumulate at voids. The preference arises from the stronger interaction between a dislocation and an interstitial than between a dislocation and a vacancy." [67]

2.2.3 Glide of small defect clusters

Both interstitial [115, 123, 124] and vacancy clusters [125] have been predicted to be highly mobile in body centered cubic metals. Self interstitial atom clusters have an extremely low migration energy (∼0.02 eV) [126] and are mobile even at low temperatures. For very small defect clusters (i.e. di- and tri- interstitials), the motion is three-dimensional due to the cluster's ability to rotate to equivalent burgers vector directions by rearrangement of the crowdions. Larger SIA clusters (larger than 4 interstitials) in iron exhibit generally only one-dimensional glide along the crowdion direction [127, 128]. For interstitial clusters of all sizes, the sequence of jumps is not random, but favors the direction of the previous motion [129].

Generally, larger loops are less mobile than small loops. Based on molecular dynamics simulations, the critical size above which the predicted mobility is practically zero is about 300 SIAs (~2.4 nm) in iron [130]. However, in TEM experiments, much larger SIA loops exhibit 1D migration above 450 K and the critical size in iron may be as large as 20 to ~30 nm [110]. In a TEM, the strain fields observed from defect clusters are 2-5nm across. When SIA clusters reach a comparable physical size, about 300 SIAs or 2.4nm in diameter, the thermally activated mobility of the cluster has decreased substantially [130]. Nevertheless, SIA clusters of this size still exhibit considerable mobility in iron. *In-situ* transmission electron microscopy experiments have enabled the direct observation of rapid one-dimensional glide, or loop hop, of microscopic

b= 1/2<111> interstitial defect clusters (Figure 26) [18, 110, 115, 124, 131]. In ultra high purity iron at 300°C, the one dimensional loop jumps observed along the <111> direction were estimated to occur at a velocity of at least 103 nm s^{-1} [18].

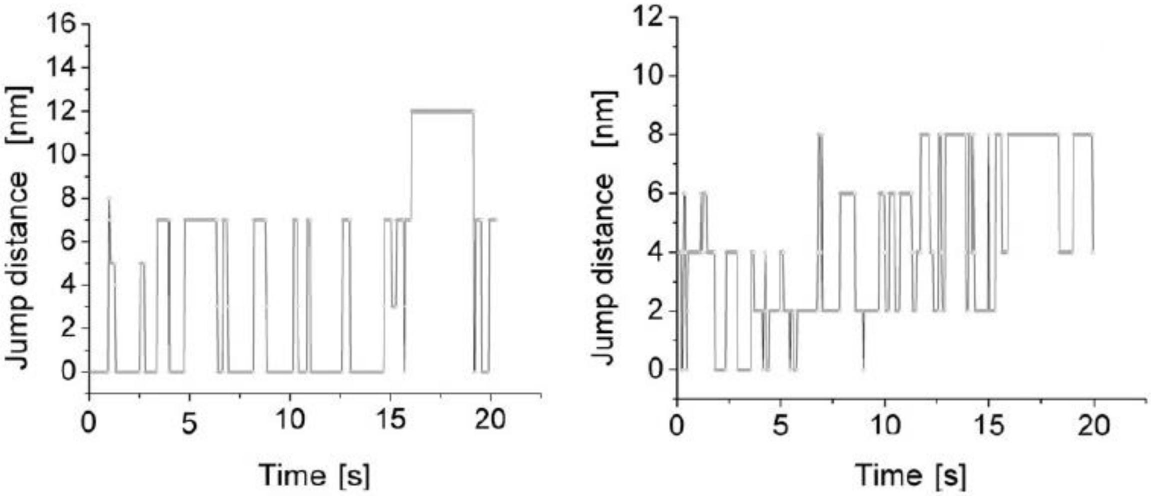

Figure 26. One-dimensional loop hop measured in pure iron [115].

Although the majority of the motion observed is one dimensional, Arakawa et al. have also shown that a microscopic defect cluster may change direction by spontaneously transforming from one 1/2<111> Burgers vector to another 1/2<111> without the influence of a visible external contact from a dislocation [110]. A change in Burgers vector may also arise from two intersecting **b**=1/2<111> clusters of approximately the same size, which react to form a loop of <100>{110} that reorients to become a stable, immobile <100>{100} loop [132]. In the likely event that one of the original **b**=1/2<111> loops is larger than the other, the smaller loop is absorbed creating a single loop and leaving the Burgers vector unchanged [69, 132, 133].

2.2.4 Growth and nucleation of loops from small defect clusters

The formation of a large number of one dimensionally mobile SIA clusters under irradiation has been used to provide a proper explanation for morphology of voids [64, 65, 134, 135], as well as the formation of SIA cluster rafts [136, 137] and the decoration of dislocation loops with SIA clusters [137, 138]. Furthermore, the reaction of defect clusters to form larger clusters plays a fundamental role in the development of the irradiated microstructure. The majority of the SIA clusters formed by cascade events are sub-microscopic, but quickly coalesce to form microscopic SIA clusters (e.g. those having a strain field visible in TEM) and, ultimately, dislocation loops [69, 115]. TEM observations have shown that larger (2-5nm) glissile defect clusters have been shown to cooperatively align to form strings of **b**=1/2<111> defect clusters. Dudarev et al. [139] showed experimentally that two adjacent 1/2[1 1 1] clusters (or small loops) undergo correlated 1D diffusion via the elastic interaction between them. They can then coalesce (Figure 27) [69, 133] into large interstitial dislocation loops with **b**=1/2<111> [18, 69, 115, 133, 140]. These large dislocation loops then continue to grow by absorbing further point defects and clusters.

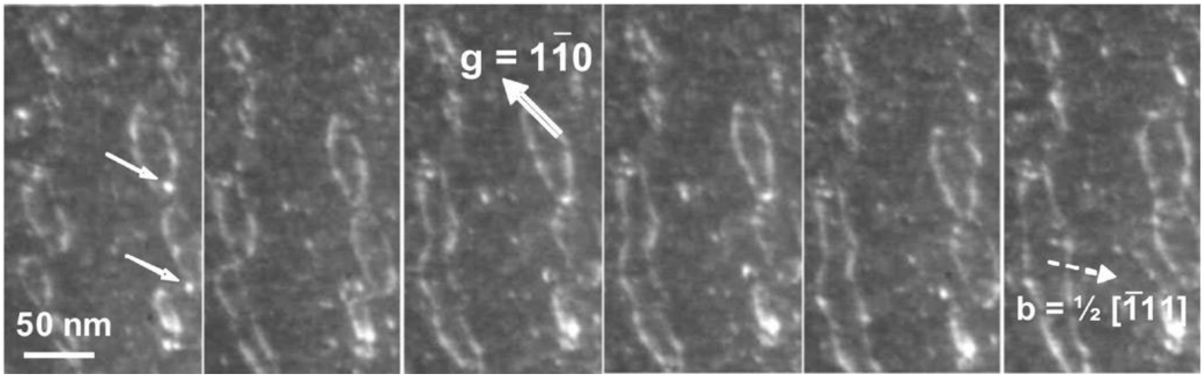

Figure 27. Series of still frames from a video recording of loop growth and coalescence in UHP Fe irradiated with 150 keV Fe+ ions at 300°C over a dose range from about 1019 ions m-2 (~6.5 dpa) to about 1.6x1019 ions m-2 (~10 dpa). Weak-beam micrographs taken with $g=1\bar{1}0$. The projection of the Burgers vector of the loops is shown [69].

2.2.5 Morphology of Irradiated Iron

The proportion of **b**=1/2<111> and **b**=<100> loops that are formed varies strongly with temperature. Trends for the relative proportions of loops with each Burgers vector observed using transmission electron microscopy of iron irradiated using iron ions are shown in Table 1. This data shows that there is a transition in the populations of defect clusters from 1/2<111> to <100> as the temperature rises, with the transition point being below room temperature. However, it should be noted that the results reported for room temperature irradiation of iron [115] were from grains with a film normal of (001) which is a favorable crystallographic orientation for slip to free surfaces [18]. This could influence the final populations of the 1/2<111> and <100> defect clusters as the glissile 1/2<111> clusters would be preferentially lost.

Table 1. Relative population fraction of b**=1/2<111> and b=<100> defect clusters in iron as a function of temperature.**

Material	Ion	Dose	T_{irr}	1/2<111>	<100>
(011) Fe [141]	50keV Fe+	10^{17} ions m^{-2}	40K	77%	23%
(001) Fe [115]	100keV Fe+	$2x10^{18}$ ions m-^{2}	RT	14%	86%
(011) UHP Fe [115]	150keV Fe+	10^{18} ions m^{-2}	300°C	10%	90%
(011) Fe [18]	150keV Fe+	10^{17} ions m^{-2}	500°C	<1%	>99%

More recent work by Yao et al. [140] confirmed there is a transition from loops with **b**=a/2<111> loops to loops with **b**=a<100> that occurs around 400°C (Figure 28). Their work along with that of Dudarev [142, 143] explained this transition as being the result of the relative stabilities and mobility of the ½<111> and <100> dislocation loops. The stable form of dislocation loop transitions from **b**=1/2<111> to **b**=<100> due to a reduction in the shear stiffness constant as iron approaches the α→γ transition temperature at 912°C due to instabilities in the magnetic spins. The calculations showed that at temperatures below 350°C, only hexagonal prismatic pure-edge dislocation loops with **b**=1/2<111> are stable, and above 550°C, only square **b**=<100> edge loops become stable. These results correlated well with the experimental observations by Yao et al. who were also able to show that the dominance of the <100> type loop at elevated temperatures is also a result of the relatively high loop mobility of **b**=a/2<111> loops. Once formed, the defect clusters can quickly migrate to free surfaces or to more stable defect structures like the <100> loops at higher temperatures.

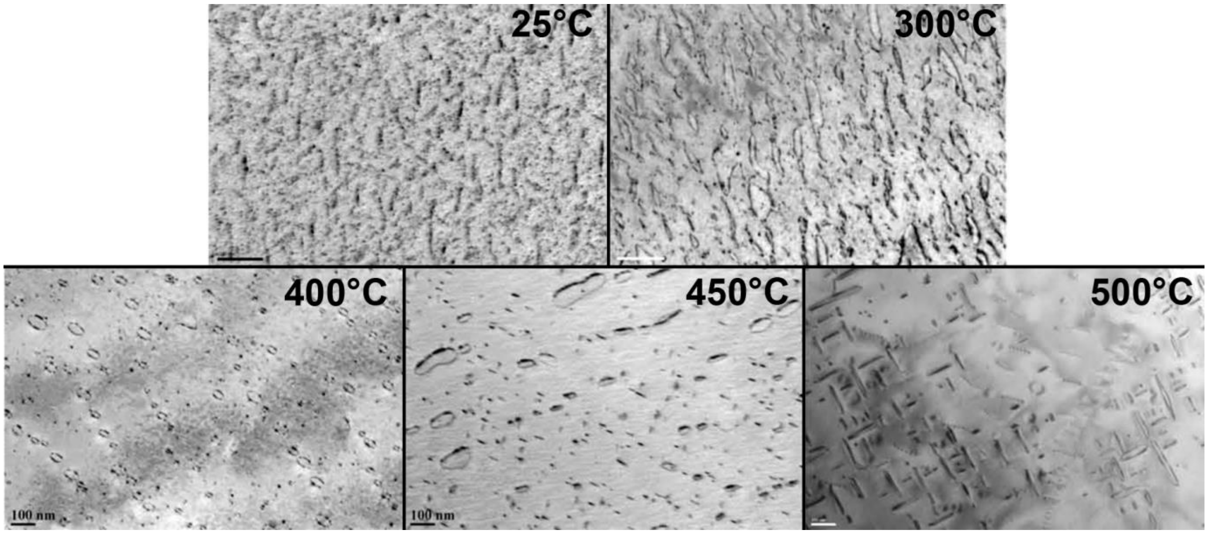

Figure 28. Temperature effects in irradiated micron grain size iron from [144].

2.3 Nanocrystalline Materials

Nanocrystalline materials are generally defined as having a grain size less than 100nm, differentiating them from microcrystalline (>1μm grain size) and ultrafine grain (100nm-1 μm grain size). Nanostructured materials can be further classified based on the number of dimensions in which the material has nanometer modulations. Thus, they can be classified into (a) layered or lamellar structures with one nano-sized dimension, (b) filamentary structures that are nano-scaled in two dimensions, and (c) equiaxed nanostructured materials that are nanoscaled in all three dimensions [145]. The majority of research on nanostructured materials is performed on equiaxed, or three-dimensional, crystallites which are most often produced and have a wide range of applications. Some research is directed toward 1D or nanolayered materials for both electronic and radiation tolerant applications [145], while only minimal work has been done on 2D-filimentary type nanostructures.

As the grain size of a material is decreased through these size regimes, processes that typically occur in the grain interior (e.g. dislocation emission from Frank-Read sources) become less influential and the properties of the grain boundaries become dominant. In materials with a grain size on the order of 10nm, about 50 vol. % of the material consists of grain boundaries [146] and the behavior is remarkably different than the microcrystalline material. At this grain size, it is theorized that grain boundary structures relax, thus further altering the properties of a nanocrystalline material.

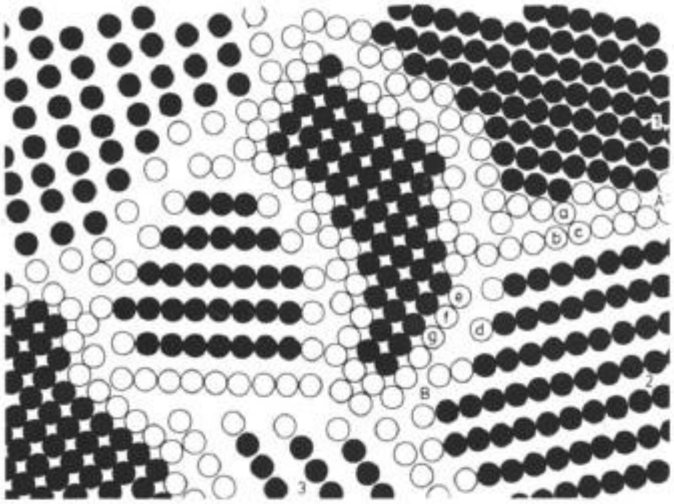

Figure 29. Schematic representation of a nanocrystalline material distinguishing between the atoms associated with the individual crystals (full circles) and those constituting the boundary network (open circles). The boundary atoms are shown in regular lattice positions but in reality will relax to form different atomic arrangements [146].

Nanostructured materials may exhibit very high strength, increased diffusivity, reduced sintering temperatures, useful catalytic properties, and attractive physical properties.

2.3.1 Production Methods for Nanocrystalline Materials

Nanocrystalline materials can be created in a number of ways, each of which provides different advantages and drawbacks. The two main categories of manufacturing techniques are top-down and bottom-up. Top-down refers to breaking down bulk, often microcrystalline, materials to smaller and smaller components until a nanocrystalline cell size is reached. The most common method of achieving this is through severe plastic deformation (SPD) of a material with the desired chemistry.

Bottom-up methods involve building a nanostructured material from the atomic level upwards. This can be done by techniques such as inert-gas condensation [147], physical/chemical vapor condensation, electrodeposition [33, 148], spray pyrolysis, high-temperature evaporation, flame synthesis, plasma synthesis sol-gel, chemical reduction, and biological techniques [145]. They generally permit precise control of the microstructure and chemistry, but are not suitable for making large monoliths. Top-down methods are useful for synthesizing large amounts of a nanocrystalline material. This category includes mechanical alloying [149], high energy ball milling [149], equal channel annual pressing [150, 151], high pressure torsion [151], and accumulative roll-bonding [152].

2.3.2 Mechanical Properties

The strength of polycrystalline materials has long been established to be a function of the grain size of the material, perhaps as far back as the late-Neolithic period [153]. Study of this effect was initiated independently by Hall [154] and Petch [155], which ultimately led to the empirical relationship

$$\sigma_y = \sigma_0 + kd^{-\frac{1}{2}}$$

where σ_y is the yield strength, σ_0 is a friction stress below which dislocations will not move in the material in the absence of grain boundaries, *k* is a constant, and *d* is the grain size. The typical textbook explanation for this trend is that strengthening occurs due to the pileup of dislocations at grain boundaries. This mechanism was first proposed by Cottrell [156] in 1958 who calculated the stress ahead of a dislocation pileup.

$$L = \frac{nGb}{\pi\tau_{xy}}$$

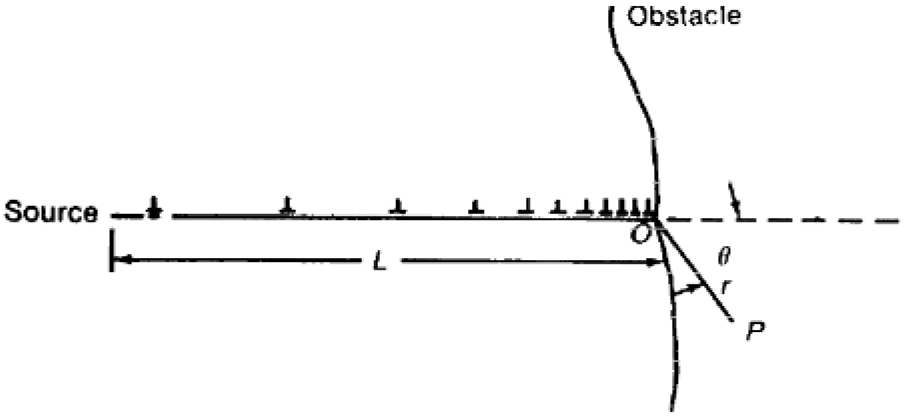

Figure 30. Dislocation pileup at an obstacle such as a grain boundary leads to a stress buildup (KL Murty, unpublished).

Dislocations emitted from Frank-Reed sources in a grain will travel to the boundary and pile up. The length of the pileup is considered to be the width of the grain. When the magnitude of the stress ahead of the pileup is high enough, a Frank-Reed source in the adjacent grain may be activated, continuing the spread of plastic deformation. The experimental results of many microcrystalline materials, including iron alloys, have been fit to the empirical relationship by Hall-Petch with some success [157-160].

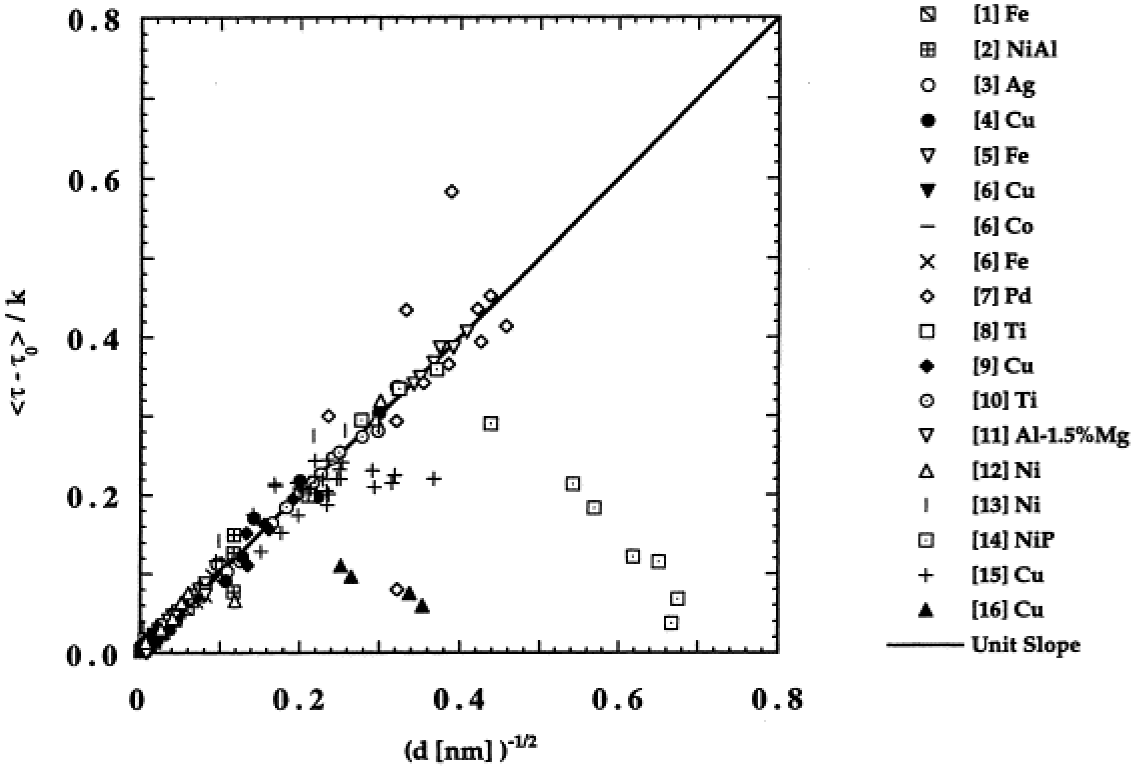

Figure 31. Compilation of scaled yield stress data for several metallic systems [160].

The Hall-Petch relationship and the primary proposed mechanism of dislocation pileup are not, however, without flaws. The Hall-Petch equation, for instance, predicts strength values approaching theoretical strength for small grain sizes. The Cottrell dislocation pileup mechanism breaks down when the grain size is on the order of the distance between two dislocations in the pileup. In some cases, too, dislocation pileups are not seen at all [145]. Other mechanisms have been proposed in order to explain the d^{-n} dependence with $n = 1/2$, including dislocation emission from grain boundary steps [161, 162] or stress concentrations at grain boundaries [163]; however, these too have their drawbacks.

Part of the difficulty in finding a solution to the Hall-Petch relationship may be in the empirical equation itself. It has been pointed out over the years that much of the available data can be fit equally well using other exponentials such as $n=1/3$ or $n=1$ [164-167], which calls into question the fundamental significance of the Hall-Petch equation. Recent work by Dunstan and Bushby [168] approaches this problem head-on, and proposes that the grain size effect is the same effect observed in the epitaxial growth of thin films, or in the mechanical testing of small scale specimens. Namely, that grain size strengthening is driven by constraints on stress and dislocation curvature according to the space available to them.

Much of the literature regarding the mechanical properties of fine grained materials is written in terms of the Hall-Petch relationship, despite the fact that the results of these experiments are among the drivers of the discussion of the validity of the $n=1/2$ relationship. Even shortly after the advent of nanocrystalline materials [169], alternative concepts for deformation were being proposed [170]. This was before experimental research by Chokshi et al. indicated that nanoindentation results for ultrafine grain Cu and Pd deviate from their microcrystalline counterparts (that is, from the Hall-Petch relationship) [171]. The results shown in Figure 32 show that a similar trend exists for iron. Below about 250nm, the microhardness of iron begins to deviate significantly from the Hall-Petch relationship. This behavior is known as Inverse Hall-Petch, because the slope can become negative.

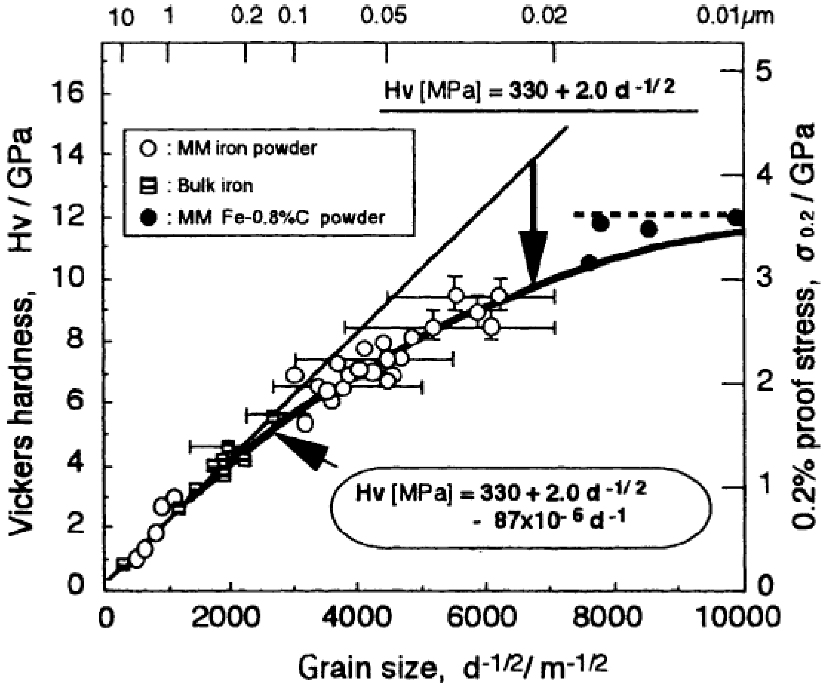

Figure 32. The hardness of iron as a function of grain size [172].

A number of models have been proposed to explain the deviation from the empirical Hall-Petch relationship. Most models for IHPE behavior fall into at least one of four categories: dislocation-based models, diffusion-based models, grain-boundary-shearing models, and two-phase-based models. Borrowing from the current Hall-Petch relationship, the following diagram (Figure 33) was devised by Koch [173] based on the work of Masumura et al. who were the first to show that the Hall–Petch plot for a wide range of materials and mean grain sizes could be divided into three distinct regimes [160]. At microcrystalline grain sizes (>1μm), dislocations are emitted from both grain boundary sources and from Frank-Reed sources. Dislocation pileup occurs at grain boundaries driving the Hall-Petch type relationship. As the grain size is decreased to the ultrafine grain regime (~100nm-1μm), grain boundary dislocations sources become increasingly important. Full dislocations are emitted from grain boundaries and sweep across the grain before hitting the far grain boundaries. Substantial changes occur in the nanocrystalline regime (<100nm). The dislocations emitted from grain boundaries are partial dislocations (at least in FCC materials where most of the work has been done). If the grain size is small enough, dislocations are not able to form in the grains, and deformation is accommodated by non-dislocation based mechanisms such as grain boundary sliding or rapid diffusion.

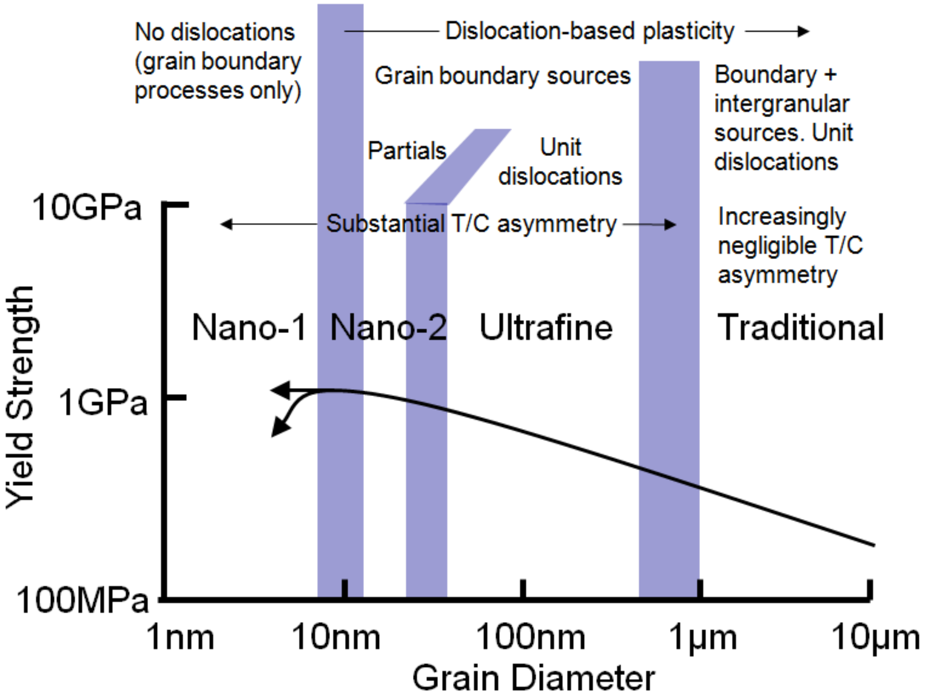

Figure 33. The hardness of iron as a function of grain size [173].

The trends outlined by Koch for Figure 33 are the result of a considerable amount of research into the mechanical behavior nanocrystalline materials, which have been the subject of over 500 publications and several review articles [174]. The vast majority of this work has been performed in FCC materials by both *in-situ* [175-179] and *ex-situ* [180, 181] transmission electron microscopy as well as molecular dynamics simulations [182-187]. Only preliminary work has been performed in BCC metals, and has mostly been confined to ex-situ mechanical testing of iron produced by severe plastic deformation [159, 172, 188-192], with some experiments on Fe thin films [193] and gas-condensated Fe [194] and some molecular dynamics simulations [195, 196].

In general, the Hall–Petch relationship has been found to be maintained for iron down to a grain size of around 200nm as is shown in Figure 32 [172]. Uniform elongation completely disappears in iron with grain size less than 1 μm [172] which is thought to arise due to the formation of characteristic shear bands in nanocrystalline iron [189]. However these shear bands result in a significant flow softening, in addition to a significant reduction in the strain rate sensitivity of the flow stress [188]. The molecular dynamics work recently performed by Jeon et al. [195] has shed some light on the deformation mechanisms of nanocrystalline iron, finding that the average flow stresses were found to increase with grain size reduction down to 14.7 nm. Below that grain size, the flow stresses were found to decrease with further grain refinement, indicating a deviation from the Hall–Petch relationship. Furthermore, the major deformation mechanism was found to be dislocation glide down to a grain size of 19.7 nm. Below that, grain boundary sliding becomes increasingly dominant until it is the primary mode of deformation at a grain size of 3.7nm. This result has not yet been confirmed experimentally, and more extensive work is needed in BCC metals to determine the primary deformation mechanisms.

2.3.3 Radiation Tolerance

Nanocrystalline materials not only present the opportunity for superhardness, high strength, ductility, corrosion resistance, and fatigue resistance, they show promise as radiation tolerant materials [174]. The observations of denuded zones in irradiated materials, outlined in Section 2.1.3 gave rise to the idea that if you decrease the grain size enough the denuded zones will overlap, dramatically reducing the amount of radiation damage remaining in the grain. This is likely to occur in nanocrystalline materials where interfacial regions can account for up to 40% of the total volume in a 10nm grain material, providing excellent sinks during the collapse of cascade defects. Among the first published images of this effect was that of Yamada et al. in 1992, republished in 1994. In the TEM image in Figure 34, denuded zones can be seen in each of the grains in a sample of $MgAl_2O_4$ irradiated with Ar^+ ions to 12 dpa at a nominal temperature of 420°C. It is clear that as the grain size decreases, the area fraction denuded of defects increasing, thus reducing the overall damage in the grain.

Figure 34. Defect-free regions adjacent to grain boundaries in MgAl2O4 irradiated with Ar+ ions to 12 dpa at a nominal temperature of 420°C [24].

Subsequent work attempting to utilize this effect in has shown that nanocrystalline grain size causes resistivity changes in irradiated Au [197, 198], leads to reduced amorphization of $MgGa_2O_4$ [199] and TiNi [30], and has been shown by TEM to reduce defect clustering in ZrO_2 [31], Pd [31], Cu–$0.5A_2O_3$ [32], and Ni [32, 33]. Work by Rose et al. [31] showed that radiation induced defect formation was prevented in ZrO_2 when the grain size reached less than 15 nm and in Pd grains when the grain size was less than 30nm (Figure 35).

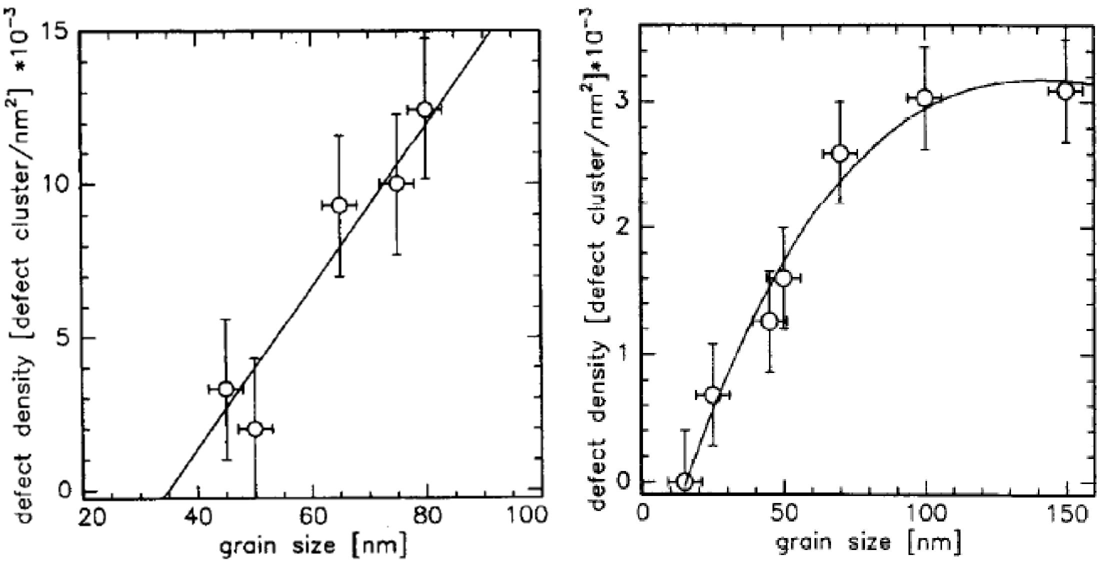

Figure 35. Grain size effect on interstitial loop formation [31].

All of the work outlined in the previous paragraph was performed *ex-situ*, and the research on the mechanisms of radiation tolerance in nanocrystalline materials is limited, particularly for iron. Research in nanocrystalline iron has heretofore been limited to modelling work. Samaras et al. [76-78] and Stoller [59, 75, 120] have recently focused their attention to nanocrystalline BCC iron. Samaras et al. used molecular dynamics to study a 15 grain, 1.4 million atom model of 12nm BCC Fe grains. Their model showed that, consistent with previous research, self interstitial atoms are extremely mobile. The interstitials are attracted to high tensile regions in grain boundaries, where they annihilate with the free volume found in these regions. The result of the high mobility of interstitials is that only vacancy defects were found to remain in the grains, allowing large vacancy structures to form. Subsequent work which included pre-existing voids showed that the voids act as sinks for interstitials, though the lower strain near the void means fewer of the interstitials are attracted to the void. The subsequent fate of vacancy defects could not be investigated in these studies because they are immobile on the timescale of the MD simulation.

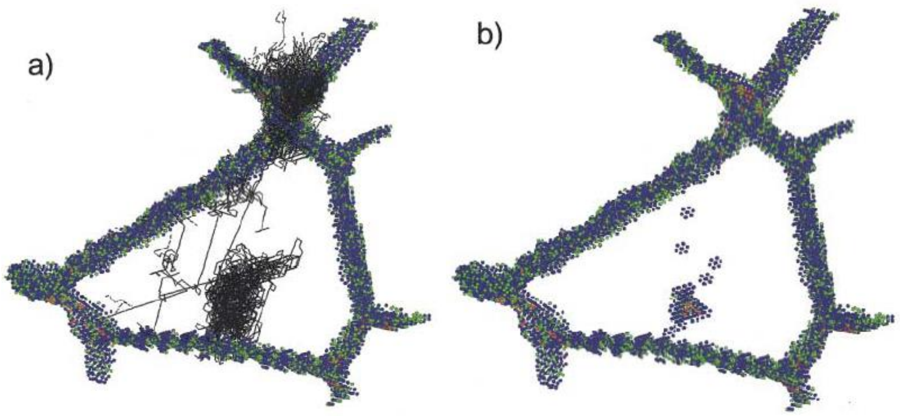

Figure 36. a) Point defect paths during cascade & b) residual defects in the grain [78].

Stoller et al. [75] investigated the effect of cascades with energies of 10-20keV and temperatures from 100-600K in 10nm grained nanocrystalline iron via molecular dynamics. Their model verified that nanocrystalline grain size has a strong influence of grain size on primary damage production including: reduced interstitial survival and clustering; excess vacancy production; and reduced formation of interstitial loops & increased void formation as compared to an intragranular cascade event [75].

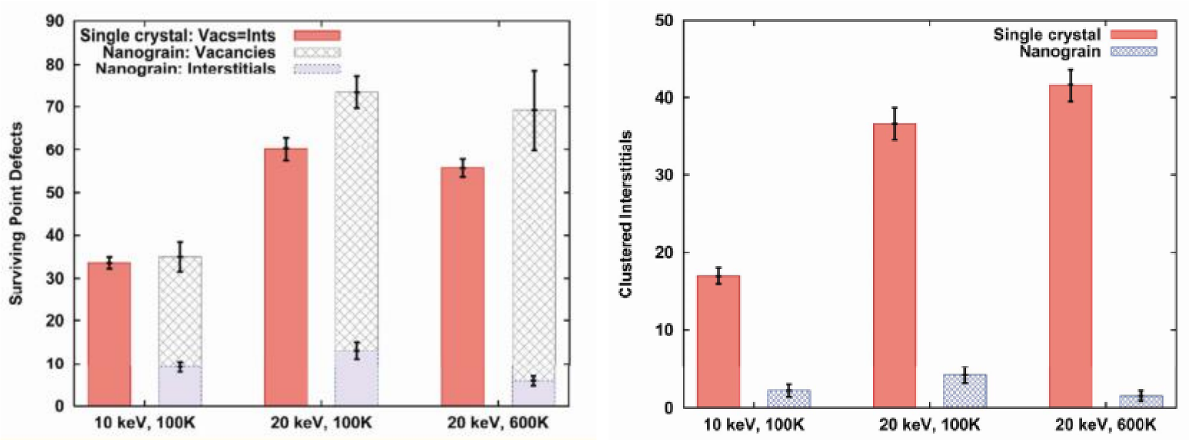

Figure 37. Defect retention in nanocrystalline iron via MD simulations [75].

Although the results of the models show a strong influence of grain size on primary damage production, the use of molecular dynamic simulations limits the solution to primary defect movement after the primary cascade event. The vacancy annihilation mechanism proposed by Bai et al. [81] is likely applicable to nanocrystalline materials as well. On longer timescales, the residual vacancies and interstitials will also diffuse driving the formation of the denuded zone free of point defect clusters along grain boundaries in many polycrystalline materials [70, 200].

This principle has also been used to create nanolayered materials [29, 201-204] specifically designed to reduce radiation damage occurring from either point defect accumulation or from the formation of helium bubbles. Demkowicz et al. created a one-dimensional reaction–diffusion model of a crystalline layer bounded by two interfaces to describe the radiation tolerance of nanolayered material (Figure 38). The result shows the reduction of average defect concentrations and concentration gradients near interfaces for l = 5 nm compared to l = 25 nm.

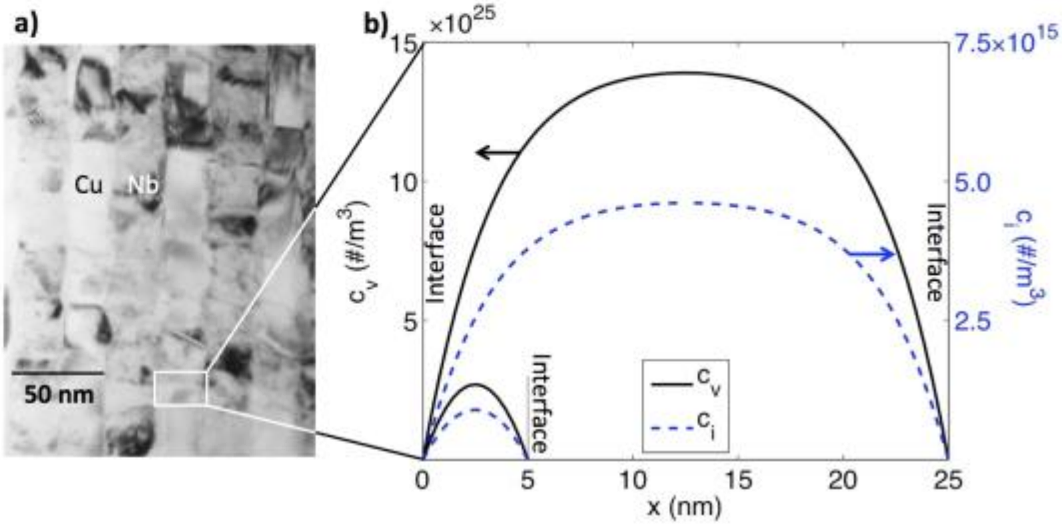

Figure 38. Point defect concentration profiles in nanolayered composites [82].

CHAPTER 3. METHODOLOGY

The research in this thesis was carried out following the streamlined sequence shown in Figure 39. This process was made possible because of collaborations with Los Alamos, Sandia, and Argonne National Laboratories that allow for an efficient synthesis→characterization→irradiation→characerization sequence, drastically reducing the opportunity for sample degradation. The details of the experimental procedure are outlined in the following sections describing the methodology used to study radiation damage in nanocrystalline BCC iron.

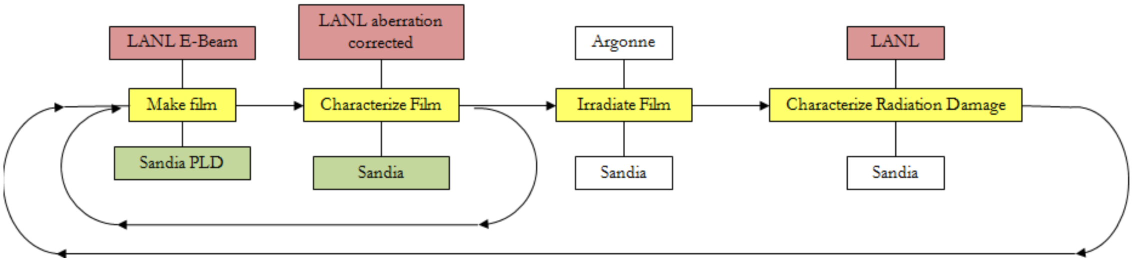

Figure 39. Streamlined experimental approach.

3.1 Deposition of Iron Thin Films

3.1.1 General Methods

Nanocrystalline materials may be manufactured by several means, but perhaps the most advantageous for transmission electron microscopy is the preparation of a free standing metal film by physical vapor deposition. Depositing a film of 80nm-120nm creates an electron transparent film that enables the direct observation of radiation damage using *in-situ* transmission electron microscopy. A planar sample of constant thickness is essential to minimize the effects of point defect loss to the surfaces which can greatly affect the observed morphology of point defect clusters and their motion [18, 35, 111, 205]. When coupled with a grain size less of <1 micron, the line length of grain boundaries present is greatly increased, providing an effective means of analyzing the interaction of defects with grain boundaries. Processes such as physical vapor deposition enable the creation of pure, fully dense materials with nanocrystalline (<100nm) grain size and a controlled grain aspect ratio and crystallographic texture.

For this work, nanocrystalline Fe and Fe-Cr films were deposited using three physical vapor techniques at the Center for Integrated Nanotechnologies at Los Alamos National Laboratory (LANL), and a fourth in the Ion Beam Laboratory at Sandia National Laboratories Albuquerque. Initial work at LANL was carried out using electron-beam deposition, sometimes combining the process with thermal evaporation of an iron wire following procedures from literature (described below). Eventually sputter deposition at LANL was chosen as the primary deposition method for the nanocrystalline films. Specimens used for the tensile experiments (Chapter 13) were created using pulsed laser deposition (PLD) at Sandia.

3.1.2 Specimen Chemistry

The specimens sputtered at LANL used a sputter target acquired from Kurt J. Lesker Company (Clairton, Pa, USA) that had a nominal composition as shown in Table 2. The composition of the sputter target was of higher purity than the 5N purity iron (so-called “Hawthorne” alloy 1A, containing about 0.01 wt% impurities including 0.013 wt% C, see Nicol et al. [206] for the full composition) alloy used by Jenkins et al. in their study of radiation damage in iron [115]. It was also higher in purity on a metals basis than the single crystal iron (99.99+%, 4N+) used in the work by Jenkins et al., and contained only slightly more carbon than the ultra-high purity (UHP) alloy used in the same study that was reported to contain 1 ppm C, 55 ppm N, 510 ppm Si and very small quantities of other impurities.

Table 2. Compositions of the alloys used in this study in comparison with that used in literature. All values are reported in ppm by weight.

	Drexel Bulk [Carpenter]	Drexel Sputter Target [Lesker]	Jenkins et al. "Hawthorne" 1A [115, 206]
Carbon	9	27	130
Manganese	20	1.5	170
Silicon	<50	44	<150
Phosphorous	<20	7.2	50
Sulfur	5	7	50
Chromium	<50	3.8	<150
Nickel	<50	12	NR
Molybdenum	<20	0.34	<150
Copper	<20	1.2	<150
Cobalt	<20	NR	NR
Titanium	<20	0.54	<150
Aluminum	<30	10	<60
Niobium	<20	<1	<150
Zirconium	<20	<1	NR
Boron	<5	3.5	NR
Nitrogen	<10	1	290
Oxygen	292	84	1100
Tungsten	NR	0.05	340
Tin	NR	0.05	<150
Vanadium	NR	0.04	<150

*NR means the value was not reported

3.1.3 Film Thickness

Time of deposition was used to control specimen thickness. To determine the time required for a given thickness, a long sputter was performed on a glass slide with on portion of the slide masked off. After deposition, the mask was removed, and the height difference between the glass slide and film was measured using a contact profilometer. The average deposition rate was calculated from the values. Subsequent depositions on sodium chloride substrates were time-controlled in order to achieve the desired thickness. After deposition, the thickness of the films was verified with one or more methods including Rutherford Backscattering Spectroscopy (RBS), X-ray Fluorescence Spectroscopy (XRF), SEM imaging, and TEM imaging.

An example of the RBS measurement is shown in Figure 40. The results, which show both film thickness and chemistry, indicate that the final film thickness is approximately 75 nm, with the surface consisting of a 10nm layer of iron oxide.

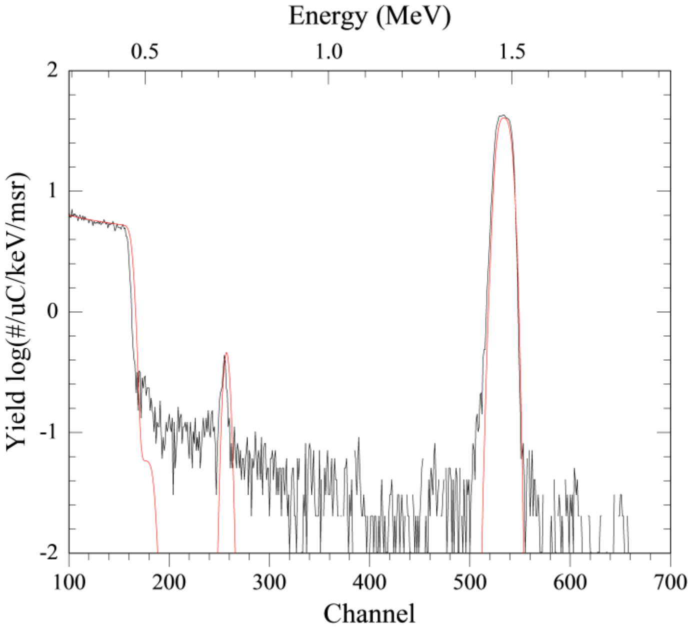

Figure 40. Rutherford Backscattering showing the film thickness of 60nm and an 8nm surface oxide layer.

This method was verified using scanning electron microscopy, which also enabled a qualitative study of the surface roughness of the films. Figure 41 shows the surface and profile of a typical sputter deposited film used in this work. The surface roughness was minimal, with slight variations in height from grain to grain of perhaps 10% of the overall thickness. Also visible on the fracture surface are the columnar grains in the film.

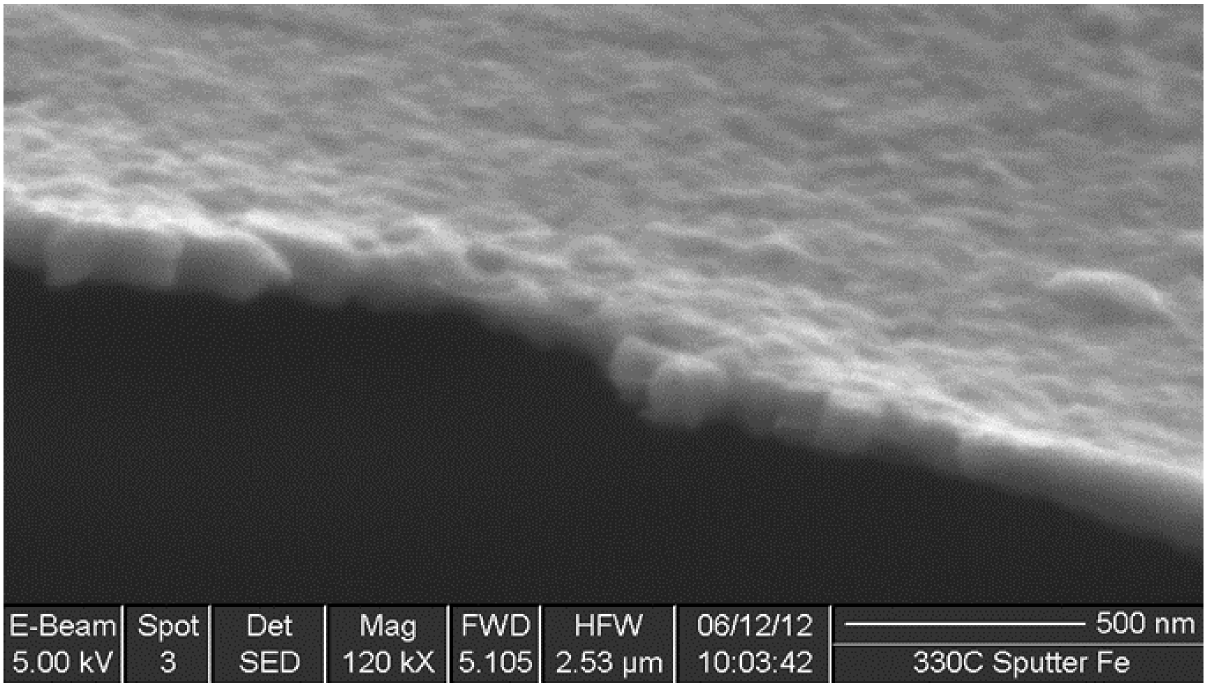

Figure 41. Secondary electron SEM image of a fracture surface of a free standing nanocrystalline iron film.

3.1.4 Substrate

To create free standing iron films, it was necessary to select a substrate that could easily be removed from the film. The most straightforward choice was a water soluble ionic salt. The most common salt is sodium chloride, which is widely available in single crystal form. NaCl with a (001) orientation normal was chosen based on literature on the deposition of iron on NaCl. Physical vapor deposition of iron on salt has long been practiced [207-209]; however, the vast majority of that research [207, 208, 210-213] was dedicated to achieving single crystal iron, and very little is published about the controlled deposition of nanocrystalline thin films. Acquiring a single crystal of iron on (100) NaCl is very difficult due to several factors including: 1) the sublimation of the salt substrate, 2) easy contamination of the salt substrate, and 3) the similar energies of the two most likely orientations.

The practice of depositing iron on salt is complicated by the relatively low vapor pressure of sodium chloride. Sublimation of the substrate increases with temperature (Figure 42), reaching ~1.0 monolayer/second at 440°C which degrades both the vacuum and the quality of the substrate surface. A competition between the sublimation and deposition process means that a low deposition rate (e.g. 1.0Å/sec) at a high temperature (i.e 450°C) generally results in a poor quality film. The two methods to mitigate this problem, lowering the temperature and increasing the deposition rate, are also limited. Lowering the temperature limits the mobility of iron, and the maximum deposition rate is limited by the deposition method. For e-beam deposition, the minimum deposition rate is determined by the energy required to maintain an electron beam and molten iron, generally around 0.2Å/sec. The maximum deposition rate is around 2.0Å/sec due to sputtering of iron in the chamber and damage to the crucible liner. Substrate temperatures between 250°C and 450°C mark the extremes of acceptable film quality, and thus the major parameters for film deposition are bounded.

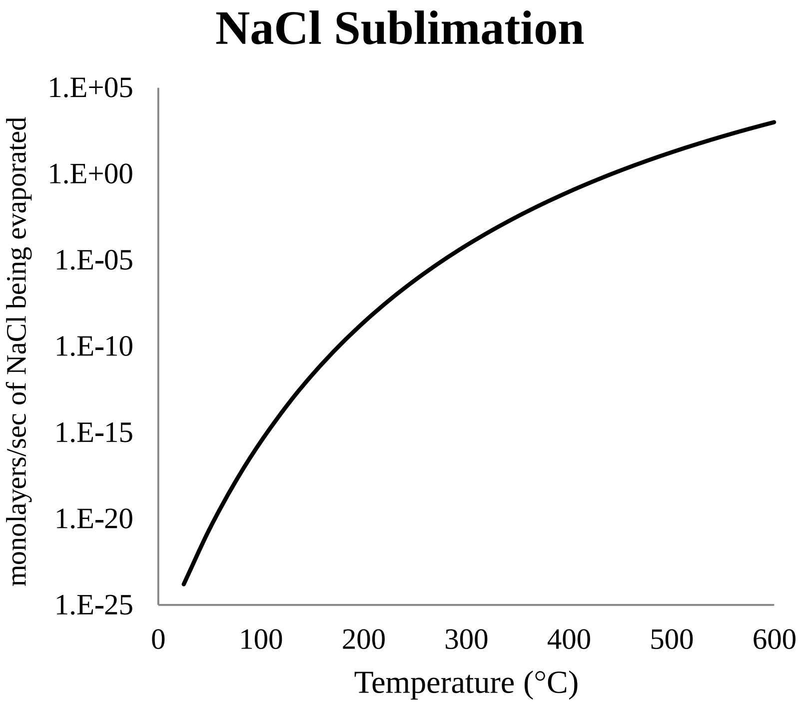

Figure 42. Sublimation rate of NaCl at elevated temperatures.

Within this parameter space, iron has been shown to deposit on (100) NaCl with intermixed grains with two primary orientations [207-210, 213, 214]:

$(100)_{Fe} \,||\, (100)_{NaCl}$ with $[110]_{Fe} \,||\, [001]_{NaCl}$

$(100)_{Fe} \,||\, (100)_{NaCl}$ with $[001]_{Fe} \,||\, [001]_{NaCl}$

The deposition of iron in these two orientations is driven by the nucleation process [Shinozaki 1969] since the nuclei of the two orientations have the same shape and the same planes exposed to the vacuum by virtue of their shared matching plane with the substrate. Therefore the surface energy is the same, and only the film-substrate interfacial energy is different. Since the energy difference is very slight the final film is, at best, a combination of these two orientations. The result is a mosaic of very small crystals with an edge length of 10^{-6} to 10^{-7}cm (i.e. nanocrystalline) [207].

Many attempts were made to consistently deposit single crystal films and while a true single crystal was never fully achieved, these results narrowed down the optimum parameters required for physical vapor deposition of iron on NaCl. For example, Collins and Heavens [210] studied the effect of deposition rate, substrate temperature, and film thickness on the microstructure of the as-deposited film. They found that it was not possible to control the orientation of films deposited at high temperature (400-500°C). Shinozaki and Sato [213] found that baking the substrate at 500°C for 30 min in a vacuum of ~$5x10^{-6}$ Torr and evaporating the iron at a deposition rate of 50-100 Å/min onto a 400°C substrate provided the statistically best films. They noted, however, that the "results still depend a great deal on the possible minor difference in the evaporation conditions, which were beyond our control".

Matthews [211] followed the work of Shinozaki with a study using a methodology previously utilized to deposit single crystal gold on salt. A single crystal of NaCl was cleaved in a vacuum of $1x10^{-9}$ Torr to provide a clean substrate and heated to 410°C. Then a two-step deposition scheme was used to build the iron film. An iron wire was first vaporized 0.6cm from the substrate, depositing a thin iron layer at a high deposition rate (~1000 Å /sec). This was immediately followed by a 500-1000Å deposition of iron at 2.0Å/sec. The resulting film was single crystal iron with the $[001]_{Fe} \,||\, [001]_{NaCl}$ orientation.

From these studies, the parameters for sputter deposition for this work were determined. Many of the previous results were replicated using sputter deposition including the two-step process of Matthews [211], but ultimately deposition techniques were used that referenced the entire body of work. The substrates were cleaned using a high temperature bake following Shinosaki [213], then the substrate temperature was held at a temperature between 370°C (from Shinosaki[213]) and 425°C (several authors [210, 211, 213]) for the deposition. The deposition rate was determined by the stability of the deposition process, since the results in literature showed little dependence on deposition rate.

3.2 Preparation of film specimens for TEM

After deposition, the iron films were removed from the substrate and transferred to TEM grids for in-situ irradiation experiments (Fig. 43). The procedure for this process begins with the preparation of 200 mesh nickel grids whose grid bars are manually painted with M-BOND™ 610 Adhesive (Ted Pella, Inc., Redding, CA, USA). Each grid is then placed on a cleaved section of film and substrate. The epoxy is allowed to cure for one hour at 175°C. Once set, the assembly is placed in a solution of 50% ethanol in deionized water to dissolve the salt. Immediately after separation of the film and grid from the salt substrate, the specimen is dried then rinsed in two containers of anhydrous methanol before being dried and placed in vacuum or desiccated storage for later use.

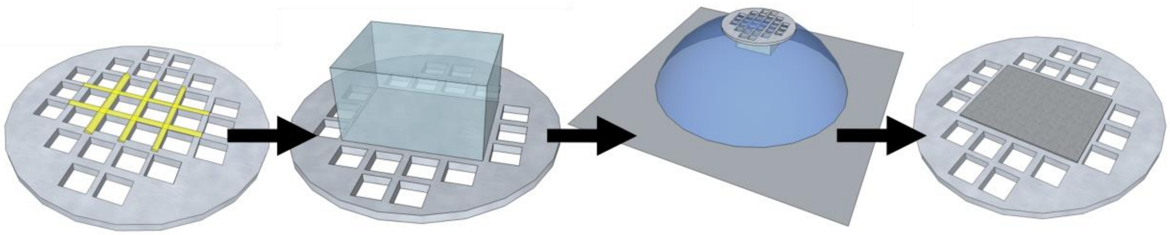

Figure 43. Transfer of Fe films from substrate to TEM grid.

Each TEM specimen prepared by this technique was marked with a focused ion beam (FIB-SEM) as shown in Figure 44. The resulting fiducials made it possible to track regions of interest throughout the annealing and irradiation processes in spite of sample drift, and to characterize the same area in multiple instruments before and after the irradiation. The markers consist of three elements. An arrow on the grid bar of the specimen maintains the location in the event of damage to the film in that grid square. A second arrow is cut into the film itself far from the region of interest and is used to locate the region of interest in the TEM. Finally, a five dot pattern defines the region of interest. The fifth point creates a reverence to orient the user in cases where the sample is rotated or flipped in the sample holder.

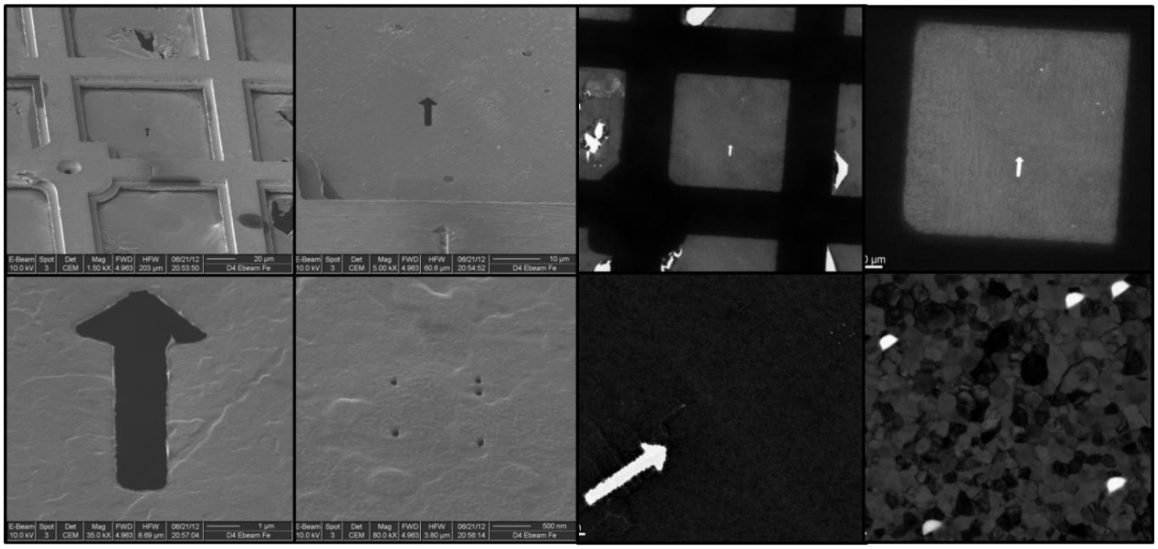

Figure 44. The left four panels show SEM images of the markers created on the Fe film by FIB milling. The right four panels show the same markers in the TEM.

During the FIB preparation, care was taken to make sure the ion beam did not traverse any region outside of the area removed by the ion beam while making the pattern. By default, the ion beam makes a set number of points and then cycles to repeat. For instance, in the case of the single spot in Figure 45A, the FIB hits a set number of x-y coordinate points (in this case all in the same location) each with a set dwell time. Once it has completed that cycle, the beam travels outside the desired region, before returning to the x-y coordinate point and starting the new cycle. This was avoided by only allowing the FIB to make one cycle per marker point, preventing the errant beam pattern shown in Figure 45A. Similarly, in Figure 45B, the FIB by default runs through a cycle on the left point, then moves to the right point for the next cycle, then returns to the left point and so on. Again, the beam is not shut off as the FIB resets, and the sample is exposed to Ga implantation. This is easily avoidable by introducing two separate patterns milled in series.

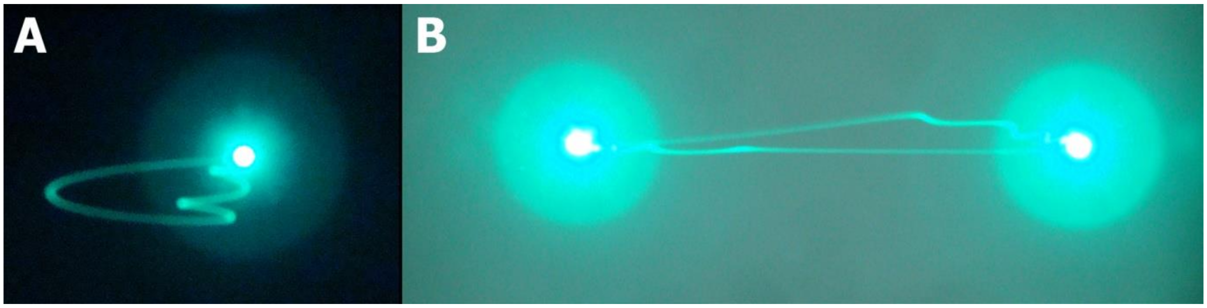

Figure 45. (A) Default path of the ion beam making a single spot. (B) default patch of the ion beam making two spots separated by a set distance.

Although errant Ga implantation was largely preventable, there was some residual damage from redeposition and possible gallium implantation from beam scatter. This damage was found to be easily removed by annealing the film well above the recrystallization onset temperature (~375°C) of iron (Figure 46). During the *in-situ* irradiations, the damage production was observed in a secondary region well outside of the region of interest (i.e. far from the area where Ga implantation and redeposition would have occurred). No visible difference in defect formation from irradiation was found between the region near the fiducial markers and in regions away from them.

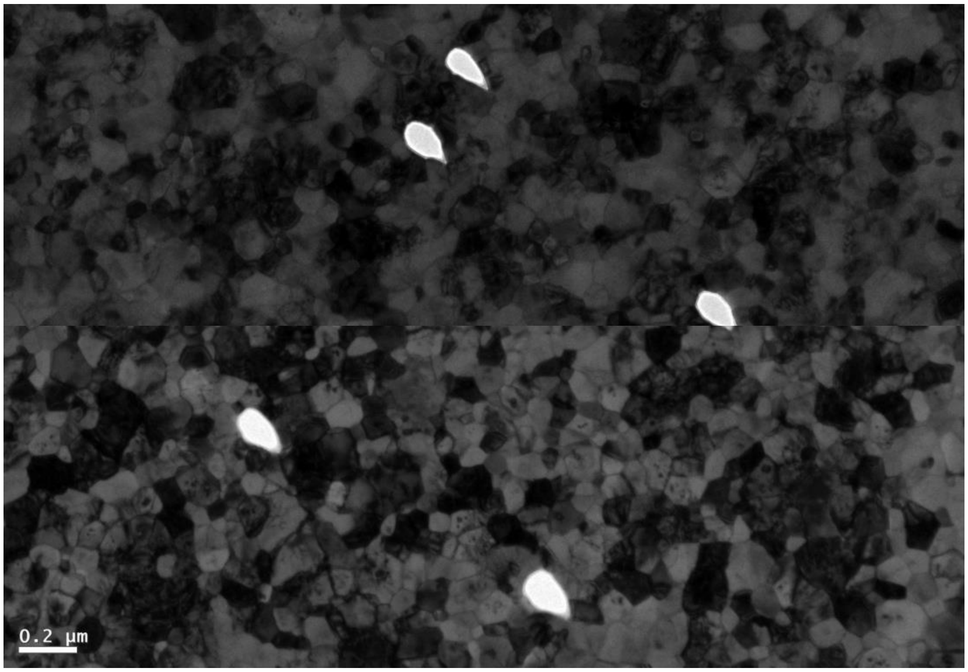

Figure 466. (top) FIB markers in an as-deposited film (bottom) the same area after a 600°C anneal showing the disappearance of the redeposition damage.

3.3 Bulk Specimen Preparation

In order to validate the experimental conditions, it was necessary to study the irradiation behavior of bulk, microcrystalline iron to compare to previous results published by Jenkins et al. [18, 46, 48, 66, 69, 115, 140]. Bulk material for this project was prepared by Carpenter Technology Corporation (Reading, PA). High purity electrolytic iron (Table 2) was melted in a vacuum induction furnace and cast as an ingot measuring 2-3/8 in x 2-3/8 in x 30 in. The ingot mold featured an insulated reservoir “hot top” above the casting to prevent casting shrinkage. Following the casting, a small a nub was removed from the bottom of the casting and used for as-cast sample chemistry.

The iron ingot was then charged into a furnace at 815°C (1500°F) and allowed to equalize before the furnace was ramped to 1065°C (1950°F) and held for 30 minutes. While at temperature, the sample was press forged down from 2-3/8 in by 2-3/8 in to 1-3/4 by 1-3/4 in. The sample was then reheated to 1065°C (1950°F) and held for 30 minutes. Then the sample was reduced in size in a similar manner to 1-1/4 in x 1-1/4 in. Following an air cool to room temperature, the samples were annealed at 760°C (1400°F) for one hour before being air cooled to room temperature (normalized). The hot top was then removed from the sample resulting in a bar 26 inches in length that was then grit blasted to clean the surface. A central portion of the bar was then sectioned using an abrasive saw and subjected to cold rolling to an 80% reduction. Rolling was performed in four steps of 20% reduction, each followed by placing the specimen in a 950°C furnace for 10 minutes to relieve stress and promote recrystallization.

Once 80% reduction was achieved, the resulting section was cut into thin 300μm sheets using electrical discharge machining. A punch was then used to make TEM disks 3mm in diameter. The disks were then flat ground using a dial grinder until they were ≲100μm. Final thinning was accomplished using electro-jet thinning. Early work was done using a Fischione Model 110 Twin Jet Electropolisher. Electropolishing was performed using a solution of 5% perchloric acid in methanol that was chilled to -25°C ±2°C. Temperature was monitored using a digital thermometer, and was controlled using a methanol bath chilled with liquid nitrogen. For the electropolish, the potential between the specimen and electrodes was set at 55V with the current free to vary. The flow rate of the electrolyte was set to between 2 and 4 on the arbitrary scale of the Fischione Model 110.

After jet thinning, the disks were characterized in a FEI XL 30 ESEM equipped with a TSL EDAX OIM 6.0 electron backscattered diffraction (EBSD) system to identify the distribution and type of GBs present in the electron transparent region.

3.4 In-situ Electron Microscopy

Each of the iron samples examined in this work were irradiated in-situ using the dual beam irradiation setup at Argonne National Laboratory's IVEM Tandem facility[215]. This setup consists of a 200kV Hitachi H-9000NAR TEM, the Intermediate Voltage Electron Microscope (IVEM), coupled with a 650kV ion implanter and a 2 MV NEC tandem Van de Graaf generator. The ion beam from these sources enters the TEM at 30° from the electron beam, permitting simultaneous irradiation and observation of materials. The irradiations were performed at controlled temperatures ranging from cryogenic to high temperature. Irradiations below room temperature (15-300K) were performed using a helium cooled double tilt TEM holder (Oxford), while irradiations at room temperature and above (300-1300K) were performed using a Gatan double tilt heating holder. The heating holder was also used to anneal each sample prior to irradiation, including those specimens that were irradiated below room temperature using the cryogenic holder.

Dose calculations were performed using the TRIM (the Transport of Ions in Matter) code in the SRIM (the Stopping and Range of Ions in Matter) program package [216]. For the *in-situ* experiments in this study, irradiations were performed using primarily using 1MeV Kr^{2+} ions accelerated using the 650kV ion implanter. A simulation of 20,000 1MeV Kr atoms was performed using the Quick Calculation of Damage (Kinchin-Pease model) setting. The calculation was performed to mimic the conditions in the IVEM-tandem facility, i.e. the ions entering a 100nm Fe foil at 30° to the surface normal. The results show that 0.1% of the ions were backscattered, and 7.17% of the ions were retained in the specimen. The dose is calculated based on the vacancies produced in per ion, as a vacancy corresponds to the formation of a Frenkel pair. For 1MeV krypton in a 100nm film, 2811.4 vacancies are created per ion in the film. The calculation of dose in terms of displacements per atom (dpa) is then:

$$dpa = \frac{vacancies\ (displacements)}{ion} \cdot \frac{1}{\text{Å}} \cdot \frac{10^8\text{Å}}{cm} \cdot \frac{ion}{cm^2} \cdot \frac{cm^3}{atom}$$

The distribution of the vacancies formed using the Kinchin-Pease model is shown in Figure 47.

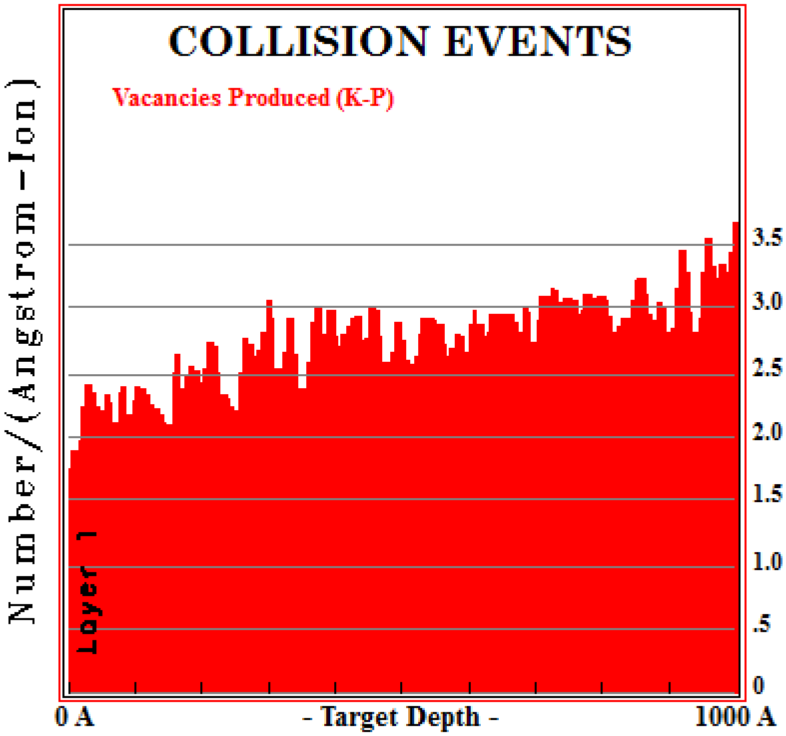

Figure 47. The distribution of vacancies for 1MeV Kr^{++} ions entering 100nm thick iron at 30° from the surface normal, calculated in TRIM by the Kinchin-Pease model.

Additional *in-situ* studies were performed using 500keV Ar^{2+} ions in order to collaborate the *ex-situ* irradiations performed at Los Alamos National Laboratory. The damage was again calculated using SRIM, which showed that 0.7% of the Ar ions were backscattered and 8.8% of the ions were retained in the specimen. For 500keV Ar ions 1057 vacancies were created per ion, resulting in a final calculated dose of 4.8x10^{14} ions cm^{-2} per dpa. The distribution of damage in the specimen is shown in Figure 48.

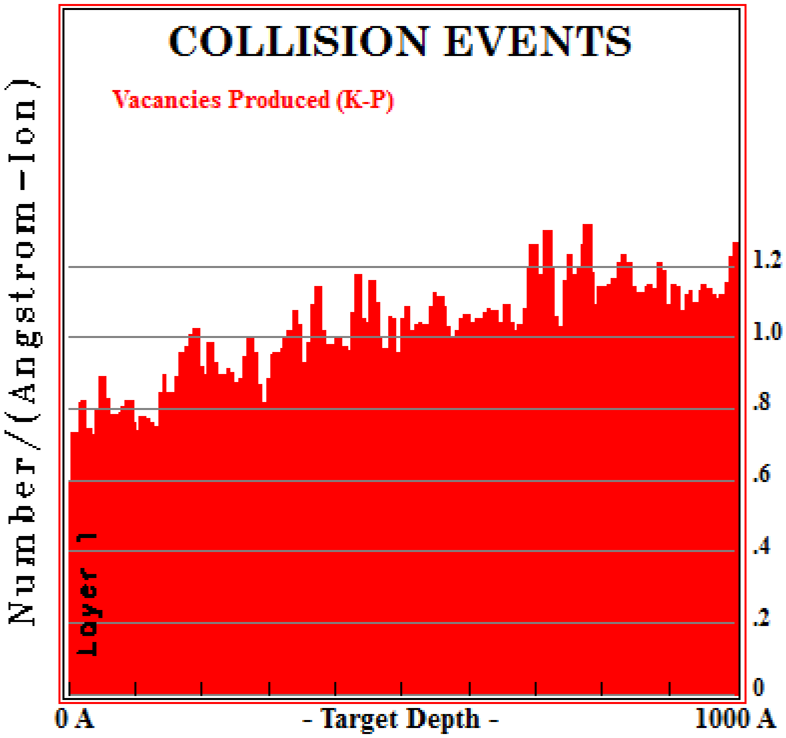

Figure 48. The distribution of vacancies for 1MeV Kr^{++} ions entering 100nm thick iron at 30° from the surface normal, calculated in TRIM by the Kinchin-Pease model.

While the Kinchin-Pease model is known to give more accurate estimates of the total dose, the Surface Sputtering / Monolayer Collision Step setting in SRIM gives a better approximation of the distribution of the damage through a thin film. An example of the results of these calculations are shown in Figure 49. The distribution of damage was similar for 1 MeV Kr^{++} and 500 keV Ar $^{++}$ ions in iron films. A significant drop-off in damage is visible at both the top (left) and bottom (right) surface of the film, but is only present a few angstroms from the surfaces.

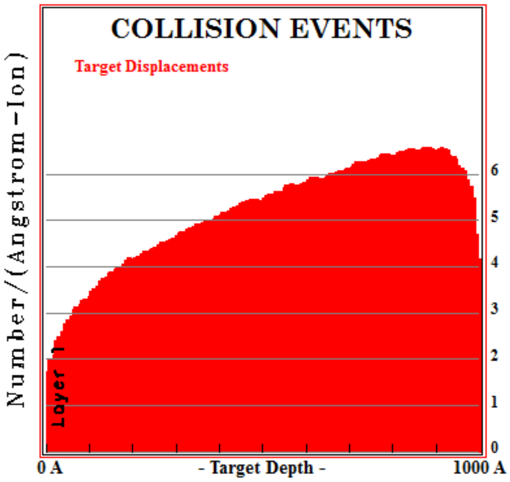

Figure 49. The distribution of vacancies for 1MeV Kr^{++} ions entering 100nm thick iron at 30° from the surface normal, calculated in TRIM using monolayer collision steps.

Irradiations were performed in segments, pausing only to take still images at set doses. At each set dose point, the ion beam was blocked so that the specimen could be imaged and tilted to return to the most favorable imaging condition, if necessary. For example, a typical irradiation would be stopped at doses of: $2x10^{14}$, $4x10^{14}$, $8x10^{14}$, $1.6\ x10^{15}$, $2.4x10^{15}$, and $4.0\ x10^{15}$ ions·cm^{-2}. This is equivalent to damage levels calculated by SRIM [216] of 0.25, 0.5, 1, 2, 3, and 5 dpa, respectively. For specific studies, the stopping points were varied. In some cases the irradiation was paused at each 1/10 dpa in order to explore low dose effects. In others, the irradiation was performed continuously to 5dpa. The dose rate during each segment of irradiations is approximately 5x10^{-11} ions-cm^{-2}-sec^{-1}, or roughly 50 cascade events per second in a 100nm diameter grain.

In-situ imaging was performed using a 200KV accelerating voltage which is below the knock-on damage threshold for iron. In the Hitachi H-9000NAR, the smallest selected area aperture covers a region approximately 500nm in diameter, and the area of illumination with a condensed beam is comparable at 200kV. Therefore it is not possible to select an imaging condition in a specific grain of choice, nor maintain that precise condition throughout the irradiation. Instead, a magnification is chosen such that a large number of grains are within the field of view. The specimen is held at zero tilt during the irradiation, and damage is observed in grains that are in a favorable imaging condition. After the irradiation, the behavior in the *in-situ* video was correlated with the crystallographic orientation maps obtained by NanoMEGAS ASTAR precession diffraction, which leads to results fairly consistent with behavior reported in literature (e.g. loop string formation along 110 directions, loop hop along 111 directions, and 100 type loop formation at 450°C) [18].

3.5 Ex-Situ Electron Microscopy

Ex-situ examination of the irradiated specimens was performed primarily using the 200kV LaB_6 JEOL-JEM 2100 TEM at Drexel University. In the JEOL 2100 TEM used to characterize these films, the largest selected area aperture covers approximately 1300nm in diameter and the smallest aperture covers a region 130nm in diameter. The small grain size (down to ~20nm) in the nanocrystalline thin films therefore makes conventional irradiated defect imaging techniques such as weak beam bright/dark field [111] difficult if not impossible. As a result, the diffraction information gathered from these materials was acquired using nanobeam diffraction (NBD), where it is possible to achieve a spot size of approximately 10nm with sufficient intensity to create a diffraction pattern.

Acquisition of diffraction information from nanocrystalline iron is further complicated by the aspect ratio of the columnar grain structure. Tilting too far in any direction results in imaging through multiple grains. This, in addition to the magnetic nature of the sample, means that imaging is best done near zero tilt. Fortunately, a typical nanocrystalline iron thin film TEM specimen contained some 10^9 grains, so the probability of finding grains in the correct diffracting condition was quite high. Therefore, analysis of the defect clusters in nanocrystalline materials was performed by finding grains that appeared to contain dislocation loops near zero tilt. Using nanobeam diffraction, it was possible to identify the imaging condition as kinematic brightfield using a 110 systematic row of reflections near a 001 pole. For the purposes of quantitative analysis (i.e. loop density and size), the resulting data points were the plots were graded with respect to the deviation from the ideal imaging condition. Only those grains that were close to the desired imaging condition were counted. Figure 50 shows an example of defect loop counting in nanocrystalline iron. A brightfield image is acquired showing defect loops in several grains. Those grains are targeted for nanobeam diffraction. If the diffraction pattern acquired closely resembles that of a kinematic brightfield imaging condition using a 110 systematic row of reflections near a 001 pole, the loops in the grain are counted and divided by the total area of the grain giving a loop density.

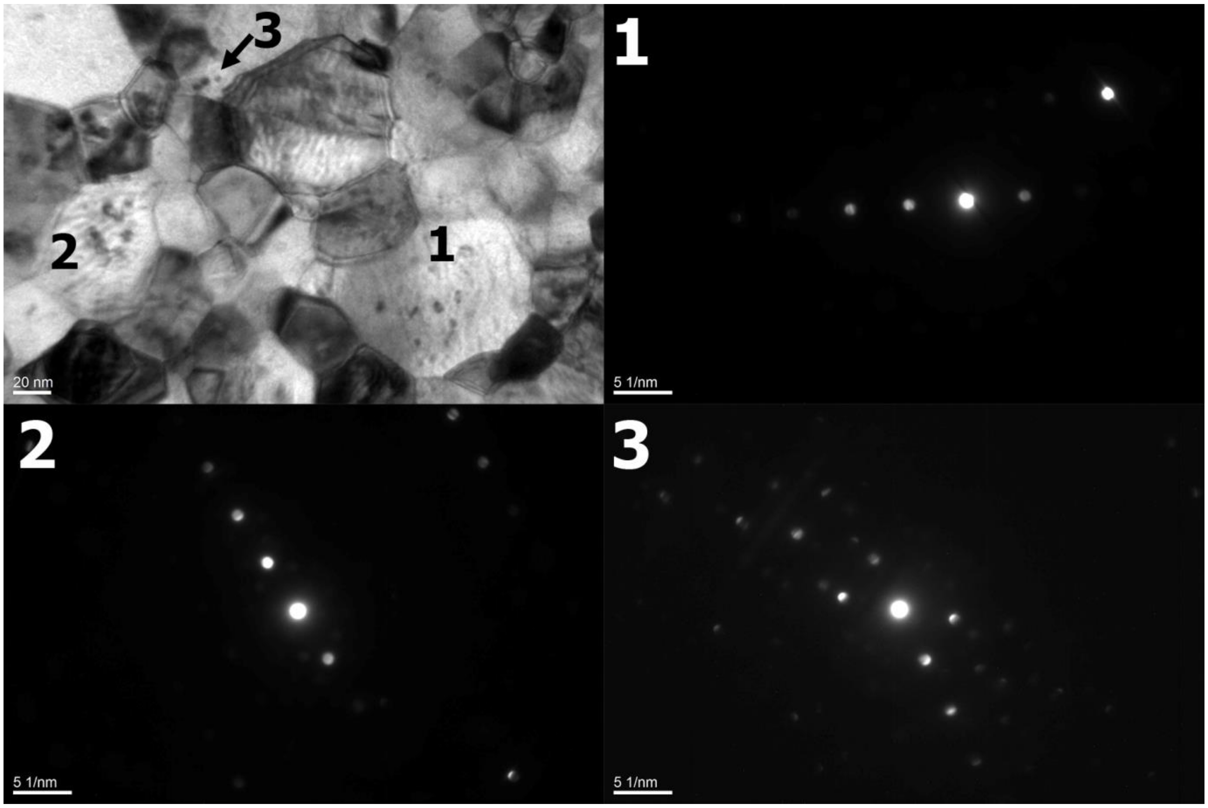

Figure 50. Brightfield TEM image of dislocation loops in nanocrystalline iron. The three numbered nanobeam diffraction patterns correspond to the numbered grains in the specimen.

To match the observations in nanocrystalline iron, subsequent imaging in the bulk materials was also performed using kinematic brightfield using 110 reflections (Figure 51). Jet thinned bulk samples were chosen that contained grains with a 001 zone axis near normal to the specimen surface. By imaging and counting only defects found in 001-normal grains, the effect of grain orientation with respect to the foil surface quantified by Jenkins et al.[18] was minimized.

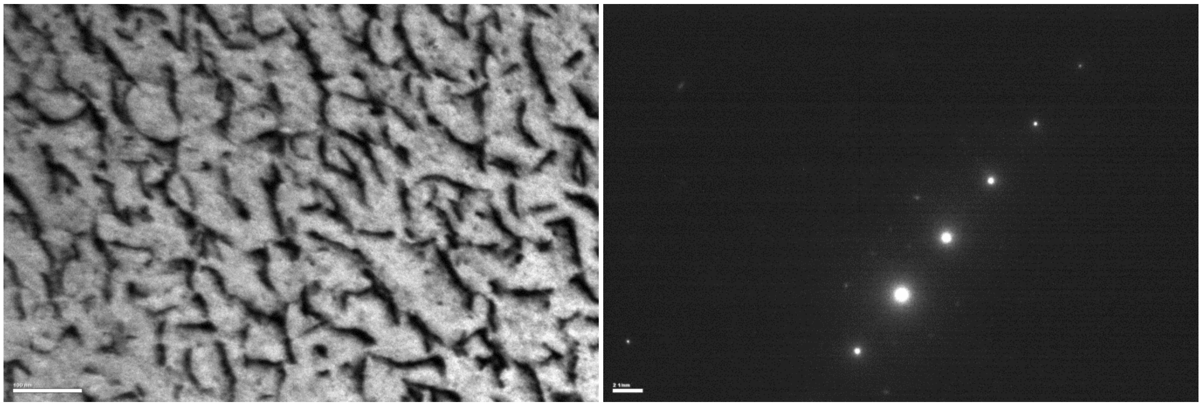

Figure 51. Brightfield TEM image of dislocation loops in microcrystalline iron and the corresponding selected area diffraction pattern.

The difficulty in acquiring diffraction patterns from small 20nm grains is further complicated by the magnetic nature of the sample, making tilting difficult. Adding to this issue is the columnar grain geometry which in tilting too far in any direction results in imaging through multiple grains. For this reason, it was not possible to determine the Burgers vector or habit plane of the dislocation loops in small grains by conventional means. To estimate the habit plane of the dislocation loops in the grains, orientation mapping was employed.

3.6 Orientation Mapping of TEM specimens

Crystallographic orientation maps were acquired using transmission electron microscopy using a system known as ASTAR by NanoMEGAS [217]. The ASTAR system (Figure 52) creates orientation maps from an array of electron diffraction patterns collected across a specimen. The system uses an external control unit known as the NanoMEGAS DigiSTAR precession unit (D) to raster the electron beam over the specimen by controlling the scan coils (B) of the TEM. At each point, the diffraction pattern is acquired by use of a dedicated high speed CCD camera (A) set to image the inclined phosphorescent screen. The diffraction patterns are captured and stored by the acquisition software (E).

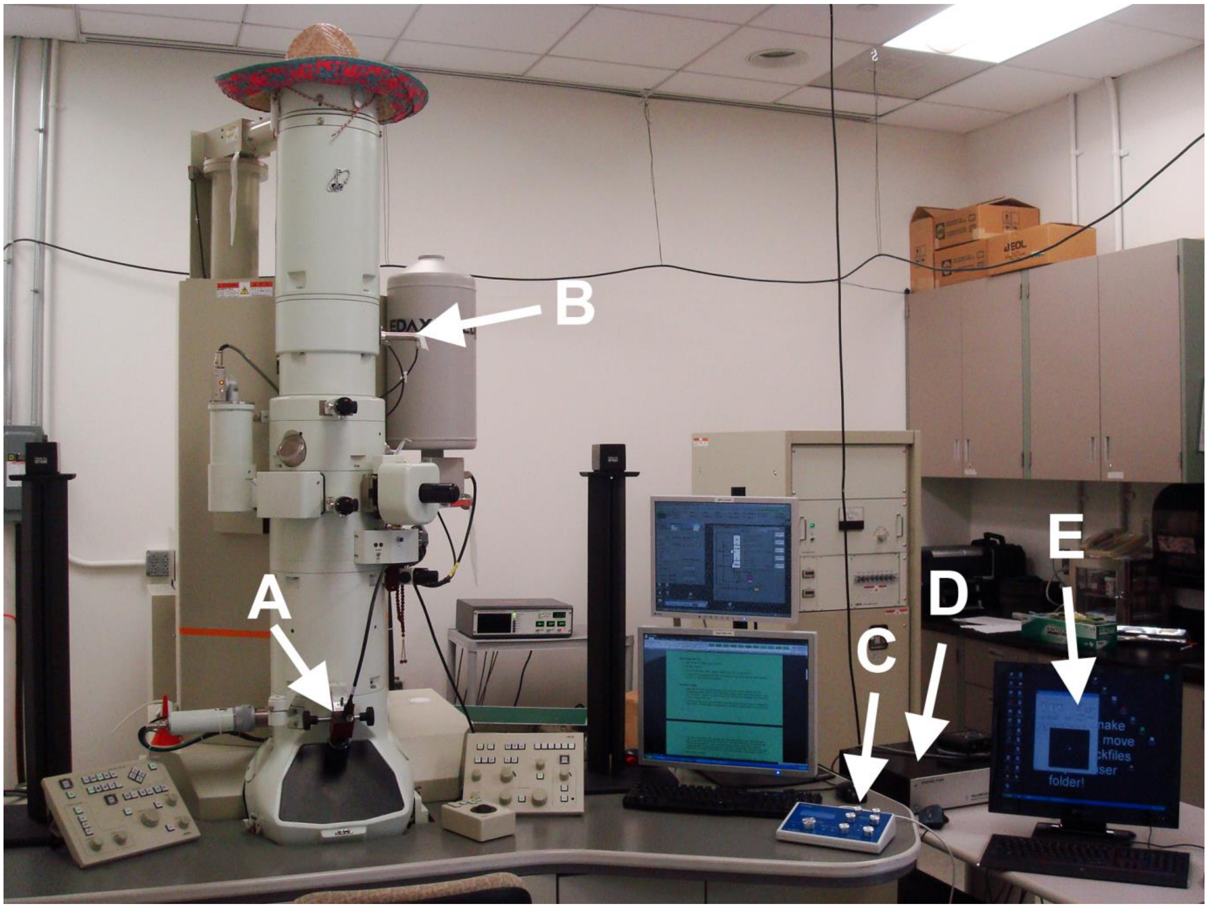

Figure 52. The NanoMEGAS ASTAR system installed on the JEOL-JEM2100 TEM at Drexel University.

The operation of the system requires that a target area of the specimen be located using bright field TEM. Once the region of interest was set (typically between 0.1μm^2 and 3.2 μm^2, the smallest condenser aperture was inserted and the TEM was aligned again. The TEM was then switched to nanobeam diffraction (NBD) mode, creating a parallel beam with a small spot size.

The final spot size was selected such that sufficient beam intensity was available to create a strong diffraction pattern. Typical spot size settings are 25nm, 15nm, 10nm, and 5nm; however, the actual spot size at each setting was approximately 30% larger than those values. The step size was then selected to provide the best results for the particular sample which was generally dictated by the grain size. Spot sizes used for this study were 10nm, 5nm, and 2nm. Typical settings for studying nanocrystalline iron films were a spot size of 15nm and a step size of 5nm.

After the scan, the orientation maps were created by correlating each spot diffraction pattern captured from the material to a template set of calculated diffraction patterns for the expected crystal system (Figure 53). Each pixel in the orientation map represents a single diffraction pattern point. A measure called "index" is used to describe the quality of the fit between the acquired and calculated diffraction pattern.

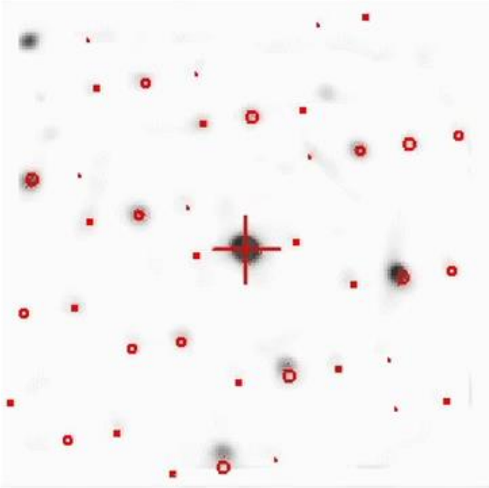

Figure 53. A calculated diffraction pattern (red) matched to the inverted diffraction pattern acquired from a nanocrystalline iron specimen in the NanoMEGAS Index software.

Since the diffraction patterns were acquired using an electron beam with a finite diameter, there were often situations where the beam acquired diffraction data from more than one grain. The system uses a measure called "reliability" to quantify the ration of the intensities of the two patterns. A reliability of 0% would indicated that each pattern has equal intensity. This measurement can also be used to create a map corresponding to the acquired orientation map. Additionally, since the ASTAR orientation maps are created from to digital files where information (e.g. about the corresponding ED pattern) can be retrieved from every pixel. It is possible to create virtual bright and dark field images by selecting specific reflections from the ED pattern.

CHAPTER 4. DEPOSITION OF NANOCRYSTALLINE IRON FILMS

4.1 Introduction

Nanocrystalline thin films have been the subject of extensive research for a range of applications including electronic materials [218, 219], wear [220, 221] and corrosion resistant surface coatings [222, 223], MEMS devices [224, 225] and as platforms for fundamental research in nuclear materials [33]. Processes such as physical vapor deposition enable the creation of pure, fully dense materials with nanocrystalline (<100nm) grain size and a controlled grain aspect ratio and crystallographic texture. In addition to film texture, the structure of the grain boundaries present is crucial to the performance of a material, affecting sink strength [226, 227], diffusivities [228, 229], and mechanical properties [230, 231]. This relationship is particularly important in nanocrystalline materials due to their high grain boundary density. Consequently, in order to tune materials for particular applications it is critical to understand how the growth of nanocrystalline materials affects the microstructure not only in terms of grain size but also with respect to texture and grain boundary character.

The grain boundary character present in a deposited thin film correlates with the texture of the film. In the absence of a crystalline substrate, induced epitaxial growth causes a deposited film to develop a preferred orientation determined primarily by the surface energy of its crystal faces. FCC and BCC metals possess {111} and {110} preferred orientations, respectively, corresponding to their respective close packed planes [232, 233]. For Fe, the tendency to form the (110) orientation is very weak and a random texture predominates. Four types of texture may arise in a film grown on a crystalline substrate: random texture, fiber texture, epitaxial alignment, or what has been termed axiotaxy – the alignment of comparably spaced planes between substrate and film [234]. It has been shown that Fe deposited on single crystal (100) NaCl substrates strongly favors a random orientation [207, 208, 210, 213]. For epitaxial growth on (100) substrate, two primary orientation relationships are observed: (100)Fe | | (100)NaCl with [110]Fe | | [001]NaCl, and (100)Fe | | (100)NaCl with [001]Fe | | [001]NaCl [207, 208, 210, 213].

Methods to control the texture of as-deposited films have involved growth process alterations that fall into two categories: (1) optimizing the equilibrium structure, or (2) attempting to drive the system to a new preferred orientation by external forces. Optimizing the equilibrium structure necessitates creating an atomically clean substrate surface and giving the adatoms sufficient mobility to enable their rearrangement into favorable orientations during nucleation and growth. Atomic mobility is a strong function of temperature [235], but can also be influenced by adjusting parameters such as bias power during sputter deposition. Controlled texture can also be achieved during the growth process by influencing the surface energy of particular crystallographic orientations through alteration of the sputter gas composition [236, 237]. Non-equilibrium preferred orientations can also be achieved by ion beam assisted deposition of PVD films, but the mechanism is not yet well understood [238, 239]. Recent efforts have focused on controlling the fractions of desired grain boundaries in electrodeposited [240] and PVD-grown [241, 242] nanocrystalline thin films. Progress in this area has been aided significantly by the development of automated crystallographic orientation microscopy (ACOM) for transmission electron microscopy (TEM), enabling orientation maps to be acquired with a step size and spot size small enough to characterize nanocrystalline materials [243-247], and permitting more complete studies of texture that may lead to microstructures tailored for optimum performance.

4.2 Methods and Procedure

In this study, changes in the microstructure of Fe thin films including grain size, texture, and grain boundary character were investigated for a range of deposition parameters (Table 3). Fe films with a target thickness of 100-150nm were deposited on polished NaCl (100) single crystal substrates by DC magnetron sputtering from a 99.9% pure Fe target. We systematically studied the effects of particular variables on the final microstructure while using the same target material, Ar gas flow at the target, and substrate material throughout: (1) substrate temperature (25°C-450°C), (2) substrate condition (polished, annealed, ion sputtered), (3) sputtering power (400W-500W), (4) sputtering bias (0W-40W), and (5) argon gas flow (0sccm-3sccm) at the substrate.

Table 3. The complete sputter parameter space explored in this study.

Parameter	Values Studied
Target Material	Pure Iron (see Table 1)
Substrate Type	(100) NaCl
Substrate Condition	As-Received (polished)
	Fresh Polish
	Freshly Cleaved in Air
	Annealed
	Ion Preclean
Substrate Temperature	Room Temperature
	250°C
	350°C
	370°C
	425°C
	450°C
Sputtering Power	400W
	500W
Sputtering Bias	0W

	25W
	40W
Gas Flow at target	30 sccm Ar
Gas Flow at substrate	0 sccm Ar
	3 sccm Ar
Chamber Pressure	2mt
	4mt

Film microstructure - porosity, grain size, and texture - was characterized using TEM and ACOM using the NanoMEGAS DigiSTAR™ precession unit and ASTAR™ analysis software. Planar TEM samples were prepared by adhering small cleaved portions of the Fe films to 200 mesh TEM grids using M-BOND™ 610 adhesive and dissolving the salt substrate using a 50/50 water-ethanol solution. The TEM grids were then placed in an SEM to examine the film surface topology and to prepare cross section liftouts using a focused ion beam (FIB). TEM characterization of the film cross section was performed to measure film thickness and microstructural changes that might have occurred during deposition.

4.3 Results

Our studies revealed that the deposition of Fe onto (100) NaCl substrates is subject to a wide variation in microstructure due to variations in the deposition process that are difficult to control, which is consistent with previous studies [208, 210, 211, 213, 214]. Careful selection of the deposition parameters can be used to deposit Fe films with varying degrees of texture ranging from randomly oriented grains to nearly single crystal. We found that the optimum substrate temperature during deposition was about 370°C, which is similar to that reported by Shinozaki and Matthews for PVD of Fe onto NaCl [211, 213]. Generally, a higher substrate temperature is desirable to promote diffusion; however, the practice of depositing Fe on the rock salt structure is complicated by the relatively high sublimation rate of NaCl which reaches about one monolayer per second by 440°C. Deposition temperatures for Fe on NaCl substrates are generally limited to below $0.4T_{mFe}$ because of the competition between the sublimation of NaCl and the deposition of Fe that both degrades the chamber vacuum and affects the quality of the deposited film. The surface condition of the substrate is also critical to the formation of a preferred texture in the sputtered film. This is particularly challenging in the case of NaCl which readily adsorbs water and other contaminants. Using *in-situ* RHEED to acquire crystallographic information from the substrate surface we examined several treatments to improve the surface quality of the NaCl substrate (Figure 54). As-received polished substrates exposed to atmosphere showed only faint diffraction rings with no sign of the single crystal rock salt structure for (100) NaCl substrates. Following a 450°C anneal and Ar ion bombardment, however, the RHEED pattern showed the expected (100) rock salt structure, indicating that the surface condition of the NaCl substrate can be substantially improved using ion bombardment prior to deposition.

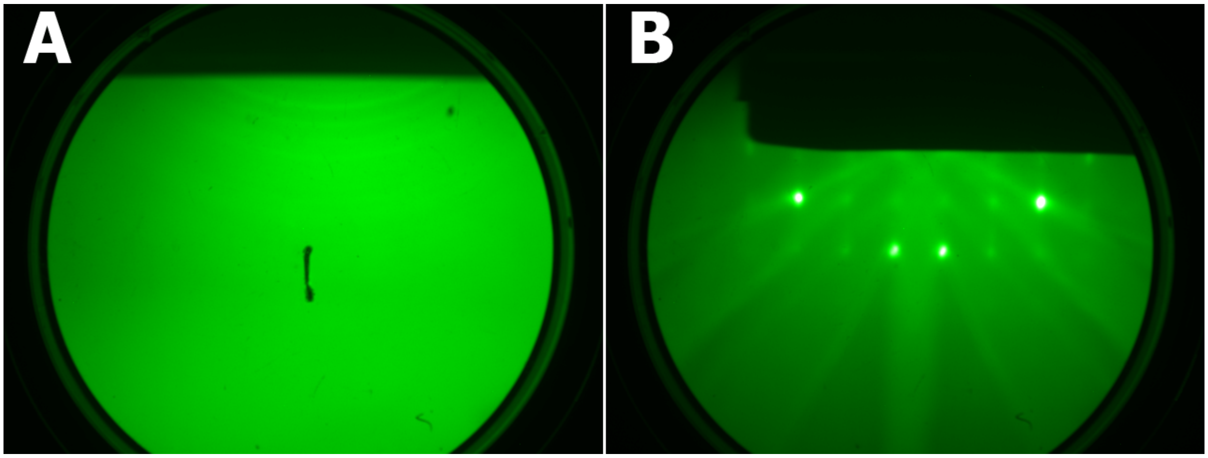

Figure 54. RHEED diffraction patterns collected from the surface of NaCl substrates (A) in the as-received condition having been exposed to air, and (B) after a 450°C anneal and 5 minute argon ion preclean.

The natural tendency for Fe films grown on (100) NaCl is to form a randomly oriented nanocrystalline microstructure. Figure 55 shows an example case where the Fe was deposited using arbitrary deposition parameters (in this case 500W sputtering power, 40W Bias, 2 mTorr chamber pressure, 30sccm Ar gas flow at the target, 4 sccm Ar gas flow at the substrate) onto a clean substrate known to produce nearly single crystal films. Despite being deposited on a clean substrate, no preferred texture is observed. The same microstructure is obtained in the reverse case in which Fe is deposited on a substrate with poor surface quality using deposition parameters known to create a strongly textured film on a crystallographically clean substrate (i.e. 400W sputtering power, 25W Bias, 4 mTorr chamber pressure, 30sccm Ar gas flow at the target). In each of these cases, the microstructure consists of grains that are equiaxed in-plane with an average grain size of ~35nm. The smallest grains observed in the as deposited films are ~15nm in diameter while the largest grains tend to be less than 75nm. High angle boundaries dominate all of these microstructures. The majority (~95%) of the grains are found to have disorientation angles greater than 15° and the remaining ~5% have boundary disorientations between 5° and 15°.

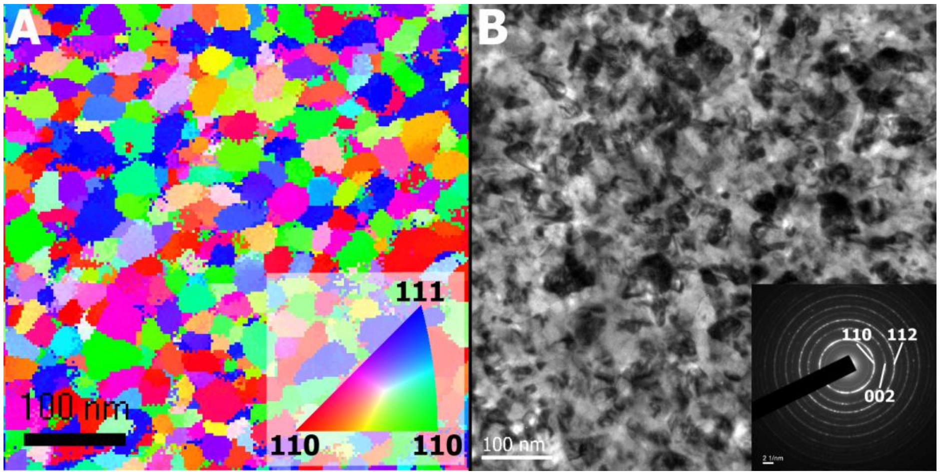

Figure 55. The microstructure of a film deposited using 500W sputtering power, 40W Bias, 2 mTorr chamber pressure, 30sccm Ar gas flow at the target, 4 sccm Ar gas flow at the substrate (A) An automated crystallographic orientation map showing the out of plane orientation (B) the corresponding TEM brightfield image and (C) conventional selected area diffraction pattern.

A cross section of an as-deposited Fe film with random texture reveals a columnar microstructure (Figure 56), which consists of small, equiaxed grains near the Fe-NaCl interface and columnar grains growing from these nuclei. In light of the lack of a preferred grain texture, it is not clear in this case whether secondary nucleation or competitive grain growth resulted in the secondary columnar microstructure. This microstructure, however, is consistent with what would be expected for depositions in which the substrate temperature is very low relative to the melting point of the target material and the mobility of the adatoms is limited. Based on the cross section microstructure, the Fe nuclei appear to form a few tens of nanometers apart and proceed to grow until they impinge upon one another to form a continuous film. At such low temperatures, the interfaces formed between the newly formed grains are generally immobile due to the low diffusion rate of the atoms. As a result, the initial grain structure arising from the nucleation processes is preserved at the base of the film.

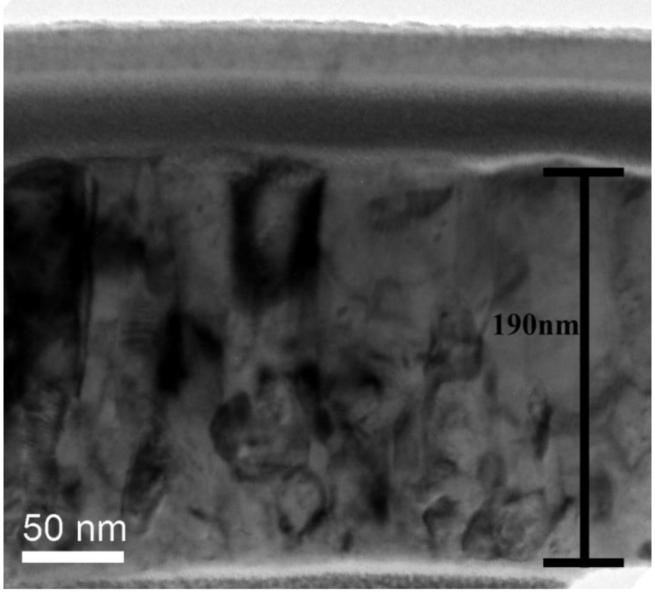

Figure 56. TEM image of the cross section of an Fe film sputter deposited on (100) NaCl at 370°C using (A) 500W sputtering power, 40W Bias, 2 mTorr chamber pressure, 30sccm Ar gas flow at the target, 4 sccm Ar gas flow at the substrate (B) 400W with a 25W bias and 30 sccm Ar at the target resulting in a 4mT chamber pressure.

Given that the 370°C substrate temperature utilized for the deposition is ~$0.36T_m$ of Fe, this type of morphology is in excellent agreement with the classic "*zone T"* in the Structure Zone Model proposed by Thornton [248]. The substrate temperature of 370°C is on the cusp or "transition zone" between the low temperature $(T/T_m < 0.3)$ "*zone 1*" domain with columnar structures defined by voided growth boundaries and the "*zone 2*" structure $(0.3 < T/T_m < 0.5)$ with columnar grains defined by metallurgical grain boundaries [249]. It was found that it is possible to transition the film microstructure from "*zone 1*" to "*zone 2*" structure by introducing a small bias (~25W) to the sputtering power. The additional energy provided by this improves the mobility of the Fe atoms, eliminating some of the shadowing issues that create the voided boundaries characteristic of "*zone 1*" microstructures (Figure 57).

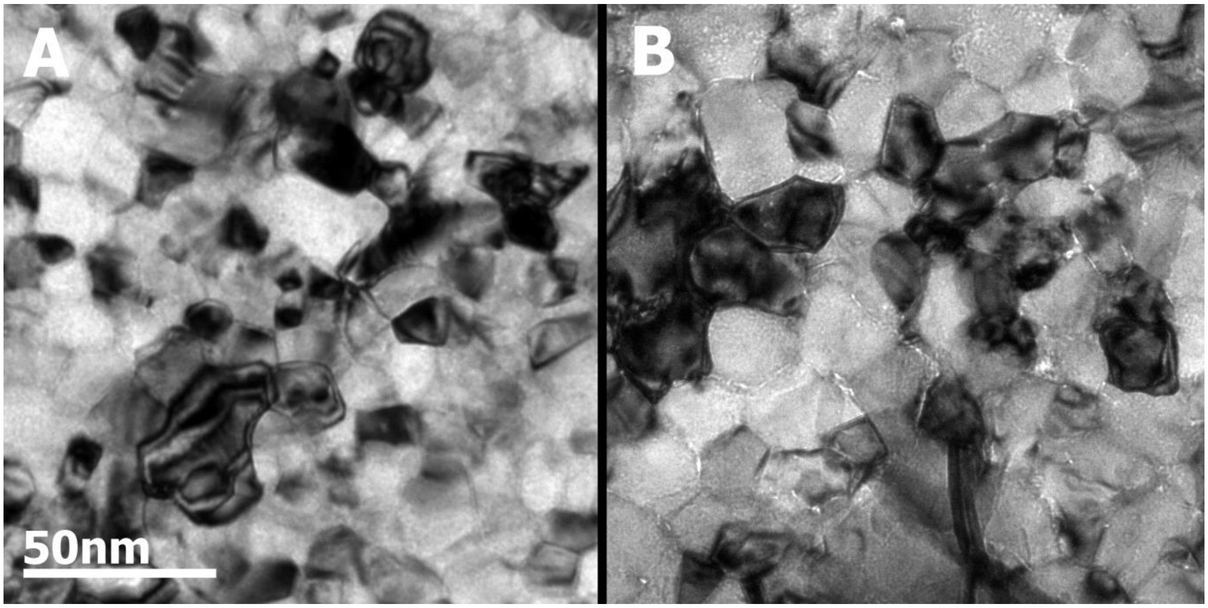

Figure 57. Underfocused images showing the influence of sputtering bias on the concentration of void structures (white) in as-deposited Fe films grown on NaCl substrates (A) The microstructure of a film deposited using 400W with a 0W bias and 30 sccm Ar at the target resulting in a 4mT chamber pressure (B) The microstructure of a film deposited using 400W with a 25W bias and 30 sccm Ar at the target resulting in a 4mT chamber pressure.

A deposition onto a clean, 370°C substrate using 400W sputtering power with a 25W bias and 30 sccm Ar at the target (4mT chamber pressure) gives the highest probability of achieving epitaxy, but still the results are mixed. The films exhibit varying ratios of *zone T* and *zone 2* type microstructures with the latter exhibiting a weak to moderate (100) fiber texture (Figure 58). The large regions of film with a strong preferred orientation (shown as red in Figure 5 (A)) consist of nanocrystalline grains having orientations with deviations of less than 5° from (100). The strong (100) fiber texture arises from a combination of the two primary orientations known to form on NaCl substrates [208, 210, 213].

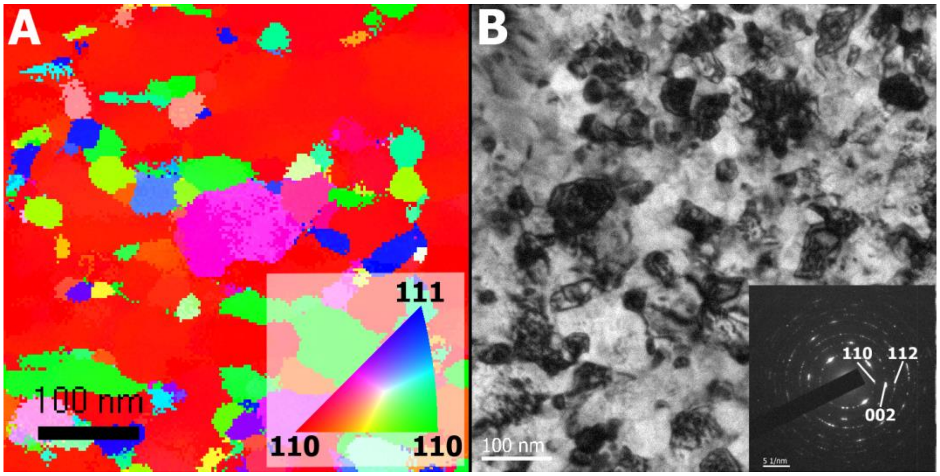

Figure 58. The microstructure of a film deposited using 400W with a 25W bias and 30 sccm Ar at the target resulting in a 4mT chamber pressure (A) An automated crystallographic orientation map showing the out of plane orientation (B) the corresponding TEM brightfield image and (C) conventional selected area diffraction pattern.

Since these two orientation configurations share the same matching plane with the substrate, they also share the same crystallographic planes exposed to the vacuum [213]. There is little difference in the energies between the [001] and [110] directions so they are therefore energetically equally likely to form, given that the surface of the substrate is atomically clean. This situation results in a classic case of fiber texture where there is a rotation around the fiber direction, yet one crystallographic axis of the film remains parallel to the substrate normal. The cross section of this film shows far fewer small equiaxed grains at the base of the film. The grain size in the fiber-textured film remains nearly the same as that in the randomly oriented film (~40nm), which is consistent with the mobility of the Fe atoms being very low and the interfaces between grains formed during impingement remaining immobile. Low angle grain boundaries with misorientations of only a few degrees dominate the film. Brück hypothesized that this structure was dominant, describing the microstructure of a so-called single crystal as a mosaic of small crystallites with small changes in orientation between them [207].

We found that starting an additional Argon gas flow of 3 sccm at the substrate 30 seconds prior to opening the shutter and maintaining that flow throughout the deposition, leads to very strong preferred orientation. The resulting microstructure (Figure 59), shows a very strong (100) fiber texture, which is typically reported as a single crystal epitaxial film for thermal and electron beam depositions [208, 213] based on the appearance of a strong crystalline diffraction pattern. A defocused diffraction pattern reveals that the strong diffraction spots are, however, the sum of the reflections from many small grains. Bright field TEM proves that the structure is polycrystalline. The majority of the film retains a nanocrystalline grain size with primarily low angle grain boundaries separating grains with strong fiber texture. In some regions, the grain boundaries are ill-defined, indicating a nearly complete coalescence of the original nuclei. By maintaining a flux of energetic ions on the film during deposition, the Fe atoms had sufficient mobility to close the gaps between crystallites as the nuclei grew together to form a continuous film. There are many isolated grains and small regions of the film where the Fe nucleated in a random orientation and retained that orientation through the thickness of the film. These grains remain bounded by random high angle boundaries.

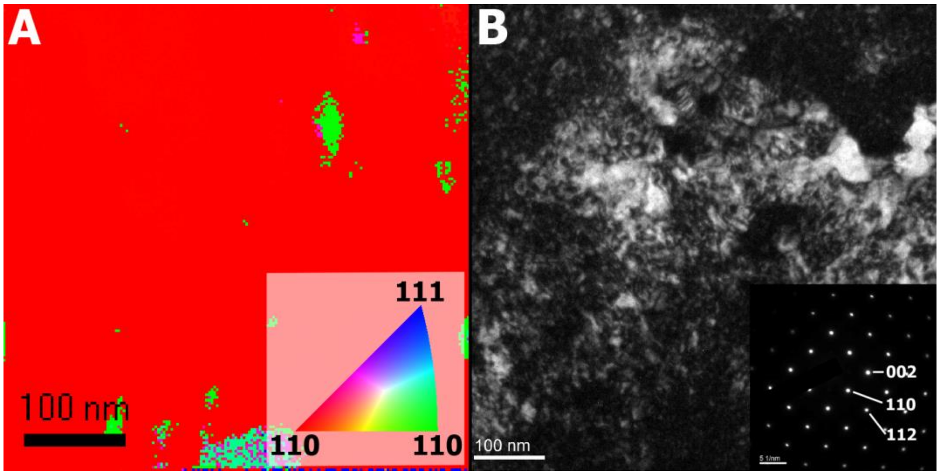

Figure 59. The microstructure of a film deposited using 400W with a 25W bias and 30 sccm Ar at the target resulting in a 4mT chamber pressure and an additional 3 sccm of Argon at the substrate (A) An automated crystallographic orientation map showing the out of plane orientation (B) the corresponding TEM brightfield image and (C) conventional selected area diffraction pattern.

4.4 Conclusions

Our results show that the deposition of Fe on (100) NaCl closely follows the Structure Zone Model proposed by Thornton [248]. Since the substrate temperature is generally limited to below 450°C, the microstructure takes on "*zone 1*", "*zone T*", or "*zone 2*" character. The deposition of Fe on (100) NaCl favors a randomly oriented grain structure, but through careful manipulation of sputter parameters, we are able to control preferred orientation. In particular, the substrate condition and energy of the Fe adatoms play a significant role in the microstructure of the as-deposited film. The formation of a fiber texture or epitaxial alignment require that the surface of the substrate be atomically clean and that the adatoms be sufficiently mobile to form equilibrium structures. By using a flow of Ar gas over the substrate prior to the deposition and maintaining it throughout we provide a brief cleaning of the substrate surface and add additional energy to the incoming Fe atoms, permitting surface diffusion to low energy configurations. By dialing in these parameters it is possible to control the preferred orientation of the film, thereby controlling the fractions of low angle and high angle grain boundaries present in the film. Films with a random texture contain predominantly high angle grain boundaries, whereas films that possess strong fiber texture contain a large fraction of low angle grain boundaries. This knowledge enables the design of engineered nanoscaled microstructures with tuned grain boundary properties for applications ranging from MEMs devices to radiation tolerant materials.

CHAPTER 5. GRAIN GROWTH IN NANOCRYSTALLINE IRON FILMS

5.1 Introduction

The high density of grain boundaries in nanocrystalline materials results in unique electrical transport properties, optical properties, and mechanical behavior (e.g. transition to inverse Hall-Petch relation). Since interfacial regions can account for up to 40% of the total volume in a 10nm grain material, these properties are strongly dependent on the structure of the grain boundaries that in turn is controlled by the method used to manufacture the material. In some cases, such as in the use of physical vapor deposition, the texture of the material can be controlled fairly precisely (as in chapter 4), offering opportunities to control the dominate grain boundary character. A polycrystalline material with randomly oriented grains will contain large population of high angle grain boundaries and the population of low angle grain boundaries will be relatively low [250], whereas a highly textured film will contain primarily low angle grain boundaries. This offers the opportunity to tune the properties of a nanocrystalline material, assuming that this microstructure can be maintained through additional processing.

Grain growth is largely dictated by grain boundary properties such as energy and mobility [247]. Recently, the relationship between grain boundary structure and grain growth has been of interest for nanocrystalline materials [247], where it was observed that the increased mobility of low energy $\Sigma3$ and $\Sigma9$ boundaries contributed to abnormal grain growth in nanocrystalline nickel. Low angle grain boundaries, those where the misorientation angle is less than about 15°, also have relatively low energy and are usually among the first to be removed from the microstructure under annealing. However, no direct comparison has been made between high angle and low angle grain boundaries in nanocrystalline materials. In this study, free standing nanocrystalline iron films are deposited by several physical vapor deposition processes. Each film is characterized using transmission electron microscopy including OIM by NANOMEGAS precession TEM to establish the influence of the deposition technique and parameters on the initial film microstructure. Annealing the films *in-situ* in the TEM with post-anneal OIM enables a direct study of how that microstructure affects grain growth

5.2 Method

In this study, iron films were deposited using sputter deposition and annealed using *in-situ* transmission electron microscopy. Two types of film microstructures were studied: a randomly oriented film and one with a strong fiber texture. The method for sputtering outlined in the previous chapter was used to create the films. The first film was grown at the optimum temperature of 370°C on a polished <100> sodium chloride substrate that had been exposed to air. The second film was deposited on a substrate from the same substrate batch after a two hour anneal at 450°C followed by an argon ion cleaning process. The films are then transferred to 3mm grids and marked with the focused ion beam (FIB) so a single region may be tracked throughout the *in-situ* experiment.

The annealing experiment was performed using a Gatan 625 heating holder in the JEOL-JEM 2100 TEM. During initial annealing experiments, the film specimens were ramped at 20°C per minute to temperatures between 300°C and 1000°C and held for variable times in order to ascertain the general behavior of the material. Subsequent experiments performed based on these initial results. For these advanced studies, NanoMEGAS automated orientation mapping was used to characterize each specimen in the as-deposited state. Then, the specimen was ramped to the first desired annealing temperature of 500°C at approximately 50°C/min. The film was held at temperature for about 10 minutes before being cooled. Cooling was accomplished by turning off the heater current and allowing the cooling water circulation system lower the temperature. The resulting cooling rate was 50-100°C/minute at higher temperatures, slowing as it reached room temperature. Once the sample was at room temperature and stabilized, orientation mapping was performed at the same site as the original map using the fiducial markers as reference points. The procedure is then repeated for the next temperatures of 600°C, 700°C, and 800°C. The approximate desired thermal profile for each sample is shown in Figure 60.

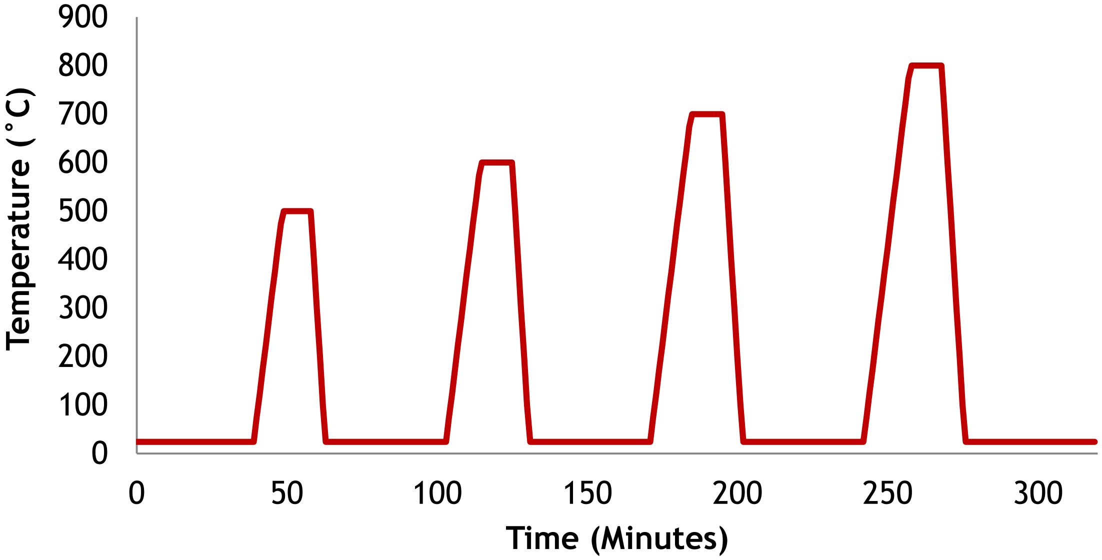

Figure 60. The thermal profile of the annealing experiments performed on nanocrystalline iron.

5.3 Results

The behavior of sputtered nanocrystalline iron films is reasonably consistent at high temperatures. Recovery begins to occur at timescales visible in the TEM (i.e. a visible change in less than ~10 minutes) at temperatures between 400°C and 600°C. The first appreciable grain growth occurs between 575°C and 625°C. When the specimen temperature is ramped to and held at any point above this temperature range, grain growth occurs rapidly for a short time (30 seconds to ~10 minutes) before tapering off. At higher temperatures, generally above ~750°C, initial grain growth occurs much more rapidly, and then often continues at a slower rate for as long as the sample is held at temperature. This new behavior becomes ubiquitous at temperatures around 900°C, where grain growth occurs very rapidly to large sizes, followed by continued moderate rate grain growth.

For more detailed study, two film specimens were annealed using the sequential heating and orientation mapping process. Grain growth appear to follow the same trends observed in the initial annealing experiments, even though the specimen was held at each temperature for 10 minutes and was cooled to room temperature to perform the orientation mapping after each step. In addition, the evolution of the microstructure observed, including grain size at each temperature, was very similar for both the fiber texture and the random texture film specimens. At each temperature, the grain growth was found to be arrested before the end of the isothermal hold, except for the case of 800°C where grain growth was continuing at a lower rate when the specimen cooling was initiated.

Figure 61 shows the orientation data acquired from the iron film grown on an as-received polished (100) NaCl substrate along with the brightfield TEM image at each temperature. The as-deposited film microstructure consists of very fine grains approximately

30nm, but this measurement had a significant amount of error due to the difficulty of identifying the extent of each grain in both brightfield and nanobeam diffraction (i.e. the raw data for the orientation map). The film had a slight {110} texture, which was consistent with the growth of a BCC metal film grown on an amorphous substrate where the preferred orientation determined primarily by the surface energy of its crystal faces [232, 233]. For Fe, the tendency to form the {110} orientation is known to be very weak, resulting in a nearly random structure.

At 500°C the TEM image was considerably sharper, owing to the reduction of diffuse scattering of the beam from defects in the microstructure. There was, however, still a large number of overlapping grains remaining. Only minimal grain growth occurred at 500°C. An example is the grain indicated with black arrow in Figure 62 where two grains (shown as green and yellow) appeared larger in the orientation map after 500°C. Grain growth continued to occur at up to 700°C. Interestingly, a third grain appeared to the left of the original two indicated by the black arrow. This new grain appeared to have absorbed the yellow grain by 800°C, while the green grain grows substantially. The final texture of the film after the series of anneals was very similar to that of the as-deposited microstructure. A slight {110} texture is still dominate. No evidence of abnormal grain growth was observed in the random texture nanocrystalline iron film.

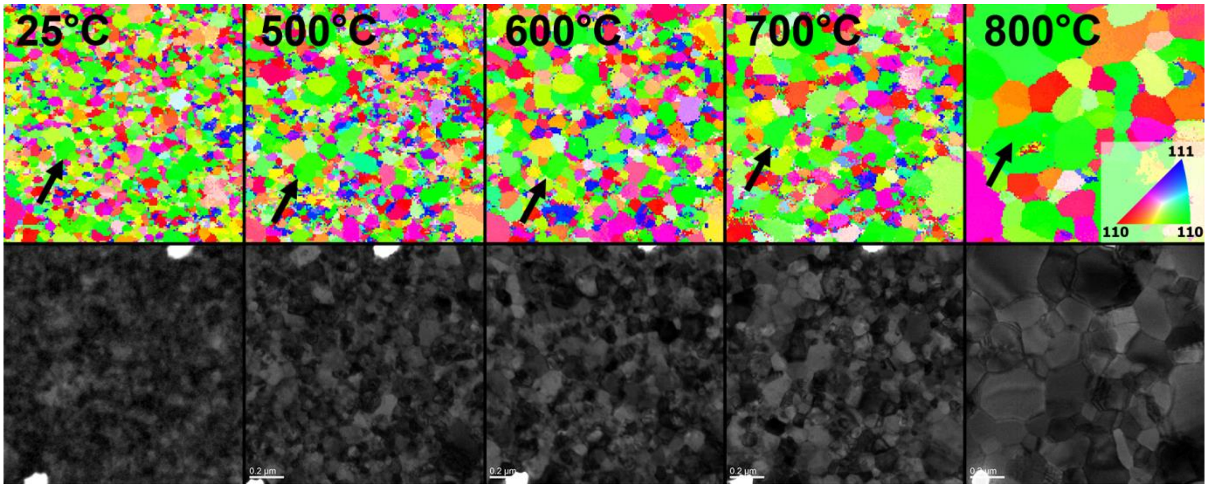

Figure 61. The annealed microstructure of a sputtered film initially possessing a randomly oriented texture.

For the film deposited on an annealed and precleaned (100) NaCl substrate, the initial microstructure consists of a strong fiber texture (Figure 62) with the (100) direction parallel with the film normal. In the orientation map acquired at the location marked by the fiducial markers on the specimen in the as-received condition (25°C in Figure 62), the overall texture appeared to be slightly off the expected (100) orientation and varied almost linearly from top of the map to the bottom. This a slight deviation was due to local bending in the thin film which was suspended between the bars of the TEM grid. The orientation data did show that there are intermittent grains with random orientation that had nucleated and grown through the film thickness. This is consistent with the microstructure found in Chapter 4. The corresponding brightfield TEM image shows that the microstructure of the as-deposited film again consisted of very fine grains that were poorly defined.

After the first anneal at 500°C it was found that, similar to the random texture film, the iron underwent recovery, resulting in a cleaner microstructure and more clearly defined grains. Some of the randomly oriented grains had already disappeared at this temperature, indicating some grain growth as well. In brightfield TEM, the grain boundaries could be clearly identified as ordered rows of dislocations consistent with low angle grain boundaries. Between 500°C and 700°C, the grains appeared to grow. During the 800°C anneal, the grain growth was far more rapid and resulted in the random grains being consumed by the grains that were close to the {100} orientation with respect to the surface normal. Even though the grains in the film appeared to fully align at 800°C (note that the specimen has tilted again, resulting in a measured orientation at the marker site that is slightly off {100}), bright field TEM clearly shows that the grain boundaries remain in the material and discrete grains are still present. Again, no evidence was found of abnormal grain growth.

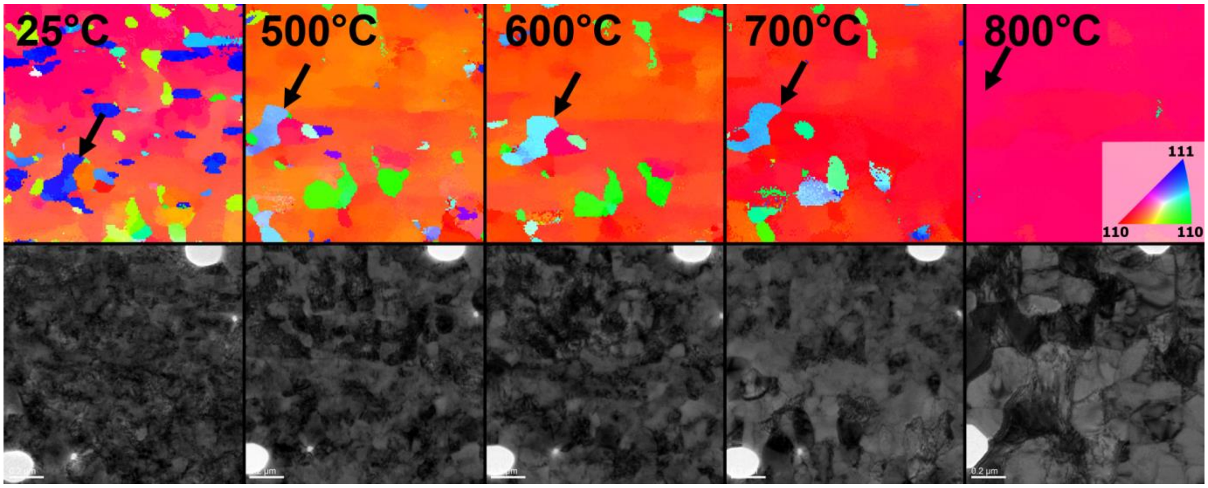

Figure 62. The annealed microstructure of a sputtered film initially possessing a strong fiber texture.

5.4 Discussion

Free standing nanocrystalline iron films show grain growth that is independent of the film texture. Both textures included in this study, the random texture and the strong fiber texture, undergo slow grain growth above 500°C and a sharp transition to rapid grain growth between 700°C and 800°C. This trend correlates well with data for ball milled nanocrystalline iron summarized by Darling et al. [251]. The data shows that pure iron undergoes a sharp transition in the grain growth rate at approximately $T/T_m=0.45$ (about 550°C) for one hour isochronal anneals. Below that temperature, the grains grow from ~15nm to ~50nm in the course of an hour. Above it, the grains reach ~200nm in size over the same time span. In nanocrystalline iron thin films, the growth rate transition appeared to occur at a higher temperature. This could be an artifact of the shorter anneal time in the TEM

It could also be the result of the columnar grain structure of the grains. Although the grain size starts as 20nm in diameter, that dimension is only in plane. The out of plane grain size is a function of the film thickness, so in this case the grains are already ~120nm in size. Therefore the driving force for grain growth is much lower. Finally, the difference in temperature could be the result of the method of manufacture. The thin film, being a sputter deposition, has a relatively low strain and well defined grain boundaries compared to ball milled powder. Therefore the stored energy is lower, resulting in a lower grain growth rate at low temperatures.

Interestingly, the initial texture of the film has no apparent influence on the growth rate of the grains, and the texture does not change greatly during the anneal. The evolution of the microstructure observed, including grain size at each temperature, was very similar for both the highly textured and the randomly textured film specimens. This implies that the driving force for grain growth in free standing films of columnar nanocrystalline iron is independent of grain boundary character and film texture. Grains were found to coarsen uniformly without strong regard for orientation, and no sign of abnormal grain growth was observed for pure nanocrystalline iron produced by sputter deposition.

CHAPTER 6. VOID PINNING EFFECTS ON GRAIN BOUNDARY MOBILITY

6.1 Introduction

Grain boundaries (GBs) play a critical role in microstructure devolution, as they act sinks for defects and precipitate atoms and they can slow and inhibit dislocation motion. In addition, GBs can migrate, increasing the average grain size and leaving behind precipitate rich regions that can impact the microstructure. Thus, GB migration must be accurately captured in order to realistically represent changes in microstructure.

Grain boundaries migrate under various driving forces, where the velocity v of a grain boundary is proportional to the driving force P according to v=MP for small driving forces. Here, M is the grain boundary mobility, which is an exponential function of temperatures. Driving forces include reducing the total GB energy (often called the curvature driving force), stored deformation energy, elastic energy, and temperature gradients [252]. Thus, grain growth is inhibited when the mobility is reduced (e.g. due to solute drag) or when the driving force is reduced or opposed [145]. Defects decorating GBs, such as solid precipitates, voids, or bubbles, apply a pinning force that opposes the driving force, slowing or even stopping all GB motion. GB pinning can drastically impact grain growth and therefore must be understood if GB migration and grain growth are to be understood.

The earliest model of GB pinning was the Zener pinning model [253], which approximated the pinning force from a single particle on a GB. He then estimated the pinning pressure for a random distribution of bubbles and determined an expression for the maximum grain size for a given precipitate radius and volume fraction. Various other researchers have built on Zener's original work [254-257]. Since then, various attempts have been made to explicitly represent the GBs and particles at the mesoscale. The earliest attempts used Monte Carlo Potts models [256, 258, 259], however the phase field method has also been applied [260-264]. The phase field model is of particular interest because it can quantitatively model the particle/pore interaction with GBs in specific materials [260, 265-267].

These mesoscale models represent the full microstructure and how it evolves with time, which provides a much more detailed description of the behavior than a mean field approach which uses a single equation to predict the evolution in the average grain size. However, the mesoscale models are also significantly more expensive. In fact, the majority of the simulations have been carried out in 2D to reduce computational expense, even though 2D simulations have been shown to not accurately represent the release of GBs from the pinning particles/pores. Another difficulty is in validating these mesoscale simulations against experiments. Some validation has been carried out by calculating the average grain size in the simulations against experimental average grain sizes. Direct comparison to experimental micrographs has been inhibited by the difficulty to characterize the microstructure evolution over time. However, new in-situ microscopy methods could be a valuable approach for validating these methods.

Microstructural evolution has traditionally been explored by taking static snapshots of the final microstructure after a series of isothermal experiments or at fixed points during an anneal [247, 268, 269]. Advances in characterization techniques have led to the prevalence of *in-situ* methods that permit time-resolved observation of microstructural evolution [33, 169, 270-273]. In particular, *in-situ* transmission electron microscopy is promising as a means to directly observe grain growth and grain boundary motion. The traditional limitation of TEM is the limited field of view, which can be overcome by examining nanocrystalline materials that offer a high density of grain boundaries within the frame. This method has been used to observe grain boundary motion caused by thermal activation [271], stress [272], and irradiation [33]. Furthermore, the ability of transmission electron microscopy to image fine precipitates and void structures in the microstructure should permit the study of grain boundary pinning.

To compare to the *in-situ* TEM data, grain boundary migration was modeled in iron thin films with nanocrystalline columnar grains by Dr. Michael Tonks at Idaho National Laboratory. The goal was to identify the minimum requirements to accurately predict the behavior of grain boundaries in films with voids. A simulation was created using inputs from *in-situ* for grain boundary mobility. The results should enable a better understanding of the evolution of the microstructure of ferritic alloys in conditions where voids and bubbles may form, for example, in the core of a nuclear reactor.

6.2 Methods and Procedures

6.2.1 Experimental Methods

The experimental portion of this study was performed using free-standing nanocrystalline iron films deposited by magnetron sputtering. Iron was deposited by sputtering a 99.9% pure iron target onto a 1cm x 1cm <100> NaCl substrate held at 370°C. The final film is a uniform iron layer approximately 120 nm in thickness with a microstructure comprised of columnar nanocrystalline grains that extend through the thickness. In-plane, the grains are equiaxed and have an average grain size of 26nm with majority of the grains falling between 15nm and 70nm in diameter. The films had no preferred orientation, so the grains were in general separated by large disorientation angles and random high angle grain boundaries once annealed.

While performing experiments for our previous work exploring the parameter space for the deposition of iron on (100) NaCl substrates, we found that the microstructure of the film could be transitioned from *zone 1* to *zone 2* type through the use of a bias during the deposition (Figure 63). Depositions using no sputtering bias were prone to high void concentrations throughout the film, particularly along grain boundaries. This is consistent with observations of atomic shadowing during deposition (i.e. *zone 1* type morphology). Increasing the sputtering bias to 25 watts resulted in a shift of film morphology into a clear *zone T* condition with true metallurgical grain boundaries and low void density. Increasing the sputtering bias to 40W results in a high spherical void concentration that is evenly distributed in plane. Upon annealing, the intergranular voids created in the *zone 1* type microstructure (25W bias) spheroidize, creating a distribution of voids along grain boundaries. By manipulating the void density of the microstructure in this way, a study of the grain boundary pinning effects of voids is possible.

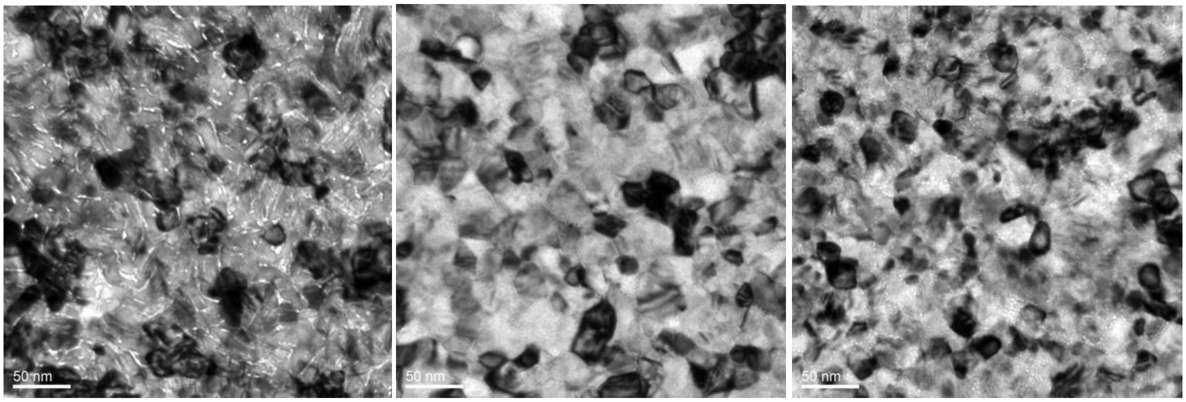

Figure 63. Influence of sputtering bias on void concentration in iron films deposited on NaCl substrates at 370°C. (left: 0W, center: 25W, right: 40W).

After deposition, the iron films were removed from the substrate and transferred to TEM grids for *in-situ* annealing experiments. Small 2mm x 2mm sections were cleaved from the original substrate and secured to 200 mesh nickel grids using M-BOND™ 610 Adhesive (Ted Pella, Inc., Redding, CA, USA). The NaCl substrate is then dissolved away using a solution of 50% ethanol in deionized water to dissolve the salt and the specimen rinsed multiple times in anhydrous methanol. The average final thickness of each deposition was verified by both scanning electron microscopy (SEM) and transmission electron microscopy (TEM) using a cross section liftout prepared using a focused ion beam (FIB).

The *in-situ* annealing experiments were performed using a Gatan 625 heating holder (Gatan, Inc, wherever, State). Each film was heated at a rate of approximately 20°C/min to the desired temperature of 900°C and held for 10-15 minutes. During the anneal, the specimen was observed in an underfocused imaging condition in order to resolve the activity of both the grain boundaries and the voids. Observations were made using a Gatan on-axis CCD camera operating with an exposure time of 0.1s. The output of the CCD camera was recorded as a screen capture at 15fps using Microsoft Expression Encoder 4. The resulting video data was then used to examine key elements of the annealing process.

The video was first virtually stabilized using Adobe Premier Pro CS5 to eliminate image movement due to thermal drift or mechanical translation. The resulting video was then manipulated at high rates (>50x speed) to identify grains in which growth occurred by boundary motion rather than what appeared to be grain rotation. To determine the velocity of the targeted grain boundaries, a virtual measuring tool calibrated from the image scale bar was overlaid on the video adjacent to the grain boundary of interest. The initial and final position of the grain boundary with respect to the measuring tool was determined at the beginning and end of the

GB's visible motion. This distance was divided by the time recorded in the video to provide an average GB velocity. Grain boundary curvature was measured by exporting individual video frames as tiff files for import into ImageJ. The draw circle tool was used to draw a circle of known radius that matched the curvature of the grain boundary, thus providing an estimate of the grain boundary curvature and driving force for GB motion.

6.2.2 Computational Methods

This work was done in collaboration with Dr. Michael Tonks at Idaho National Laboratory who performed simulations to model the interaction of GBs with voids in Fe nanocrystalline thin films using a phase field model based on that presented in Millett and Tonks [267]. However, we add the directional model of bulk, surface, and GB diffusion from Ahmed et al. [274]. In the model, grains are represented by order parameters η_i equal to one within a corresponding grain and equal to zero in the other grains, assuming isotropic GB properties. The voids are represented with a conserved vacancy concentration c equal one within a void and some small concentration with the bulk. The variables evolve to minimize the total free energy in the system, representing the microstructure evolution. The free energy of the system is defined in terms of the model variables as

$$F = \int_V \left(\mu f(c,\eta_i) + \frac{\kappa_c}{2}|\nabla c|^2 + \sum_i \frac{\kappa_i}{2}|\nabla \eta_i|^2 \right) dV, \tag{1}$$

where κ_c is the interfacial parameter for c, κ_i is the interfacial parameter for the ith order parameter and μ is the bulk energy parameter. The bulk energy term is defined as

$$f(c,\eta_i) = \sum_i \left(\frac{\eta_i^4}{4} - \frac{\eta_i^2}{2} \right) + \left(\frac{c^4}{4} - \frac{c^2}{2} \right) + \gamma_{GB} \sum_i \sum_{j>i} \eta_i^2 \eta_j^2 + \gamma_c \sum_i c^2 \eta_i^2 \tag{2}$$

where γ_{GB} is typically set to 1.5 to ensure a symmetric diffuse interface [275] and γ_c is defined by the surface energy to GB energy ratio.

The evolution of the concentration c is defined by a Cahn-Hilliard equation according to

$$\frac{\partial c}{\partial t} = \nabla \cdot \mathbf{M} \nabla \frac{\partial F}{\partial c(\mathbf{r}, t)} \tag{3}$$

where **M** is the concentration mobility matrix that accounts for directional diffusion along surfaces and GBs. The evolution of the order parameters η_i is defined by an Allen-Cahn equation, as

$$\frac{\partial \eta_i}{\partial t} = -L \frac{\partial F}{\partial \eta_i} \tag{4}$$

where L is the order parameter mobility and for this model it is assumed to be equal for all GBs.

The model has a number of parameters that must be determined as functions of measurable quantities in order to make a material specific model. These quantities are the GB energy σ_{GB}, surface energy σ_s, vacancy or gas bulk vacancy diffusivity D_{bulk}, and the GB mobility M_{GB}. For the order parameter values, we use the model presented in Moelans et al. [275], which gives the relationships

$$\begin{aligned} \kappa_i &= \frac{3}{4}\sigma_{GB} l_{GB} && (5) \\ L &= \frac{4}{3}\frac{M_{GB}}{l_{GB}} && (6) \\ \mu &= 6\frac{\sigma_{GB}}{l_{GB}}. && (7) \end{aligned}$$

where l_w is the interfacial width that defines the width of the diffuse interfaces in the phase field model. The mobility can be determined by the fact that the concentration evolution should follow Fick's law of diffusion for $c \ll 1$ removed from a GB, such that

$$\mathbf{M} = \mathbf{D}/\frac{\partial^2 f}{\partial c^2} = \mathbf{D}/(2\mu(\gamma_c - 1)) \tag{8}$$

The parameter γ_c is set by the ratio of the surface energy to the GB energy, i.e.

$$\gamma_c = \gamma_{GB}\frac{\sigma_s}{\sigma_{GB}} = \frac{3}{2}\frac{\sigma_s}{\sigma_{GB}} \tag{9}$$

2

The concentration c impacts the free energy in the same manner as η_i, therefore

$$\kappa_c = \frac{3}{4}\sigma_s l_{GB}. \tag{10}$$

The gas diffusivity matrix defines the total diffusivity due to bulk, surface and GB diffusion following the model from Ahmed et al. [19]. The diffusivity matrix is equal to

$$\mathbf{D} = D_{bulk}\left(\hat{\mathbf{D}}_b + \hat{\mathbf{D}}_s + \hat{\mathbf{D}}_{GB}\right) \tag{11}$$

where the bulk diffusivity

$$D_{bulk} = D_0 e^{-\frac{E_m}{k_b T}} \tag{12}$$

with the diffusivity prefactor D_0, formation energy E_m, the Boltzman constant k_b, and the temperature T. The individual normalized diffusivity tensors are determined as

$$\hat{\mathbf{D}}_b = w_b \mathbf{I} \tag{13}$$

$$\hat{\mathbf{D}}_s = w_s c^2(1 - c^2)\mathbf{T}_s \tag{14}$$

$$\hat{\mathbf{D}}_{GB} = w_{GB}\sum_{i=1}\sum_{j\neq i}\eta_i\eta_j\mathbf{T}_{GB}, \tag{15}$$

where the surface projection tensor is a function of the concentration according to

$$T_s = \mathbf{I} - \frac{\nabla c}{|\nabla c|}\otimes\frac{\nabla c}{|\nabla c|}. \tag{16}$$

The GB projection tensor is a function of the order parameters as

$$T_{GB} = \mathbf{I} - \frac{\nabla\eta_i - \nabla\eta_j}{|\nabla\eta_i - \nabla\eta_j|}\otimes\frac{\nabla\eta_i - \nabla\eta_j}{|\nabla\eta_i - \nabla\eta_j|}. \tag{17}$$

The phase field equations are solved using the finite element method in the MARMOT mesoscale modeling code [276]. The order parameters are solved in the manner outlined in that paper. The concentration is solved by splitting the fourth order Cahn-Hilliard equation into two second order equations in the manner summarized in Zhang et al. [277]. All of the equations are solved simultaneously using implicit time integration.

To model GB and void interaction in Fe thin films, we require values for GB mobility and energy in Fe. We also need the vacancy diffusivity pre factor D_0, the vacancy migration energy in Fe, and Fe surface energy. In order to facilitate comparisons to the TEM data, we use the GB mobility estimated from the in situ TEM experiments at T = 900°C, i.e. $M_{GB} = 2.2\times10^{-14}$ m^4/Js. The GB energy $\sigma_{GB} = 1.2$ J/m^2, is a typical value for Fe GBs [278]. The vacancy diffusivity pre factor is taken from experiments as $D_0 = 6.0\times10^{-4}$ m^2/s and the vacancy migration energy E_m = 1.24 eV [24]. For the surface energy, we use $\sigma_s = 1.2$ eV, as it is a typical value for an Fe surface [279].

6.3 Results

6.3.1 Experimental Results

The first grain growth visible during *in-situ* TEM anneals of nanocrystalline Fe thin films occurs around 500°C. This is consistent with findings for equiaxed nanocrystalline iron produced by severe plastic deformation [251]. For the first result, the specimen was ramped directly to 800°C at a rate of 30°C/min. At that heating rate, grain growth only occurs for about 10 minutes before the sample reaches the isothermal hold. Grain boundary mobility was measured from the video acquired during the first stages of the hold. Many of the grain growth appears to occur via grain rotation, similar to what has been observed in other nanocrystalline materials [271]. However, it is often difficult to distinguish true grain rotation from changes in diffraction condition due to thermal drift of the film. Grain boundaries suitable for determination of grain boundary mobility were identified in the video and used to determine experimental grain boundary mobility. An example grain boundary is indicated by the lower arrow in Figure 64a. This boundary shows no sign of voids when imaged in the underfocused brightfield condition. The second triple junction of the grain boundary is hidden below the grain indicated by the upper arrow, and can be seen in Figure 64b as the grain begins to rotate. The motion of the grain boundary of interest is initiated when the dark grain is annealed out, allowing the upper triple junction of the grain boundary to break free. The boundary of interest moves independently (Figure 64c-e) for 13nm until it is met by a boundary from the adjacent grain growing in the opposite direction. During this process the grain boundary maintained a nearly constant curvature (within the error of measurement) of 100nm±5nm. The velocity of the boundary was calculated to be 1.38×10^{-10} m/s.

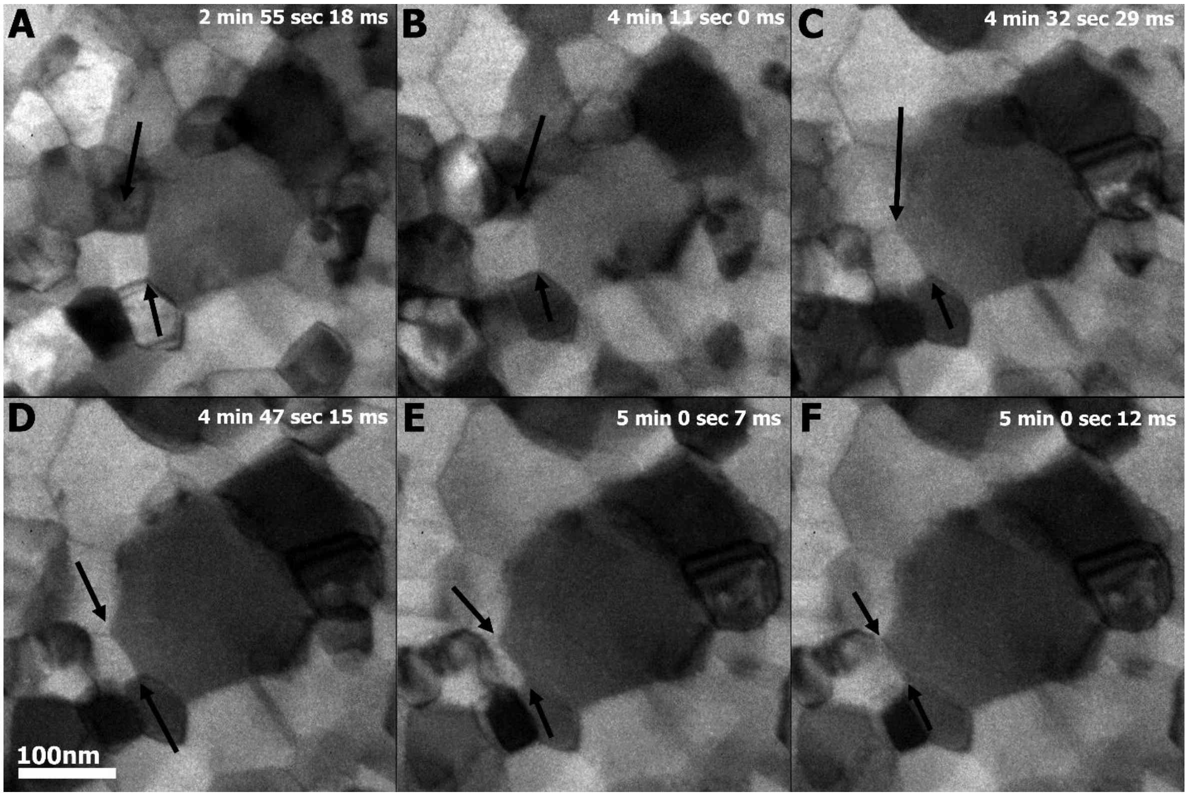

Figure 64. *In-situ* TEM brightfield images of grain boundary motion in columnar nanocrystalline Fe at 800°C.

To examine the effect of voids on the mobility of grain boundaries, a second Fe film specimen was annealed *in-situ*. The microstructure of the as-deposited film is shown in Figure 65a, and consists of randomly oriented nanocrystalline grains bounded by regions of void space. As the specimen is heated to 500°C, the diffusion rate of iron is high enough to permit the planar voids to lower their interfacial energy by spheroidizing. The voids are trapped along the grain boundaries and at triple junctions. In this case, the grain boundaries largely remain pinned until significantly higher temperatures, so that at 500°C grain growth is not observed during the *in-situ* anneal.

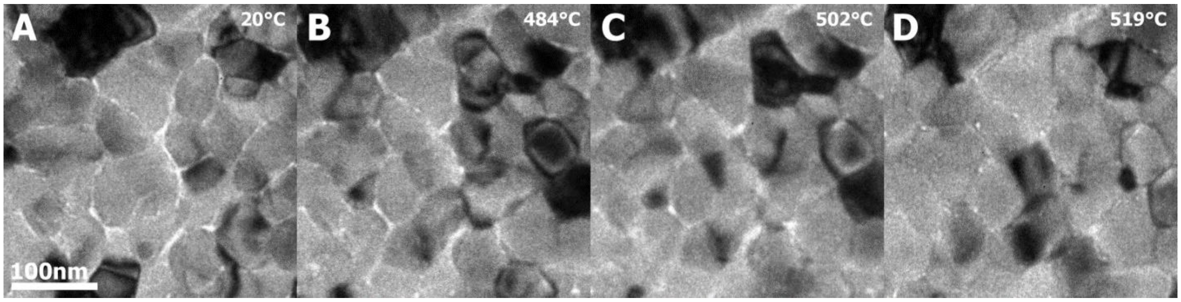

Figure 65. The formation of spherical voids in a nanocrystalline Fe thin film annealed to 500°C.

The film was heated to 900°C and held for several minutes. The grain boundary shown in Figure 66 is pinned by a series of voids along its length. At this point it has a radius of curvature of approximately 120nm±5nm. During the isothermal hold, the boundary begins to move. The boundary requires just over 90 seconds at temperature to clear the void obstacles, during which time it travels approximately 12nm with a velocity of $1.29\text{x}10^{-10}$ m/s. After the grain boundary breaks free, it travels an additional 17nm in approximately 1/30 of a second (less than one frame of video), giving it a velocity nearly three orders of magnitude larger at $1.7\text{x}10^{-7}$ m/s. After breaking free the boundary curvature changes to approximately 155nm±5nm.

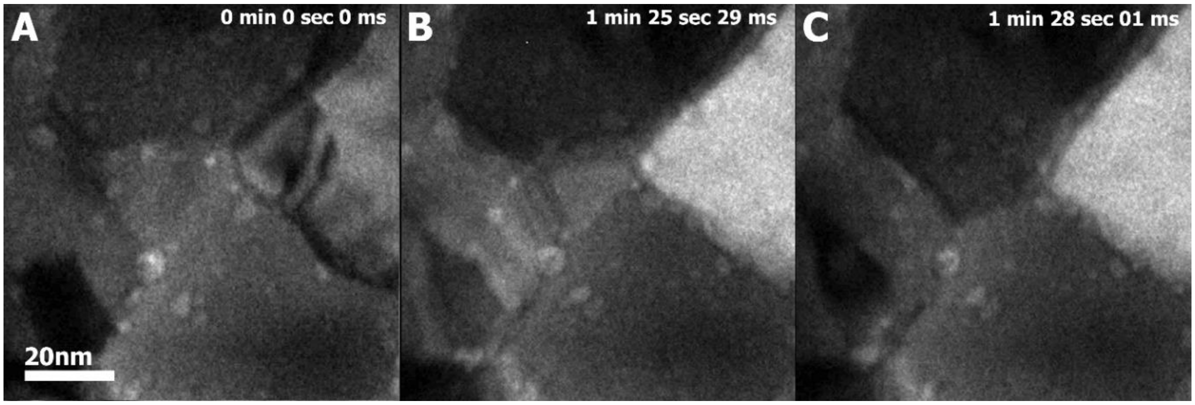

Figure 66. *In-situ* TEM brightfield images of grain boundary motion in columnar nanocrystalline Fe at 900°C: (A) shows the original location of the boundary lined with large voids. (B) after 1 minute and 25 seconds the boundary has progressed approximately 12nm across the voided region (C).

6.3.2 Simulation Results

Using the information acquired from the *in-situ* TEM experiments, a simulation was created of a 200 nm by 200 nm thin film with 28 grains, such that the average initial grain size was 38 nm. Grain boundary migration was simulated using both 2D and 3D simulations. The simulation shown in Figure 67 was created using a criteria that the voids (vacancy concentration) are held constant and only the grains evolve.

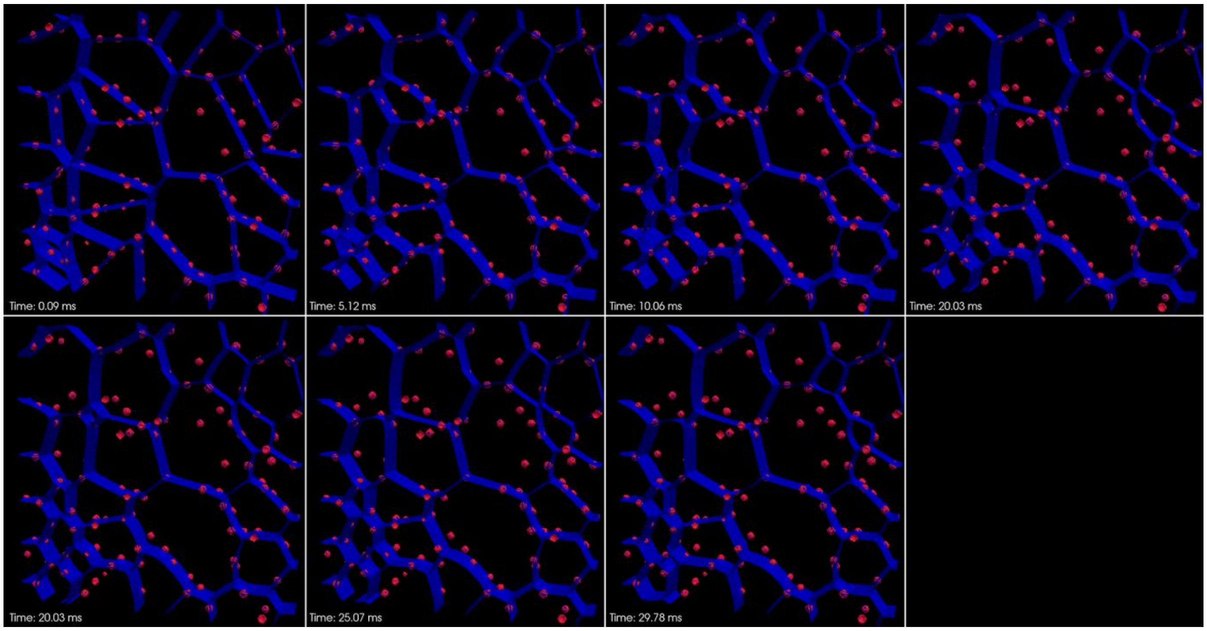

Figure 67. Simulation results showing 5ms time steps from the model.

6.4 Discussion

In the initial results, grain boundary motion is found to be altered by the presence of voids, but not to the extent seen in the experimental results. In the simulation, the boundary curvature is quickly minimized as would be expected for grain growth in a pure, microcrystalline metal where grain boundary curvature is the primary driver for grain growth. This action is performed in the simulation despite the presence of voids along the grain boundaries. In the experimental results, the curvature of the grain boundary is maintained until the boundary becomes completely unpinned, suggesting that the nanocrystalline iron films contain a larger number of voids along the grain boundary that pin its entire length. The void density is so high in the Fe films that all of the boundaries are pinned by voids and therefore the curvature of the boundaries cannot change much until one breaks free. Further work is required to better approximate the behavior of nanocrystalline metals with voids at grain boundaries.

CHAPTER 7. IRRADIATION OF BULK MICROCRYSTALLINE IRON

7.1 Introduction

Historically, research to study the effect of irradiation on metals has largely been performed using materials with a grain size on the order of microns. This is particularly true for irradiations of iron seeking to understand the fundamental processes affecting the morphology of defect structures in the matrix. From the first unsuccessful work by Hull (Hull, D., and Mogford, I. Phil. Mag 6 (1961) 535) and Baker [105], and the first successful work by Eyre [106], these studies have utilized large grain polycrystalline or single crystal iron as a means to determine the effects of radiation on the BCC structure.

A long series of work by a lineage of researchers by Dr. Mike Jenkins, his students, and collaborators [18, 42, 46, 48, 66, 69, 109, 115, 139, 140, 206, 280] has been performed using micron grain size iron, culminating in a series of papers detailing the *in-situ* irradiation of iron as a function of dose [69, 115], temperature [140], and chromium content [18, 69, 115]. The most detailed studies of radiation damage in iron to date used primarily 100–150 keV Fe^+ self ions and some Xe^+ ions [18, 69, 115, 140]. The work of these authors was heavily referenced as a basis for interpreting the results for irradiation of nanocrystalline iron films. There are, however, slight differences in the defect production for different ions. Jenkins et al. irradiated iron to low doses using Fe^+, Ge^+, Kr^+, Xe^+ and W^+ ions and found a that the defect production rate for each ion species is different. Iron ions, for instance, produced no visible damage in iron at the doses studied, while 80 keV Ge^+ and heavier ions produced visible damage. The irradiations for this work were performed primarily with Kr^{++} ions, so in order to compare to the work done in literature it was necessary to irradiate a similar microcrystalline specimen prepared from bulk using the exact irradiation parameters (ion species, energy, dose rate, and temperature) used to investigate the irradiation behavior of nanocrystalline films.

The *in-situ* irradiations were performed at Argonne National Laboratory using the *in-situ* TEM irradiation setup at the IVEM Tandem facility which consists of a 650KeV ion implanter directed into a Hitachi H-9000NAR TEM at 30° from the electron beam [215]. This system permitted the use of 1 MeV Kr^{++} ions for irradiation.

Additional *ex-situ* ion irradiations were performed to supplement the work from the IVEM facility and for specific experiments such as the irradiation of the tensile bars for *in-situ* mechanical behavior. Most of the *ex-situ* irradiations were performed using a 200keV implanter at Los Alamos National Laboratory. The implanter was not capable of producing as heavy or high energy of ions as the IVEM facility, so irradiations were limited to using 400keV Ar^{++} ions. Again a comparative study was required to ensure that the damage achieved with the 400 keV Ar^{++} ions was similar to that produced by 1 MeV Kr^{++} ions.

7.2 General Methods

To create microcrystalline TEM specimens from bulk for direct comparison to literature, TEM specimens were prepared following the procedure outlined in Section 3.3. High-purity iron (Table 2) was prepared by Carpenter Technology Corporation (Reading, PA). Electrical discharge machining (EDM) was used to section the bulk iron into thin plates approximately 250μm in thickness. The sheets were then mechanically thinned to a thickness of 100μm before 3mm disks were punched from the material. Using a twin jet electropolisher, the disks were thinned to electron transparency with a solution of 5% perchloric acid in methanol at -30°C. They were then rinsed several times in anhydrous methanol and stored in vials of clean anhydrous methanol.

To match the observations in nanocrystalline iron, subsequent imaging in the bulk materials was also performed using kinematic brightfield using 110 reflections. Jet thinned bulk samples were chosen that contained grains with a 001 zone axis near normal to the specimen surface. By imaging and counting only defects found in 001-normal grains, the effect of grain orientation with respect to the foil surface quantified by Jenkins et al. [18] was minimized. Images were also taken in regions of the grain where the thickness was comparable to that of the free standing iron films (~150nm) used for studying nanocrystalline iron. The thickness was measured by measuring the apparent height of a grain boundary while tilting from -35° to +35° about an axis parallel to the boundary.

Irradiations were performed at Argonne National Laboratory using the *in-situ* TEM irradiation setup at the IVEM Tandem facility which consists of a 650KeV ion implanter directed into a Hitachi H-9000NAR TEM at 30° from the electron beam [215]. Each sample was stabilized at 300°C and imaged before being irradiated. Irradiations were performed in segments, pausing only to take still images at doses, calculated by SRIM [216], of 0.1, 0.25, 0.5, 1, 2, 3, 4, and 5 dpa.

7.3 Krypton irradiations

The behavior of iron under irradiation by 1 MeV Kr^{++} ions was found to be similar to what was observed by Jenkins et al. in irradiations using 100–150 keV Fe^{+} ions when compared using the calculated dose (i.e. dpa). The first TEM visible clusters were observed around $2x10^{14}$ Kr ions-cm^{-2} or approximately 0.25 dpa, similar to the observation of Jenkins et al. that the first 2-4nm TEM visible clusters form at around 0.1-0.3 dpa. The number density of the TEM visible defect clusters was found to increase until approximately $8x10^{14}$-1.6 $x10^{15}$ Kr ions-cm^{-2} (1-2dpa), then the defect clusters were found to coalesce into dislocation loops between 2.4x10^{15} Kr ions-cm^{-2} (3 dpa) and 4.0 x10^{15} (5dpa).

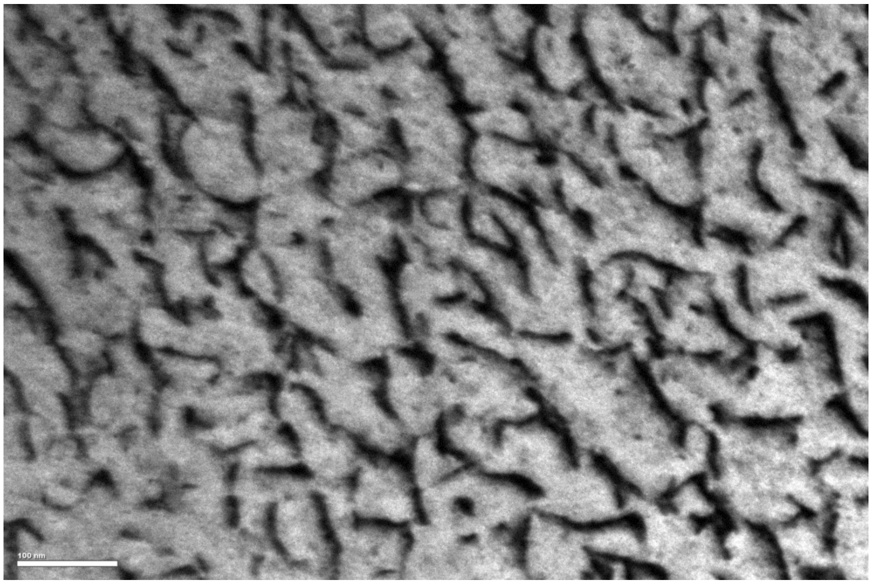

Figure 68. A TEM micrograph of microcrystalline iron irradiated to 5dpa using 1 MeV Kr^{++} ions. A tangled network of dislocations formed from b=1/2<111> dislocation loops.

7.4 Argon irradiations

Argon ion irradiations were performed with 400 keV Ar^{++} ions at Argonne to match the *ex-situ* irradiations. At this ion mass and energy, 4.8x10^{14} Ar ions-cm^{-2} were required to achieve 1dpa. The behavior of iron under irradiation by 400 keV Kr^{++} ions was found to be similar to both the observations of Jenkins et al. in irradiations using 100–150 keV Fe^{+} ions, and with irradiations performed using by 1 MeV Kr^{++} ions. Again a tangled network of dislocations is formed when the sample is irradiated to 5dpa at 300°C (Figure 69). The damage at each dose level was found to be qualitatively similar, beginning with the formation of discrete microscopic defect clusters which then coalesce into large loops.

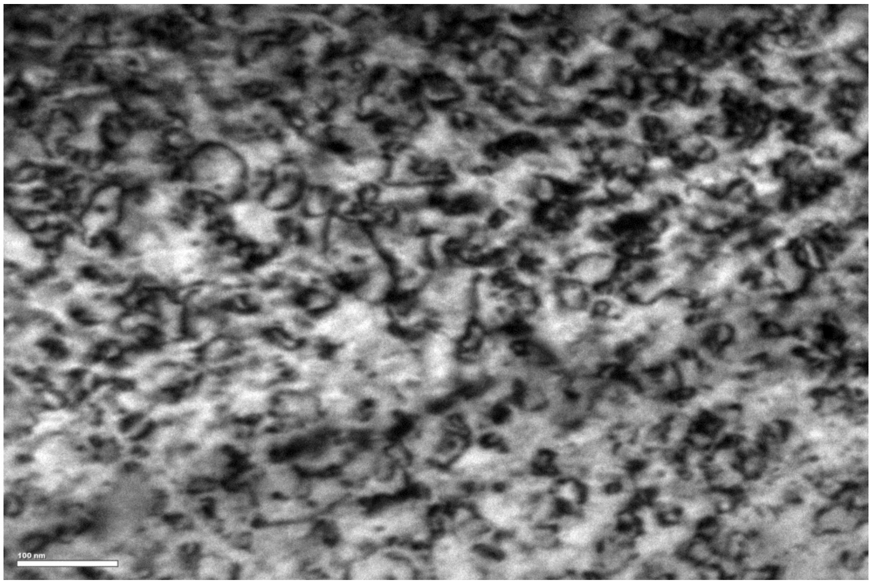

Figure 69. A TEM micrograph of microcrystalline iron irradiated to 5dpa using 500 keV Ar^{+++} ions. A tangled network of dislocations formed from b=1/2<111> dislocation loops.

The microstructure shown in Figure 69 is confirmation that the calculated target dose of 2.4x10^{15} Ar ions-cm^{-2} achieves approximately the same level of damage (5dpa) as when the specimen is irradiated with 4.0 x10^{15} Ar ions-cm^{-2}. Furthermore, it shows that the temperature control of the *in-situ* TEM holder is sufficient to replicate the results of a specimen mounted in direct contact with a large water cooled heater block assembly, lending more credence to irradiations, particularly temperature dependence work, performed in the TEM at Argonne.

7.5 Thickness Effect Compensation

To determine the critical thickness for radiation damage in iron films, it was necessary to determine the thickness of a TEM specimen and correlate the irradiated microstructure at that point. For this purpose, a micron grain size specimen was prepared by jet thinning pure iron in accordance with Section 3.3. The sample was irradiated at Argonne National Laboratory using the IVEM-tandem facility. Doubly charged krypton ions were used to irradiate the specimen to a dose equivalent to approximately 5dpa (4.0 x10^{15} ions·cm^{-2}) while the specimen was held at 300°C. The irradiated microstructure was compared to what has been reported in literature at various points during the irradiation. In large areas of the specimen, the structure of the dislocations present was nearly identical to that reported by Jenkins et al. for irradiations of iron at 300°C [69, 115]. By 5dpa, large dislocation loops had grown until they had just started to interact to form a tangled network of dislocations.

A region of the specimen was then located where a wide variation in thickness was visible within the field of view (Figure 70). In this area the thickness of the iron ranged from near zero at the jet-thinned hole to a thickness that was no longer electron transparent. In this region a distinct change in the morphology of the dislocation loops was observed. In thin areas (Region C), the dislocations loops are discrete and formed at right angles. These dislocation loops appeared to lie along the <100> directions. Region B is representative of the microstructure observed by Jenkins et al. for 300°C irradiations in "thick" regions, and consisted of a tangled network of dislocation loops. Region A was similar to that of Region B, but due to the increased thickness it becomes difficult to discern the loops. Eventually the thickness becomes too great for sufficient image intensity.

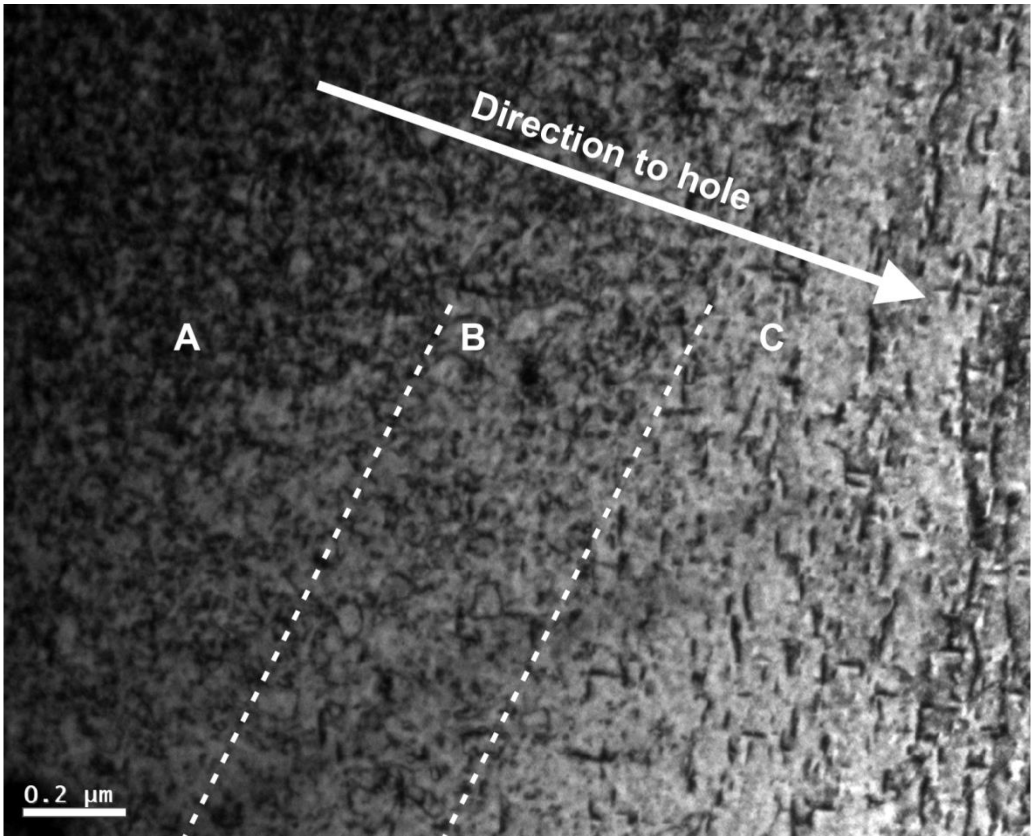

Figure 70. TEM brightfield images of a region near the hole in grain boundary in micron grain size iron. The thickness of the specimen decreases closer to the hole. Region B is representative of the microstructure observed by Jenkins et al. consisting of a tangled network of dislocation loops. Region A is similar but due to the increased thickness it becomes difficult to discern the loops. Region C, however, shows a distinct change in loop morphology.

The thickness effect observed in the iron specimen irradiated to 5dpa at 300°C using Kr^{++} ions is similar to that reported by Jenkins et al. in an UHP Fe foil irradiated with 150 keV Fe^{+} ions at to a dose of 10^{-19} m $^{-2}$ (about 6.5 dpa) at RT [115]. In that case, strings of **b**=1/2<111> dislocation loops are seen in thicker areas lining up more or less parallel to projection of the [110] direction. These loop strings are the precursor to the large finger loops at

300°C. In contrast, thin areas of foil contained only isolated dislocation loops with **b**=<100> Burgers vectors.

The region shown in Figure 70 was located near a grain boundary that extended radially from the jet-thinned hole in the specimen. This permitted a simple tilting experiment to determine the approximate thickness of the specimen at each point. The sample was tilted about an axis that ran parallel to the grain boundary (Figure 71). At each tilt where the grain boundary was visible, the projected width of the grain boundary was measured at two points that correspond with the white dotted lines in Figure 70.

Figure 71. TEM brightfield images of a grain boundary in micron grain size iron. The boundary is tilted to the extents of the TEM holder about the axis of the grain boundary from (a) -37.3° through (b) 0° and (c) 34.1°. The inclined GB can be seen as a wedge shape in (a) and (c), and a thin line in (b).

The results of this measurement and calculation are shown in Figure 72. The average thickness calculated for the transition from the **b**=<100> type dislocation loops to the **b**=1/2<111> dislocation loops is 58nm. The transition from nearly discrete **b**=1/2<111> loops to a thick tangled network of dislocations occurs around 140nm. For this reason, the thin film depositions used to study irradiation damage in nanocrystalline and ultrafine grained materials were created with a target thickness of 100nm.

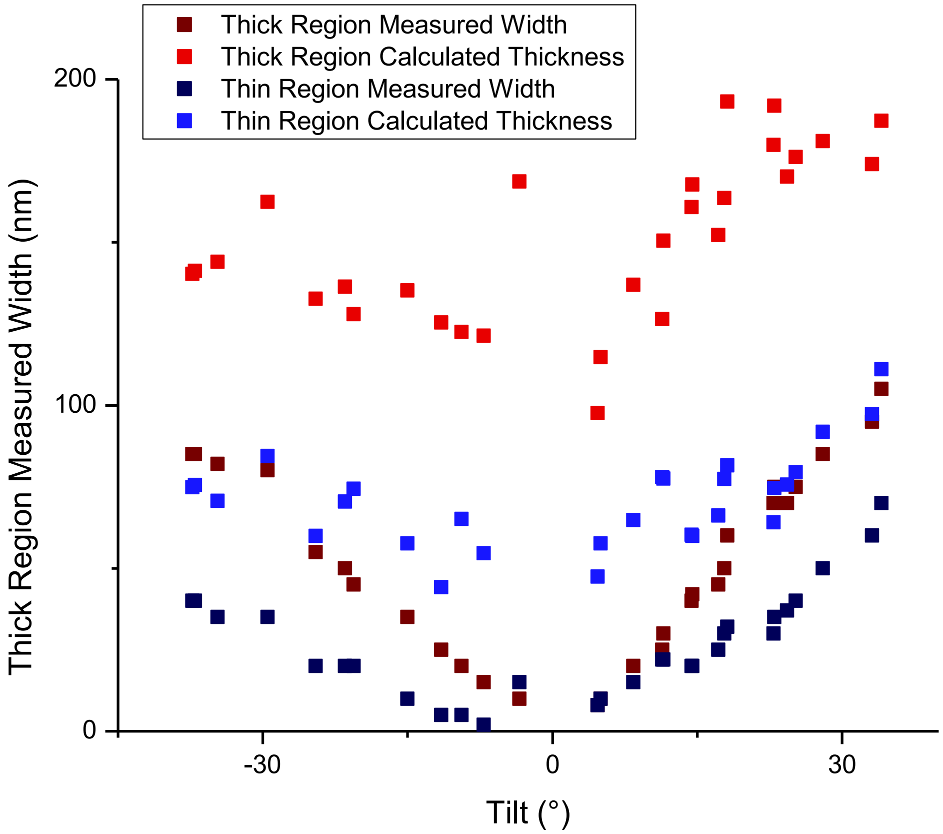

Figure 72. Measured width of the grain boundary projection from brightfield TEM images and the calculated thickness of the foil from the angle away from the tilt with the smallest visible boundary width (i.e. edge on).

7.6 Conclusions

This chapter was included to verify the irradiations used in the remainder of the thesis. Based on the results for the irradiation of a jet thinned microcrystalline iron specimen, it can be concluded that irradiations performed using 1MeV Kr^{++} ions (at a dose rate of $8x10^{14}$ ions cm^{-2} per dpa as calculated by SRIM) provide comparable results to those produced by Jenkins et al.

[18, 69, 115] using 100–150 keV Fe^+ self ions and some Xe^+ ions at the same facility. Likewise, it was found that 4.8×10^{14} Ar^{+++} ions-cm^{-2} per dpa gave similar results to 1MeV Kr^{++} ions as well as the results by Jenkins et al. It was found that such results were only directly comparable where the thickness of the specimen exceeded approximately 70nm, which was used as a minimum specimen thickness for the work in this thesis.

CHAPTER 8. GRAIN SIZE EFFECT UNDER IRRADIATION IN IRON

8.1 Introduction

The need for new materials that are resistant to radiation damage is a pressing issue for applications ranging from nuclear reactors to solar materials and sensors. When combined with stress and high temperatures (~300°C) in a nuclear reactor core, for example, irradiation of a material by high energy neutrons produced in the fission chain reaction results in the formation of interstitials and vacancies in concentrations far above thermal equilibrium which ultimately leads to material failures such as swelling and embrittlement [21, 35, 88, 281, 282]. Candidate materials for next generation nuclear reactors, which are expected to operate at higher temperatures and neutron fluxes, are being designed to utilize extrinsic microstructural features such as grain boundaries, dislocations, and precipitates as a means to improve radiation resistance and mechanical properties [6, 17, 282-285]. Grain boundaries are considered a means control radiation damage [28, 29] based on observations that they can yield regions of low defect density called denuded zones [21-24, 26, 27]. Nanocrystalline materials are a subject of great interest, as a small enough grain size in a material leads to a sufficiently high density of grain boundaries acting as defect sinks to reduce the amount of damage occurring from radiation cascades. This effect has already been shown to reduce resistivity changes in irradiated Au [197, 198], to reduce amorphization of $MgGa_2O_4$ [199] and TiNi [30], and has been shown by TEM to reduce defect clustering in ZrO_2 [31], Pd [31], Cu–$0.5A_2O_3$ [32], and Ni [32, 33]. However, the mechanisms by which radiation tolerance occurs in nanocrystalline materials, in particular the role of grain boundary character, is not clear. Before truly predictive materials development for radiation tolerance can arise, a comprehensive understanding of how the interplay between grain size, grain boundary character, and the mechanisms for the action of a grain boundary sink contribute to the radiation tolerance of a material will be required.

Cascade events that occur at or near a grain boundary lose a large fraction of the interstitials formed during the cascade due to spontaneous recombination with the boundary event [75-79]. The immediate result is a higher survival rate for vacancies following the cascade [75, 81]. Interstitials that are loaded into the boundary may then annihilate vacancies remaining in the grain through a non-diffusive process, reducing the residual concentration [81]. These point defect annihilation processes at grain boundaries create a concentration gradient, driving the diffusion of freely mobile interstitials and vacancies to the boundary [23, 26, 82]. Point defects bound in interstitial clusters and dislocation loops may also be transported to the boundary by mobile dislocation clusters and loops, or through pipe diffusion along immobile frank loops that have grown close to the boundary by climb [33, 98]. The end result of the transport of defects to the boundary by these processes are denuded zones from 10's of nanometers to a few microns in width in polycrystalline materials [21, 22, 27], despite the fact that the recombination mechanisms operate within a few nanometers of the grain boundary.

The mechanisms involving the absorption of point defects at a grain boundary are dependent on the binding energies of interstitials and vacancies with the boundary, which are in turn dependent on the grain boundary character (GBC) [278, 286-288]. Likewise, it has been theorized that the formation of denuded zones along grain boundaries is also dependent on grain boundary character [23, 24, 26, 27, 71, 226, 227, 289-292]. There still remains a question as to if or when grain boundary character breaks down as the grain size is reduced from coarse-grain to nanocrystalline [293, 294]; that is, whether the boundaries retain their structure [295] or the atoms relax into a gas-like disorder [146]. Recent research [175, 296] has shown that the interface at a grain boundary in nanocrystalline copper and nickel can retain a structure much like that of micron grain size materials even at grain sizes down to 30nm. Ranganathan et al. showed that in 7nm palladium, the boundary structure contains elements of equilibrium boundaries but due to the small grain size contains regions of disorder at triple junctions [297]. Their results also showed that at such small grain sizes the boundary curvature results in a constantly changing boundary structure with regions of high and low energy. Whether or not the grain boundaries in a material retain some equilibrium structure appears strongly dependent on processing conditions as well as grain size. The details will have a significant effect on the behavior of nanocrystalline materials, but have yet to be elucidated.

8.2 Methods and Procedures

In this work, we follow the behavior of grain boundaries under irradiation in three grain size regimes in pure iron: coarse grain (>1μm), ultrafine (1μm-100nm), and nanocrystalline (<100nm). Specifically, we show how grain boundary character and density affect the boundary sink mechanism by using *in-situ* transmission electron microscopy coupled with heavy ion irradiation. Coarse grain (>1μm) polycrystalline iron with low dislocation density allows for the investigation of defect absorption at grain boundaries for grain sizes relevant to low alloy steel used as structural components in light water nuclear reactors, and for comparison with previous irradiation studies in literature. Specimens with ultrafine (1μm-100nm) grain size are representative of nanostructured ferritic alloys such as oxide dispersion strengthened (ODS) steel which typically has grain sizes as small as several hundred nanometers. Finally, samples with grain sizes from 100nm down to about 20nm allows us to study how the radiation behavior of iron changes as the grain size is reduced to the nanocrystalline regime for enhanced radiation tolerance. Preparation of these samples is described in the methods section. Grain size and orientation information in each specimen were determined using SEM-based electron backscatter diffraction (EBSD) or by NanoMEGAS ASTAR precession diffraction in the TEM [217, 243]. Samples were irradiated *in-situ* at 300°C using 1MeV Kr^{2+} ions at Argonne National Laboratory's IVEM Tandem facility (see Chapter 3 for detail).

8.3 Results

Examples of the microstructure in iron after irradiation to 5 dpa are shown in Figure 73 for each of the grain size ranges: coarse grain polycrystalline (>1μm), ultrafine grain (100nm-1μm, and nanocrystalline (<100nm). In microcrystalline iron, the irradiated microstructure (Fig. 73a) in regions thicker than 75nm irradiated to approximately 5dpa is similar to observations reported in literature [18, 69, 115] and consists of a densely entangled dislocation network created by the interaction of growing **b**=1/2<111> finger type interstitial loops. In the 150nm thick ultrafine grain iron films (Fig 73b), the finger loops are visible but are significantly smaller in size. They have not grown large enough to impinge on each other and form the tangled dislocation network that is characteristic of coarse grain polycrystalline iron at this dose. The effect of grain boundary sinks is more pronounced in nanocrystalline iron films. Here, the larger finger type loops are notably absent, and the irradiated microstructure consists of small discrete dislocation loops. The defect cluster size restriction indicates that point defects or defect clusters are being lost to the grain boundary sinks before the damage can accumulate.

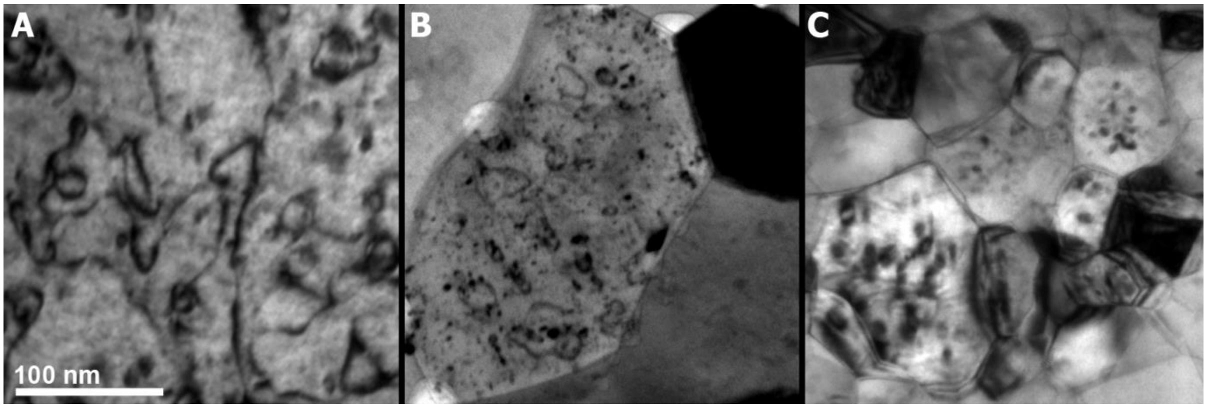

Figure 73. A comparison of the Transmission electron microscope images of the dislocation loops formed in pure iron after irradiation to 5dpa at 300°C as a function of grain size. (A) In microcrystalline iron (grain size > 1μm) iron, large dislocation tangles are formed by growing b=1/2<111> loops. (B) In free-standing ultrafine grain iron films (~500nm grain size), similar behavior is observed although now the loop size is truncated. (C) In nanocrystalline grains (15-100nm), the size of the dislocation loops decreases further until a minimum loop size of 3-5nm is reached. Note that in (B) and (C) only certain grains are in the proper orientation for loop contrast.

In larger grains, such as those found in the ultrafine grain and coarse grain specimens, the overlap of large dislocation loops and small defect clusters makes measuring dislocation loop size and density difficult. However, the discrete dislocation loops found in smaller grains such as those in the nanocrystalline (<100nm) samples, make measurements achievable. Plotted as a function of grain diameter (Fig. 74a), the size of dislocation loops measured within the nanocrystalline grains continues to decrease with until the grain size reaches about 80nm. In grains below 80nm in size, the mean size of dislocation loops measured remains nearly constant at around 5nm. Defect clusters of 2-5nm are the minimum observable defect size in the TEM. These defects with a strain field on the order of 2-5nm likely form within cascades or from the overlap of multiple cascade events [46, 98]. Occasionally larger loops are found near the center of the grains and appear to form when two or more of the smaller defect clusters come in contact. However, the growth of these defect structures is limited to less than about 12nm in grains smaller than 80nm in size.

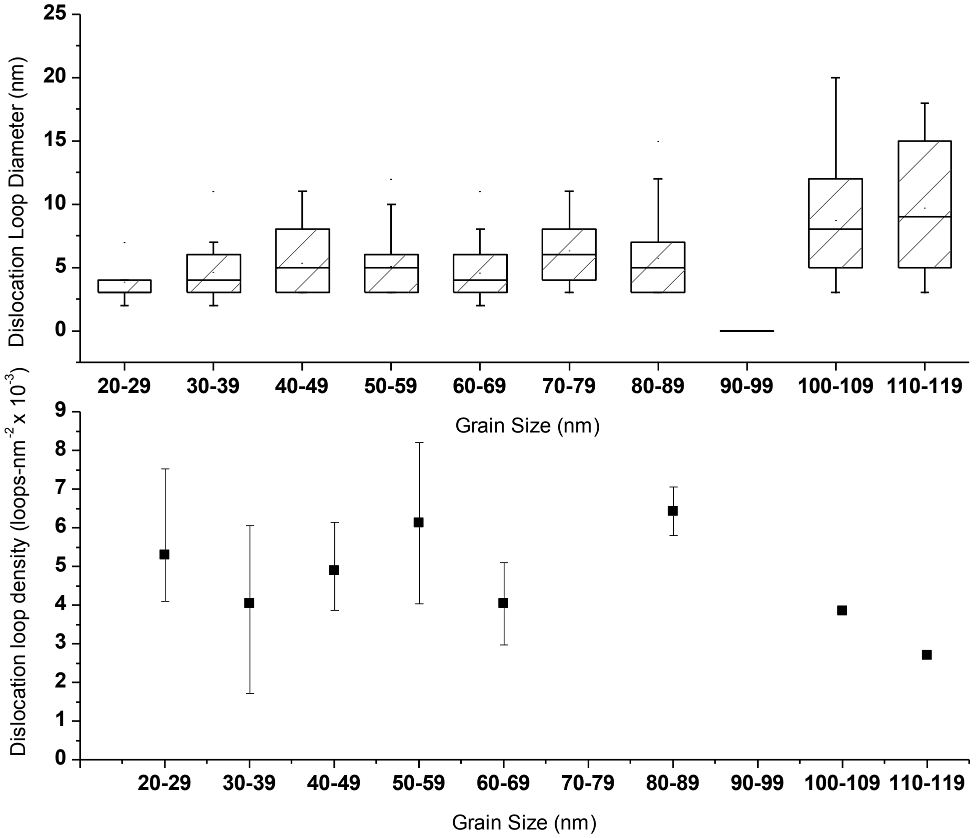

Figure 74. Quantitative analysis of the defects found in grains where the images acquired corresponded closely to the desired kinematical brightfield with a 110 systematic row of reflections. The results show that (top) the apparent diameter of the dislocation loops in a given grain is proportionate to the grain size. Small defect clusters are increasingly less able to coalesce to form the large finger loops as grain size decreases. (bottom) The defect density increases as grain size decreases due inability of the defects to form large finger loops in smaller grains. At the smallest grain sizes, the defect density falls off sharply.

8.4 Discussion

It is clear from the TEM micrographs in Figure 73 and the quantitative measurements of loop size (Fig. 74) that there is a strong influence of grain size on dislocation loop size. However, the defect density results from the quantitative defect analysis do not show a clear trend of decreasing density like that reported by Rose et al. [31]. After a 5dpa dose of irradiation, the upper limit of defect density in iron grains between ~30nm and ~80nm is around 6-8x10^{-3} defect clusters per square nanometer. This value is almost identical to that measured using similar imaging conditions in coarse grain polycrystalline iron of comparable thickness after a dose of approximately 3dpa. That dose, in coarse grain or single crystal iron irradiated at 300°C, is representative of the period when the density of 2-5nm defect clusters has reached its maximum. At higher doses, the defect clusters align to form loop strings along <110> directions which then coalesce into large **b**=1/2<111> type finger loops [18, 69, 115]. In nanocrystalline grains below about 80-100nm, this process is impeded by the loss of point defects to grain boundaries. As a result, the density of small defect clusters remains relatively high.

The size of the defect loops is affected in all of the samples observed with grain sizes below about 500nm, but the population of TEM visible defect clusters shows a wide variation from grain to grain. Defect density appears to be unaffected in grains where there is no prominent denuded zone, as shown in the top row of Figure 75. However, a number of grain boundaries in iron contain a very well defined denuded zone, such as the examples of boundaries in polycrystalline, ultrafine grain, and nanocrystalline iron shown on the bottom row in Figure 75. Figure 75d shows a grain boundary in polycrystalline iron that has an asymmetric denuded zone with an apparent width of approximately 15nm on one side of the boundary and 30nm on the other. In the ultrafine grain (Fig. 75e) and nanocrystalline grain (Fig. 75f) films, the width of the region with low defect density is similar to the denuded zone observed in bulk iron (~30nm). The result is that as the grain size is decreased the denuded zone comprises a larger portion of the grain and the average defect density is greatly reduced. For the grain with a diameter of approximately 60nm in Figure 75f, the defect density is roughly 2x10^{-3} defects-nm^{-2}, significantly lower than the nominal value for coarse grain iron. The data point for this grain is highlighted as a red circle in the defect density plot in Figure 74b. Clearly, some grain boundaries have a greater influence on the formation of a denuded zone, which has significant influence on the ability of a nanocrystalline material to reduce radiation damage.

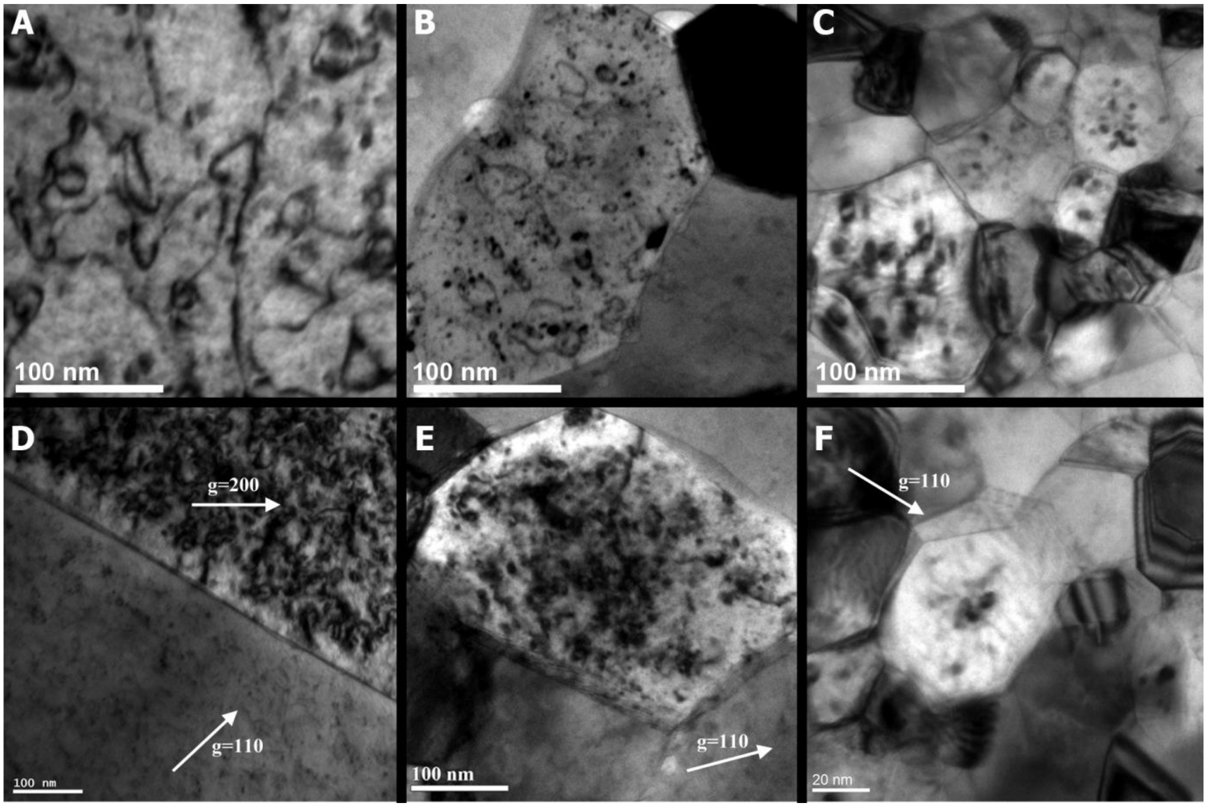

Figure 75. The denuded zone effect in select grains from (A) polycrystalline, (B) ultrafine grain, and (C) nanocrystalline grains in pure iron. Diffusion of point defects to grain boundary sinks contributes to a decreased density and size of dislocation loops in irradiated iron. As the grain size decreases, this effect becomes more significant.

Much of the theory for the formation of denuded zones relies on the inherent efficiency of a grain boundary sink that arises due to the structure of the grain boundary [278]. Therefore it was of interest to determine whether any trends could be found in the relationship between grain boundary character and the presence of denuded zones at grain boundaries in nanocrystalline iron. In fact, two types of denuded zones were observed, a clearly defined denuded zone on the order of 10-30nm in width with a low population of defect clusters/loops, and wide denuded zones (~50-100nm) characterized by a decreasing dislocation loop size approaching the boundary. The correlation between grain boundary character (in terms of disorientation) was found to be very weak, indicating that more than factor determines the formation of a denuded zone in polycrystalline materials.

8.4.1 Inherent Sink Strength (GBC)

Figure 76 highlights a grain in an ultrafine grain film in which each grain boundary had clearly different denuded zone widths. This type of arrangement was common in both small grain iron specimen types (i.e. ultrafine grain and nanocrystalline). By correlating misorientation information with brightfield TEM images, it was found that both low angle and high angle grain boundaries had a denuded zones. In some cases, the formation of a denuded zone could be correlated with a specific grain boundary character, as could best be determined experimentally. An example of this is the uppermost grain boundary in the yellow grain in Figure 76, which was identified as being a low angle grain boundary with a disorientation of 11.0° (111). The denuded zone at this grain boundary is very sharply defined and is 20-30nm in width.

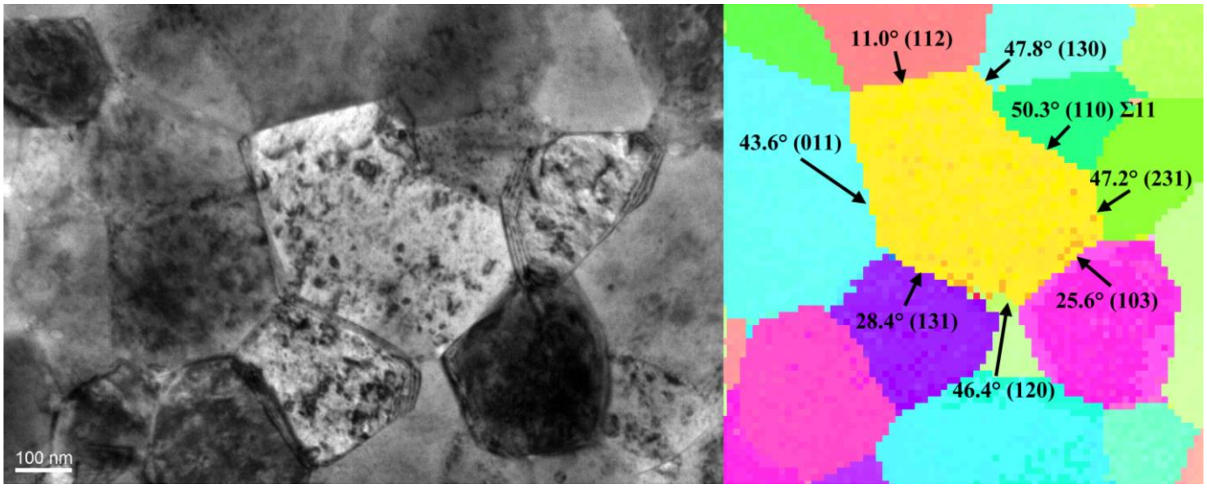

Figure 76. (A) A brightfield TEM image of a grain in ultrafine grain pure iron showing the concentration of dislocation loops along the boundaries. Coupled with a pole figure map (B) acquired by NanoMEGAS ASTAR orientation mapping in the TEM, the effect of grain boundary character on the width of the denuded zone in the grain is shown.

A grain boundary in microcrystalline iron was identified with a similar orientation to the low angle (11.0° <111>) boundary in Figure 76. The microcrystalline boundary, shown in Figure 75d, has a misorientation of 12.6° <112> (Figure 77). In the 11.0° <111> boundary in the ultrafine grain iron, the upper (red) grain normal is 17.65° from the <001> direction, or 1.77° from <218>. The lower (yellow) grain has an orientation that is 20.35° from <001>, or 2.00° from <103>. For the microcrystalline specimen, the lower grain (red) is 14.30° from <001> or 1.62° from <218>. The upper (yellow) grain is 22.83° from <001> or 4.39° from <103>. Therefore the disorientation, surface normal, and imaging conditions are similar in both cases. Likewise, there is a denuded zone at each boundary measuring 20-30nm in width.

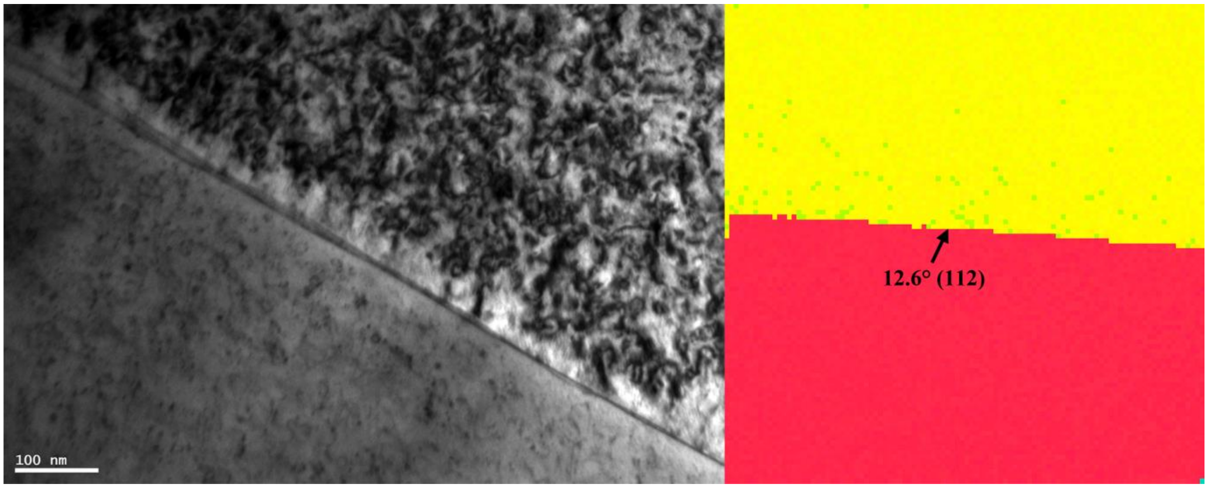

Figure 77. (A) A brightfield TEM image of a grain boundary in microcrystalline pure iron showing the concentration of dislocation loops along the boundary on the upper side. Coupled with a pole figure map (B) acquired by NanoMEGAS ASTAR orientation mapping in the TEM, the effect of grain boundary character on the width of the denuded zone in the grain is shown.

8.4.2 Strain Near GBs

The remainder of the grain boundaries shown in Figure 76 are high angle grain boundaries. Most of the boundaries in the grain are high angle boundaries and have very narrow denuded zones. Some of these grain boundaries, however, have denuded zones of varying widths. In most cases, the denuded zones that form next to the high angle grain boundaries are not sharply denuded. Instead of being a large decrease in the population of dislocation loops, these regions appear to be gradual decreases in the size of the dislocation loops closer to the grain boundary.

Using the data collected in orientation maps created using NanoMEGAS automated crystallographic orientation mapping in the TEM, Nye tensor maps were calculated to describe the number of geometrically necessary dislocations to account for local curvature in the orientation of the grain. Areas of large calculated necessary dislocation density were present in regions near grain boundaries that appeared denuded. Figure 78 shows the results of these calculations for the grain shown in Figure 76. The white arrow shows how the area of high geometrically necessary dislocation density corresponds to the denuded zone. Similar observations can be made about the other two grain boundaries at the lower end of the grain. This correlation was also observed in multiple grains found in multiple thin film samples.

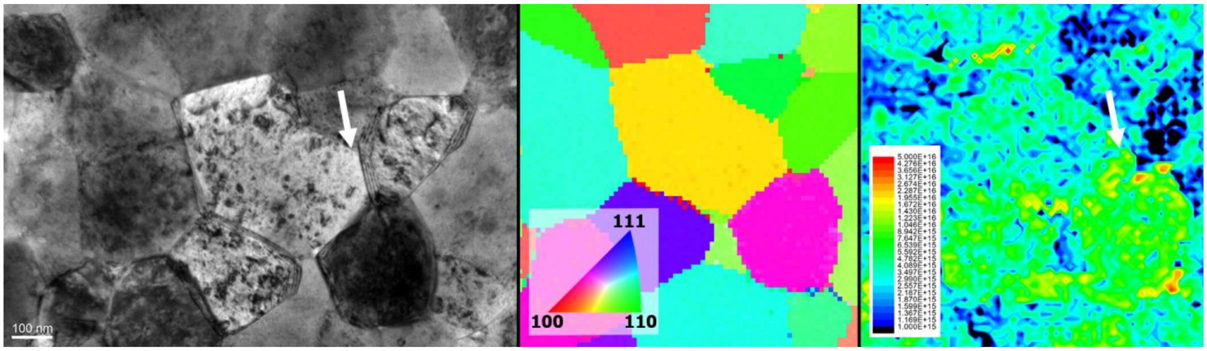

Figure 78. (left) A brightfield TEM image of a grain boundary in ultrafine grain pure iron showing the concentration of dislocation loops along the grain boundaries. A calculated map of the calculated geometrically necessary dislocations required to account for orientation changes within a grain is shown at right. Denuded zones correspond to areas requiring higher numbers of geometrically necessary dislocations.

The absence of dislocations in this region may indicate that a large amount of elastic strain is present at the grain boundary. It was unclear, however, whether the strain affected the formation of a denuded zone, or was a consequence of the irradiation itself. To answer this question, similar calculations were performed on nanocrystalline iron films in the annealed, but unirradiated condition. Figure 79 shows the Nye tensor map calculated for the film in Chapter 5 after an 800°C irradiation. Regions of higher theoretically necessary geometric dislocations, shown as yellow/orange, are present in the grains particularly near the grain boundaries. This showed that the strained regions were present prior to irradiation, and therefore represented intrinsic strain in the material not an effect of the irradiation.

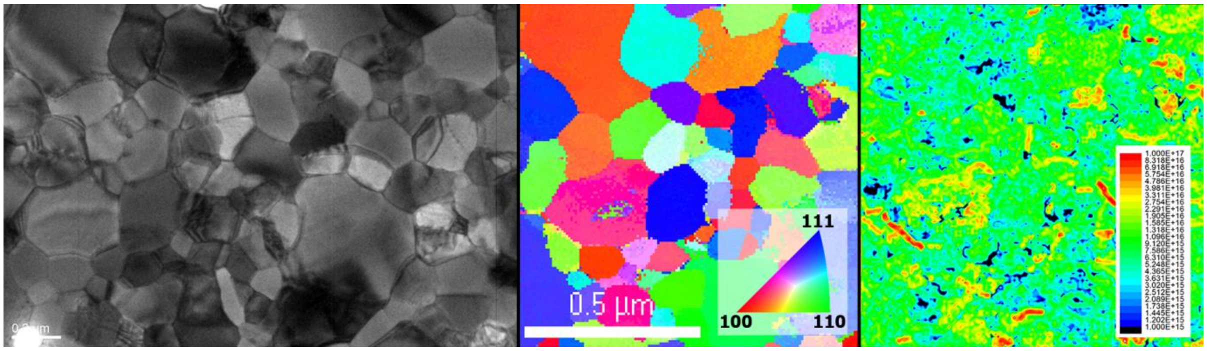

Figure 79. (left) A brightfield TEM image of a sputtered iron film annealed to 800°C (center) the orientation map collected from the region and (right) the resulting Nye tensor map showing the geometrically necessary dislocation density to account for orientation changes. High angle GBs (>15°C have been excluded from the calculation.

8.4.3 Non-Equilibrium GB Structure

Grain boundaries in nanocrystalline iron films produced by sputter deposition and annealed were found to show preferential formation of denuded zones at certain grain boundaries in grains down to about 20nm, suggesting that equilibrium grain boundary structures are present to very small grain sizes. An example of this behavior is shown in a 40nm grain in Figure 80. The small grain has clearly defined denuded zones at three of its grain boundaries, but defect clusters form right up to the boundary for the other three boundaries. High resolution TEM of the grain boundary was not possible in the films used for irradiation due to the choice to use relatively thick (>120nm) films to minimize the free surface effect. Instead, thin (<50nm)

Fe films were deposited on NaCl substrates using the same parameters, then annealed *in-situ*. The resulting films show that after annealing the crystalline nature of the grain is preserved right up to the grain boundary even in small grains.

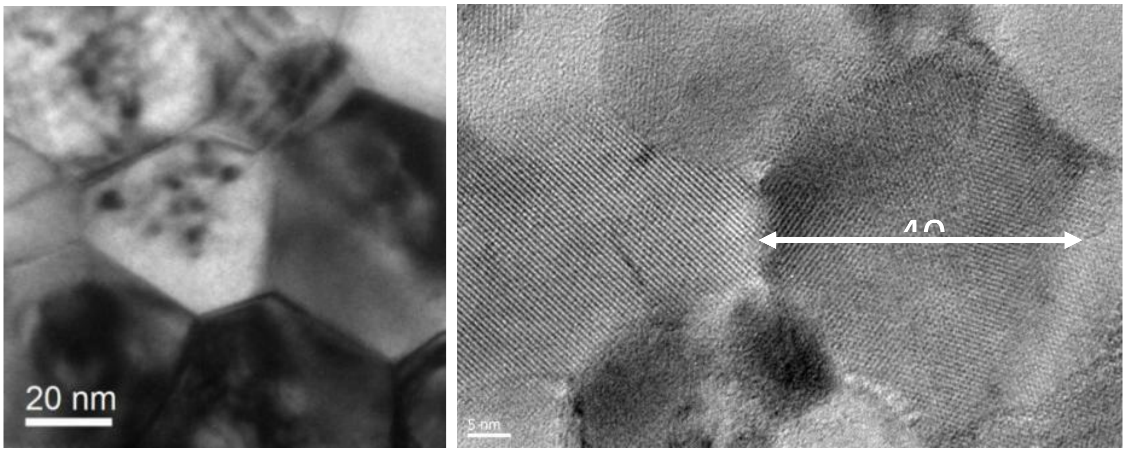

Figure 80. (left) Predominant denuded zones are visible at half of the grain boundaries in a 40nm grain in iron. (right) HRTEM of a thin nanocrystalline iron film shows that grains retain crystalline structure up to the grain boundary interface, suggesting near-equilibrium grain boundary structures.

Although the annealed nanocrystalline thin films used in this study retained nearly equilibrium grain boundary structures down to the nanoscale due to the annealing process, the techniques used to produce many nanomaterials are thought to lead to a non-equilibrium grain boundary structure. An example of this is in nanocrystalline materials produced by severe plastic deformation (SPD), a technique commonly used to produce oxide dispersion strengthened (ODS) steels for nuclear reactor applications. Therefore it was of interest to also understand what the breakdown of equilibrium grain boundary means for the performance of a radiation tolerant material. Non-equilibrium grain boundaries have increased amounts of both strain and free volume, which could enable the boundary to act as an efficient sink.

High resolution transmission electron microscopy of nanocrystalline iron films (Figure 81) showed that unannealed films have a microstructure that includes ill-defined grain boundaries. Once annealed, the same films show well defined grain boundaries with narrow interfaces which is an indication of near-equilibrium structure. The majority of the experiments performed in nanocrystalline iron were done in the latter type of film; however, initial experiments designed to compare equilibrium and non-equilibrium grain boundaries as defect sinks were carried out by irradiating an as-deposited film and comparing the results to those acquired by irradiating a fully annealed film (i.e. 600°C anneal). During irradiation, qualitative observations indicated a lower damage level in the less annealed iron films as a function of dose. The differences by 5dpa are slight. In both materials, the microstructure contains primarily small dislocation loops or clusters roughly 3-5nm in diameter; however, the annealed films also contained larger dislocation loops up to ~20nm in diameter.

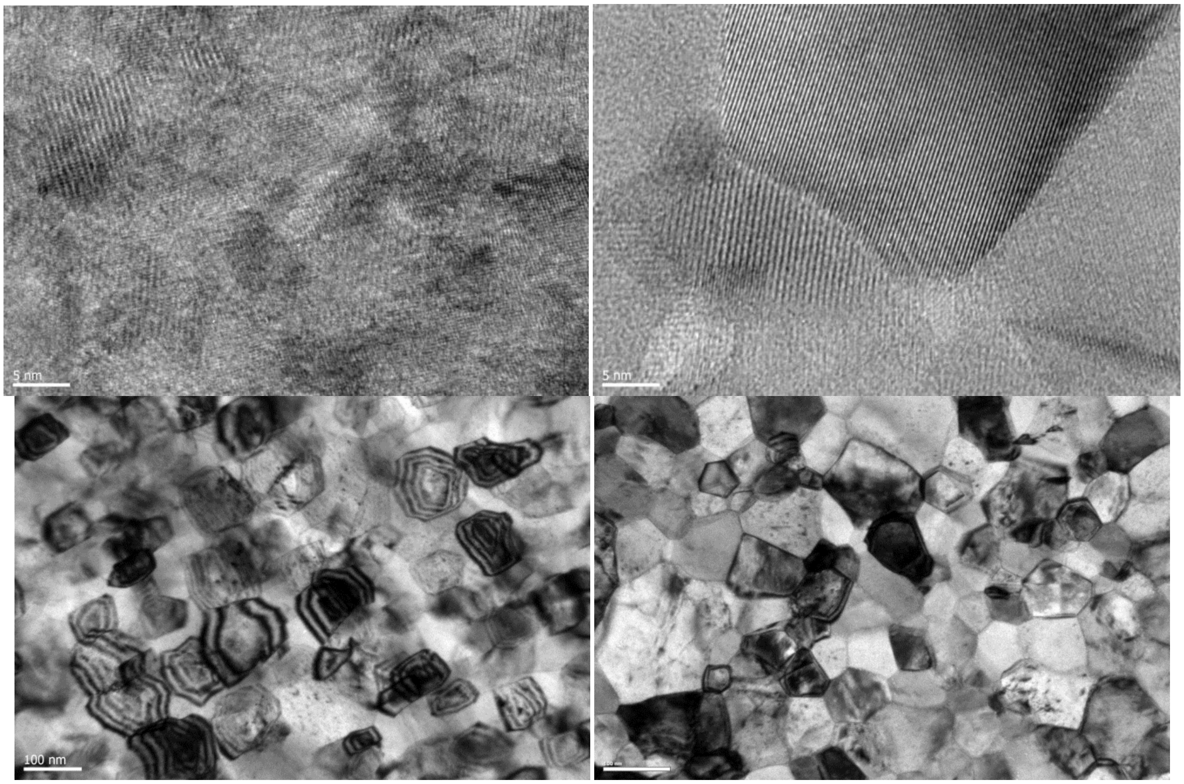

Figure 81. (top left) HRTEM of an as-deposited iron film showing poorly defined GBs compared to (top right) the same film annealed to 600°C for 10 minutes. (bottom left) shows the irradiation of an as-deposited nanocrystalline iron thin film to 5dpa at 300°C. Note the strong extinction bands, a classic sign of high amounts of strain at a non-equilibrium GB. (lower right) Irradiation of an annealed film to 5dpa at 300°C showing larger dislocation loops.

Molecular dynamics simulations performed by Dr. Garritt Tucker (Drexel) showed that excess free volume does contribute to a decreased survival rate of point defects in cascades that occur in close proximity to the grain boundary. For the simulation, a 3keV primary knock-on atom (PKA) was created at 3nm from the grain boundary plane in a bicrystal simulation. The simulation was run at room temperature to observe the collapse of the cascade at two grain boundaries: a $\Sigma5$ (210)<001> symmetric tilt grain boundary (~53° misorientation angle), and boundary with the same misorientation but with artificially introduced excess free volume. The result, shown in Figure 82, indicates that the defect survival rate is higher for the equilibrium boundary structure, at least in the case of the Σ5 boundary.

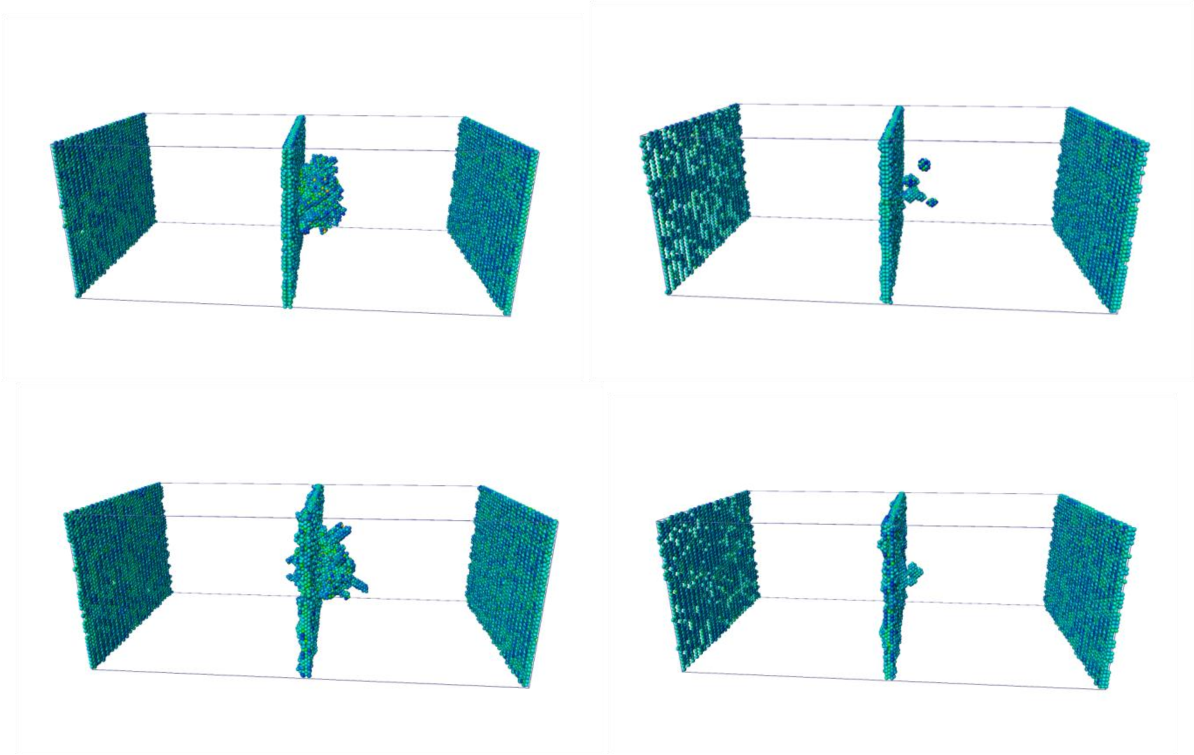

Figure 82. Cascade collapse into a Σ5 (210)<001> symmetric tilt grain boundary at room temperature. Atoms colored according to potential energy. (top left) Peak damage after the cascade for the equilibrium GB structure. (top right) Remaining defects after 80ps. (bottom left) Peak damage in an iron bicrystal with a non-equilibrium Σ5 (210)<001> symmetric tilt GB. (bottom right) Remaining defects after 80ps.

8.5 Conclusions

The radiation resistance of nanocrystalline iron is not solely dependent on the density of boundaries, but also on the ability of the grain boundaries to form a denuded zone. The formation of a denuded zone at a grain boundary appears to be not simply a function of grain boundary character, but also depends on the level of strain near the boundary and whether the boundary has retained its equilibrium structure. Perhaps most critical, the factors that contribute to the formation of the denuded zone in coarse grain polycrystalline materials continue to operate at very small length scales. Even in very small grains, such as the 40nm iron grain in Figure 80, the irradiation behavior is dependent on the interplay between the grain boundary character and the mobility of feely mobile point defects and defect clusters. These results show that nanocrystalline materials have the potential to be developed as an effective radiation tolerant material, but grain size alone may not be sufficient to take full advantage of the microstructure to create a radiation tolerant material. Strong character dependence of grain boundary sinks has significant implications at very small grain sizes. At grain sizes less than ~60 nm, the denuded zones formed by strong defect sinks can significantly reduce the defect concentration. In a case where all of the boundaries in the grain are strong defect sinks with denuded zones of about 30nm, the entire grain may be denuded (Figure 83). If a significant fraction of the grain boundaries around a grain are poor defect sinks, the defect density may be equal to that of a coarse grain material (although at this grain size the defect size is still significantly affected). As the grain size continues to decrease, it is more likely that any given grain will exhibit good radiation tolerance. When the grain size approaches the maximum width of a denuded zone in a material under those conditions (i.e. temperature and dose rate), any one boundary that acts as a strong defect sink creates a situation where the defect density in the entire grain is significantly reduced.

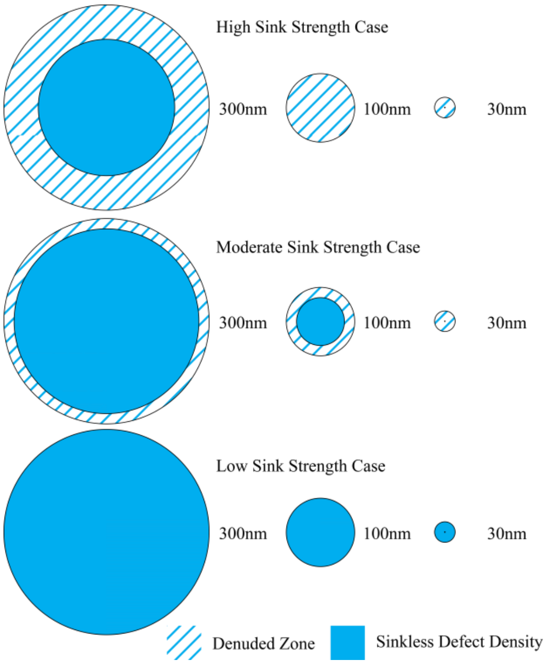

Figure 83. The effect of sink strength variation on the ability of a small grained material to effectively reduce radiation damage.

This result has two significant implications. First, that nanocrystalline materials can be designed using grain boundary engineering practices for increased radiation tolerance, and second, that studies of grain boundary character in microcrystalline materials or bicrystals can be extrapolated to the nanoscale. A complete comprehension of the factors leading to the formation of a denuded zone will enable grain boundary engineering of advanced materials (e.g. ferritic alloys) for nuclear applications that far outperform current alloys, enabling an entirely new generation of nuclear reactor designs to be implemented.

CHAPTER 9. EFFECT OF DEFECT CLUSTER LOSS TO GRAIN BOUNDARIES ON THE IRRADIATED MICROSTRUCTURE OF IRON

9.1 Introduction

Designing truly radiation tolerant alloys will require a fundamental understanding of radiation damage in materials. The response of a material to irradiation strongly depends on the number and characteristics of point defects created during the cascade event and the ultimate fate of the interstitials and vacancies [35, 36, 64, 298]. The collapse of a radiation cascade creates interstitials and vacancies in three forms: isolated defects, mobile defect clusters, and immobile defect clusters. It has become recognized that the distribution of the defect population between these feature types, or the production bias, is critical to the behavior of the material [64, 65]. Molecular dynamics simulations in iron suggest that interstitials readily form clusters and that vacancy clustering is minor which has significant implications for the swelling resistance of iron [64, 98, 118, 127]. Very small defect clusters (i.e. di- and tri- interstitials) are very mobile, and can rotate to equivalent burgers vector directions by rearrangement of the crowdions. Larger clusters of crowdions (i.e. 4-19 interstitials) in iron exhibit only one-dimensional glide along the crowdion direction [127, 128]. Using transmission electron microscopy, rapid one dimensional glide, or loop hop, of **b**= 1/2<111> interstitial defect clusters has been observed experimentally [18, 124, 131]. Loop hop has been shown to play a fundamental role in the development of the irradiated microstructure of iron as the glissile defect clusters cooperatively align to form strings of **b**=1/2<111> defect clusters which coalesce to form large interstitial dislocation loops with 1/2<111> Burgers vectors [18, 69, 115]. It is the buildup of the defect clusters and dislocation loops in iron that results in a degradation of the mechanical properties though radiation hardening [282].

Glissile defect clusters are also able to diffuse to defect sinks such as grain boundaries, dislocations, or precipitates. These structures are all characteristic attributes of ferritic/martensitic steel and nanostructured ferritic alloys (NFAs) or oxide dispersion strengthened (ODS) steel candidate materials for the next generation of nuclear reactors [7, 152, 285, 299-302]. Grain boundaries have been shown to have a significant contribution to the loss of point defects, which is particularly advantageous as the grain size of a material is decreased [26, 28, 29]. Several mechanisms have been proposed for the absorption of point defects by grain boundaries ranging from the collapse of cascade events to the absorption of small defect clusters [33, 75, 81, 303]. However the precise mechanisms operating to remove point defects, and in particular defect clusters, from the interior of the grain are still unknown. In light of the important role glissile defect clusters play in the radiation response of iron, it is particularly important to understand how the interstitials and vacancies clusters are transported to sinks such as grain boundaries, and how those point defects are absorbed at the boundary.

In previous work we examined the behavior of grain boundaries in pure iron as the grain size is reduced from polycrystalline (>1μm) to nanocrystalline (<100nm) [304]. The mechanisms that operate to remove defects at a grain boundary appear to be the same in polycrystalline and nanocrystalline materials, but due to the higher density of grain boundaries in the nanocrystalline material there is a greater contribution to the resistance to radiation from grain boundaries. The greater effect on defect concentration was found to arise due to the character of the grain boundaries, as the defect loss to grain boundaries does exhibit a strong dependence on boundary disorientation. *In-situ* irradiations hinted that defect clusters and dislocation loops may be large contributors to defect loss at grain boundaries at all grain sizes. Understanding the mechanisms of defect cluster loss at grain boundaries may be key to optimizing the microstructure of fine-grained NFA steel for advanced nuclear reactors, particularly in light of the important role that interstitial defect clusters have in the formation of the irradiated microstructure in iron.

9.2 Methods and Procedures

9.2.1 Experimental Methods

Free-standing iron films with a constant thickness and small columnar grains provide an effective means to study the interaction of defects with grain boundaries, particularly when coupled with a grain size less than one micron which greatly increases the line length of grain boundary present in the field of view of a transmission electron microscope. The iron films used for this study were deposited using magnetron sputtering of high purity iron onto sodium chloride substrates at Los Alamos National Laboratory. A uniform iron layer with a target thickness of 60-150nm was deposited on <100> NaCl substrates held at 370°C. The average final thickness was verified using cross sections prepared by focused ion beam (FIB) milling and transmission electron microscopy (TEM). For irradiation, specimens were prepared by mounting the thin, planar iron films on 200mesh TEM grids. The as-deposited films were then annealed to 650°C to achieve a mean grain size of approximately 35nm, or to 850°C for an ultrafine (~100-500nm) grain structure. The grain size in each specimen was determined using electron backscatter diffraction (EBSD) in the SEM and orientation maps obtained by NanoMEGAS ASTAR precession diffraction in the TEM [217, 243], which also permits the behavior defect clusters at grain boundaries under irradiation to be correlated with the GB misorientation.

Each of the iron samples was irradiated *in-situ* with the dual beam irradiation setup at Argonne National Laboratory's IVEM Tandem facility, which consists of a 650KeV ion implanter directed into a Hitachi H-9000NAR TEM at 30° from the electron beam [215]. Each sample was stabilized at 300°C and imaged before being irradiated with 1MeV Kr^{2+} ions. Irradiations were performed in segments, pausing only to take still images at select doses until the samples reached the target dose of 5 dpa as calculated by SRIM [216]. Imaging was performed using a 200KV accelerating voltage which is below the knock-on damage threshold for iron. In the Hitachi H-9000NAR, the smallest selected area aperture covers a region approximately 500nm in diameter, and the area of illumination with a condensed beam is comparable at 200kV. Therefore it is not possible to select an imaging condition in a specific grain of choice, nor maintain that precise condition throughout the irradiation. Instead, a magnification is chosen such that a large number of grains are within the field of view. The specimen is held at zero tilt during the irradiation, and damage is observed in grains that are in a favorable imaging condition. Due to the dynamic nature of the experiments, it was not possible to directly determine the nature of the loops in motion. In some cases, the behavior in the *in-situ* video could be correlated with nanobeam diffraction and the crystallographic orientation maps obtained by NanoMEGAS diffraction ex-situ in an attempt to determine the character of the defect.

9.3 Experimental Results

9.3.1 Proximity Annihilation

Under continuous irradiation by Kr^{++} ions it was found that small 2-5nm defect clusters could form in very close proximity to grain boundaries (Figure 84a-d). Defect clusters in iron become visible over several frames of video, and sometimes on the order of minutes. This has been explained as the result of a requirement for multiple overlapping cascades to induce stable loop formation and the result of local point defect diffusion after the cascade [48, 141] wherein the defect cluster grows by the capture additional freely mobile interstitials and glissile loops produced by nearby cascades [64]. The formation of a defect cluster so near the boundary indicates that initially the cluster is either sessile or its Burgers vector lies parallel to the grain boundary.

The initial stability of the defect cluster near the grain boundary is similar to what is observed as the decoration of dislocations wherein a SIA cluster may be trapped in the stress field of a dislocation [65, 138]. For the example case shown in Figure 84, the cluster eventually becomes unstable and the cluster is lost to the grain boundary (Figure 84e-h). Such a trapped loop can either be absorbed by the grain boundary after performing Burgers vector changes substantial climb, or be detrapped by thermal activation [65]. It is known that very small defect clusters (i.e. di- and tri- interstitials) in iron can spontaneously rotate to equivalent burgers vector directions by rearrangement of the crowdions. However, molecular dynamics simulations of larger clusters of crowdions (i.e. 4-19 interstitials) in iron show that motion is due solely to one-dimensional glide along the crowdion direction [127]. Visible defects in the TEM are likely much larger than the critical size for Burgers vector rotation (in fact, only 1-D loop hop has been observed in TEM [18, 124, 131]) so it is unlikely that such spontaneous behavior is responsible for the sudden instability unless the behavior is influenced by the proximity of the grain boundary. Growth of the defect cluster by point defect capture leading to contact with the grain boundary, or a change in Burgers vector by sudden rearrangement of the defect cluster by an overlapping cascade may trigger its collapse into the grain boundary. Unfortunately these events are below the temporal and spatial resolution of *in-situ* transmission electron microscopy. Only an indication of such a change can be inferred from TEM by comparing the appearance of the strain field around the defect cluster micrographs in Figure 84c and e.

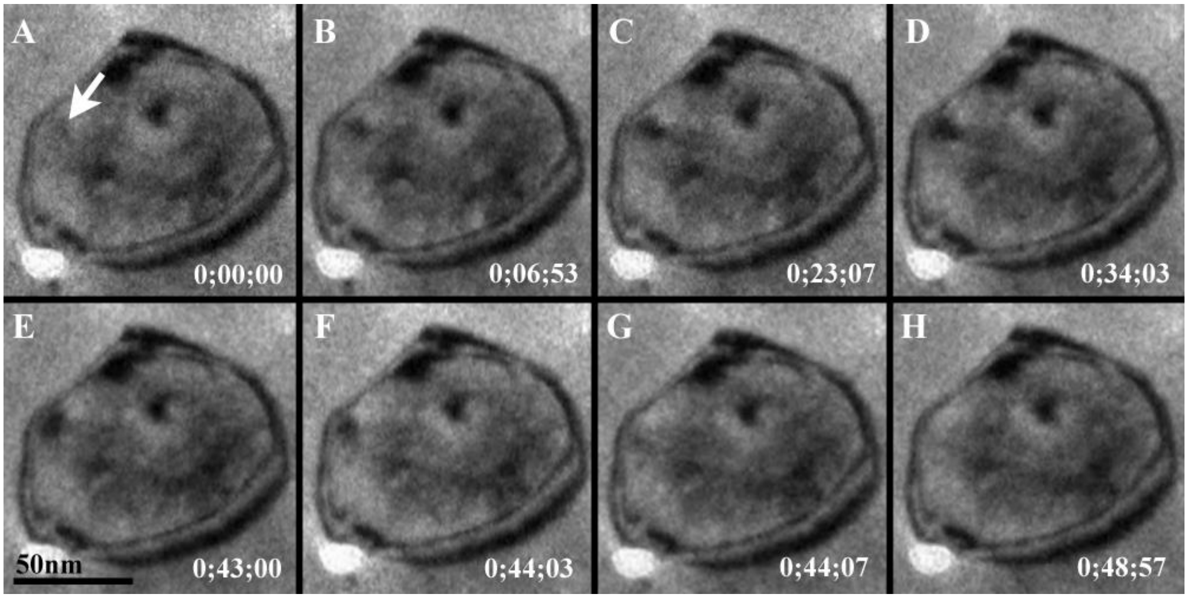

Figure 84. A-D) Formation of a TEM-resolvable defect cluster near a grain boundary over several minutes. E-F) The defect cluster becomes unstable and is then lost to the grain boundary in just a few seconds.

9.3.2 Loss due to Directional Loop Hop

Rapid one dimensional glide of **b**= 1/2<111> defect clusters has been observed experimentally in single crystal or large grain iron, far away from grain boundaries, using transmission electron microscopy [18, 124, 131]. The small loops are seen to "hop", or rapidly diffuse over distances of up to 10nm or more. In ultra high purity iron at 300°C, the one dimensional loop jumps observed along the <111> direction were estimated to occur at a velocity of at least 103 nm s^{-1} [18]. Similar behavior was observed in the fine-grained iron films used for this study; however, in nanocrystalline iron the density of grain boundaries is such that the probability of jumps of this type occurring near grain boundaries is much higher. Accordingly, the small 2-4 nm loops were repeatedly observed jumping to grain boundaries and being annihilated. One of those cases is shown in Figure 85. A small defect cluster was observed exhibiting one-dimensional loop hop for 3-4 minutes. The motion appears to be random and the loop hops seem to be over relatively large distances (~10-20nm).

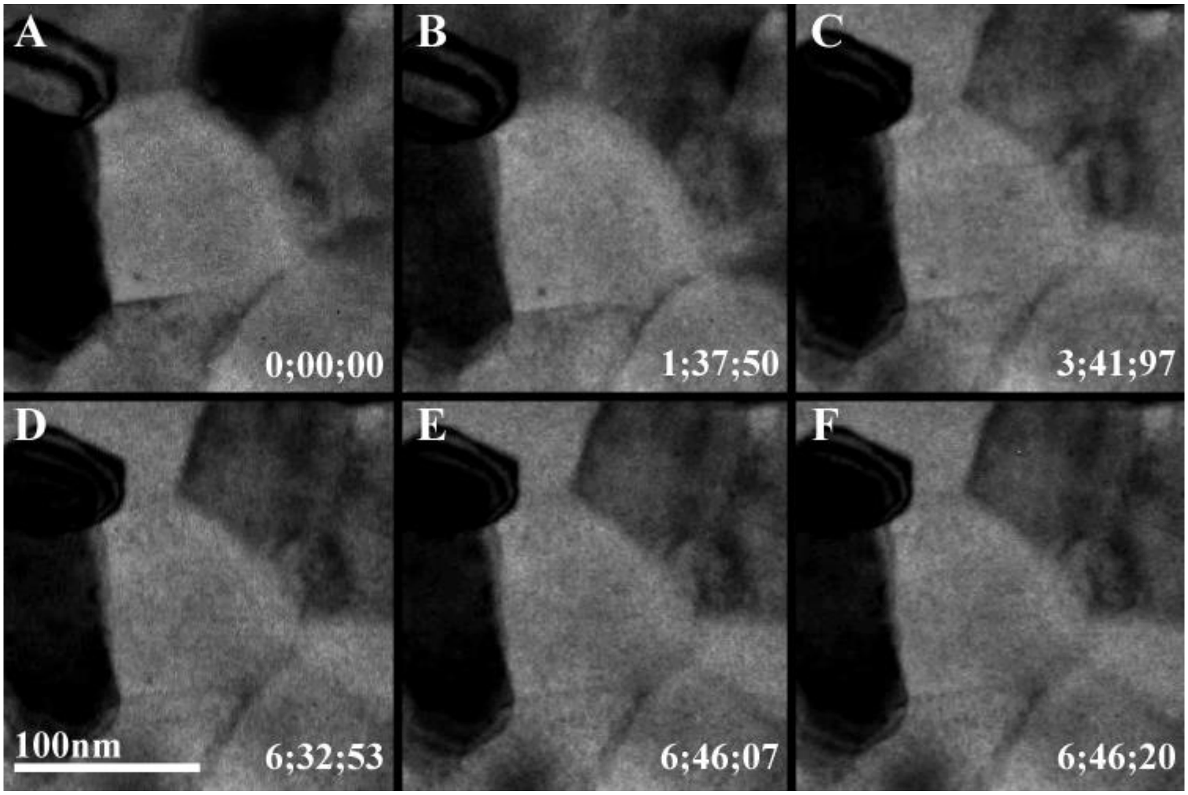

Figure 85. Stills from video of the in-situ irradiation of iron recorded at 15 frames per second. A small defect cluster in the lower left of the central grain undergoes random one dimensional loop hop occurring in nanocrystalline iron, eventually becoming preferential leading to annihilation of the defect cluster at a grain boundary. A-D are select images taken during the motion of the defect cluster. The actual motion occurs much more rapidly. In frame E, the defect has stretched or split and is in contact with

the boundary. By the next frame the cluster has been absorbed by the grain boundary. Time is in min;seconds;hundreths of a second.

The loop is seen to undergo a rapid series of small one dimensional jumps. Eventually until the random motion brings it in close proximity to the grain boundary. After that point, the motion of the defect cluster becomes more rapid, with the loop hops occurring over very short distances. This motion is captured in Figure 86 which shows the relative distance of the small defect cluster from a grain boundary as a function of time. There is a clear preferential jump direction that creates a net movement of the defect cluster to the grain boundary. In Figure 85E, the final jump of the defect cluster is captured in a frame of the video. The defect cluster appears stretched or split, with a small spot of contrast still visible were the full cluster was located in the previous frame. A second spot of faint contrast appears at the grain boundary at this time. By the next frame, the cluster has been lost from the grain.

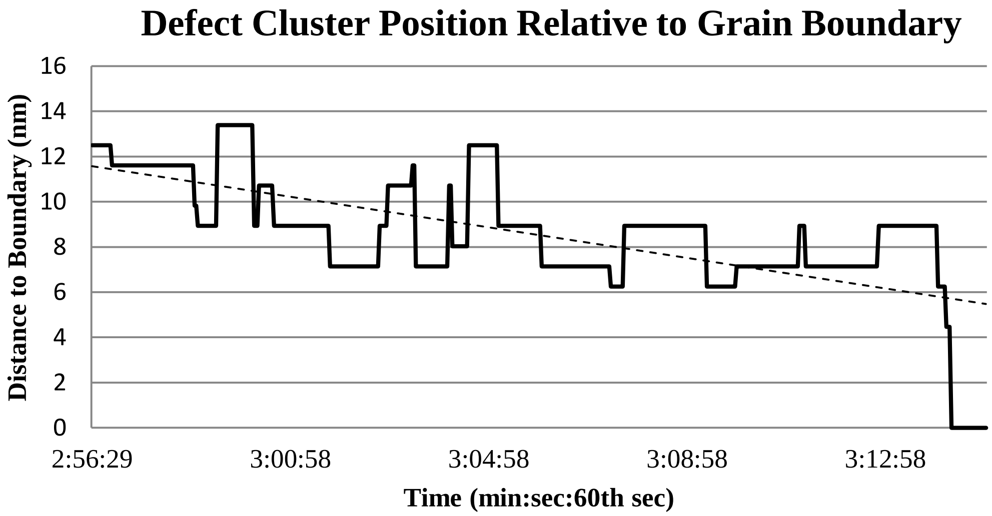

Figure 86. Dislocation loop hop with a net migration to a grain boundary before annihilation.

9.3.3 Effect on Microstructure

The loss of small defect clusters to grain boundaries has direct implications on the development of the irradiated microstructure within the material. These glissile clusters have been shown to cooperatively align by an as yet unclear mechanism to form strings of **b**=1/2<111> defect clusters generally along the <110> direction [18, 69, 115]. The small clusters then coalesce to form large interstitial dislocation loops with 1/2<111> Burgers vectors. During the irradiation of an 80nm thick nanocrystalline iron film, the small 2-4nm loops have reached sufficient density to begin interacting to form "loop strings" by a dose of about $8x10^{14}$ ions cm^{-2} (~1dpa). Figure 87 shows a sequence of stills taken from an *in-situ* video of irradiation from about 0.8dpa through 2dpa. Initially there is a relatively low density of defect clusters (Fig. 3a) with a relatively uniform distribution. As the dose increases, the number of visible clusters also increases, and the additional defects appear to arrange in a line of discrete point defect clusters. Figure 87b-d shows the formation of a defect cluster just outside of the linear feature. After growing steadily in size, possibly by capture of additional point defects, the entire cluster appears to be absorbed in the linear defect structure.

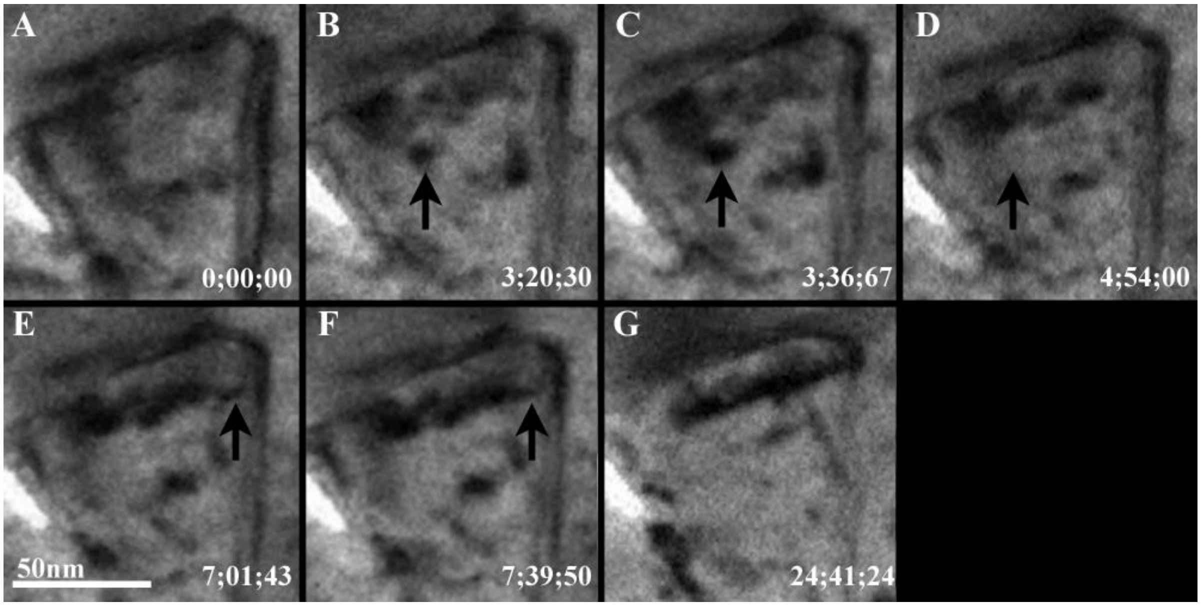

Figure 87. The cooperative alignment of defect clusters leads to the formation of a single dislocation loop in nanocrystalline iron irradiated at 300°C with 1MeV Kr^{++} ions. The string of defect clusters may only be as long as the grain, and is often shorter due to the presence of denuded zones. Time is in min;seconds;hundreths of a second.

This type of behavior continues for some time. Figure 87e and 87f show the formation of a small dislocation structure which then aligns with the pre-existing linear feature. In the strong contrast condition present during the final stages of loop alignment it was difficult to discern the departure of the individual nature of the loops. However, by approximately 2dpa and after about 20 minutes, the individual clusters are gone and have been replaced by a single large dislocation loop. It should be noted that this dislocation loop was not able to grow larger than the grain in which it formed. Defect clusters that would build additional length on the prerequisite loop string are lost to the grain boundaries by the processes described in the previous sections before they can coalesce into the larger loop. Therefore the ultimate size of the dislocations loops that form from the dislocation loop strings is dictated by the grain size of the material.

9.4 Discussion and Conclusions

The results of the *in-situ* irradiations show that defect clusters and dislocation loops large enough to be visible using transmission electron microscopy (i.e. with a strain field larger than ~2nm) contribute significantly to point defect transport to grain boundaries as they glide to and annihilate at grain boundaries. It has been shown that cascade events that occur at or near grain boundaries lose a significant portion of their point defects to the boundary as the cascade collapses [75]. However, small 2-4 nm defect clusters may still grow in close proximity to grain boundaries even when the growth process occurs over several minutes. Eventually, many of these defect clusters become unstable, and collapse into the grain boundary. The process by which this action occurs is unclear because the action of the defect is obscured by the strain field in the TEM image, and often occurs between the frames acquired by the CCD camera. Small dislocation clusters that form in the interior of the grain may also be lost to grain boundaries as they glide to the boundary by a biased one-dimensional loop hop similar to what has previously been observed experimentally using transmission electron microscopy [18, 124, 131].

The collapse of defect clusters into grain boundaries removes a portion of the clusters from the matrix before they can contribute to the development of **b**=1/2<111> defect cluster strings that act as the precursor to larger interstitial dislocation loops with 1/2<111> Burgers vectors [18, 69, 115]. It also prevents the loop strings from exceeding the size of a grain (generally they do not exceed the diameter of the grain minus the denuded zone). Large dislocation structures that are able to form in iron near a grain boundary are likely to be lost to the grain boundary. Interactions between an immobile dislocation and other cascades and dislocation structures may eventually initiate the movement of the dislocation toward a boundary where it can be annihilated.

All of these processes aid in the formation of the denuded zone commonly found along grain boundaries in irradiated materials. The efficiency of grain boundaries as sinks for defect clusters underlines their significance in the design of a radiation tolerant material. The presence of a high volume fraction of grain boundaries implies that dislocation clusters that form are more likely to be close enough to a grain boundary that they will be annihilated before reaching a stable size. These mechanisms become more important when the grain size is small. These results are particularly important in light of the role that glissile interstitial defect clusters have in the formation of the irradiated microstructure in iron, and will help inform the optimization of fine-grained nanostructured ferritic alloys (NFA) steel for advanced nuclear reactors.

CHAPTER 10. TEMPERATURE EFFECTS ON DEFECT MORPHOLOGY IN IRRADIATED IRON

10.1 Introduction

Microscopically visible dislocation loops in BCC iron are perfect dislocation loops without stacking faults [110] and possess Burgers vectors of **b**=1/2<111> and **b**=<100> [69, 115]. Experimental observations using transmission electron microscopy have shown that the habit plane of the 1/2<111> loops ranges from approximately {110} to {111}, while the <100> loops lie on {100}[110, 112, 113]. Interstitial dislocation loops with **b**=1/2<111> form from the coalescence of smaller, one-dimensionally mobile defect clusters that are created in high energy cascades [305, 306]. These small **b**=1/2<111> defects undergo correlated 1D diffusion via the elastic interaction between them [139], coarsening [113, 133, 307, 308] to form larger immobile interstitial loops resulting in a decrease of the total dislocation line length [309]. Jenkins et al. [69, 115] showed this process for a wide range of radiation dose in iron. The formation of **b**=<100> loops in iron is unique for BCC metals and a number of mechanisms have been proposed for their formation [112, 142, 310]. For example, they have been shown to form directly in a cascade [311], through the coalescence of two loops with **b**=1/2<111> Burgers vectors [113, 132, 133], and from the spontaneous switch of the Burgers from 1/2<111> to <100> [110, 113]. Once formed, **b**=<100> loops also grow by the biased absorption of mobile b**=**1/2<111> loops to TEM visible sizes [132].

The proportion of loops that are formed with each Burgers vector varies strongly with temperature. Trends for the relative proportions of **b**=1/2<111> and **b**=<100> loops observed using transmission electron microscopy of iron irradiated using iron ions are shown in Table 1.

This data shows that there is a transition in the populations of defect clusters from 1/2<111> to <100> as the temperature rises, with the transition point being below room temperature. However, it should be noted that the results reported for room temperature irradiation of iron [115] were from grains with a film normal of (001) which is a favorable crystallographic orientation for slip to free surfaces [18]. This could influence the final populations of the 1/2<111> and <100> defect clusters as the glissile 1/2<111> clusters would be preferentially lost.

More recent work by Yao et al. [140] confirmed there is a transition from loops with **b**=a/2<111> loops to loops with **b**=a<100> that occurs around 400°C (Figure 28). Their work along with that of Dudarev [142, 143] explained this transition as being the result of the relative stabilities and mobility of the ½<111> and <100> dislocation loops. The stable form of dislocation loop transitions from **b**=1/2<111> to **b**=<100> due to a reduction in the shear stiffness constant as iron approaches the α→γ transition temperature at 912°C due to instabilities in the magnetic spins. The calculations showed that at temperatures below 350°C, only hexagonal prismatic pure-edge dislocation loops with **b**=1/2<111> are stable, and above 550°C, only square **b**=<100> edge loops become stable. These results correlated well with the experimental observations by Yao et al. who were also able to show that the dominance of the <100> type loop at elevated temperatures is also a result of the relatively high loop mobility of **b**=a/2<111> loops. Once formed, the defect clusters can quickly migrate to free surfaces or to more stable defect structures like the <100> loops at higher temperatures.

In this work, we attempt to examine the effect of introducing a high density of grain boundary sinks on the morphology of the dislocation loops produced in nanocrystalline iron over a range of temperatures. Specifically, we are interested in how the loss of mobile defect structures at grain boundary sinks affects the formation of the irradiated microstructure. The presence of a high sink density has been shown to dramatically affect the final microstructure in part due to their ability to absorb defect clusters which would otherwise play a significant role in the formation of large dislocation loops [113, 133, 307, 308]. A study of similar principles over a range of temperatures provides valuable insights on how the grain boundary sinks operate to remove defects generated under irradiation; in particular, how the expected loss of a large population of the more mobile **b**=1/2<111> defect clusters to sinks affects the transition temperature from a microstructure dominated by **b**=1/2<111> dislocation loops to a microstructure that is mostly **b**=<100> loops. Using in-situ transmission electron microscopy, we were able to directly observe the activity of defect clusters and dislocation loops in nanocrystalline iron under ion irradiation.

10.2 Methods

10.2.1 Experimental Methods

To create nanocrystalline iron specimens suitable for transmission electron microscopy, iron films were deposited using magnetron sputtering onto sodium chloride substrates. A uniform iron layer with a target thickness of 100-150nm was deposited on <100> NaCl substrates held at 370°C. The average final thickness was verified using cross sections prepared by focused ion beam (FIB) milling and transmission electron microscopy (TEM). For irradiation, specimens were prepared by mounting the thin, planar iron films on 200mesh TEM grids. The as-deposited films were then annealed to 650°C in the TEM to achieve a mean grain size of approximately 35nm.

Each of the iron samples examined in this work were irradiated in-situ using the dual beam irradiation setup at Argonne National Laboratory's IVEM Tandem facility [215]. The irradiations were performed at controlled temperatures ranging from cryogenic to high temperature. Irradiations below room temperature (15-300K) were performed using a helium cooled double tilt TEM holder (Oxford), while irradiations at room temperature and above (300-1300K) were performed using a Gatan double tilt heating holder. The irradiations were performed using primarily using 1MeV Kr^{2+} ions accelerated using the 650kV ion implanter. Irradiations were performed in segments, pausing only to take still images at set doses. At each set dose point, the ion beam was blocked so that the specimen could be imaged and tilted to return to the most favorable imaging condition, if necessary. For example, a typical irradiation would be stopped at doses of: $2x10^{14}$, $4x10^{14}$, $8x10^{14}$, $1.6\ x10^{15}$, $2.4x10^{15}$, and $4.0\ x10^{15}$ $ions \cdot cm^{-2}$. This is equivalent to damage levels calculated by SRIM [216] of 0.25, 0.5, 1, 2, 3, and 5 dpa, respectively.

In-situ imaging was performed using a 200KV accelerating voltage which is below the knock-on damage threshold for iron. In the Hitachi H-9000NAR, the smallest selected area aperture covers a region approximately 500nm in diameter, and the area of illumination with a condensed beam is comparable at 200kV. Therefore it is not possible to select an imaging condition in a specific grain of choice, nor maintain that precise condition throughout the irradiation. Instead, a magnification is chosen such that a large number of grains are within the field of view. The specimen is held at zero tilt during the irradiation, and damage is observed in grains that are in a favorable imaging condition. After the irradiation, the behavior in the *in-situ* video was correlated with the crystallographic orientation maps obtained by NanoMEGAS ASTAR precession diffraction in the TEM [217, 243], which leads to results fairly consistent with behavior reported in literature (e.g. loop string formation along 110 directions, loop hop along 111 directions, and 100 type loop formation at 450°C) [18, 69, 115, 140].

10.2.2 Simulation Methods

Molecular Dynamics simulations were performed in order to better understand the processes occurring on timescales too short to capture using *in-situ* TEM. For the simulation, it is important to select the appropriate potential. For this study, an FS-type potential was selected after the work of Mendelev et al. [312] which gives the correct ranking of SIA formation energies at 0K (i.e. $E_{110\text{-db}} < E_{111\text{-db}} < E_{100\text{-db}}$). A bicrystal of 902,880 Fe atoms was constructed with a $\Sigma5$ 36.87° [001](310) symmetric tilt GB. Periodic boundary conditions were applied to all the boundaries of the supercell with dimensions of (lx=162.8 Å, ly=397.4 Å, and lz=162.5 Å. Before the simulation was performed, the grain boundary structure was relaxed via energy minimization. Then a dislocation loop was introduced by inserting an extra half plane of atoms such that the center of the loop was 5nm away from a grain boundary. The dislocation loop consisted of 595 SIAs creating a loop 6nm in diameter with **b** = $a_0/2[111]$, **n** = (111). Finally, NPT MD simulation was run on the whole system with zero pressure at a temperature of 100K.

10.3 Results

The microstructures of nanocrystalline iron irradiated to a dose of approximately 4.0 $\times10^{15}$ ions$\cdot$cm^{-2} (5dpa) are shown in Figure 88. The figure clearly shows a trend similar to that observed by Robertson et al. [100] and Jenkins et al. [18, 69, 115, 140] for irradiations of single crystal and large grain (>1μm) size iron at this range of temperatures in that there is a distinct transition from primarily **b**=1/2<111> dislocation loops to a majority **b**=<100> dislocation loops. However, the transition occurs between 400°C and 450°C which is lower than what was observed in large grain iron by Yao et al. [140]. At a temperature of 500°C, even the **b**=<100> loops are no longer stable, resulting in a dramatic drop in the population of dislocation loops in the microstructure.

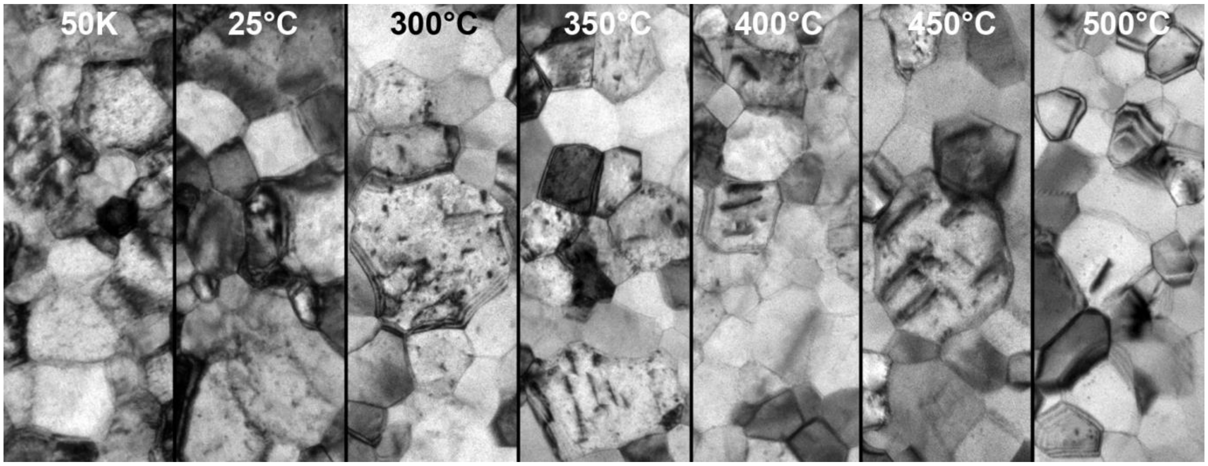

Figure 88. The variation in microstructure in nanocrystalline iron as a function of temperature. Note that only certain grains are in proper diffracting condition to create contrast from dislocation loops.

10.3.1 T=50K

The microstructure of nanocrystalline iron irradiated at 50K is shown in Figure 89. Each grain contained a high density of evenly distributed small (2-4nm or smaller) defect clusters. The matrix of the grains had a mottled appearance that disappeared as the specimen was allowed to return to room temperature; however no defect clusters were directly observed changing during the anneal.

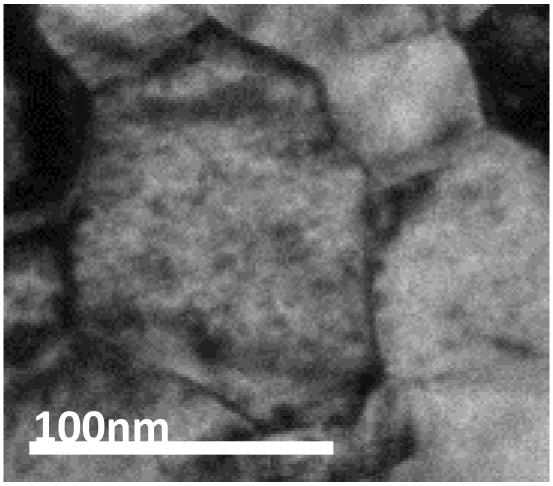

Figure 89. Final microstructure of nanocrystalline iron irradiated to 5dpa at 50K.

The mottled appearance of the matrix during the cryogenic irradiation is likely the result of incoherent scattering contrast that arose from a large number of interstitials frozen into the matrix. At 50K, the specimen is slightly below Stage I recovery and all thermal interstitial motion is halted [313]. This is supported by the fact that the mottled appearance disappeared as the specimen was allowed to return to room temperature. Although mono and di-insterstitials are immobile at such low temperatures, 2-4nm clusters observed at the early stages of irradiation exhibited one-dimensional glide motion, also referred to as loop hop, along the 110 directions (Figure 90). The motion of the defect clusters was found to occur only over short distances of less than 10nm, and was only observed under active irradiation. As the dose increased, the apparent mobility of these defect clusters was somewhat reduced.

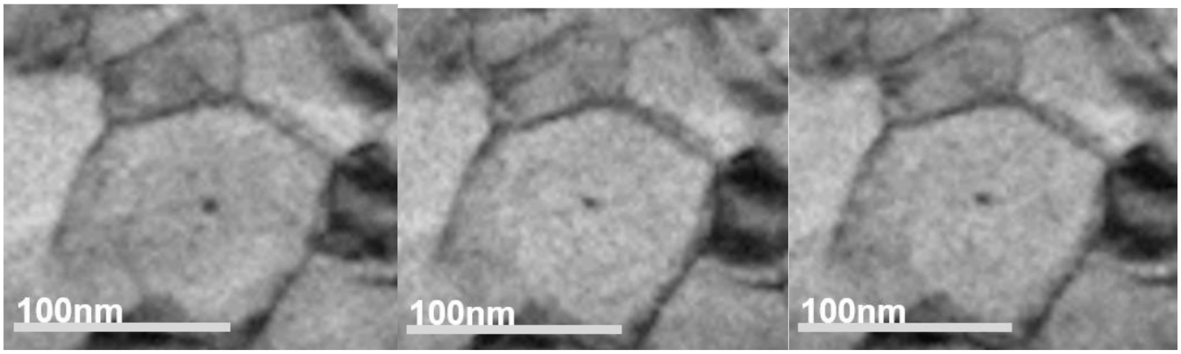

Figure 90. 1-D loop hop of a defect cluster in nanocrystalline iron irradiated at 50K.

10.3.2 T=25°C

In iron irradiated at room temperature, the resulting microstructure at a dose of 5dpa again consisted of individual 2-4nm defect clusters evenly distributed across the grains. With the increase in temperature, the mottled appearance that was observed in the 50K irradiation disappears. This result is not surprising as SIA's as well as di- and tri-interstitials are fully mobile by 25°C.

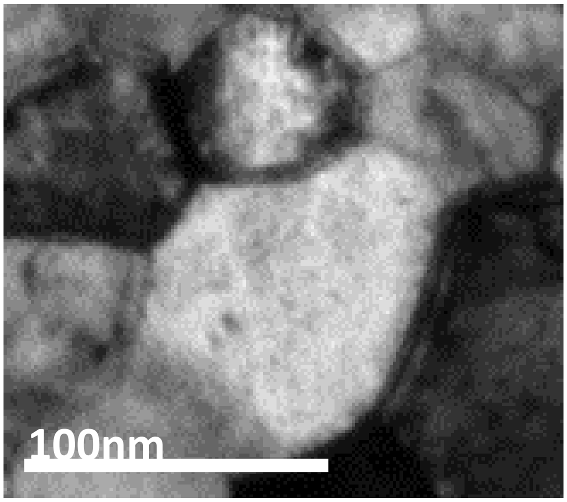

Figure 91. Final irradiated microstructure in NC Fe irradiated to 5dpa at room temperature.

The mobility of **b**=1/2<111> defect clusters also appeared to increase slightly, so the observed one dimensional glide of **b**=1/2<111> defect clusters was more prevalent and occurred over larger distances on the order of 30nm (Figure 92). The observed one dimensional glide of **b**=1/2<111> defect clusters did result in the loss of some clusters to defect sinks, but they were typically replaced by clusters formed under cascades. However, the loss of defects to grain boundaries at 25°C was sufficient to prevent the formation of organized arrangements of small dislocations clusters which have been referred to as loop chains, strings, and rafts [18, 137, 140].

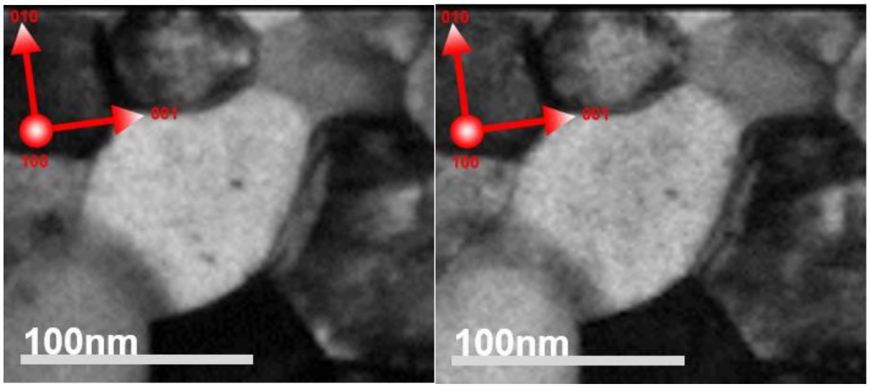

Figure 92. Still frames from TEM irradiations of nanocrystalline iron at 50K showing the extremes of motion for a small defect cluster by 1-D loop hop.

10.3.3 T=300°C

At 300°C, we find that loop size is proportional to the grain size in the material. Small (2-4) defect clusters remain the dominant form of defects observed using TEM, with the occasional loop reaching about 10nm in size. At 300°C, thermal energy is sufficient to permit the co coalescence of defect clusters into larger dislocation loops in iron aided by the increased mobility of **b**=1/2<111> defect clusters [113, 133, 307, 308]. The same increased mobility in nanocrystalline materials results in a substantial flux of point defects to sinks in the form of defect clusters [33], resulting in a decreased rate of coalescence and subsequent loop growth. Only in the largest grains (~100nm) are large >~30nm, irregular **b**=1/2<111> type dislocation loops found. The microstructure shown in Figure 1 for 300°C shows an example of a larger grain containing extended dislocation structures which are consistent in morphology and habit plane with **b**=1/2<111> loops observed in micron grain size iron by Jenkins et al. This microstructure has been described in detail in the previous chapters.

In cases where large dislocation loops formed in the grain, it was found that they exhibited a finite lifetime. Figure 93 shows the formation and loss of a **b**=1/2<111> type interstitial dislocation loop in nanocrystalline iron. The first eight frames of Figure 93 show the steady state growth of a **b**=1/2<111> dislocation loop under constant irradiation. When the loop grows large enough to make contact with a grain boundary (Frame 9), the dislocation line immediately disappears into the grain boundary (Frame 10). This initiates a process that removes the dislocation loop from the grain over the course of several minutes (Frame 11-20). The implication is that the grain boundary must be accommodating or transporting the interstitials that comprise the extra half plane of atoms in the dislocation loop. However, the process by which this occurs is not immediately available using in-situ TEM microscopy.

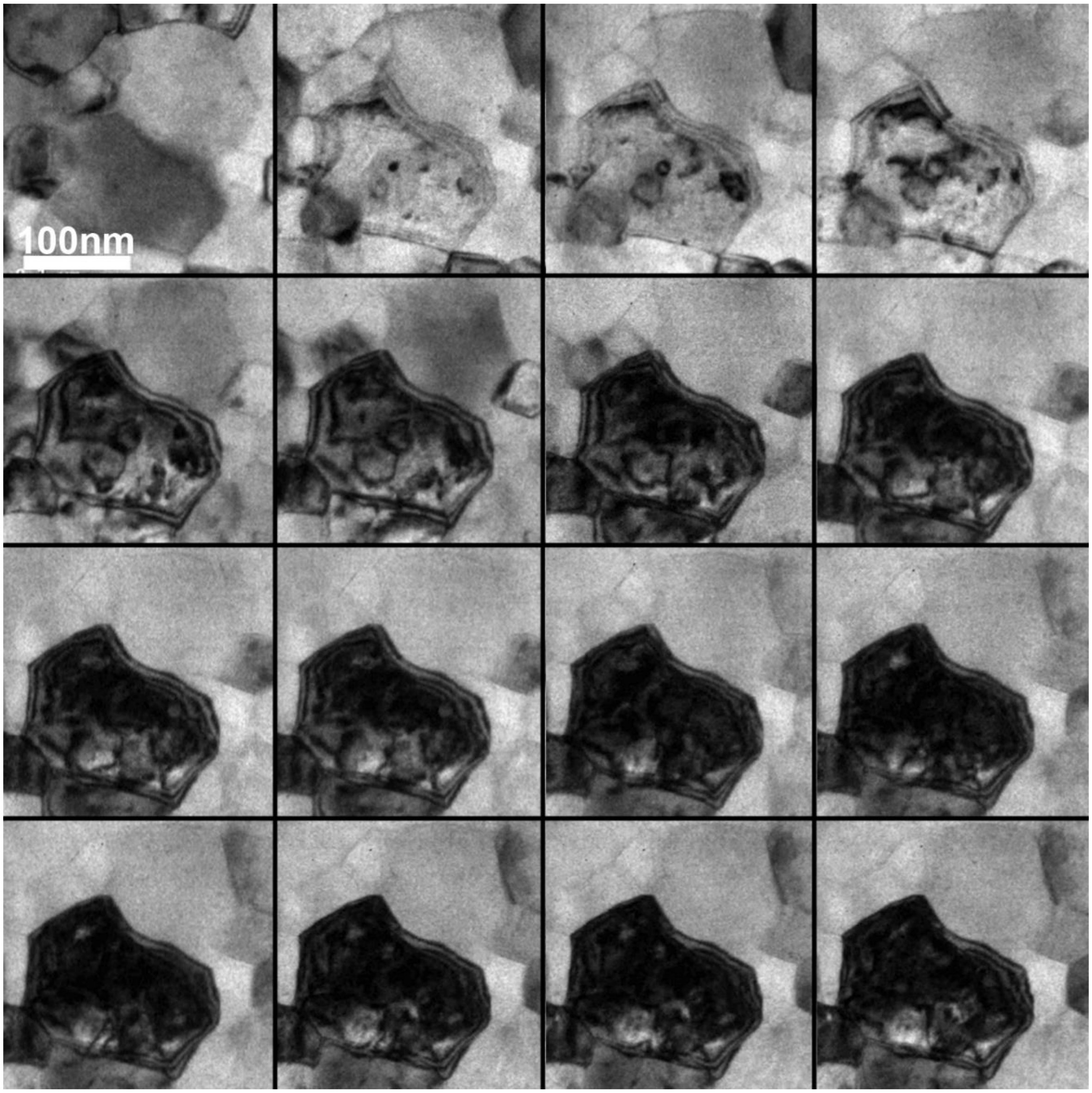

Figure 93. A small defect cluster (frame 1) grows by climb (frame 2-8) until it makes contact with a grain boundary (frame 9-10). At that point, the dislocation loop begins to rapidly shrink while being pulled toward the boundary (frame 11-20).

Another example of this is shown in Figure 94. This time, the dislocation loop is near a triple junction in ultrafine grain iron, and appears to completely reorient before disappearing into the grain boundary.

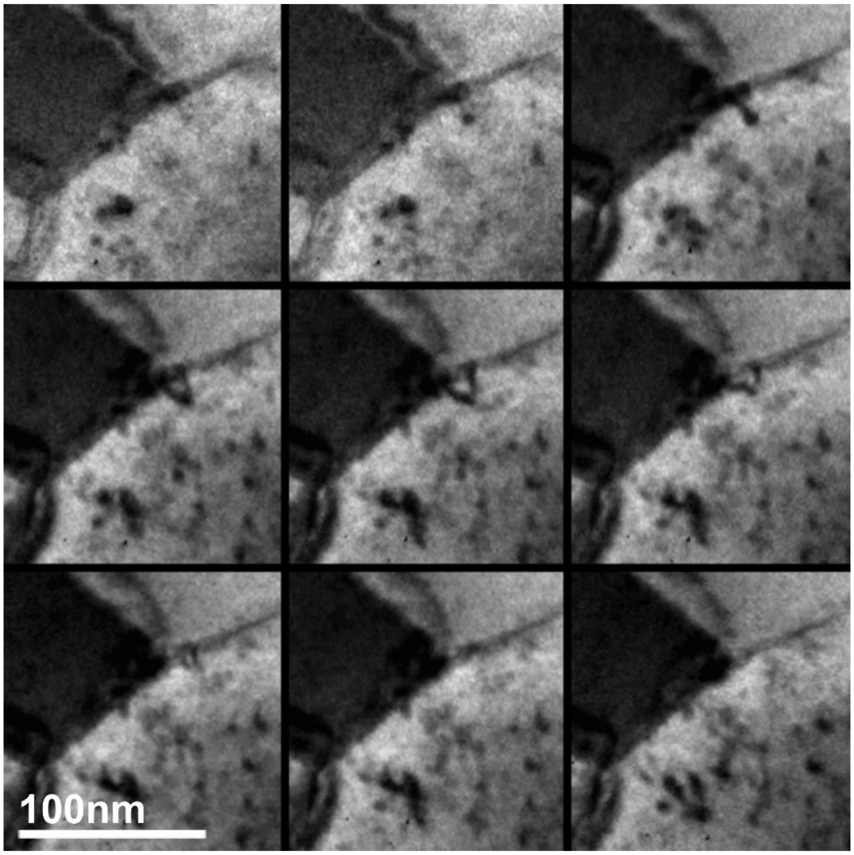

Figure 94. Alternate video of defect loop loss to a GB at 300°C. Doesn't show the whole loop, or the formation process, but does show the final stages that the previous figure doesn't show clearly.

Another mechanism was observed in nanocrystalline iron under irradiation at 300°C. In the sequence of images shown in Figure 95, a dislocation loop) appears to glide to the grain boundary. This dislocation loop was observed to have formed by the coalescence of a defect cluster string that self assembled over a few dpa. Once the dislocation loop coalesced, it begins to move across the grain. Its motion impeded by other dislocation loops in the grain that act as pinning sites for the dislocation. Eventually, the dislocation reaches the grain boundary and is annihilated. Only this one example was found in nanocrystalline iron.

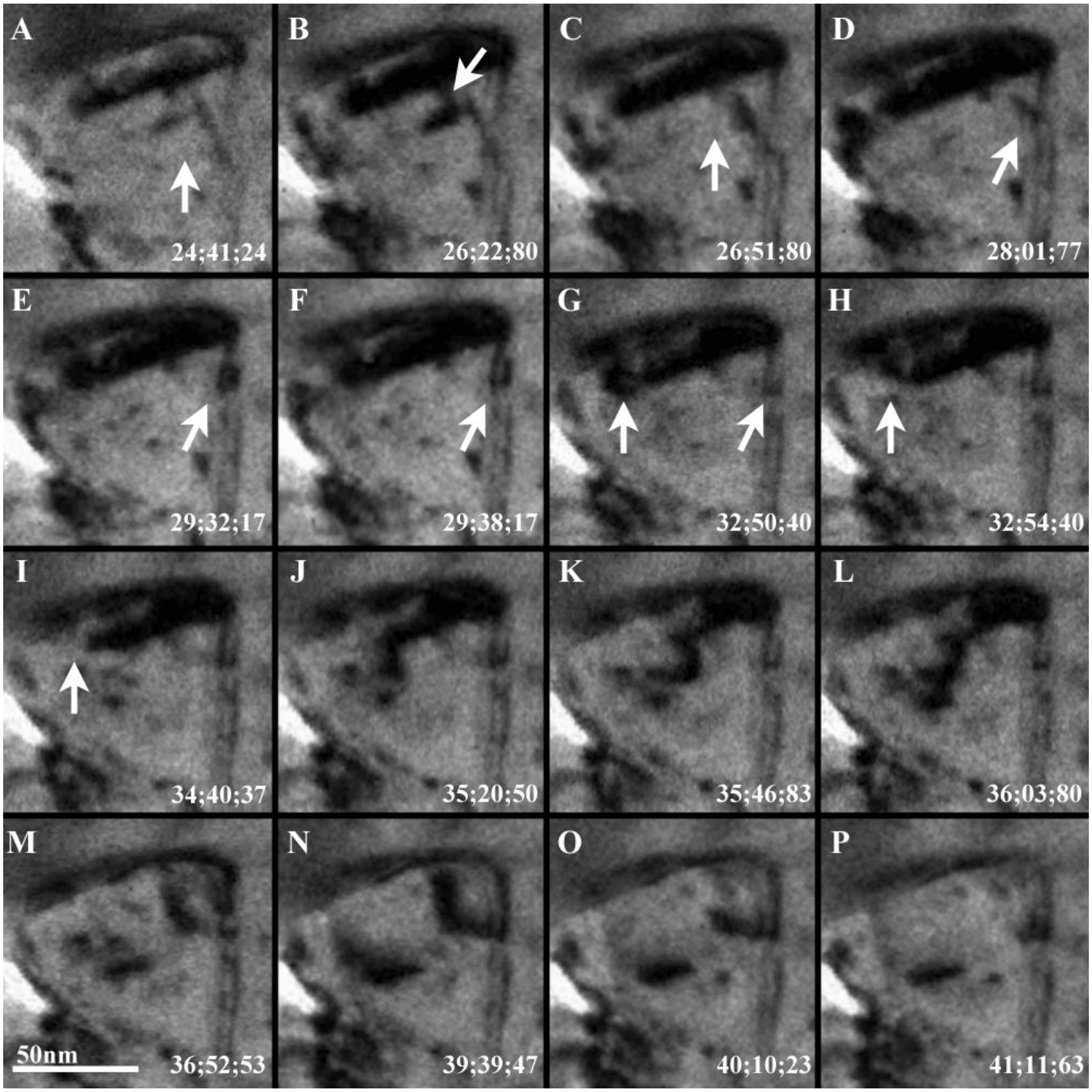

Figure 95. A series of dislocation loops gliding to grain boundaries, including a large dislocation loop that originally formed from the cooperative alignment of defect clusters. Time is in min;seconds;hundreths of a second.

Another case, presented in Figure 96, appeared to show yet another distinct mechanism for absorption of dislocation loops. In this case, a dislocation loop with a habit plane consistent with a **b**=1/2<111> loop forms near a grain boundary. The loop grows through the accumulation of point defects and some coalescence events with smaller clusters until it makes contact with a grain boundary. The dislocation loop undergoes a series of rotations before being absorbed by the grain boundary in less than a frame of video (approximately 1/10th of a second). The process for absorption is beyond the capability of *in-situ* electron microscopy.

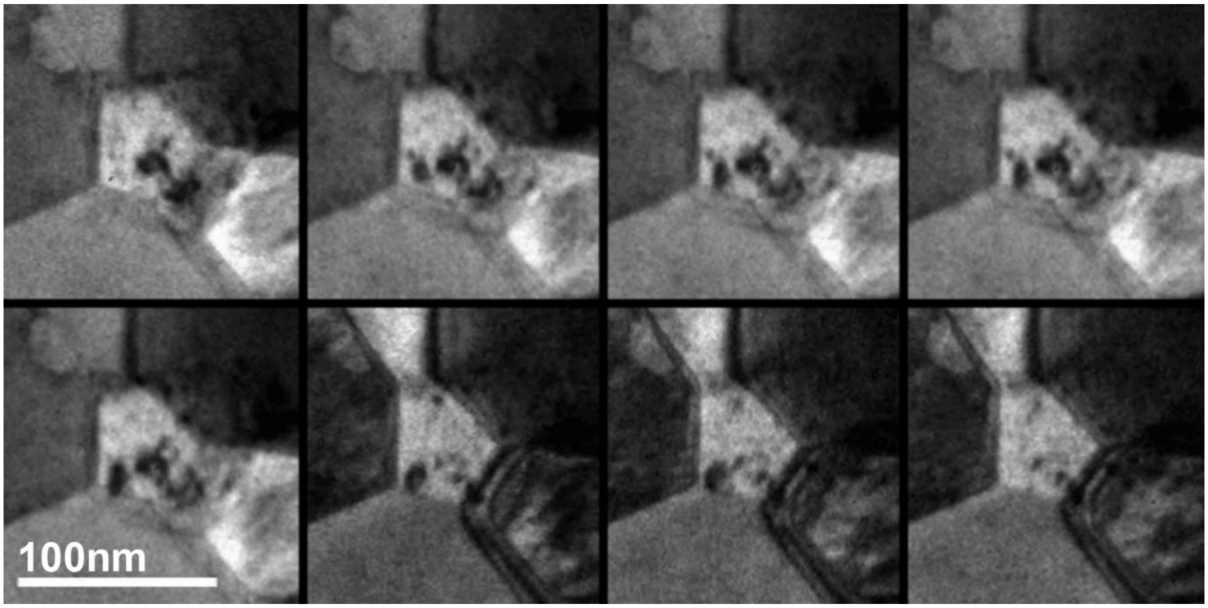

Figure 96. The formation and loss of a dislocation loop in iron. Although sessile in nature, the loop can grow to contact the grain boundary through climb. In this case the dislocation loop appears to be lost to the grain boundary in less than a frame of video.

10.3.4 350°C and 400°C

For nanocrystalline iron irradiated to 5dpa at both 350°C and 400°C, the dislocation structures with sufficient line length to be correlated with an approximate habit plane appear to lie along the 110 direction, which is consistent with **b**=1/2<111> loops. These loops do not show the irregular shape found at lower temperatures, an observation which is again consistent with observations in micron grain size iron [140]. At these temperatures, small glissile

b=1/2<111> defect clusters were not observed. Since defect clusters in iron are thought to arise from overlapping cascades, it may be that the mobility of the defects created in a single cascade is high enough that they escape to defect sinks such as large stable dislocation loops or grain boundaries before growing to TEM visible size. Any defect clusters that grow to TEM visible size remain static and grow a uniform rate. Figure 97 shows the formation of several dislocations in a group of nanocrystalline grains with similar orientations. The dislocation loops that form Frames 1-8 are largely independent of the grain size unlike those found in iron irradiated at 300°C. They, too, however are lost to grain boundaries in many instances. Once the defect comes in contact with the grain boundary (Figure 97 Frame 8), the dislocation loop appears to shrink starting with the part furthest from the grain boundary. This process was repeated in many instances throughout the irradiation, but was not observed when the ion beam was inactive.

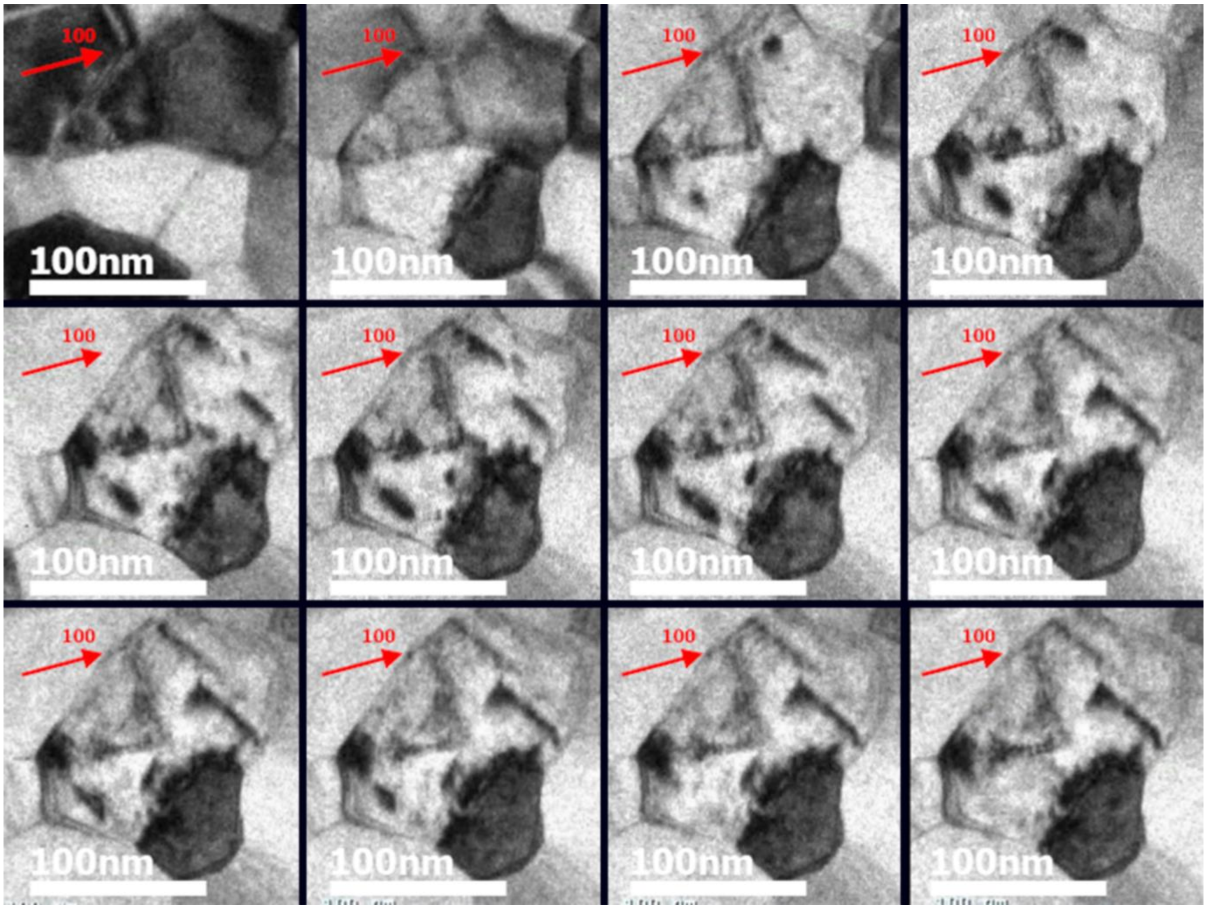

Figure 97. Irradiation at 400°C showing the formation of what appear to be prismatic b=1/2<111> type loops based on that diffraction information. Morphologically they appear to be more like the b=<100> type loops, and behave in a similar manner.

10.3.4 450°C

By 450°C, nearly all of the dislocation loops present lie along 100 directions, indicating they are **b**=<100> type loops. Smaller **b**=1/2<111> loops can only be found sporadically throughout the microstructure. Under irradiation, defect loops what appear to form along the 110 direction quickly reorient onto one of the 100 planes. This process is similar to that observed by Marian et al. [314]. Once formed, the **b**=<100> loops are moderately stable. Although many of the **b**=<100> loops are stable in the grain for many minutes under irradiation, they are almost inevitably lost to grain boundaries. The loss of these loops to grain boundaries also appeared to occur only under constant irradiation. They remained stable in the grains once irradiation was halted, even at 450°C.

Dislocation loops with 100 Burgers vectors were observed to collapse into grain boundaries by two mechanisms. The first mechanism is similar in appearance to the loss of **b**=1/2<111> dislocations loops that is shown in Figure 3. The **b**=<100> dislocation loop forms by growing from a small defect cluster (Figure 4 Frame 1-2). In its initial state, the dislocation loop appeared to lie on a 110 plane. When the loops reached a diameter of a few nanometers, they appear to reorient onto 100 planes. The dislocation loop in Figure 98 undergoes this transformation between Frame 2 and 3 in Figure 98. Once the **b=**<100> loop has formed, it grows until it makes contact with the grain boundary. When contact is made, the dislocation loop was absorbed (Frame 4-9) into the grain boundary. This type of absorption mechanism was the most prevalent at 450°C.

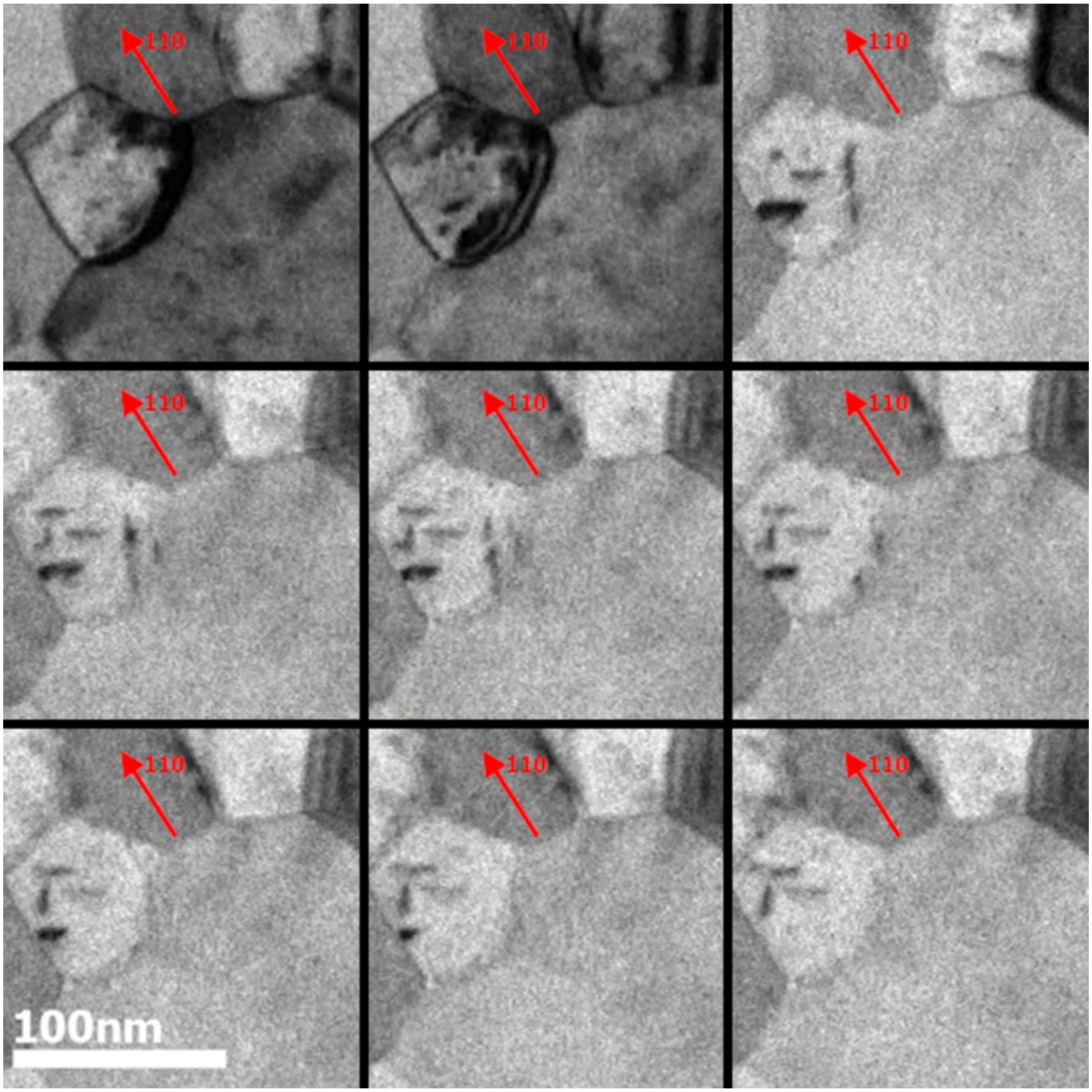

Figure 98. Disappearance of a dislocation loop at a grain boundary due to apparent pipe diffusion.

Dislocation loops with a habit plane of 100 were also seen moving toward a grain boundary in a direction parallel to their Burgers vector. An example of this is shown in Figure 99. In this case, a dislocation loop forms perpendicular to an existing loop, and with a habit plane along <100>. The dislocation loop reaches its maximum size (as seen in the TEM) by

Frame 3, then begins to glide toward the grain boundary along its cylinder. That motion transports the defects to the grain boundary (Frame 4-6) where the defect cluster is annihilated. This behavior was not as common as the mechanism shown in Figure 98, but did occur frequently at this temperature.

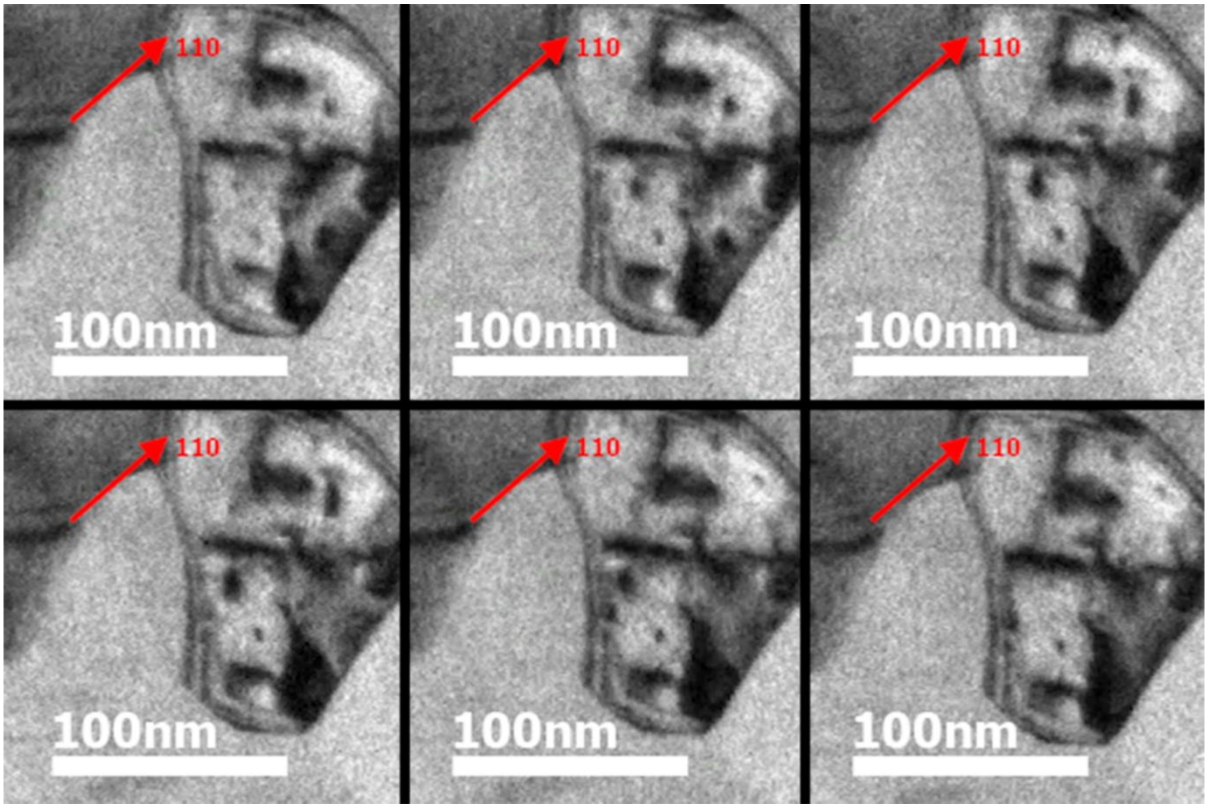

Figure 99. At 450°C, A b=<100> dislocation loop forms (frames 1-3), then starts to move toward the boundary (frames 3-5) before being absorbed (frames 5-6). Other b=<100> loops are still moderately stable, and remain in the grain during this time.

There are also examples of the mechanism shown in Figure 98 where very large dislocation loops are absorbed at the grain boundary. In Figure 100, a large **b**=<100> type dislocation loop grows by coalescence of several smaller loops before making contact with the grain boundary.

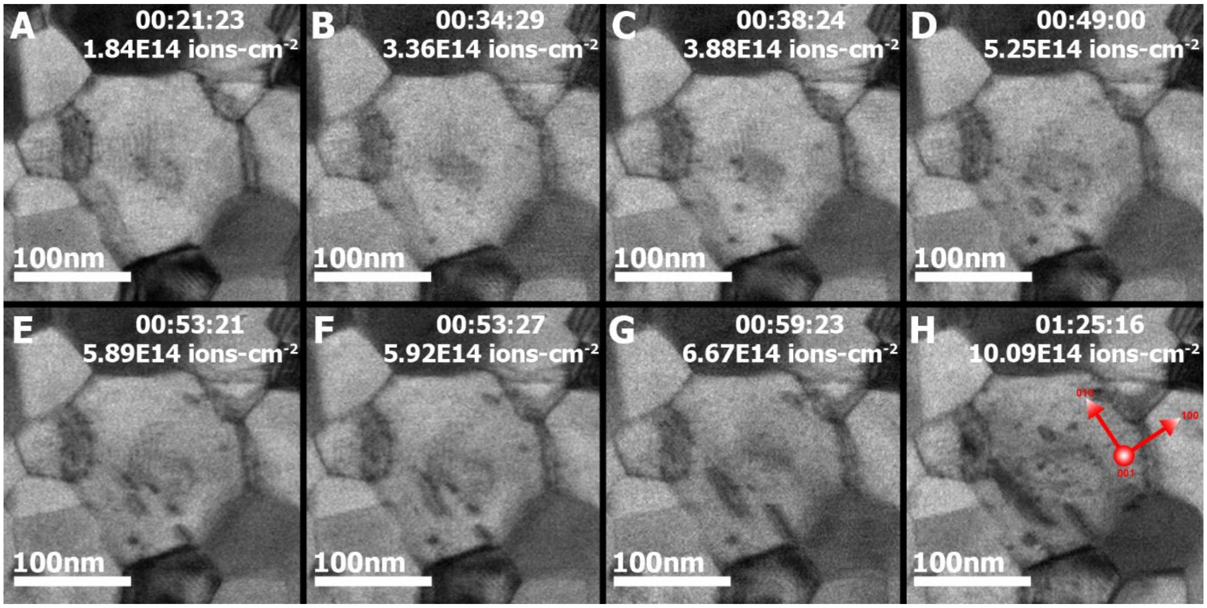

Figure 100. Growth of a b=<100> dislocation loop in nanocrystalline iron irradiated at 450°C.

Once contact is made with the grain boundary, the **b=<100>** type loop begins to shrink toward the grain boundary (Figure 101). The process is not continuous, but instead occurs in several stages. Several decreases in size occur in less than a frame of video, and are indicated by the pairs of frames (e.g. Figure 101 A and B). Between the times indicated in Frame F and H, the loop appears to slowly shrink over time, as well as change in contrast before final absorption in H-I. Near the end of this process, a smaller dislocation loop appears in the adjacent grain and growths slightly while the remainder of the original loop disappears. This process appeared to indicate that in some circumstances, the grain boundary may not be capable of absorbing such large amounts of point defects.

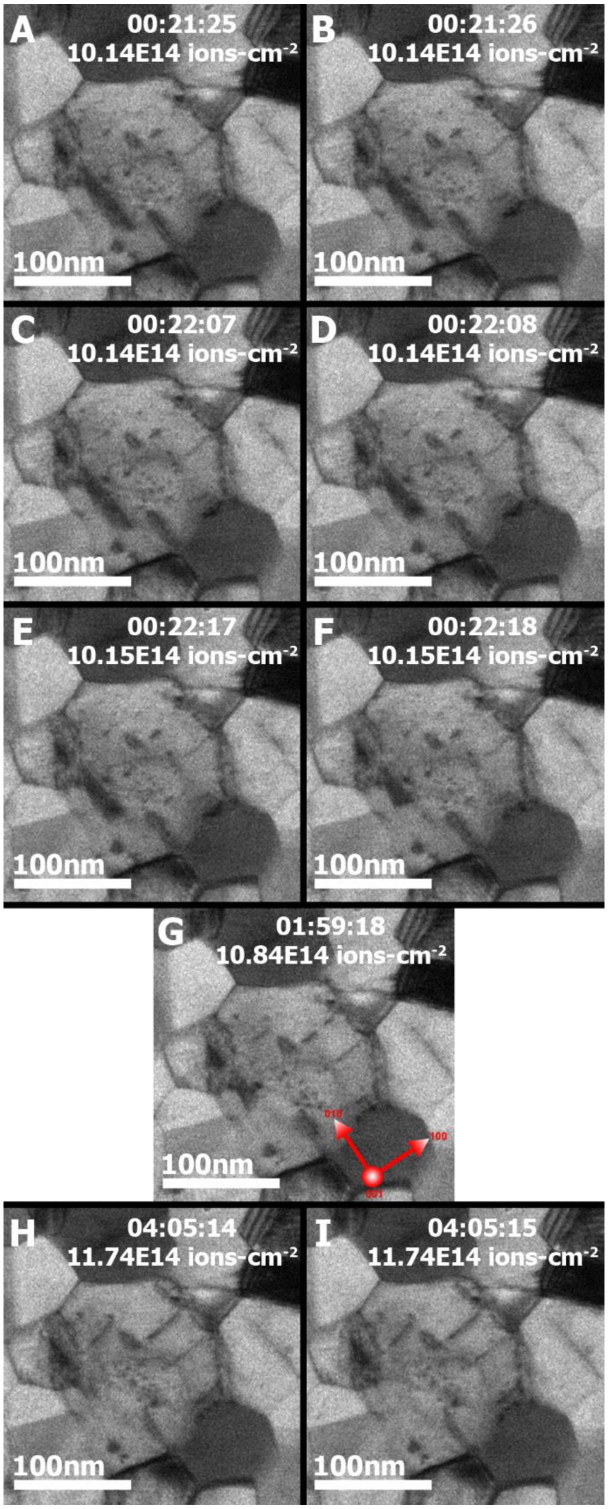

Figure 101. Disappearance of a b=<100> dislocation loop at a grain boundary in nanocrystalline iron irradiated at 450°C.

10.3.5 500°C

The behavior of nanocrystalline iron at 500°C is remarkably different than that of micron grain size and single crystal iron. Very few dislocation loops were observed to form during the irradiation, and the majority of those were immediately lost to the grain boundary. Figure 102 shows an example of a dislocation loop that begins moving toward the grain boundary even as it is forming. The mechanism is likely climb, assisted by thermal activation at this temperature. As a result of the high mobility of the dislocation loops coupled with a high density of grain boundary sinks, the loop population in the film is very low (as shown in Figure 88). Every dislocation loop observed in iron irradiated at 500°C was found to lie along a 100 direction.

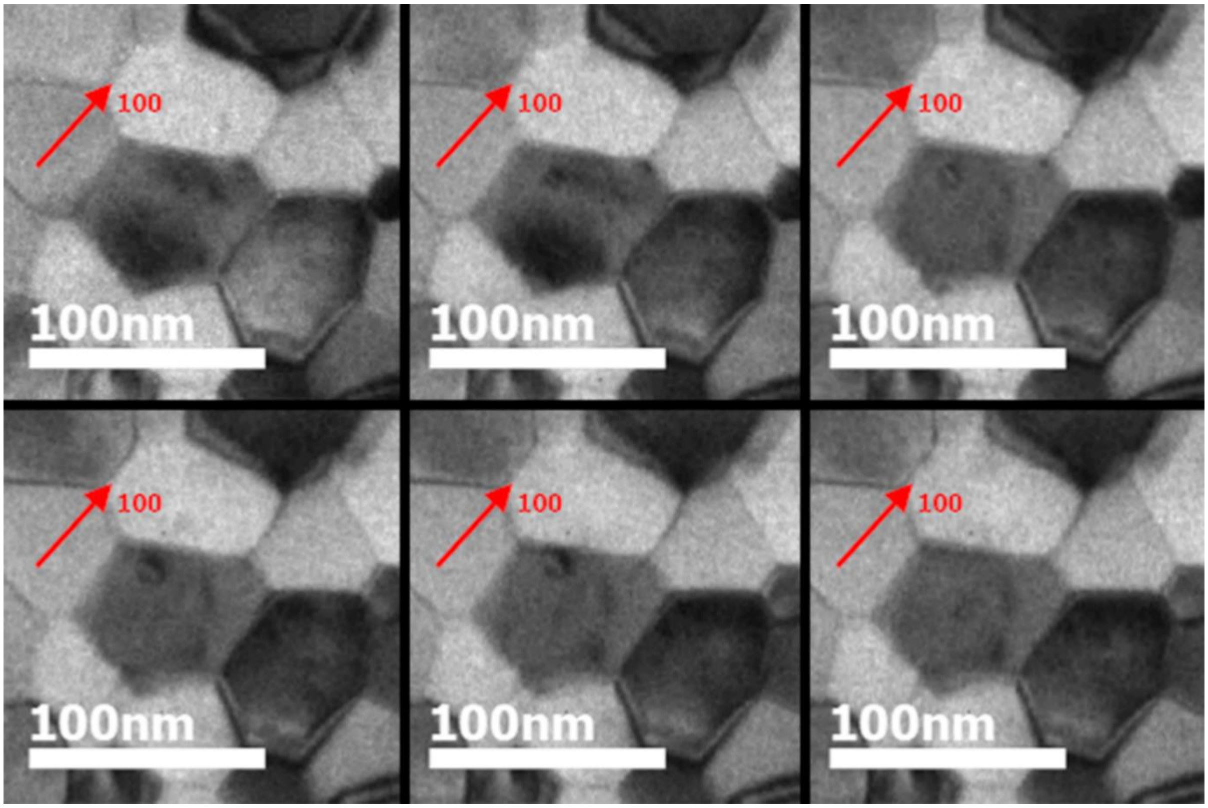

Figure 102. A b=<100> dislocation loop forming (frames 1-4) and rapidly moving toward the grain boundary (frames 3-5) before being absorbed (frames 5-6).

10.3.1 Simulation Results

In the sequence of images shown in Figure 96, the dislocation loop undergoes a series of apparent changes in its habit plane. Using the orientation data from the NanoMEGAS ACOM scans, it is possible to determine where the 110 planes lie in the crystal, and the position of the dislocation loop can be analyzed relative to those directions. It can be seen in Figure 96 that the dislocation loop appears as though it forms along one of the 110 directions, but then rotates to another 110 plane as it grows. This rotation and growth occurs suddenly in the in-situ video, indicating an interaction with another defect cluster or loop not visible in the grain. The 110 habit plane growth is consistent with a dislocation loop having a Burgers vector of 1/2<111>. After that, the loop makes several small rotations before being absorbed into the boundary.

The results from that experimental observation can be directly compared to the results of the molecular dynamics simulation. The initial results for the simulation of a 6nm **b**=1/2<111> dislocation loop near a Σ5 36.87° [001](310) symmetric tilt GB are shown in Figure 103. The dislocation loop is absorbed at the grain boundary in less than 25ps from a distance of 5nm away. Before being absorbed, the dislocation loop undergoes a rotation that represents a change in habit plane. The extra half plane of atoms is accommodated by the grain boundary with minimal grain boundary migration.

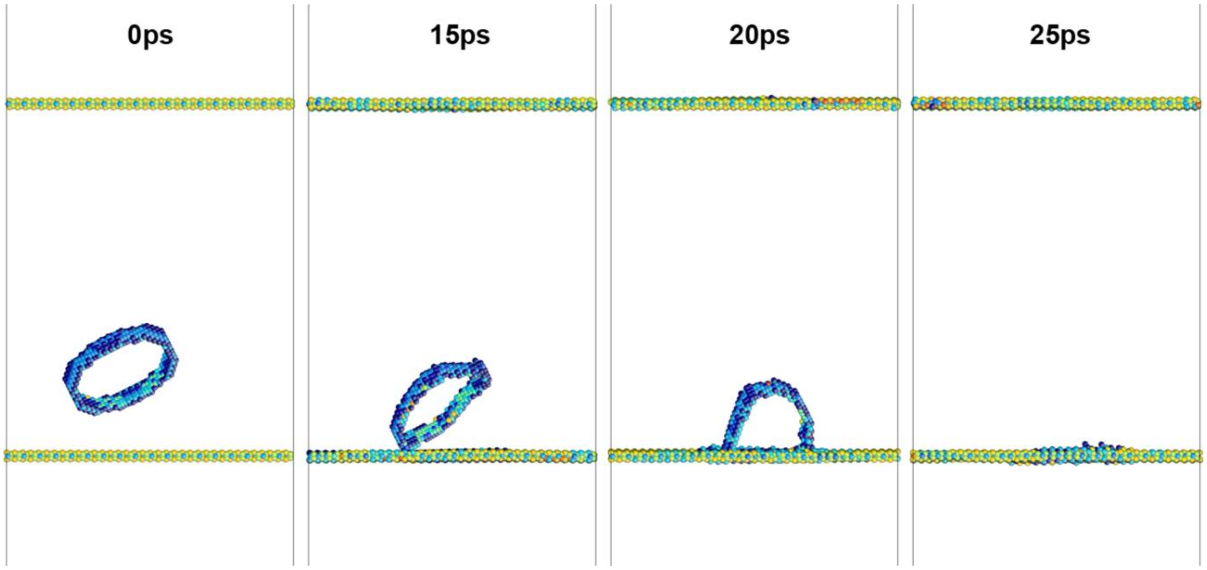

Figure 103. Molecular dynamics simulation of a 6nm b=1/2<111> dislocation loop near a Σ5 36.87o [001](310) symmetric tilt GB. The dislocation loop is completely absorbed by the grain boundary in less than 25ps.

10.4 Discussion

The change in the dislocation loop content of irradiated from **b**=1/2<111> to **b**=<100> as the temperature of irradiation is increased has been attributed to the mobility and stability *of sub-microscopic* defect clusters [140]. Here we have shown that the mobility of the defect clusters does play a significant role in the formation of the irradiated microstructure. By introducing a large number of defect sinks, the more mobile **b**=1/2<111> defect clusters and small loops are quickly removed from the matrix, stunting the growth of large dislocations loops at 300°C and slightly lowering the transition temperature from primarily **b**=1/2<111> to **b**=<100> dominated microstructures when compared to the results observed by Jenkins and Yao [140].

Furthermore, we have shown that a dramatic change is the mobility of the *microscopic* defect clusters and dislocation loops contributes significantly to the change in the irradiated microstructure as the temperature of the material during irradiation is increased from 50K to 500°C. TEM-visible defect clusters and large dislocation loops with Burgers vectors of 1/2<111> and <100> all exhibit significant mobility that contributes to the loss of interstitials to defect sinks. When the grain size of the material is greatly decrease, such as in nanocrystalline materials, this becomes increasingly important. An understanding of how these defect structures are absorbed and accommodated by the grain boundaries will be crucial to designing future radiation tolerant materials for nuclear reactors.

Single vacancies, single interstitials, and sub-microscopic defect clusters (i.e. less than about 2nm [315]) all contribute to the flux of point defects to grain boundary sinks. In addition, we have shown in previous work that microscopic defect clusters (those visible in the TEM as 3-5nm strain fields) and discrete dislocation loops may also be lost to grain boundaries and contribute to the formation of the denuded zone. Appreciably sized defect clusters and dislocation loops can and do form in close proximity to grain boundaries, even in regions that as a whole appear denuded. Other authors have also shown that dislocation loops are capable of forming and growing near grain boundaries during quenching and subsequent annealing of zinc [316] and under a constant flux of interstitials from ion irradiation. The retention of large agglomerations of defects is strongly dependent on the mobility of the cluster/loop itself, and is therefore dependent on temperature. Small **b**=1/2<111> clusters are mobile even at cryogenic temperatures and are seen being lost at grain boundaries. Larger **b**=1/2<111> dislocation loops are more active at elevated temperatures (300-450°C). Defect clusters and dislocation loops with **b**=<100> become mobile enough to be lost to grain boundaries at temperatures of 400-500°C. There has been significant interest in the interactions of dislocation loops with free surfaces both in terms of theory [317, 318] and experiments [23, 24, 74, 319] due to its effect on observed radiation damage in thin foils used for transmission electron microscopy [18, 114, 205]. There have been some calculations on the long range forces of a grain boundary on a dislocation loop [320, 321], but there is a definite lack of understanding as to how defect loops are lost at grain boundaries under irradiation. These initial results shed light on a mechanism of point defect absorption that has not been explored in great detail, but stands to be a major contributor to the final irradiated microstructure of a material. Understanding how dislocation loops are absorbed by grain boundaries will be essential to designing radiation tolerant materials.

CHAPTER 11. EFFECT OF CHROMIUM CONTENT ON THE RADIATION BEHAVIOR

11.1 Introduction

The near-term practical motivation for this research is to understand the fundamental processes that drive radiation tolerance in advanced ferritic alloys are being considered as candidate materials for next generation nuclear reactors. These materials contain high densities of dislocations, grain boundaries, and precipitates, all of which act as sinks for interstitials and vacancies. The majority of these alloys also utilize substantial amounts of chromium (>9%) to increase strength and corrosion resistance. Therefore, it is important to also evaluate the behavior of model iron-chrome alloys to understand the mechanisms operating in the type of material that is likely to be used in future reactors. To this end, several researchers of radiation damage in pure iron have also looked at the behavior of iron chrome alloys, usually simultaneously [18, 69, 115]. In order to study the principal mechanisms driving the behavior of ferritic materials under irradiation, it is necessary to break the microstructure into its constituent components. The simplest case is to observe radiation damage in single crystal iron with low defect density or far from grain boundaries in very large grain polycrystalline iron. In previous chapters, the influence of grain boundaries on the radiation tolerance of pure iron has been covered in some detail. The objective of this work was to understand how solid solution chromium (i.e. at atomic fractions similar to those used in candidate nanostructured steels such as HT-9 and ODS steel) affects the radiation tolerance of nanocrystalline iron.

11.2 Methods

For this study, iron and chrome were sputter co-deposited onto (100) NaCl substrates from 99.9% pure sputter targets from Kurt Lesker Company. The sputtered films were deposited to 100nm in thickness, well above that required to prevent surface effects on the retention of point defects and dislocations. The as-deposited microstructure consists of columnar grains that measure 20-100nm in diameter, and approximately 35nm in average grain size. Therefore the distance from a given point in the grain to a grain boundary is significantly less than the distance to the free surface. Once these films were deposited, they were secured to nickel TEM grids using M-Bond epoxy and the salt substrate was dissolved using a 50-50 water/ethanol solution. The TEM specimens were then annealed *in-situ* shortly before irradiation using a Gatan 628 heating holder in the TEM. This annealing process removes the smaller equiaxed grains at the base of the film along with the residual point defects created during the deposition process.

Once annealed, each sample was irradiated *in-situ* using the Hitachi H-9000NAR IVEM-Tandem at Argonne National Laboratory. They were irradiated using 1MeV Kr^{++} ions at approximately 10^{-3} dpa-sec^{-1} to a total dose of approximately 5dpa at 300°C for the results presented here.

11.3 Results

Due to the high density of grain boundaries in nanocrystalline iron, many instances of TEM-visible defect clusters formed near grain boundaries are found in the material. These defect clusters are often unstable and eventually collapse into the grain boundary. Even larger dislocation loops can easily be absorbed by the grain boundary, which would require that the grain boundary be very efficient in moving the defects away from the site of contact. This action appears to contribute to the formation of the denuded zone at the grain boundary in pure iron. The same phenomena is visible in coarse-grain, ultrafine grain, and nanocrystalline grain size materials.

In nanocrystalline (<100nm grain size) iron and iron-chrome, brightfield transmission electron microscopy was used to measure the areal density of point defect clusters in 120nm thick films. The results show that the defect cluster density is relatively unchanged as a function of grain size for both iron and iron-chrome. It should be noted, however, that in the pure iron material there are many examples of very small grains where the defect density is sharply lower. This same trend is not observed in Fe-9Cr (Figure 104).

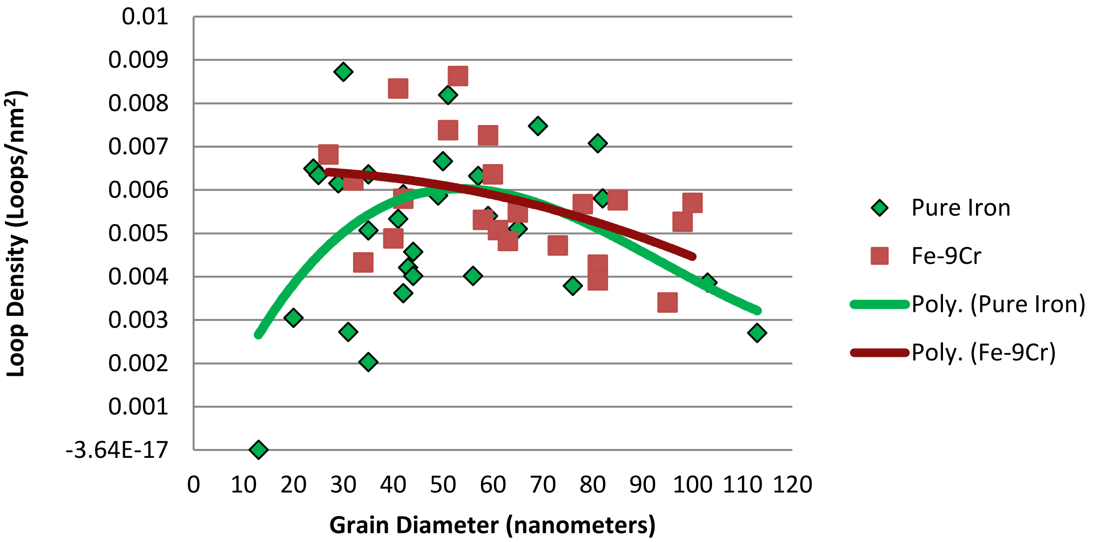

Figure 104. Effect of Grain Size on Dislocation Cluster Density in pure Fe and Fe-9Cr.

In large grain iron irradiated to 5dpa at 300°C, similar behavior is observed to that seen in work by Jenkins et al. [69, 115] for coarse grain iron. The small 2-4nm defect clusters observed in pure iron form rapidly and often disappear while the ion beam is active. These clusters are also very mobile, which permits the growth of larger **b**=1/2<111> finger type loops by coalescence. The final size of the loops observed in the grains is commensurate with the size of the grain. That is, as the grain size is decreased, the average diameter of the dislocation loops measured in the grain also decreases. At a grain size of around 300nm, the dislocation loops form tangled networks of **b**=1/2<111> dislocations. By the nanocrystalline grain size regime, or less than 100nm, the dislocation loops are discrete and measure in size approximately 20nm. Grains less than about 80nm contain primarily small 2-5nm defect clusters, with some larger loops up to ~10nm in diameter.

In Fe-9Cr, the mobility of the small defect clusters appears to be greatly reduced. Once formed, the defect clusters were not observed moving long distances to coalesce or annihilate at grain boundaries. Fewer denuded zones were observed in nanocrystalline iron-chrome irradiated at 300°C, which appears to correlate with the decreased mobility of the defect clusters. The measured dislocation loop size appears to be largely independent of grain size, although I still need to measure these at larger grain sizes (~100-120nm). The dislocation loops found in Fe-9Cr irradiated at 300°C appear to be **b**=<100> type loops, unlike those found in the pure iron.

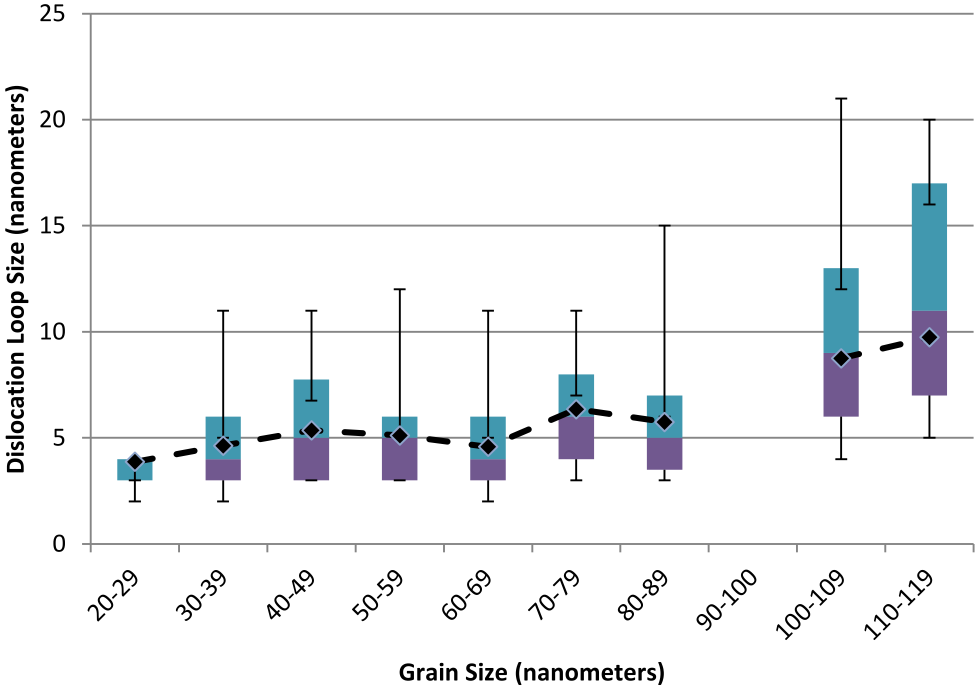

Figure 105. Effect of Grain Size on Dislocation Cluster Size in pure Fe.

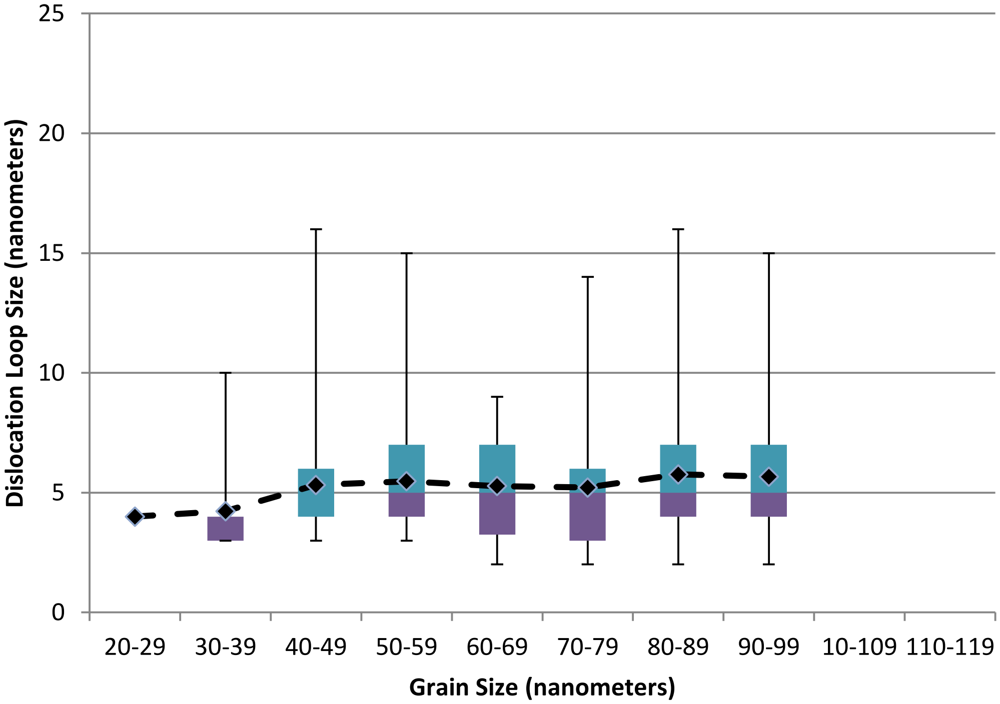

Figure 106. Effect of Grain Size on Dislocation Cluster Size in Fe- 9Cr.

11.4 Discussion

Experimentally, similar defect cluster concentrations were observed in Fe and Fe-9Cr. The size of the dislocation loops observed in pure iron decreases dramatically with grain size, especially in the 300nm to 80nm range. Dislocation loops in the Fe-9Cr appear to be more uniform in size across the range of grain sizes. In addition, the morphology of the loops is different between the two materials. In pure Fe, loops were found consistent with the appearance of **b**=1/2<111> reported in literature. For Fe-9Cr, the morphology is closer to that of **b**=<100> loops found primarily in higher temperature irradiations of pure iron. There is a decrease in the mobility of the defect clusters corresponding to this change in loop type from **b**=1/2<111> to **b**=<100>. In pure iron, a change from **b**=1/2<111> to **b**=<100> occurs with increasing temperature, indicating that it occurs with increasing mobility of clusters.

The greater mobility of defect clusters in pure iron also appears to correspond with the formation of the denuded zone, as greater denuded zones were observed in pure iron than in Fe-9Cr. However, it is not clear if the formation of the denuded zone is purely due to the mobility of defect clusters, or the diffusion of individual interstitials to the grain boundary. Furthermore, we do not have a good understanding of how the vacancies formed in the cascade contribute to the morphology of the dislocation loops formed under irradiation or the formation of a denuded zone at 300°C.

CHAPTER 12. MECHANICAL BEHAVIOR OF NANOCRYSTALLINE IRON

12.1 Introduction

The strength of polycrystalline materials has long been established to be a function of the grain size of the material. Academic study of this effect was initiated independently by Hall [154] and Petch [155], which ultimately led to the empirical relationship

$$\sigma_y = \sigma_0 + kd^{-\frac{1}{2}}$$

where σ_y is the yield strength, σ_0 is a friction stress below which dislocations will not move in the material in the absence of grain boundaries, k is a constant, and d is the grain size.

The advent of nanocrystalline materials [146, 169] revealed that at small enough grain sizes, a deviation from the Hall-Petch relationship is observed. Masumura et al. [160] were the first to show that the Hall–Petch plot for a wide range of materials and mean grain sizes could be divided into three distinct regimes, each defined by the activation of new deformation mechanisms (Figure 107).

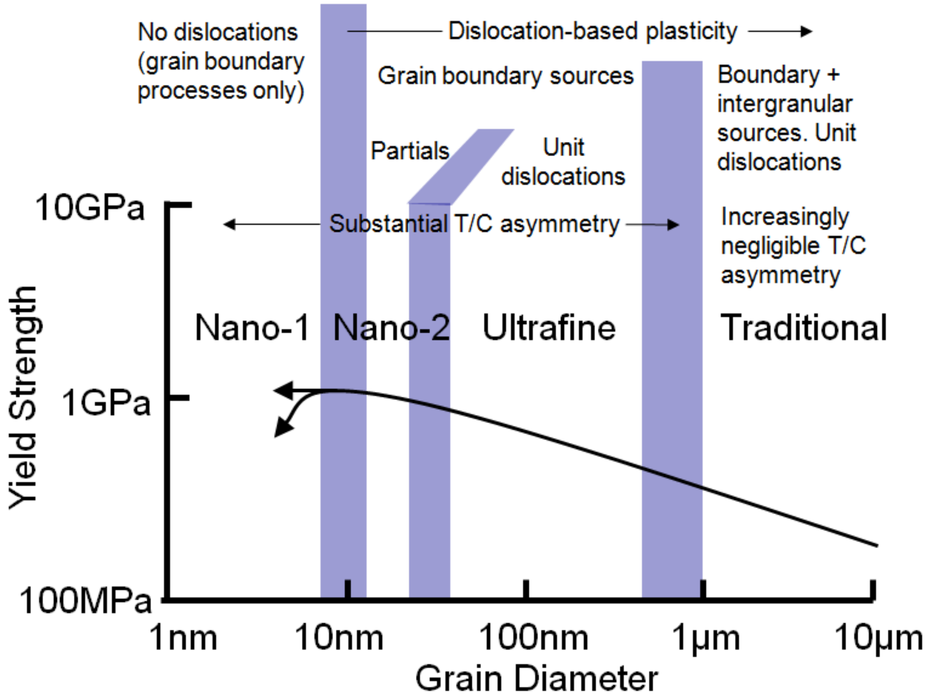

Figure 107. Deformation mechanisms as a function of grain size [173].

The trends outlined in Figure 107 are the result of a considerable amount of research into the mechanical behavior nanocrystalline materials, which have been the subject of over 500 publications and several review articles [174]. The vast majority of this work has been performed in FCC materials by both *in-situ* [175-179] and *ex-situ* [180, 181] transmission electron microscopy as well as molecular dynamics simulations [182-187].

In general, BCC metals such as iron appear to follow a similar trend. The Hall–Petch relationship has been found to be maintained for iron down to a grain size of around 200nm before a sharp deviation (IHPR) is observed (Figure 32) [172]. However, only preliminary work has been performed in BCC metals and has mostly been confined to ex-situ mechanical testing of iron produced by severe plastic deformation [159, 172, 188-192], with some experiments on Fe thin films [193] and gas-condensated Fe [194]. These experiments have shown that uniform elongation completely disappears in iron with grain size less than 1 μm [172] which is thought to arise due to the formation of characteristic shear bands in nanocrystalline iron [189]. However these shear bands result in a significant flow softening, in addition to a significant reduction in the strain rate sensitivity of the flow stress [188].

Insights on the actual mechanisms of deformation for iron have come from a select molecular dynamics simulations [195, 196] performed on nanocrystalline iron. The molecular dynamics work recently performed by Jeon et al. [195] has shed some light on the deformation mechanisms of nanocrystalline iron, finding that the average flow stresses were found to increase with grain size reduction down to 14.7 nm. Below that grain size, the flow stresses were found to decrease with further grain refinement, indicating a deviation from the Hall–Petch relationship. Furthermore, the major deformation mechanism was found to be dislocation glide down to a grain size of 19.7 nm. Below that, grain boundary sliding becomes increasingly dominant until it is the primary mode of deformation at a grain size of 3.7nm.

The results of Jeon et al. have not yet been confirmed experimentally, and more extensive work is needed in BCC metals to determine the primary deformation mechanisms. This work was intended to provide the first *in-situ* TEM testing of nanocrystalline iron to determine the deformation mechanisms of the material. Furthermore, the same experiments were to be performed on irradiated nanocrystalline iron in an attempt to understand how nanocrystalline iron responds to irradiation in terms of its mechanical properties.

12.2 Methods

This study was performed using free-standing nanocrystalline iron films deposited by two methods. For one set of films, iron was deposited at Los Alamos National Laboratory by sputtering a 99.9% pure iron target onto a 1cm x 1cm <100> NaCl substrate held at 370°C following a procedure similar to what is outlined in Chapter 3. The final film was a uniform iron layer approximately 120 nm in thickness with a microstructure comprised of columnar nanocrystalline grains that extend through the thickness. In-plane, the grains are equiaxed and have an average grain size of 26nm with majority of the grains falling between 15nm and 70nm in diameter. The films had no preferred orientation and therefore contain primarily random high angle grain boundaries. The second set of films was deposited onto NaCl substrates using pulsed laser deposition at Sandia National Laboratories. These films were similar in geometry and microstructure to the films deposited at LANL.

After deposition, the iron films were removed from the substrate and transferred to stainless steel tensile jigs (Figure 108) for *in-situ* tensile experiments. To create the test specimens, 5mm x 2mm sections were cleaved from the original substrate and secured to the tensile jig using M-BOND™ 610 Adhesive (Ted Pella, Inc., Redding, CA, USA). The NaCl substrate is then dissolved away using a solution of 50% ethanol in deionized water to dissolve the salt and the specimen rinsed multiple times in anhydrous methanol. The average final thickness of each deposition was verified by both scanning electron microscopy (SEM) and transmission electron microscopy (TEM) using a cross section liftout prepared using a focused ion beam (FIB).

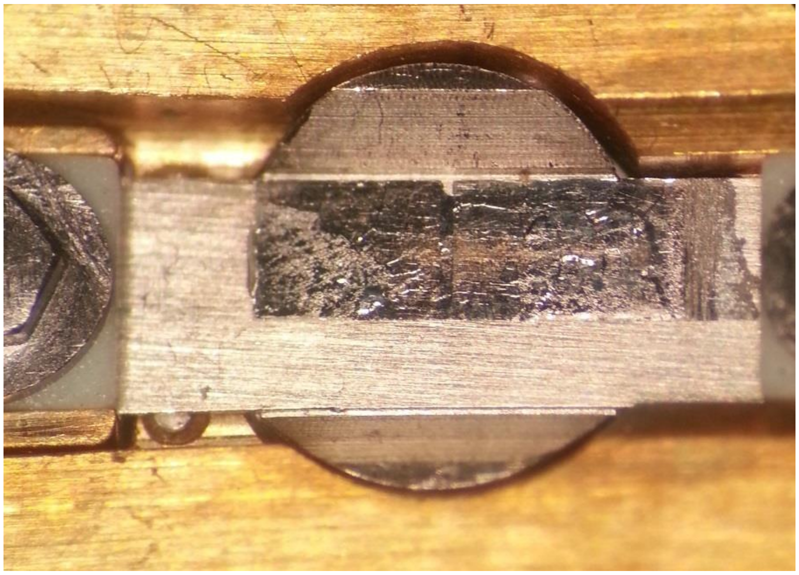

Figure 108. Thin iron film mounted on a stainless steel tensile test jig in the TEM holder.

The *in-situ* tensile experiments were performed using a Gatan heating-straining holder (Gatan, Inc). Each specimen was pulled in tension using low magnification in the TEM until a crack initiated. Once a tear was found in the film, the magnification was increased. When possible, the crack tip was characterized using NanoMEGAS automated orientation mapping before additional strain was applied. Often this was not possible due to specimen drift. Once the target area was characterized, the TEM was returned to bright field imaging conditions, and screen capture software was initiated to record the straining process. Observations were made using a Gatan on-axis CCD camera operating with an exposure time of 0.05s. The output of the CCD camera was recorded as a screen capture at 30fps using Camtasia screen capture software. Strain was then applied to the specimen in small increments, pausing in order to maintain the region of interest.

Most of the time, failure occurred very rapidly (in less than one video frame) and over a much longer length than what was visible at the selected magnification. However, if the fracture occurred slowly, the test was paused and another orientation map was acquired after the crack tip progressed the majority of the way across the viewing area.

The resulting video data was then used *ex-post facto* to examine key elements of the straining process. The video was first virtually stabilized using Adobe Premier Pro CS5 to eliminate image movement due to thermal drift or mechanical translation. The resulting video speed was then manipulated to identify interesting phenomena that occurred during the test. The observations were correlated with the orientation information to gain some insight as to the deformation mechanisms operating in nanocrystalline iron.

12.3 Results

On macroscopic length scales, the thin film nanocrystalline iron specimens were found to fail in a manner consistent with brittle fracture. The fracture occurs rapidly and without significant plastic deformation of the film. This is in contradiction with classical fracture mechanics which predict that the fracture toughness of a two dimensional material (plane stress) is greater than that in plain strain because the material within the crack tip stress field is situated close to a free surface and is therefore able to deform in the out of plane direction. Such behavior has been noted previously and explained as the reduced dislocation mobility resulting from the difficulty of forming dislocations in small grained materials and the prevalence of obstacles to dislocation motion (i.e. grain boundaries)[322]. Initial plastic deformation was found to be confined to a region about 100-200nm in radius ahead of the crack tip. Most of the dislocation activity was confined to a region within 100nm of the tip during fracture. The small size of the plastic zone is consistent with reduced dislocation mobility [322].

A more detailed look at the fracture surface reveals two distinct failure modes. In one case, intergranular fracture occurs along the grain boundaries as shown in Figure 109 A-G. The boundary appears to open up without plastic deformation of the nearby grains. This type of fracture occurred most often in grains where the boundary was perpendicular to the applied stress, as is the case of the boundary indicated with the black arrow in Figure 109. This is indicative of void growth at the boundaries preceding failure. There is also the possibility that the voids are preexisting from the deposition process (see Figure 65 and related text in Chapter 6), leading to premature intergranular failure.

There were many instances where the grain boundaries did not fail and the crack tip was forced to progress through a grain. An example of this case can also be seen in Figure 109. At the start there are two grains at the crack tip separated by a grain boundary indicated with a black arrow. As the specimen is loaded, dislocations sweep across the upper grain from top left to bottom right. As they do so, the grain boundary is slowly removed from the iron by Frame D. As the void opens up, the single grain is pulled in almost uniaxial tension in the direction of the applied stress. In Frame G, the grain has begun to form a necked region indicating that the grain has surpassed the ultimate tensile strength. Necking continues until it reaches a maximum at Frame H just before final fracture. The deformed grain achieves an elongation in excess of 150% between the time it appears to be a single grain (Frame D) to just before final Fracture (Frame H).

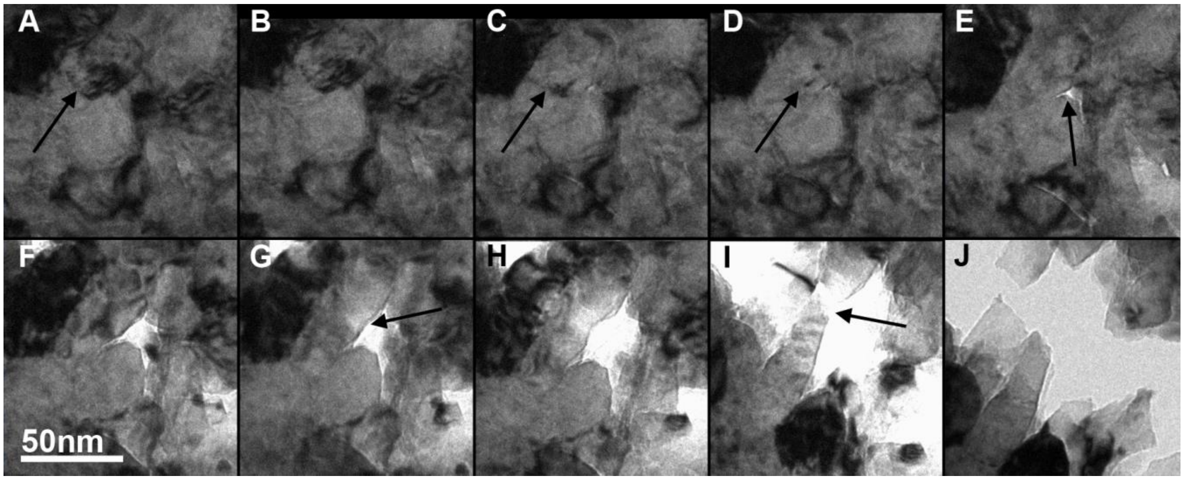

Figure 109. Ductile fracture of nanocrystalline iron. (a) initial microstructure at the crack tip (b) dislocations sweep across grain (c) remains of grain boundary glide into second boundary (d) elongation of the grain under load (e) fracture of nearby grain at the boundary (f) extent of elastic deformation (g) onset of necking in the grain (h) maximum necking (i) final fracture (j) contrast balanced image of final fracture surface.

Direct evidence was found that the ductile elongation of the grain in Figure 109 was due to the motion of dislocations. Figure 110 shows a situation similar to the previous one, where the crack tip must bisect a grain. In this case, the grain is oriented such that it is in a diffracting condition that permits the observations of dislocations. The motion of the dislocations is very rapid, occurring at a rate that is largely too fast for the camera frame rate; however, the indication is that dislocations appear to move from the grain boundaries at the top and bottom of the grain toward the crack tip in the center of the grain. The direction of motion is parallel to the direction of the externally applied stress.

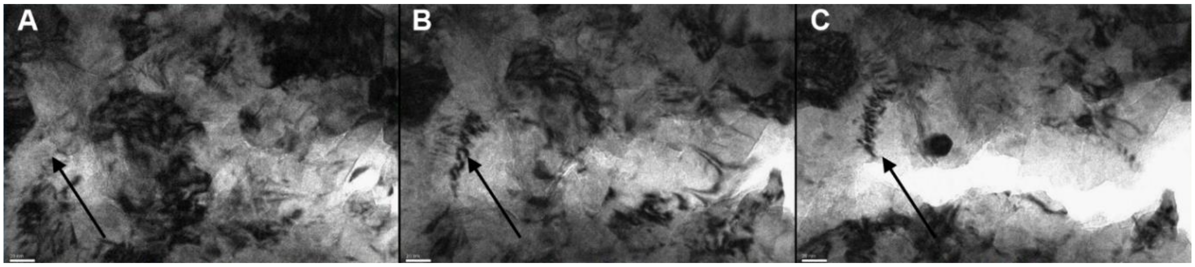

Figure 110. Dislocation motion in nanocrystalline iron. The direction of dislocation motion is toward the crack from either side. Dislocations move along a direction nearly parallel to the applied stress.

Dislocations in each grain in the plastically deformed area appear to always lie along the 110 direction (Figure 111). Due to the small grain size, it was not possible to perform a full Burgers vector analysis, but this is consistent with the activation of **b**=1/2<111> edge dislocations in BCC iron. The particular 110 direction on which the dislocations are found to lie is generally close to perpendicular to the direction of applied stress.

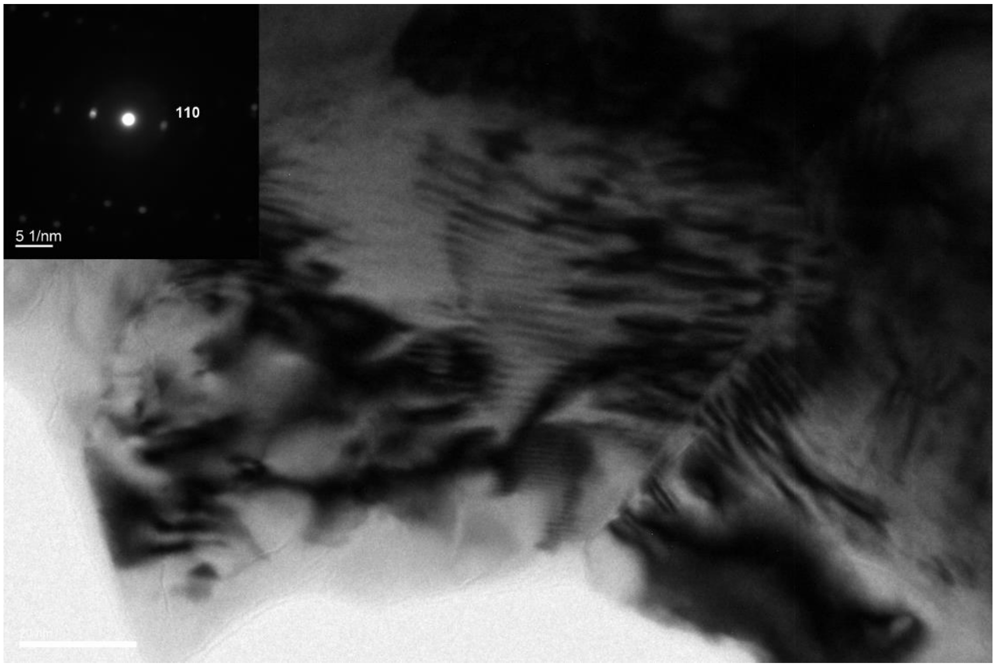

Figure 111. Dislocations lie along the 110 direction, consistent with b**=1/2<111> edge dislocations in BCC materials.**

Figure 112 is an example of a case where orientation data was acquired before and after the progression of the crack tip in the film specimen. The crack tip is just visible at top center left of the brightfield TEM image in Frame A. The direction of the applied stress is approximately 30 degrees from vertical on the page. In this portion of the experiment, the crack tip progressed in a relatively controlled manner, and it was possible to observe dislocation motion under loading, and pause the straining experiment to take a new orientation map after the tip advanced.

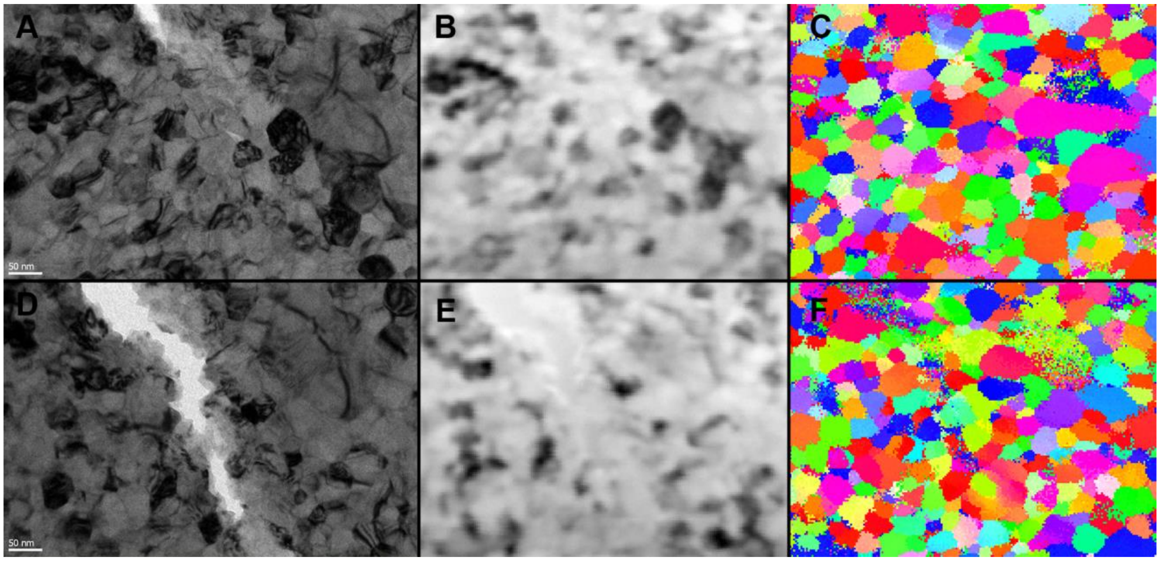

Figure 112. Advancement of the crack tip as recorded using bright field TEM and NanoMEGAS orientation mapping.

The orientation data can be used to look for evidence for the mechanisms of plastic deformation in nanocrystalline iron. The change in disorientation between adjacent grains before and after the advancement of the crack tip is shown in Figure 113 for the identifiable grains within the region of plastic deformation. A few of the grains showed significant rotation, but this was only found in grains that were directly in the fracture path and appeared to be plastically deformed similar to what is shown in Figure 109 and 110. The minimal amount of grain rotation is not surprising given the columnar nature of the microstructure which limits the rotation to one axis of rotation.

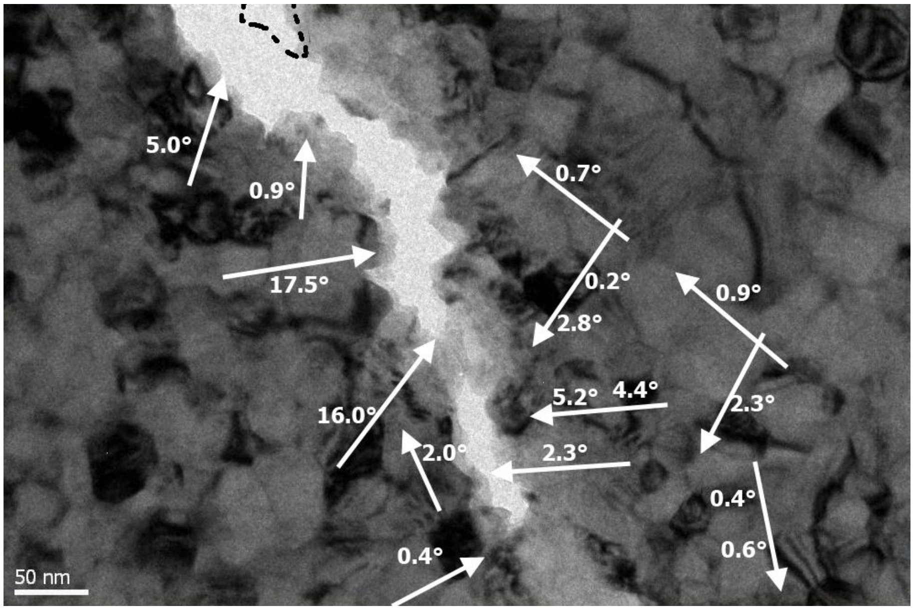

Figure 113. The change in disorientation between adjacent grains before and after the advancement of the crack tip.

Grain rotation is an indication of grain boundary sliding, and for nanocrystalline materials this process has been shown to be responsible for the nucleation of dislocations at triple junctions. Analysis of the diffraction data from the orientation map showed that all of the dislocations were along a 110 direction and traversed in the direction of the crack. Grains that showed the most disorientation change were associated with grains that contained dislocations during deformation.

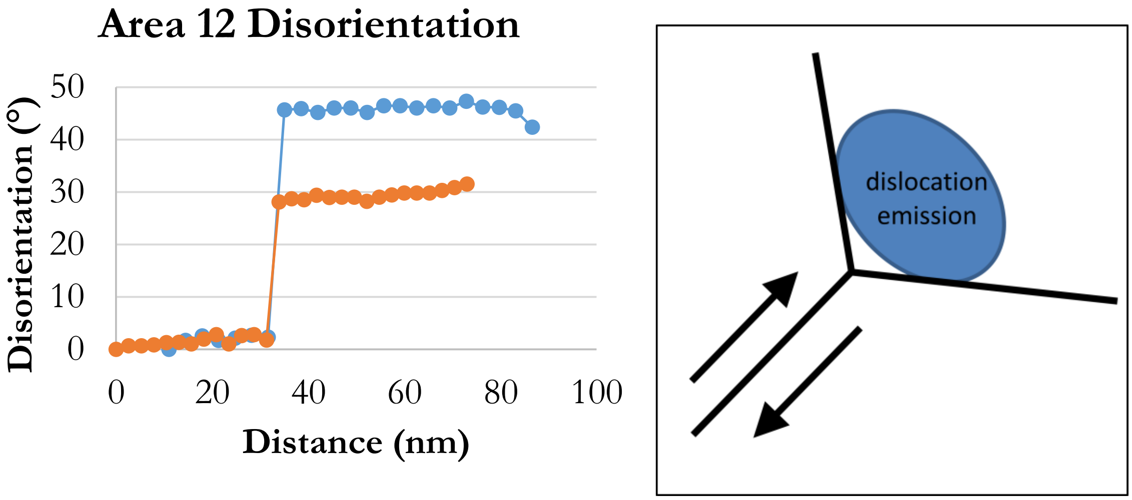

Figure 114. The change in disorientation between adjacent grains before and after the advancement of the crack tip associate with grain boundary sliding which may promote dislocation emission at triple junctions in nanocrystalline materials.

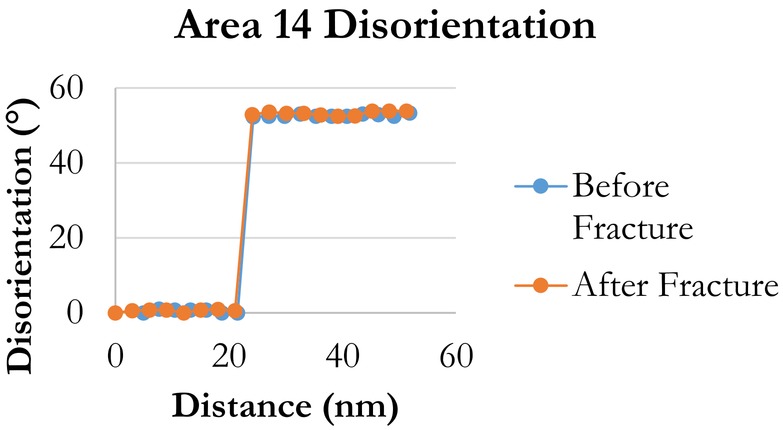

Figure 115. Grains further from the crack tip do not show the same disorientation changes.

The grain orientation maps also indicate the presence of grain growth under loading. In Figure 109A, a case was shown where the dislocations sweeping through a grain removed a grain boundary, leaving a single grain which was then bisected by the crack tip. A similar phenomena occurred in the portion of the test shown in Figure 116. Before the fracture, the orientation map data clearly shows two grains in the region indicated with a white arrow. The grains are separated by a 30° high angle grain boundary. After the fracture tip has progressed, the two grains appear to be a single grain in brightfield TEM, and the orientation data no longer shows a sharp transition indicative of a grain boundary interface.

Figure 116. Grains further from the crack tip do not show the same disorientation changes.

12.4 Discussion

Nanocrystalline iron films produced by physical vapor deposition were mechanically tested using *in-situ* TEM. For as-deposited films, failure occurs through localized fracture. This is largely attributable to the fact that large regions of the film fail by intergranular fracture due to incomplete grain boundaries in as-deposited films (zone 1 type microstructure). Even when grain boundaries hold, plastic deformation occurs in a relatively small region within approximately 100nm of the crack tip. The plastic deformation primarily occurs by slip of dislocations that lie along the 110 direction, consistent with **b**=1/2<111> edge dislocations in BCC iron. Changes in the disorientation between grains were observed during the fracture, indicating that some grain boundary sliding is occurring. The grain boundary sliding could account for the source of dislocations, as the shearing motion of two grains nucleates dislocations at the triple junction in the third grain.

CHAPTER 13. CONCLUSIONS

In-situ transmission electron microscopy was used to observe the evolution of the microstructure in iron irradiated to dose levels up to ~20dpa, commensurate with those experienced by a structural component in the core of a nuclear reactor over its lifetime. This research focused primarily on the how grain boundaries affect the formation of dislocation loops from the accumulation of interstitials and vacancies created in the cascade. The following conclusions were drawn from this research:

- The size of dislocation loops found in iron is proportional to grain size. In microcrystalline iron irradiated to ~5dpa, dislocation loops are typically on the order of several hundred nanometers in length or form large tangled networks where the length is indeterminable. In ultrafine grain iron, the dislocation loops are about 10% of the grain size. That is, for a grain size of 300nm, the average dislocation loops tend to be about 30nm in diameter. This trend continues down to the nanocrystalline size such that a grain with a diameter of 80nm contains loops mainly 5-10nm in size. At the smallest grain sizes, a plateau is reached and nearly all of the grains contain defect clusters of 2-7nm. The smallest of these clusters are the minimal observable size in the TEM, and the larger 7nm long loops form from the coalescence of two of the smaller 2-3nm clusters.
- The population of defect clusters in microcrystalline iron irradiated at 300°C reaches a peak around 1-2dpa, shortly before the clusters begin to coalesce into larger loops. In nanocrystalline iron irradiated at 300°C, the population of defect clusters found at 5dpa (~6 x 10^{-3} loops·nm^{-2}) is on the same order of magnitude as the values reported for microcrystalline iron (~1 x 10^{-3} loops·nm^{-2}) [115] at 1-2dpa. This indicates that the formation of TEM visible defect clusters is not entirely impeded by the loss of point

defects to grain boundaries even in nanocrystalline grains. It does show, however, that the population of the defect clusters does remain stable to significantly higher doses without forming large dislocation loops.

- The width of the denude zone fluctuates from grain boundary to grain boundary. This is clearly illustrated in nanocrystalline and ultrafine grains where denuded zones up to 30nm in width were observed along some grain boundaries while others had no denuded zone at all. The variation in sink strength from boundary to boundary was found to hold true even at the smallest grain sizes (~20nm) observed experimentally. This variation is presumably the result of the differing potency of different grain boundaries as defect sinks; however, no major correlation was found between grain boundary character and sink strength. More investigation is required in this area.
- Only in these denuded zones is the population of the defect clusters significantly reduced. For the population of defect clusters to be affected in a nanocrystalline material, the grain boundaries must be strong sinks capable of forming denuded zones. Since there is variation in the sink strength of the boundary, there is a significant variation in the population of defect clusters from grain to grain in nanocrystalline iron. A grain with denuded zones on all sides (indicating strong sinks) has a very low defect cluster population, while a grain without the denuded zone (weak sinks) at its borders retains a high population of defect clusters.
- The population of defect clusters in nanocrystalline iron reaches a steady level by 1-2dpa. After that dose, a constant population of defect clusters in the nanocrystalline material is maintained by the absorption of clusters at defect sinks such as free surfaces and grain boundaries. Evidence of grain boundaries absorbing defect clusters was observed in both

nanocrystalline and ultrafine grain iron specimens. It is likely that this behavior also occurs along grain boundaries in microcrystalline iron; however the events are less likely to be observed in TEM due to the decreased line length of grain boundary.

- Defect clusters may be removed from the grain interior as well as the region immediately adjacent to the grain boundary. This is made possible by one dimensional loop/cluster hop in which a complex of point defects can move tens of nanometers at speeds greater than 103 nm s^{-1} [18]. This motion tends to favor a particular direction, resulting in a net motion of the cluster along its Burgers vector. Since the distance to a grain boundary in nanocrystalline material is on the same order of magnitude of this motion, one dimensional loop hop often transports a defect cluster to a grain boundary, thus providing an effective mechanism for the long range transport of point defects to the sink.
- Large dislocation loops that form in iron can also be absorbed by the grain boundary, which has significant implications for the microstructure of irradiated nanocrystalline iron. The type and number of these dislocation loops that remain in the grain is strongly dependent on the mobility of the defect structure. For example, dislocation loops with **b**=1/2<111> have a higher mobility at lower temperatures and are preferentially lost to the grain boundaries over the relatively sessile **b**=<100> type loops. At 300°C some large (>10m) **b**=1/2<111> loops are lost to the grain boundary but the microstructure is still predominantly **b**=1/2<111> type loops. At 350°C and 400°C, the **b**=1/2<111> loops were observed moving very rapidly to grain boundaries, leaving behind increasingly larger fractions of **b**=<100> type loops. The **b**=<100> type loops, too,

were more rapidly lost to grain boundaries as the temperature increased until at 500°C, the loops were completely unstable in nanocrystalline iron and few if any were observed.

- Experimental observations of dislocation loop absorption indicated two distinctly different behaviors of dislocation loops at grain boundaries. In one case, the loop appeared to move along its Burgers vector by glide/climb until it reached a grain boundary where it was immediately annihilated. This process occurred frequently for **b**=1/2<111> type loops around 300°C, and for **b**=<100> type loops near 500°C. The second type of behavior observed occurred for **b**=1/2<111> type loops in the 350°C-400°C irradiations, and for **b**=<100> type loops at temperatures greater than ~350°C (with increasing speed and frequency as the temperature increased). These loops grew under constant irradiation until the edge of the loop came in contact with the grain boundary. When contact with the grain boundary was initiated, the loop appeared to shrink starting with the side furthest from the grain boundary. This process continued until the entire loop disappeared, generally over the course of up to 30 minutes. The time and appearance of this second mechanism indicates a pipe diffusion process. In both cases, the grain boundary able to remove a dislocation loop from the grain, indicating the ability to accommodate a considerably large number of point defects.

CHAPTER 14. FUTURE WORK

The preceding chapters have outlined a direct study of the interactions of point defects with grain boundaries utilizing nanocrystalline iron as a means to observe a large line length of boundaries in a given experiment. There is very little work of this nature, and it has raised a number of questions that should be the subject of ongoing research. In addition, the studies of the free standing iron films (deposition, annealing, void pinning, and mechanical behavior) were only completed insofar as they applied to the study of radiation damage. There is much that can be done to develop a more comprehensive understanding of each of these topics, which are outlined in the following sections.

14.1 Film Deposition

The process of depositing iron on sodium chloride is one that has been a problem of significant interest, and surprising complexity, since at least the time of Brück's publication in 1936 [207]. The low substrate temperature necessitated by the sublimation of NaCl and the ease of surface contamination combined with the close energy between the two most stable orientations makes depositing a true single crystal film exceptionally difficult. For the deposition work in this thesis, the deposition techniques used to achieve the desired microstructures were based on empirical observations. Future work in this area would use more advanced characterization techniques to investigate the variables involved in the deposition.

Profilometry and scanning probe microscopy (SPM) should be used to understand the surface roughness effects of the substrate on the deposition, and could be performed before and after the potential substrate treatments such as a high temperature anneal or precleaning using ion bombardment. Similarly, auger electron spectroscopy (AES) could be used to examine the amount of contamination on the surface of the substrate. Reflection high-energy electron diffraction (RHEED) could be used during the deposition of the film to understand the nucleation and growth of the film *in-situ*. After deposition, the profilometry/SPM and AES measurements could be applied to the surface of the film to understand the effect of deposition parameters on the surface roughness. Transmission electron microscopy should be used to more precisely characterize the substrate-film interface. Preparing a planar specimen with the Fe-NaCl interface intact would permit a direct study of the orientation relationship between the NaCl and Fe. Similarly, a liftout made with focused ion beam (FIB) milling would permit a study of the NaCl-Fe interface. These advanced techniques may provide some insight to factors that are most critical to depositing a single crystal film over one with strong fiber texture or a fully random texture.

If a single crystal film can be achieved on the sodium chloride substrates, the next step would be to utilize this method to create thin film bicrystals by depositing onto bicrystal salt substrates. In this way, single boundaries with desired characteristics (e.g. pure tilt, pure twist, or a mixture) could be studied to isolate the effects of grain boundary character on sink strength in irradiated iron.

14.2 Irradiation Experiments

14.1.1 Defect Characterization

While the use of nanocrystalline films has significant advantages for studying the interactions of defects with grain boundaries (e.g. a higher probably of witnessing absorption events), it does have definite limitations. Full characterization of the defect structures requires being able to tilt a single grain to multiple reflections in order to determine **g·b**. With nanocrystalline materials the spot size of the instrument is larger than the diameter of the grain. Even in nanobeam mode with the LaB_6 JEOL 2100, the spot size is around 20nm and it does not carry enough intensity to create the Kickuchi bands necessary for identifying the proper imaging conditions. In addition, the diameter of the grains is very small compared to the thickness of the film, so any tilting will result in picking up diffraction information from surrounding grains.

As a result, the defect information acquired in this paper was done by extrapolating diffraction information from the orientation maps generated using the NanoMEGAS system. Future work should focus on using more advanced characterization techniques to identify the interstitial/vacancy nature of the loops remaining in nanocrystalline iron after irradiation. One possible technique is low angle annular dark-field STEM [323], which enables the microscopist to image defect contrast while maintaining directly interpretable atomic resolution. This technique has been used to perform defect analysis in polycrystalline Ni-based super alloys with some success.

14.1.2 Defect Cluster Counts

Another result of the limitations of acquiring diffraction information from nanocrystalline grains is that defect counts were necessarily biased to the high end. The number of defects visible in a grain was only considered valid if it met two criteria. The first is that the diffraction pattern had to approximately match what would be considered a weak-beam bright field condition set up by conventional selected area diffraction. There was some margin of error in this assessment due to the lack of Kikuchi bands to use as reference. The second criteria, designed to account for the error in the diffracting condition, was that some defects had to be clearly visible in the grain. By default, this excludes any grain that had abnormally low dislocation loop densities, thereby biasing the defect count results. It is possible that the radiation resistance of nanocrystalline iron, and therefore the sink strength, is greater than what is reported in this text. Future work should attempt to account for this. Again, the use of low angle annular dark-field STEM technique developed by Phillips et al. provides a viable means to accomplish this task. It may also be possible to perform adequate defect cluster counts with FEG probe TEM, which would provide greater imaging resolution, intensity, and stronger diffraction patterns from more precise areas.

14.1.2 Grain Boundary Character Effects

Nanocrystalline iron films showed clearly that there is an effect from grain boundary character on radiation damage in iron. However, there are a number of complicating factors that are introduced in a nanocrystalline thin film. A grain boundary in the film may be non-equilibrium, since the films were not annealed for very long periods of time. When the grain size is reduced to <100nm, there is also a much more pronounce influence from triple junctions, which are thought to have substantial influence on the properties of nanocrystalline materials. Similarly, the small grain size necessitates that there be more curvature in a given grain boundary, which leads to a change in boundary character along the length of the boundary.

In order to separate these issues out from the material, bicrystal specimens should be the subject of future study, both experimentally and through simulations. The ability to systematically vary the grain boundary structure would be more suitable for a study of grain boundary character effects than the microstructure of a nanocrystalline material. The method for creating such films is explained in the section on film deposition.

14.1.3 Equilibrium vs. Non-equilibrium Grain Boundaries

Initial experiments were carried out by irradiating an under-annealed film (i.e. one annealed to ~450°C) and comparing the results to those acquired by irradiating a fully annealed film (i.e. 600°C anneal). During irradiation, qualitative observations indicated a lower damage level in the less annealed iron films as a function of dose. The differences by 5dpa, however, were slight, leading to the conclusion that perhaps the smaller grain size and greater scattering contrast was responsible for much of the effects witnessed. However, these results spurred an additional exploration into the effects of a non-equilibrium grain boundary, specifically one that contains excess free volume with respect to the lowest energy configuration for a given misorientation.

Molecular dynamics simulations performed by Dr. Garritt Tucker (Drexel) show that excess free volume does contribute to a decreased survival rate of point defects in cascades that occur in close proximity to the grain boundary. For the simulation, a 3keV primary knock-on atom (PKA) was created at 3nm from the grain boundary plane in a bicrystal simulation. The simulation was run at room temperature to observe the collapse of the cascade at two grain boundaries: a Σ5 (210)<001> symmetric tilt grain boundary (~53° misorientation angle), and boundary with the same misorientation but with artificially introduced excess free volume. The result indicates that the defect survival rate is higher for the equilibrium boundary structure, at least in the case of the Σ5 boundary.

Future work may explore the effect using experiments in materials specifically created to contain a large fraction of non-equilibrium grain boundaries. This may be accomplished in two ways. The first is to continue work with the nanocrystalline films.

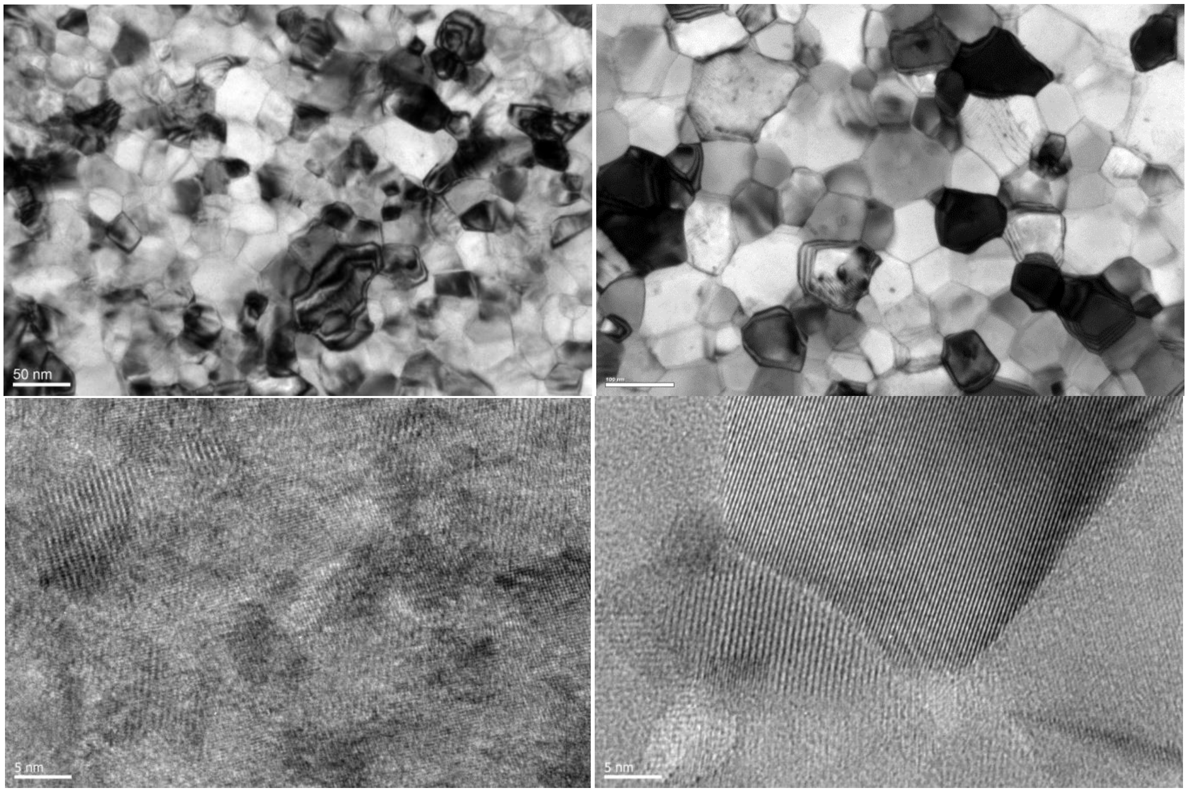

Figure 117. (left) As-deposited nanocrystalline iron thin film with a large number of atoms in nonequilibrium positions. (right) The same film annealed to 600°C showing nearly equilibrium grain boundaries.

Nanocrystalline materials produced by severe plastic deformation also contain a large number of non-equilibrium grain boundaries. This fact could be utilized for future work should the nanocrystalline iron thin film experiments not work out. At the time of writing this thesis, work is already underway to create nanocrystalline iron from the split cast iron material described in the methods section. Equal channel annular pressing (ECAP) has been attempted with marginal success, and high pressure torsion (HPT) has been performed by Carpenter Technologies. These materials have an average grain size on the order of several hundred nanometers, which can be achieved in thin films with equilibrium boundaries.

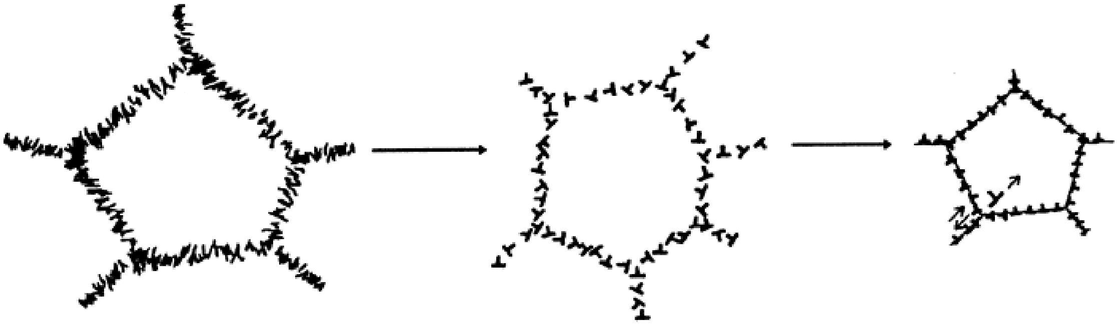

Figure 118. Grain boundary evolution at different stages during severe plastic deformation [151].

14.1.2 Chemistry Effects

The effects of solute atoms on the efficiency of grain boundary sinks was only given cursory attention in this work, and remained confined to the study its effect on the formation and mobility of defect structures. Introducing chromium to iron also creates additional complexity with the introduction of radiation induced segregation, which was beyond the scope of this project. Future work should investigate the segregation of chromium in nanocrystalline Fe-Cr films. This work could be performed with transmission electron microscopy techniques such as electron energy loss spectroscopy (EELS) and Energy filtered transmission electron microscopy (EFTEM). Local sites could be lifted out of the film using focused ion beam (FIB) and made into needles for atom probe tomography (APT). This information could be correlated with *in-situ* electron microscopy used to observe defect cluster motion and the formation of any denuded regions, enabling a more complete study of how defect clusters and dislocation loops act to transport solute atoms to the grain boundary.

14.3 Straining Experiments

The next logical step for straining experiments would be to perform tests using a more refined setup. For the next generation of tensile tests, there are a number of evolutionary changes that can be made to drastically improve the success of the operation. Firstly, the film specimens should be annealed in a furnace designed to heat only the central part of the film away from the epoxy under vacuum to achieve the clean microstructure shown in at 500-600°C in Chapter 5. Once the films are annealed on the straining jig, the Focused Ion Beam (FIB) should be used to remove all of the film except a small bar across the gap in the straining jig. This would serve two purposes, first to localize the area where the specimen could fracture, making the test more precise. Second, it would create an appropriate sample geometry to minimize the effects from plane stress. The FIB should also be used to place small fiducial markers on the specimen, preferably by using E-beam deposited tungsten to create a visible marker on the surface. Alternatively, small holes can be made in the film in a similar manner as the fiducial markers described in Chapter 3.

BIBLIOGRAPHY

[1] J. Conti, in: O.o.E.A. U.S. Energy Information Administration, U.S. Department of Energy (Ed.), Washington, DC, 2013.
[2] DOE, in: N.E.R.A.C.a.t.G.I.I. Forum (Ed.), 2002.
[3] IAEA, in: I.A.E. Agency (Ed.), International Atomic Energy Agency, Vienna, 2013.
[4] EIA, 2014.
[5] E.A. Kenik, J.T. Busby, Radiation-induced degradation of stainless steel light water reactor internals, Materials Science and Engineering: R: Reports. 73 (2012) 67.
[6] J.T. Busby, R.K. Nanstad, R.E. Stoller, Z. Feng, D.J. Naus, Materials Degradation in Light Water Reactors: Life After 60, Oak Ridge National Laboratory, 2008.

[7] G.R. Odette, M.J. Alinger, B.D. Wirth, Recent Developments in Irradiation-Resistant Steels, Annual Review of Materials Research. 38 (2008) 471.

[8] K. Ehrlich, J. Konys, L. Heikinheimo, Materials for high performance light water reactors, Journal of Nuclear Materials. 327 (2004) 140.

[9] K. Ehrlich, The development of structural materials for fusion reactors, Philosophical Transactions of the Royal Society of London. Series A:
Mathematical, Physical and Engineering Sciences. 357 (1999) 595.

[10] S.J. Zinkle, N.M. Ghoniem, Operating temperature windows for fusion reactor structural materials, Fusion Engineering and Design. 51–52 (2000) 55.

[11] W.R. Corwin, U.S. Generation IV Reactor Integrated Materials Technology Program, Journal Name: Nuclear Engineering and Technology; Journal Volume: 38; Journal Issue: 7. (2006) Medium: X; Size: 1.

[12] T.R. Allen, J.T. Busby, R.L. Klueh, S.A. Maloy, M.B. Toloczko, Cladding and duct materials for advanced nuclear recycle reactors, JOM. 60 (2008) 15.

[13] G.S. Was, Materials degradation in fission reactors: Lessons learned of relevance to fusion reactor systems, Journal of Nuclear Materials. 367–370, Part A (2007) 11.

[14] K.L. Murty, I. Charit, Structural materials for Gen-IV nuclear reactors: Challenges and opportunities, Journal of Nuclear Materials. 383 (2008) 189.

[15] T. Abram, S. Ion, Generation-IV nuclear power: A review of the state of the science, Energy Policy. 36 (2008) 4323.

[16] L.K. Mansur, A.F. Rowcliffe, R.K. Nanstad, S.J. Zinkle, W.R. Corwin, R.E. Stoller, Materials needs for fusion, Generation IV fission reactors and spallation neutron sources – similarities and differences, Journal of Nuclear Materials. 329–333, Part A (2004) 166.

[17] S.J. Zinkle, J.T. Busby, Structural materials for fission & fusion energy, Materials Today. 12 (2009) 12.

[18] M.L. Jenkins, Z. Yao, M. Hernández-Mayoral, M.A. Kirk, Dynamic observations of heavy-ion damage in Fe and Fe–Cr alloys, Journal of Nuclear Materials. 389 (2009) 197.

[19] J.H. Lee, R. Kasada, A. Kimura, T. Okuda, M. Inoue, S. Ukai, S. Ohnuki, T. Fujisawa, F. Abe, Influence of alloy composition and temperature on corrosion behavior of ODS ferritic steels, Journal of Nuclear Materials. 417 (2011) 1225.

[20] V. de Castro, E.A. Marquis, S. Lozano-Perez, R. Pareja, M.L. Jenkins, Stability of nanoscale secondary phases in an oxide dispersion strengthened Fe–12Cr alloy, Acta Materialia. 59 (2011) 3927.

[21] E.A. Little, R. Bullough, M.H. Wood, On the Swelling Resistance of Ferritic Steel, Proceedings of the Royal Society of London. A. Mathematical and Physical Sciences. 372 (1980) 565.

[22] R. Schaeublin, D. Gelles, M. Victoria, Microstructure of irradiated ferritic/martensitic steels in relation to mechanical properties, Journal of Nuclear Materials. 307-311 (2002) 197.

[23] S.J. Zinkle, Microstructure of ion irradiated ceramic insulators, Nuclear Instruments and Methods in Physics Research B: Beam Interactions with Materials and Atoms. 91 (1994) 234.

[24] R. Yamada, S.J. Zinkle, G. Philip Pells, Microstructure of Al_2O_3 and $MgAl_2O_4$ preimplanted with H, He, C and irradiated with Ar^+ ions, Journal of Nuclear Materials. 209 (1994) 191.

[25] J.L. Brimhall, B. Mastel, T.K. Bierlein, Thermal stability of radiation produced defects in molybdenum, Acta Metallurgica. 16 (1968) 781.

[26] W.Z. Han, M.J. Demkowicz, E.G. Fu, Y.Q. Wang, A. Misra, Effect of grain boundary character on sink efficiency, Acta Materialia. 60 (2012) 6341.
[27] M. Griffiths, R.W. Gilbert, C.E. Coleman, Grain boundary sinks in neutron-irradiated Zr and Zr-alloys, Journal of Nuclear Materials. 159 (1988) 405.
[28] G. Ackland, Controlling radiation damage, Science (New York, N.Y.). 327 (2010) 1587.
[29] A. Misra, L. Thilly, Structural metals at extremes, MRS Bulletin. 35 (2010) 1.
[30] A.R. Kilmametov, D.V. Gunderov, R.Z. Valiev, A.G. Balogh, H. Hahn, Enhanced ion irradiation resistance of bulk nanocrystalline TiNi alloy, Scripta Materialia. 59 (2008) 1027.
[31] M. Rose, A.G. Balogh, H. Hahn, Instability of irradiation induced defects in nanostructured materials, Nuclear Instruments and Methods in Physics Research B. 127/128 (1997) 119.
[32] N. Nita, R. Schaeublin, M. Victoria, Impact of irradiation on the microstructure of nanocrystalline materials, Journal of Nuclear Materials. 329-333 (2004) 953.
[33] C. Sun, M. Song, K.Y. Yu, Y. Chen, M. Kirk, M. Li, H. Wang, X. Zhang, In situ Evidence of Defect Cluster Absorption by Grain Boundaries in Kr Ion Irradiated Nanocrystalline Ni, Metall and Mat Trans A. 44 (2013) 1966.
[34] B.N. Singh, Impacts of damage production and accumulation on materials performance in irradiation environment, Journal of Nuclear Materials. 258–263, Part 1 (1998) 18.
[35] G. Was, Fundamentals of Radiation Materials Science, Springer, New York, 2007.
[36] M. Nastasi, J.W. Mayer, J.K. Hirvonen, Ion-Solid Interactions: Fundamentals and Applications, Cambridge University Press, New York, NY, 1996.
[37] C.P. Flynn, R.S. Averback, Electron-phonon interactions in energetic displacement cascades, Physical Review B. 38 (1988) 7118.
[38] C. Domain, C.S. Becquart, L. Malerba, Simulation of radiation damage in Fe alloys: an object kinetic Monte Carlo approach, Journal of Nuclear Materials. 335 (2004) 121.
[39] C.A. English, M.L. Jenkins, Insight into Cascade Processes Arising from Studies of Cascade Collapse, Materials Science Forum. 15-18 (1987) 1003.
[40] A.Y. Stathopoulos, The study of heavy-ion damage in pure copper, Philosophical Magazine A. 44 (1981) 285.
[41] A.Y. Stathopoulos, C.A. English, Vacancy loop formation in heavy-ion irradiated Cu alloys, Journal of Nuclear Materials. 108–109 (1982) 69.
[42] M.L. Jenkins, A weak-beam electron microscopy analysis of defect clusters in heavy-ion irradiated silver and copper, Philosophical Magazine. 29 (1974) 813.
[43] T. Schober, Defects produced in silver by kev silver ion bombardment, physica status solidi (a). 1 (1970) 307.
[44] K.L. Merkle, L.R. Singer, J.R. Wrobel, ENERGY DEPENDENCE OF CASCADE CLUSTER FORMATION IN GOLD, Applied Physics Letters. 17 (1970) 6.
[45] T.M. Robinson, M.L. Jenkins, Heavy-ion irradiation of nickel and nickel alloys, Philosophical Magazine A. 43 (1981) 999.
[46] M.A. Kirk, I.M. Robertson, M.L. Jenkins, C.A. English, T.J. Black, J.S. Vetrano, The collapse of defect cascades to dislocation loops, Journal of Nuclear Materials. 149 (1987) 21.
[47] K. Kitagawa, K. Yamakawa, H. Fukushima, T. Yoshiie, Y. Hayashi, H. Yoshida, Y. Shimomura, M. Kiritani, Ion-irradiation experiment for the fundamental studies of damage evolution of fusion materials, Journal of Nuclear Materials. 133–134 (1985) 395.
[48] M.L. Jenkins, C.A. English, B.L. Eyre, Heavy-ion irradiation of α-iron, Philosophical Magazine A. 38 (1978) 97.

[49] V.F. Häussermann, Elektronenmikroskopische untersuchung der strahlenschädigung in kupfer durch schwere ionen im keV-energiebereich, Philosophical Magazine. 25 (1972) 537.
[50] H. Föll, M. Wilkens, Transmission electron microscope studies of dislocation loops in heavy-ion irradiated H.C.P. cobalt, physica status solidi (a). 39 (1977) 561.
[51] W.J. Phythian, B.L. Eyre, D.J. Bacon, C.A. English, Characterization of heavy-ion damage in ruthenium, Philosophical Magazine A. 55 (1987) 757.
[52] M.L. Jenkins, M. Wilkens, Transmission electron microscopy studies of displacement cascades in Cu3Au, Philosophical Magazine. 34 (1976) 1155.
[53] M.L. Jenkins, C.A. English, Characterization of displacement cascade damage in ordered alloys using transmission electron microscopy, Journal of Nuclear Materials. 108–109 (1982) 46.
[54] J.B. Gibson, A.N. Goland, M. Milgram, G.H. Vineyard, Dynamics of radiation damage, Physical Review. 120 (1960) 1229.
[55] C. Erginsoy, G.H. Vineyard, A. Englert, Dynamics of radiation damage in a body-centered cubic lattice, Physical Review. 133 (1964) A595.
[56] M.W. Guinan, J.H. Kinney, Molecular dynamic calculations of energetic displacement cascades, Journal of Nuclear Materials. 104 (1981) 1319.
[57] D.J. Bacon, A.F. Calder, J.M. Harder, S.J. Wooding, Computer simulation of low-energy displacement events in pure bcc and hcp metals, Journal of Nuclear Materials. 205 (1993) 52.
[58] W.J. Phythian, R.E. Stoller, A.J.E. Foreman, A.F. Calder, D.J. Bacon, A comparison of displacement cascades in copper and iron by molecular dynamics and its application to microstructural evolution, Journal of Nuclear Materials. 223 (1995) 245.
[59] R.E. Stoller, The role of cascade energy and temperature in primary defect formation in iron, Journal of Nuclear Materials. 276 (2000) 22.
[60] D.J. Bacon, F. Gao, Y.N. Osetsky, The primary damage state in fcc, bcc and hcp metals as seen in molecular dynamics simulations, Journal of Nuclear Materials. 276 (2000) 1.
[61] C.S. Becquart, C. Domain, J.C. van Duysen, J.M. Raulot, The role of Cu in displacement cascades examined by molecular dynamics, Journal of Nuclear Materials. 294 (2001) 274.
[62] C.S. Becquart, C. Domain, A. Legris, J.C. Van Duysen, Influence of the interatomic potentials on molecular dynamics simulations of displacement cascades, Journal of Nuclear Materials. 280 (2000) 73.
[63] R.A. Johnson, Interstitials and Vacancies in α Iron, Physical Review. 134 (1964) A1329.
[64] B.N. Singh, S.I. Golubov, H. Trinkaus, A. Serra, Y.N. Osetsky, A.V. Barashev, Aspects of microstructure evolution under cascade damage conditions, Journal of Nuclear Materials. 251 (1997) 107.
[65] S.I. Golubov, B.N. Singh, H. Trinkaus, Defect accumulation in fcc and bcc metals and alloys under cascade damage conditions – Towards a generalisation of the production bias model, Journal of Nuclear Materials. 276 (2000) 78.
[66] M.L. Jenkins, M.A. Kirk, W.J. Phythian, Experimental studies of cascade phenomena in metals, Journal of Nuclear Materials. 205 (1993) 16.
[67] P.T. Heald, The preferential trapping of interstitials at dislocations, Philosophical Magazine. 31 (1975) 551.
[68] D.A. Terentyev, T.P.C. Klaver, P. Olsson, M.C. Marinica, F. Willaime, C. Domain, L. Malerba, Self-Trapped Interstitial-Type Defects in Iron, Physical Review Letters. 100 (2008) 145503.

[69] M. Hernández-Mayoral, Z. Yao, M.L. Jenkins, M.A. Kirk, Heavy-ion irradiations of Fe and Fe–Cr model alloys Part 2: Damage evolution in thin-foils at higher doses, Philosophical Magazine. 88 (2008) 2881.

[70] S.J. Zinkle, K. Farrell, Void swelling and defect cluster formation in reactor-irradiated copper, Journal of Nuclear Materials. 168 (1989) 262.

[71] A.H. King, D.A. Smith, On the mechanisms of point-defect absorption by grain and twin boundaries, Philosophical Magazine A. 42 (1980) 495.

[72] L.K. Mansur, M.H. Yoo, Advances in the theory of swelling in irradiated metals and alloys, Journal of Nuclear Materials. 85–86, Part 1 (1979) 523.

[73] N.Q. Lam, S.J. Rothman, R. Sizmanns, Steady-state point-defect diffusion profiles in solids during irradiation, Radiation Effects. 23 (1974) 53.

[74] P.B. Hirsch, J. Silcox, R.E. Smallman, K.H. Westmacott, Dislocation loops in quenched aluminium, Philosophical Magazine. 3 (1958) 897.

[75] R.E. Stoller, P.J. Kamenski, Y.N. Osetsky, Length-scale Effects in Cascade Damage Production in Iron, MRS Proceedings. 1125 (2008) 131.

[76] M. Samaras, P. Derlet, H. Van Swygenhoven, M. Victoria, Computer Simulation of Displacement Cascades in Nanocrystalline Ni, Physical Review Letters. 88 (2002) 125505.

[77] M. Samaras, P.M. Derlet, H.V. Swygenhoven, M. Victoria, Atomic scale modelling of the primary damage state of irradiated fcc and bcc nanocrystalline metals, Journal of Nuclear Materials. 351 (2006) 47.

[78] M. Samaras, W. Hoffelner, M. Victoria, Irradiation of pre-existing voids in nanocrystalline iron, Journal of Nuclear Materials. 352 (2006) 50.

[79] K. Sugio, Y. Shimomura, T.D.d.l. Rubia, Computer Simulation of Displacement Damage Cascade Formation near Sigma 5 Twist Boundary in Silver, Journal of the Physical Society of Japan. 67 (1998) 882.

[80] M. Samaras, P.M. Derlet, H.V. Swygenhoven, M. Victoria, Atomic scale modelling of the primary damage state of irradiated fcc and bcc nanocrystalline metals, Journal of Nuclear Materials. 351 (2006) 47.

[81] X.-M. Bai, A.F. Voter, R.G. Hoagland, M. Nastasi, B.P. Uberuaga, Efficient Annealing of Radiation Damage Near Grain Boundaries via Interstitial Emission, Science. 327 (2010) 1631.

[82] M.J. Demkowicz, R.G. Hoagland, B.P. Uberuaga, A. Misra, Influence of interface sink strength on the reduction of radiation-induced defect concentrations and fluxes in materials with large interface area per unit volume, Physical Review B. 84 (2011) 104102.

[83] D.M. Gruen, A.R. Krauss, S. Susman, M. Venugopalan, M. Ron, Gibbsian and radiation‐induced segregation in Cu–Li and Al–Li alloys, Journal of Vacuum Science & Technology A. 1 (1983) 924.

[84] R.A. Erck, L.E. Rehn, Kinetics of radiation-induced segregation in molybdenum-rhenium alloys, Journal of Nuclear Materials. 168 (1989) 208.

[85] W. Wagner, L.E. Rehn, H. Wiedersich, V. Naundorf, Radiation-induced segregation in Ni-Cu alloys, Physical Review B. 28 (1983) 6780.

[86] T.R. Allen, J.T. Busby, G.S. Was, E.A. Kenik, On the mechanism of radiation-induced segregation in austenitic Fe–Cr–Ni alloys, Journal of Nuclear Materials. 255 (1998) 44.

[87] T.R. Allen, L. Tan, G.S. Was, E.A. Kenik, Thermal and radiation-induced segregation in model Ni-base alloys, Journal of Nuclear Materials. 361 (2007) 174.

[88] S. Ohnuki, H. Takahashi, T. Takeyama, Void swelling and segregation of solute in ion-irradiated ferritic steels, Journal of Nuclear Materials. 104 (1981) 1121.

[89] S.R. Ortner, A stem study of the effect of precipitation on grain boundary chemistry in AISI 304 steel, Acta Metallurgica et Materialia. 39 (1991) 341.
[90] J.M. Titchmarsh, S. Dumbill, On the measurement of radiation-induced segregation (RIS) at point defect sinks, Journal of Nuclear Materials. 227 (1996) 203.
[91] S. Dumbill, Ph.D. Ph.D. Thesis, University of Birmingham, 1992.
[92] R.G. Faulkner, Radiation-induced grain boundary segregation in nuclear reactor steels, Journal of Nuclear Materials. 251 (1997) 269.
[93] J.T. Busby, J. Gan, M. Daniels, G.S. Was, S.M. Bruemmer, D.J. Edwards, E.A. Kenik, Ninth International Symposium on Environmental Degradation of Materials in Nuclear Power Systems—Water Reactors, John Wiley & Sons, Inc., 1999, p. 1089.
[94] J.T. Busby, G.S. Was, E.A. Kenik, Isolating the effect of radiation-induced segregation in irradiation-assisted stress corrosion cracking of austenitic stainless steels, Journal of Nuclear Materials. 302 (2002) 20.
[95] G.S. Was, J.T. Busby, T. Allen, E.A. Kenik, A. Jensson, S.M. Bruemmer, J. Gan, A.D. Edwards, P.M. Scott, P.L. Andreson, Emulation of neutron irradiation effects with protons: validation of principle, Journal of Nuclear Materials. 300 (2002) 198.
[96] M. Nastar, E. Clouet, Mean field theories for the description of diffusion and phase transformations controlled by diffusion, Royal Society of Chemistry, Cambridge, ROYAUME-UNI, 2004.
[97] M. Nastar, Segregation at grain boundaries: from equilibrium to irradiation induced steady states, Philosophical Magazine. 85 (2005) 641.
[98] B.N. Singh, J.H. Evans, Significant differences in defect accumulation behaviour between fcc and bcc crystals under cascade damage conditions, Journal of Nuclear Materials. 226 (1995) 277.
[99] P.R. Okamoto, L.E. Rehn, Radiation-induced segregation in binary and ternary alloys, Journal of Nuclear Materials. 83 (1979) 2.
[100] I.M. Robertson, C.A. Schuh, J.S. Vetrano, N.D. Browning, D.P. Field, D.J. Jensen, M.K. Miller, I. Baker, D.C. Dunand, R. Dunin-Borkowski, B. Kabius, T. Kelly, S. Lozano-Perez, A. Misra, G.S. Rohrer, A.D. Rollett, M.L. Taheri, G.B. Thompson, M. Uchic, X.-L. Wang, G. Was, Towards an integrated materials characterization toolbox, Journal of Materials Research. 26 (2011) 1341.
[101] D.G. Brandon, The structure of high-angle grain boundaries, Acta Metallurgica. 14 (1966) 1479.
[102] T.S. Duh, J.J. Kai, F.R. Chen, Effects of grain boundary misorientation on solute segregation in thermally sensitized and proton-irradiated 304 stainless steel, Journal of Nuclear Materials. 283–287, Part 1 (2000) 198.
[103] N. Sakaguchi, S. Watanabe, H. Takahashi, R.G. Faulkner, A multi-scale approach to radiation-induced segregation at various grain boundaries, Journal of Nuclear Materials. 329–333, Part B (2004) 1166.
[104] D. Hull, I.L. Mogford, Precipitation and irradiation hardening in iron, Philosophical Magazine. 6 (1961) 535.
[105] A.J. Baker, Ph.D., Metallurgical Department, University of Cambridge, 1961.
[106] B.L. Eyre, Direct observations of neutron irradiation damage in α-iron, Philosophical Magazine. 7 (1962) 2107.
[107] B.L. Eyre, Observations of slip bands in irradiated pure iron, Philosophical Magazine. 7 (1962) 1609.

[108] B.C. Masters, Dislocation Loops in Irradiated Iron, Nature. 200 (1963) 254.
[109] M.L. Jenkins, Characterisation of radiation-damage microstructures by TEM, Journal of Nuclear Materials. 216 (1994) 124.
[110] K. Arakawa, M. Hatanaka, E. Kuramoto, K. Ono, H. Mori, Changes in the Burgers Vector of Perfect Dislocation Loops without Contact with the External Dislocations, Physical Review Letters. 96 (2006) 125506.
[111] M.L. Jenkins, M.A. Kirk, Characterization of Radiation Damage by Transmission Electron Microscopy, Institute of Physics Publishing, Philadelphia, 2001.
[112] B.L. Eyre, R. Bullough, On the formation of interstitial loops in b.c.c. metals, Philosophical Magazine. 12 (1965) 31.
[113] B.C. Masters, Dislocation loops in irradiated iron, Philosophical Magazine. 11 (1965) 881.
[114] A.E. Ward, S.B. Fisher, Dislocation loop growth in pure iron under electron irradiation, Journal of Nuclear Materials. 166 (1989) 227.
[115] Z. Yao, M. Hernández-Mayoral, M.L. Jenkins, M.A. Kirk, Heavy-ion irradiations of Fe and Fe–Cr model alloys Part 1: Damage evolution in thin-foils at lower doses, Philosophical Magazine. 88 (2008) 2851.
[116] S.J. Zinkle, B.N. Singh, Microstructure of neutron-irradiated iron before and after tensile deformation, Journal of Nuclear Materials. 351 (2006) 269.
[117] M.R. Gilbert, S.L. Dudarev, P.M. Derlet, D.G. Pettifor, Structure and metastability of mesoscopic vacancy and interstitial loop defects in iron and tungsten, Journal of Physics: Condensed Matter. 20 (2008) 345214.
[118] A.F. Calder, D.J. Bacon, A molecular dynamics study of displacement cascades in α-iron, Journal of Nuclear Materials. 207 (1993) 25.
[119] M. Finnis, MOLDY6: A molecular dynamics program for simulation of pure metals, UKAEA Atomic Energy Research Establishment Theoretical Physics Division, 1988.
[120] R.E. Stoller, The effect of free surfaces on cascade damage production in iron, Journal of Nuclear Materials. 307–311, Part 2 (2002) 935.
[121] R.E. Stoller, Primary damage formation in irradiated materials, JOM. 48 (1996) 23.
[122] L. Malerba, Molecular dynamics simulation of displacement cascades in α-Fe: A critical review, Journal of Nuclear Materials. 351 (2006) 28.
[123] H. Trinkaus, B.N. Singh, A.J.E. Foreman, Glide of interstitial loops produced under cascade damage conditions: Possible effects on void formation, Journal of Nuclear Materials. 199 (1992) 1.
[124] K. Arakawa, K. Ono, M. Isshiki, K. Mimura, M. Uchikoshi, H. Mori, Observation of the One-Dimensional Diffusion of Nanometer-Sized Dislocation Loops, Science. 318 (2007) 956.
[125] Y.N. Osetsky, D.J. Bacon, A. Serra, Thermally activated glide of small dislocation loops in metals, Philosophical Magazine Letters. 79 (1999) 273.
[126] M.A. Puigvi, Y.N. Osetsky, A. Serra, Interactions between vacancy and glissile interstitial clusters in iron and copper, Materials Science and Engineering: A. 365 (2004) 101.
[127] Y.N. Osetsky, D.J. Bacon, A. Serra, B.N. Singh, S.I. Golubov, Stability and mobility of defect clusters and dislocation loops in metals, Journal of Nuclear Materials. 276 (2000) 65.
[128] A.V. Barashev, Y.N. Osetsky, D.J. Bacon, Mechanism of one-dimensional glide of self-interstitial atom clusters in α-iron, Philosophical Magazine A. 80 (2000) 2709.

[129] B.D. Wirth, G.R. Odette, D. Maroudas, G.E. Lucas, Dislocation loop structure, energy and mobility of self-interstitial atom clusters in bcc iron, Journal of Nuclear Materials. 276 (2000) 33.
[130] Y.N. Osetsky, D.J. Bacon, A. Serra, B.N. Singh, S.I. Golubov, One-dimensional atomic transport by clusters of self-interstitial atoms in iron and copper, Philosophical Magazine. 83 (2003) 61.
[131] T. Hamaoka, Y. Satoh, H. Matsui, One-dimensional motion of interstitial clusters in iron-based binary alloys observed using a high-voltage electron microscope, Journal of Nuclear Materials. 433 (2013) 180.
[132] J. Marian, B.D. Wirth, J.M. Perlado, Mechanism of Formation and Growth of <100>Interstitial Loops in Ferritic Materials, Physical Review Letters. 88 (2002) 255507.
[133] K. Arakawa, T. Amino, H. Mori, Direct observation of the coalescence process between nanoscale dislocation loops with different Burgers vectors, Acta Materialia. 59 (2011) 141.
[134] H. Trinkaus, B.N. Singh, A.J.E. Foreman, Impact of glissile interstitial loop production in cascades on defect accumulation in the transient, Journal of Nuclear Materials. 206 (1993) 200.
[135] B.N. Singh, M. Eldrup, S.J. Zinkle, S.I. Golubov, On grain-size-dependent void swelling in pure copper irradiated with fission neutrons, Philosophical Magazine A. 82 (2002) 1137.
[136] J.L. Brimhall, B. Mastel, Neutron irradiated molybdenum-relationship of microstructure to irradiation temperature, Radiation Effects. 3 (1970) 203.
[137] M. Wen, N.M. Ghoniem *, B.N. Singh, Dislocation decoration and raft formation in irradiated materials, Philosophical Magazine. 85 (2005) 2561.
[138] H. Trinkaus, B.N. Singh, A.J.E. Foreman, Segregation of cascade induced interstitial loops at dislocations: possible effect on initiation of plastic deformation, Journal of Nuclear Materials. 251 (1997) 172.
[139] S.L. Dudarev, M.R. Gilbert, K. Arakawa, H. Mori, Z. Yao, M.L. Jenkins, P.M. Derlet, Langevin model for real-time Brownian dynamics of interacting nanodefects in irradiated metals, Physical Review B. 81 (2010) 224107.
[140] Z. Yao, M.L. Jenkins, M. Hernández-Mayoral, M.A. Kirk, The temperature dependence of heavy-ion damage in iron: A microstructural transition at elevated temperatures, Philosophical Magazine. 90 (2010) 4623.
[141] I.M. Robertson, W.E. King, M.A. Kirk, Formation of dislocation loops in iron by self-ion irradiations at 40K, Scripta Materialia. 18 (1984) 317.
[142] S.L. Dudarev, P.M. Derlet, R. Bullough, The magnetic origin of anomalous high-temperature stability of dislocation loops in iron and iron-based alloys, Journal of Nuclear Materials. 386–388 (2009) 45.
[143] S.L. Dudarev, R. Bullough, P.M. Derlet, Effect of the α to γ Phase Transition on the Stability of Dislocation Loops in bcc Iron, Physical Review Letters. 100 (2008) 135503.
[144] Z. Yao, M.L. Jenkins, M.A. Kirk, M. Hernández-Mayoral, The Second Workshop on the Use of In Situ EM / Ion Accelerator Techniques in the Study of Radiation Damage in Solids, Albuquerque, NM, 2011.
[145] C.C. Koch, Nanostructured Materials: Processing, Properties and Applications,, William Andrew, Norwich, New York, 2007.
[146] R. Birringer, Nanocrystalline materials, Materials Science and Engineering: A. 117 (1989) 33.

[147] C. Granqvist, L. Kish, W. Marlow, Gas Phase Nanoparticle Synthesis, Kluwer Academic, Dordrecht, The Netherlands, 2004.

[148] A.A. Karimpoor, U. Erb, K.T. Aust, G. Palumbo, High strength nanocrystalline cobalt with high tensile ductility, Scripta Materialia. 49 (2003) 651.

[149] C. Suryanarayana, Mechanical alloying and milling, Progress in Materials Science. 46 (2001) 1.

[150] V.M. Segal, Materials processing by simple shear, Materials Science and Engineering: A. 197 (1995) 157.

[151] R.Z. Valiev, R.K. Islamgaliev, I.V. Alexandrov, Bulk nanostructured materials from severe plastic deformation, Progress in Materials Science. 45 (2000) 103.

[152] J. Saito, T. Suda, S. Yamashita, S. Ohnuki, H. Takahashi, N. Akasaka, M. Nishida, S. Ukai, Void formation and microstructural development in oxide dispersion strengthened ferritic steels during electron-irradiation, Journal of Nuclear Materials. 258–263, Part 2 (1998) 1264.

[153] K. Hattar, Ph.D., University of Illinois at Urbana-Champaign, Urbana, Illinois, 2009.

[154] E.O. Hall, The Deformation and Ageing of Mild Steel: III Discussion of Results, Proceedings of the Physical Society. Section B. 64 (1951) 747.

[155] N.J. Petch, The Cleavage Strength of Polycrystals, J. Iron Steel Inst. 174 (1953) 25.

[156] A.H. Cottrell, THEORY OF BRITTLE FRACTURE IN STEEL AND SIMILAR METALS, Journal Name: Trans. Met. Soc. AIME; Journal Volume: Vol: 212; Other Information: Orig. Receipt Date: 31-DEC-58. (1958) Medium: X; Size: Pages: 192.

[157] A. Cracknell, N.J. Petch, Frictional forces on dislocation arrays at the lower yield point in iron, Acta Metallurgica. 3 (1955) 186.

[158] J. Heslop, N.J. Petch, Dislocation locking and fracture in α-iron, Philosophical Magazine. 2 (1957) 649.

[159] J.S.C. Jang, C.C. Koch, The hall-petch relationship in nanocrystalline iron produced by ball milling, Scripta Metallurgica et Materialia. 24 (1990) 1599.

[160] R.A. Masumura, P.M. Hazzledine, C.S. Pande, Yield stress of fine grained materials, Acta Materialia. 46 (1998) 4527.

[161] J.C. Li, Petch relation and grain boundary sources, Transactions of the Metallurgical Society of AIME. 227 (1963) 239.

[162] J.C.M. Li, Y.T. Chou, The role of dislocations in the flow stress grain size relationships, Metall and Materi Trans. 1 (1970) 1145.

[163] M.A. Meyersm, E. Ashworth, A model for the effect of grain size on the yield stress of metals, Philosophical Magazine A. 46 (1982) 737.

[164] M.A. Meyers, K.K. Chawla, Mechanical metallurgy: principles and applications, Prentice-Hall Englewood Cliffs, NJ, 1984.

[165] W. Baldwin Jr, Yield strength of metals as a function of grain size, Acta Metallurgica. 6 (1958) 139.

[166] T. Christman, Grain boundary strengthening exponent in conventional and ultrafine microstructures, Scripta metallurgica et materialia. 28 (1993) 1495.

[167] J.R. Weertman, Hall-Petch strengthening in nanocrystalline metals, Materials Science and Engineering: A. 166 (1993) 161.

[168] D.J. Dunstan, A.J. Bushby, Grain size dependence of the strength of metals: The Hall–Petch effect does not scale as the inverse square root of grain size, International Journal of Plasticity. 53 (2014) 56.

[169] R. Birringer, H. Gleiter, H.P. Klein, P. Marquardt, Nanocrystalline materials an approach to a novel solid structure with gas-like disorder?, Physics Letters A. 102 (1984) 365.

[170] J. Horváth, R. Birringer, H. Gleiter, Diffusion in nanocrystalline material, Solid State Communications. 62 (1987) 319.

[171] A.H. Chokshi, A. Rosen, J. Karch, H. Gleiter, On the validity of the hall-petch relationship in nanocrystalline materials, Scripta Metallurgica. 23 (1989) 1679.

[172] S. Takaki, K. Kawasaki, Y. Kimura, Mechanical properties of ultra fine grained steels, Journal of Materials Processing Technology. 117 (2001) 359.

[173] C.C. Koch, Bulk Nanostructured Materials, 2009, p. 1.

[174] C.S. Pande, K.P. Cooper, Nanomechanics of Hall–Petch relationship in nanocrystalline materials, Progress in Materials Science. 54 (2009) 689.

[175] K.S. Kumar, S. Suresh, M.F. Chisholm, J.A. Horton, P. Wang, Deformation of electrodeposited nanocrystalline nickel, Acta Materialia. 51 (2003) 387.

[176] R.C. Hugo, H. Kung, J.R. Weertman, R. Mitra, J.A. Knapp, D.M. Follstaedt, In-situ TEM tensile testing of DC magnetron sputtered and pulsed laser deposited Ni thin films, Acta Materialia. 51 (2003) 1937.

[177] Z. Shan, E.A. Stach, J.M.K. Wiezorek, J.A. Knapp, D.M. Follstaedt, S.X. Mao, Grain Boundary-Mediated Plasticity in Nanocrystalline Nickel, Science. 305 (2004) 654.

[178] K.M. Youssef, R.O. Scattergood, K.L. Murty, J.A. Horton, C.C. Koch, Ultrahigh strength and high ductility of bulk nanocrystalline copper, Applied Physics Letters. 87 (2005).

[179] M.A. Haque, M.T.A. Saif, Deformation mechanisms in free-standing nanoscale thin films: A quantitative in situ transmission electron microscope study, Proceedings of the National Academy of Sciences of the United States of America. 101 (2004) 6335.

[180] X.L. Wu, X.Z. Liao, S.G. Srinivasan, F. Zhou, E.J. Lavernia, R.Z. Valiev, Y.T. Zhu, New Deformation Twinning Mechanism Generates Zero Macroscopic Strain in Nanocrystalline Metals, Physical Review Letters. 100 (2008) 095701.

[181] F. Dalla Torre, H. Van Swygenhoven, M. Victoria, Nanocrystalline electrodeposited Ni: microstructure and tensile properties, Acta Materialia. 50 (2002) 3957.

[182] J. Schiotz, F.D. Di Tolla, K.W. Jacobsen, Softening of nanocrystalline metals at very small grain sizes, Nature. 391 (1998) 561.

[183] J. Schiøtz, K.W. Jacobsen, A Maximum in the Strength of Nanocrystalline Copper, Science. 301 (2003) 1357.

[184] H. Van Swygenhoven, P.M. Derlet, A.G. Froseth, Stacking fault energies and slip in nanocrystalline metals, Nat Mater. 3 (2004) 399.

[185] H. Van Swygenhoven, P.M. Derlet, A.G. Frøseth, Nucleation and propagation of dislocations in nanocrystalline fcc metals, Acta Materialia. 54 (2006) 1975.

[186] V. Yamakov, D. Wolf, S.R. Phillpot, A.K. Mukherjee, H. Gleiter, Dislocation processes in the deformation of nanocrystalline aluminium by molecular-dynamics simulation, Nat Mater. 1 (2002) 45.

[187] R.K. Rajgarhia, D.E. Spearot, A. Saxena, Plastic deformation of nanocrystalline copper-antimony alloys, Journal of Materials Research. 25 (2010) 411.

[188] Q. Wei, L. Kecskes, T. Jiao, K.T. Hartwig, K.T. Ramesh, E. Ma, Adiabatic shear banding in ultrafine-grained Fe processed by severe plastic deformation, Acta Materialia. 52 (2004) 1859.

[189] D. Jia, K.T. Ramesh, E. Ma, Effects of nanocrystalline and ultrafine grain sizes on constitutive behavior and shear bands in iron, Acta Materialia. 51 (2003) 3495.

[190] D. Jia, K.T. Ramesh, E. Ma, Failure mode and dynamic behavior of nanophase iron under compression, Scripta Materialia. 42 (1999) 73.

[191] T.R. Malow, C.C. Koch, P.Q. Miraglia, K.L. Murty, Compressive mechanical behavior of nanocrystalline Fe investigated with an automated ball indentation technique, Materials Science and Engineering: A. 252 (1998) 36.

[192] D. Jang, M. Atzmon, Grain-size dependence of plastic deformation in nanocrystalline Fe, Journal of Applied Physics. 93 (2003) 9282.

[193] J.B. Savader, M.R. Scanlon, R.C. Cammarata, D.T. Smith, C. Hayzelden, Nanoindentation study of sputtered nanocrystalline iron thin films, Scripta Materialia. 36 (1997) 29.

[194] G.E. Fougere, J.R. Weertman, R.W. Siegel, Processing and mechanical behavior of nanocrystalline Fe, Nanostructured Materials. 5 (1995) 127.

[195] J.B. Jeon, B.-J. Lee, Y.W. Chang, Molecular dynamics simulation study of the effect of grain size on the deformation behavior of nanocrystalline body-centered cubic iron, Scripta Materialia. 64 (2011) 494.

[196] A. Latapie, D. Farkas, Effect of grain size on the elastic properties of nanocrystalline α-iron, Scripta Materialia. 48 (2003) 611.

[197] Y. Chimi, A. Iwase, N. Ishikawa, M. Kobiyama, T. Inami, T. Kambara, S. Okuda, Swift heavy ion irradiation effects in nanocrystalline gold, Nuclear Instruments and Methods in Physics Research Section B: Beam Interactions with Materials and Atoms. 245 (2006) 171.

[198] Y. Chimi, A. Iwase, N. Ishikawa, M. Kobiyama, T. Inami, S. Okuda, Accumulation and recovery of defects in ion-irradiated nanocrystalline gold, Journal of Nuclear Materials. 297 (2001) 355.

[199] T.D. Shen, S. Feng, M. Tang, J.a. Valdez, Y. Wang, K.E. Sickafus, Enhanced radiation tolerance in nanocrystalline MgGa[sub 2]O[sub 4], Applied Physics Letters. 90 (2007) 263115.

[200] J.A. Hudson, D.J. Mazey, R.S. Nelson, Void Formation in Nickel During 20 MeV C++ Irradiation at 525°C, Journal of Nuclear Materials. 41 (1971) 241.

[201] I.J. Beyerlein, A. Caro, M.J. Demkowicz, N.A. Mara, A. Misra, B.P. Uberuaga, Radiation damage tolerant nanomaterials, Materials Today. 16 (2013) 443.

[202] E.G. Fu, A. Misra, H. Wang, L. Shao, X. Zhang, Interface enabled defects reduction in helium ion irradiated Cu/V nanolayers, Journal of Nuclear Materials. 407 (2010) 178.

[203] N. Li, E.G. Fu, H. Wang, J.J. Carter, L. Shao, S.A. Maloy, A. Misra, X. Zhang, He ion irradiation damage in Fe/W nanolayer films, Journal of Nuclear Materials. 389 (2009) 233.

[204] A. Misra, M.J. Demkowicz, X. Zhang, R.G. Hoagland, The radiation damage tolerance of ultra-high strength nanolayered composites, JOM. 59 (2007) 62.

[205] M. Li, M.A. Kirk, P.M. Baldo, D. Xu, B.D. Wirth, Study of defect evolution by TEM with in situ ion irradiation and coordinated modeling, Philosophical Magazine. 92 (2012) 2048.

[206] A.C. Nicol, M.L. Jenkins, M.A. Kirk, Matrix Damage in Iron, MRS Online Proceedings Library. 650 (2000) null.

[207] L. Bruck, Die Struktur dünner auf Steinsalz aufgedampfter Metallschichten, Annalen der Physik. 5 (1936) 233.

[208] S. Shirai, Structure of Fe Films Deposited on Annealed Rock Salt, Proceedings of the Physico-Mathematical Society of Japan. 20 (1938) 855.

[209] S. Shinji, Structures of Fe Films Deposited on Crystals of Some Alkali Halides, Proceedings of the Physico-Mathematical Society of Japan. 19 (1937) 937.

[210] L.E. Collins, O.S. Heavens, The Epitaxial Growth and Oxidation of Nickel, Cobalt and Iron on Rocksalt, Proceedings of the Physical Society. 70 (1957) 265.
[211] J.W. Matthews, Technique for preparing single-crystal films of iron on clean sodium chloride substrates, Applied Physics Letters. 7 (1965) 255.
[212] J.W. Matthews, Growth of FCC metals on sodium chloride substrates, The Journal of Vacuum Science and Technology. 3 (1965) 133.
[213] S. Shinozaki, H. Sato, Orientation Dependence of Nucleation of Iron on NaCl Substrates, Journal of Vacuum Science & Technology. 6 (1969) 534.
[214] S. Shinozaki, H. Sato, Need of Contamination for the Epitaxial Growth of Iron on Rocksalt, Journal of Applied Physics. 36 (1965) 2320.
[215] C.W. Allen, L.L. Funk, E.A. Ryan, New Instrumentation in Argonne's Hvem-Tandem Facility: Expanded Capability for in Situ Ion Beam Studies, MRS Online Proceedings Library. 396 (1995).
[216] J.F. Ziegler, M.D. Ziegler, J.P. Biersack, SRIM – The stopping and range of ions in matter (2010), Nuclear Instruments and Methods in Physics Research Section B: Beam Interactions with Materials and Atoms. 268 (2010) 1818.
[217] J. Portillo, E.F. Rauch, S. Nicolopoulos, M. Gemmi, D. Bultreys, Precession Electron Diffraction Assisted Orientation Mapping in the Transmission Electron Microscope, Materials Science Forum. 644 (2010) 1.
[218] S.T. Chang, I.C. Leu, M.H. Hon, Electrodeposition of nanocrystalline SnO2 coatings with two-layer microstructure, Journal of Crystal Growth. 273 (2004) 195.
[219] L. Del Bianco, C. Ballesteros, J.M. Rojo, A. Hernando, Magnetically Ordered fcc Structure at the Relaxed Grain Boundaries of Pure Nanocrystalline Fe, Physical Review Letters. 81 (1998) 4500.
[220] N. Sunwang, P. Wangyao, Y. Boonyongmaneerat, The effects of heat treatments on hardness and wear resistance in Ni–W alloy coatings, Surface and Coatings Technology. 206 (2011) 1096.
[221] F. Su, C. Liu, P. Huang, Friction and wear of nanocrystalline Co and Co–W alloy coatings produced by pulse reverse electrodeposition, Wear. 300 (2013) 114.
[222] R.B. Inturi, Z. Szklarska-Smialowska, Localized Corrosion of Nanocrystalline 304 Type Stainless Steel Films, Corrosion. 48 (1992) 398.
[223] R. Mishra, R. Balasubramaniam, Effect of nanocrystalline grain size on the electrochemical and corrosion behavior of nickel, Corrosion Science. 46 (2004) 3019.
[224] E. Pellicer, A. Varea, S. Pané, B.J. Nelson, E. Menéndez, M. Estrader, S. Suriñach, M.D. Baró, J. Nogués, J. Sort, Nanocrystalline Electroplated Cu–Ni: Metallic Thin Films with Enhanced Mechanical Properties and Tunable Magnetic Behavior, Advanced Functional Materials. 20 (2010) 983.
[225] A.V. Sumant, O. Auciello, R.W. Carpick, S. Srinivasan, J.E. Butler, Ultrananocrystalline and Nanocrystalline Diamond Thin Films for MEMS/NEMS Applications, MRS Bulletin. 35 (2010) 281.
[226] R.W. Siegel, S.M. Chang, R.W. Balluffi, Vacancy loss at grain boundaries in quenched polycrystalline gold, Acta Metallurgica. 28 (1980) 249.
[227] M. Dollar, H. Gleiter, Point defect annihilation at grain boundaries in gold, Scripta Metallurgica. 19 (1985) 481.

[228] T. Fujita, Z. Horita, T.G. Langdon, Using grain boundary engineering to evaluate the diffusion characteristics in ultrafine-grained Al–Mg and Al–Zn alloys, Materials Science and Engineering: A. 371 (2004) 241.

[229] C. Herzig, S. Divinski, Y. Mishin, Bulk and interface boundary diffusion in group IV hexagonal close-packed metals and alloys, Metall and Mat Trans A. 33 (2002) 765.

[230] R.G. Hoagland, R.J. Kurtz, The relation between grain-boundary structure and sliding resistance, Philosophical Magazine A. 82 (2002) 1073.

[231] T. Watanabe, S. Tsurekawa, Toughening of brittle materials by grain boundary engineering, Materials Science and Engineering: A. 387–389 (2004) 447.

[232] P.J. Dobson, B.J. Hopkins, Preferred orientation in metal films deposited on glass, Thin Solid Films. 5 (1970) 97.

[233] J.M.E. Harper, K.P. Rodbell, E.G. Colgan, R.H. Hammond, Control of in-plane texture of body centered cubic metal thin films, Journal of Applied Physics. 82 (1997) 4319.

[234] C. Detavernier, A.S. Ozcan, J. Jordan-Sweet, E.A. Stach, J. Tersoff, F.M. Ross, C. Lavoie, An off-normal fibre-like texture in thin films on single-crystal substrates, Nature. 426 (2003) 641.

[235] C.V. Thompson, STRUCTURE EVOLUTION DURING PROCESSING OF POLYCRYSTALLINE FILMS, Annual Review of Materials Science. 30 (2000) 159.

[236] N. Fujimura, T. Nishihara, S. Goto, J. Xu, T. Ito, Control of preferred orientation for ZnOx films: control of self-texture, Journal of Crystal Growth. 130 (1993) 269.

[237] R. Bouregba, G. Poullain, B. Vilquin, H. Murray, Orientation control of textured PZT thin films sputtered on silicon substrate with TiOx seeding, Materials Research Bulletin. 35 (2000) 1381.

[238] G.N. Van Wyk, H.J. Smith, Crystalline reorientation due to ion bombardment, Nuclear Instruments and Methods. 170 (1980) 433.

[239] Y.S. Jung, Study on texture evolution and properties of silver thin films prepared by sputtering deposition, Applied Surface Science. 221 (2004) 281.

[240] K. Schüler, B. Philippi, M. Weinmann, V.M. Marx, H. Vehoff, Effects of processing on texture, internal stresses and mechanical properties during the pulsed electrodeposition of nanocrystalline and ultrafine-grained nickel, Acta Materialia. 61 (2013) 3945.

[241] K. Barmak, W.E. Archibald, A.D. Rollett, S. Ta'asan, D. Kinderlehrer, Grain Boundary Properties and Grain Growth: Al Foils, Al Films, MRS Online Proceedings Library. 819 (2004) null.

[242] A.D. Darbal, K.J. Ganesh, X. Liu, S.-B. Lee, J. Ledonne, T. Sun, B. Yao, A.P. Warren, G.S. Rohrer, A.D. Rollett, P.J. Ferreira, K.R. Coffey, K. Barmak, Grain Boundary Character Distribution of Nanocrystalline Cu Thin Films Using Stereological Analysis of Transmission Electron Microscope Orientation Maps, Microscopy and Microanalysis. 19 (2013) 111.

[243] A.D. Darbal, M. Gemmi, J. Portillo, E. Rauch, S. Nicolopoulos, Nanoscale Automated Phase and Orientation Mapping in the TEM, Microscopy Today. 20 (2012) 38.

[244] M. Seyring, X. Song, M. Rettenmayr, Advance in Orientation Microscopy: Quantitative Analysis of Nanocrystalline Structures, ACS Nano. 5 (2011) 2580.

[245] S. Rajasekhara, K.J. Ganesh, K. Hattar, J.A. Knapp, P.J. Ferreira, Evidence of metastable hcp phase grains in as-deposited nanocrystalline nickel films, Scripta Materialia. 67 (2012) 189.

[246] J.G. Brons, G.B. Thompson, Orientation Mapping via Precession-Enhanced Electron Diffraction and Its Applications in Materials Science, JOM. 66 (2014) 165.

[247] J.G. Brons, G.B. Thompson, A comparison of grain boundary evolution during grain growth in fcc metals, Acta Materialia. 61 (2013) 3936.

[248] J.A. Thornton, High Rate Thick Film Growth, Annual Review of Materials Science. 7 (1977) 239.

[249] J.A. Thornton, The microstructure of sputter-deposited coatings, Journal of Vacuum Science & Technology A. 4 (1986) 3059.

[250] H. Van Swygenhoven, D. Farkas, A. Caro, Grain-boundary structures in polycrystalline metals at the nanoscale, Physical Review B. 62 (2000) 831.

[251] K.A. Darling, R.N. Chan, P.Z. Wong, J.E. Semones, R.O. Scattergood, C.C. Koch, Grain-size stabilization in nanocrystalline FeZr alloys, Scripta Materialia. 59 (2008) 530.

[252] G. Gottstein, L.S. Shvindlerman, Grain Boundary Migration in Metals: Thermodynamics, Kinetics, Applications, CRC Press, Boca Raton, Florida, 2009.

[253] C.S. Smith, Introduction to Grains, Phases, and Interfaces - an Interpretation of Microstructure, Transactions of AIME. 175 (1948) 15.

[254] T. Gladman, On the Theory of the Effect of Precipitate Particles on Grain Growth in Metals, Proceedings of the Royal Society of London. Series A. Mathematical and Physical Sciences. 294 (1966) 298.

[255] M. Ashby, J. Harper, J. Lewis, The interaction of crystal boundaries with second-phase particles, Trans Met Soc AIME. 245 (1969) 413.

[256] D.J. Srolovitz, M.P. Anderson, P.S. Sahni, G.S. Grest, Computer simulation of grain growth—II. Grain size distribution, topology, and local dynamics, Acta Metallurgica. 32 (1984) 793.

[257] M. Hillert, Inhibition of grain growth by second-phase particles, Acta Metallurgica. 36 (1988) 3177.

[258] M.P. Anderson, G.S. Grest, R.D. Doherty, K. Li, D.J. Srolovitz, Inhibition of grain growth by second phase particles: Three dimensional Monte Carlo computer simulations, Scripta Metallurgica. 23 (1989) 753.

[259] M. Miodownik, E.A. Holm, G.N. Hassold, Highly parallel computer simulations of particle pinning: zener vindicated, Scripta Materialia. 42 (2000) 1173.

[260] D. Fan, L.-Q. Chen, S.-P.P. Chen, Numerical Simulation of Zener Pinning with Growing Second-Phase Particles, Journal of the American Ceramic Society. 81 (1998) 526.

[261] N. Moelans, B. Blanpain, P. Wollants, Pinning effect of second-phase particles on grain growth in polycrystalline films studied by 3-D phase field simulations, Acta Materialia. 55 (2007) 2173.

[262] N. Moelans, B. Blanpain, P. Wollants, Phase field simulations of grain growth in two-dimensional systems containing finely dispersed second-phase particles, Acta Materialia. 54 (2006) 1175.

[263] N. Moelans, B. Blanpain, P. Wollants, A phase field model for the simulation of grain growth in materials containing finely dispersed incoherent second-phase particles, Acta Materialia. 53 (2005) 1771.

[264] P.C. Millett, D. Wolf, T. Desai, S. Rokkam, A. El-Azab, Phase-field simulation of thermal conductivity in porous polycrystalline microstructures, Journal of Applied Physics. 104 (2008).

[265] P.C. Millett, A. El-Azab, S. Rokkam, M. Tonks, D. Wolf, Phase-field simulation of irradiated metals: Part I: Void kinetics, Computational Materials Science. 50 (2011) 949.

[266] P.C. Millett, A. El-Azab, D. Wolf, Phase-field simulation of irradiated metals: Part II: Gas bubble kinetics, Computational Materials Science. 50 (2011) 960.

[267] P.C. Millett, M. Tonks, Meso-scale modeling of the influence of intergranular gas bubbles on effective thermal conductivity, Journal of Nuclear Materials. 412 (2011) 281.

[268] Z.H. Cao, H.M. Lu, X.K. Meng, Barrier layer and annealing temperature dependent microstructure evolution of nanocrystalline Cu films, Materials Chemistry and Physics. 117 (2009) 321.

[269] R. Dannenberg, E.A. Stach, J.R. Groza, B.J. Dresser, In-situ TEM observations of abnormal grain growth, coarsening, and substrate de-wetting in nanocrystalline Ag thin films, Thin Solid Films. 370 (2000) 54.

[270] K. Pantleon, M.A.J. Somers, Interpretation of microstructure evolution during self-annealing and thermal annealing of nanocrystalline electrodeposits—A comparative study, Materials Science and Engineering: A. 528 (2010) 65.

[271] K.E. Harris, V.V. Singh, A.H. King, Grain rotation in thin films of gold, Acta Materialia. 46 (1998) 2623.

[272] M. Legros, D.S. Gianola, K.J. Hemker, In situ TEM observations of fast grain-boundary motion in stressed nanocrystalline aluminum films, Acta Materialia. 56 (2008) 3380.

[273] D.A. Molodov, U. Czubayko, G. Gottstein, L.S. Shvindlerman, On the effect of purity and orientation on grain boundary motion, Acta Materialia. 46 (1998) 553.

[274] K. Ahmed, C.A. Yablinsky, A. Schulte, T. Allen, A. El-Azab, Phase field modeling of the effect of porosity on grain growth kinetics in polycrystalline ceramics, Modelling and Simulation in Materials Science and Engineering. 21 (2013) 065005.

[275] N. Moelans, B. Blanpain, P. Wollants, Quantitative analysis of grain boundary properties in a generalized phase field model for grain growth in anisotropic systems, Physical Review B. 78 (2008) 024113.

[276] M.R. Tonks, D. Gaston, P.C. Millett, D. Andrs, P. Talbot, An object-oriented finite element framework for multiphysics phase field simulations, Computational Materials Science. 51 (2012) 20.

[277] L. Zhang, M.R. Tonks, D. Gaston, J.W. Peterson, D. Andrs, P.C. Millett, B.S. Biner, A quantitative comparison between and elements for solving the Cahn–Hilliard equation, Journal of Computational Physics. 236 (2013) 74.

[278] M.a. Tschopp, K.N. Solanki, F. Gao, X. Sun, M.a. Khaleel, M.F. Horstemeyer, Probing grain boundary sink strength at the nanoscale: Energetics and length scales of vacancy and interstitial absorption by grain boundaries in α-Fe, Physical Review B. 85 (2012) 064108.

[279] M.J.S. Spencer, A. Hung, I.K. Snook, I. Yarovsky, Density functional theory study of the relaxation and energy of iron surfaces, Surface Science. 513 (2002) 389.

[280] M.R. Gilbert, Z. Yao, M.A. Kirk, M.L. Jenkins, S.L. Dudarev, Vacancy defects in Fe: Comparison between simulation and experiment, Journal of Nuclear Materials. 386–388 (2009) 36.

[281] G.S. Was, J.P. Wharry, B. Frisbie, B.D. Wirth, D. Morgan, J.D. Tucker, T.R. Allen, Assessment of radiation-induced segregation mechanisms in austenitic and ferritic–martensitic alloys, Journal of Nuclear Materials. 411 (2011) 41.

[282] M. Victoria, N. Baluc, C. Bailat, Y. Dai, M.I. Luppo, R. Scha̋ublin, B.N. Singh, The microstructure and associated tensile properties of irradiated fcc and bcc metals, Journal of Nuclear Materials. 276 (2000) 114.

[283] P. Yvon, F. Carré, Structural materials challenges for advanced reactor systems, Journal of Nuclear Materials. 385 (2009) 217.
[284] T. Allen, J. Busby, M. Meyer, D. Petti, Materials challenges for nuclear systems, Materials Today. 13 (2010) 14.
[285] R.K. Nanstad, D.A. McClintock, D.T. Hoelzer, L. Tan, T.R. Allen, High temperature irradiation effects in selected Generation IV structural alloys, Journal of Nuclear Materials. 392 (2009) 331.
[286] M.A. Tschopp, M.F. Horstemeyer, F. Gao, X. Sun, M. Khaleel, Energetic driving force for preferential binding of self-interstitial atoms to Fe grain boundaries over vacancies, Scripta Materialia. 64 (2011) 908.
[287] X.-M. Bai, L.J. Vernon, R.G. Hoagland, A.F. Voter, M. Nastasi, B.P. Uberuaga, Role of atomic structure on grain boundary-defect interactions in Cu, Physical Review B. 85 (2012) 214103.
[288] J. Chen, T. Sekiguchi, D. Yang, F. Yin, K. Kido, S. Tsurekawa, Electron-beam-induced current study of grain boundaries in multicrystalline silicon, Journal of Applied Physics. 96 (2004) 5490.
[289] P.A. Thorsen, J.B. Bilde-Sørensen, B.N. Singh, Bubble formation at grain boundaries in helium implanted copper, Scripta Materialia. 51 (2004) 557.
[290] R.S. Barnes, G.B. Redding, A.H. Cottrbll, The observation of vacancy sources in metals, Philosophical Magazine. 3 (1958) 97.
[291] S.J. Zinkle, R.L. Sindelar, Defect microstructures in neutron-irradiated copper and stainless steel, Journal of Nuclear Materials. 155–157, Part 2 (1988) 1196.
[292] M.J. Demkowicz, O. Anderoglu, X. Zhang, A. Misra, The influence of ∑3 twin boundaries on the formation of radiation-induced defect clusters in nanotwinned Cu, Journal of Materials Research. 26 (2011) 1666.
[293] C. Suryanarayana, The structure and properties of nanocrystalline materials: Issues and concerns, JOM. 54 (2002) 24.
[294] S.C. Tjong, H. Chen, Nanocrystalline materials and coatings, Materials Science and Engineering: R: Reports. 45 (2004) 1.
[295] R.W. Siegel, G.J. Thomas, Grain boundaries in nanophase materials, Ultramicroscopy. 40 (1992) 376.
[296] K.S. Kumar, H. Van Swygenhoven, S. Suresh, Mechanical behavior of nanocrystalline metals and alloys, Acta Materialia. 51 (2003) 5743.
[297] S. Ranganathan, R. Divakar, V.S. Raghunathan, Interface structures in nanocrystalline materials, Scripta Materialia. 44 (2001) 1169.
[298] B.D. Wirth, How does radiation damage materials?, Science. 318 (2007) 923.
[299] G.R. Odette, D.T. Hoelzer, Irradiation-tolerant nanostructured ferritic alloys: Transforming helium from a liability to an asset, JOM. 62 (2010) 84.
[300] J.R. Rieken, I.E. Anderson, M.J. Kramer, G.R. Odette, E. Stergar, E. Haney, Reactive gas atomization processing for Fe-based ODS alloys, Journal of Nuclear Materials. 428 (2012) 65.
[301] S. Ukai, M. Fujiwara, Perspective of ODS alloys application in nuclear environments, Journal of Nuclear Materials. 307–311, Part 1 (2002) 749.
[302] V.V. Kolomytkin, Zones of radiation point defect instability near the [100] (010) edge dislocation in α-Fe, Journal of Nuclear Materials. 149 (1987) 321.

[303] S.J. Zinkle, Microstructure of ion irradiated ceramic insulators, Nuclear Instruments and Methods in Physics Research Section B: Beam Interactions with Materials and Atoms. 91 (1994) 234.

[304] G.A. Vetterick, C.M. Barr, J.K. Baldwin, M.A. Kirk, P.M. Baldo, A. Misra, M.L. Taheri, Toward radiation tolerant materials design, in preparation. (2013).

[305] D.J. Bacon, T. Diaz de la Rubia, Molecular dynamics computer simulations of displacement cascades in metals, Journal of Nuclear Materials. 216 (1994) 275.

[306] N. Soneda, T.D. de la Rubia, Defect production, annealing kinetics and damage evolution in α-Fe: An atomic-scale computer simulation, Philosophical Magazine A. 78 (1998) 995.

[307] Y.N. Osetsky, A. Serra, V. Priego, Interactions between mobile dislocation loops in Cu and α-Fe, Journal of Nuclear Materials. 276 (2000) 202.

[308] D. Terentyev, L. Malerba, Interaction of 〈100〉 and ½〈111〉 dislocation loops with point defects in ferritic alloys, Journal of Nuclear Materials. 377 (2008) 141.

[309] D. Terentyev, L. Malerba, P. Klaver, P. Olsson, Formation of stable sessile interstitial complexes in reactions between glissile dislocation loops in bcc Fe, Journal of Nuclear Materials. 382 (2008) 126.

[310] H. Xu, R.E. Stoller, Y.N. Osetsky, D. Terentyev, Solving the Puzzle of <100>Interstitial Loop Formation in bcc Iron, Physical Review Letters. 110 (2013) 265503.

[311] A.F. Calder, D.J. Bacon, A.V. Barashev, Y.N. Osetsky, Effect of mass of the primary knock-on atom on displacement cascade debris in α -iron, Philosophical Magazine Letters. 88 (2008) 43.

[312] M.I. Mendelev, S. Han, D.J. Srolovitz, G.J. Ackland, D.Y. Sun, M. Asta, Development of new interatomic potentials appropriate for crystalline and liquid iron, Philosophical Magazine. 83 (2003) 3977.

[313] A. Seeger, D. Schumacher, W. Schilling, J. Diehl, in: A. Seeger, D. Schumacher, W. Schilling, J. Diehl (Eds.), The International Conference on Vacancies and Interstitials in Metals, North-Holland Publishing Company, Jülich, Germany, 1968.

[314] J. Marian, B.D. Wirth, R. Schäublin, J.M. Perlado, T. Díaz de la Rubia, 〈100〉 -Loop characterization in α-Fe: comparison between experiments and modeling, Journal of Nuclear Materials. 307–311, Part 2 (2002) 871.

[315] M.A. Puigvi, Y.N. Osetsky, A. Serra, Point-defect clusters and dislocation loops in bcc metals: Continuum and atomistic study, Philosophical Magazine. 83 (2003) 857.

[316] P.S. Dobson, R.E. Smallman, The Climb of Dislocation Loops in Zinc, Proceedings of the Royal Society of London. Series A. Mathematical and Physical Sciences. 293 (1966) 423.

[317] J. Baštecká, Interaction of dislocation loop with free surface, Cechoslovackij fiziceskij zurnal B. 14 (1964) 430.

[318] T.A. Khraishi, H.M. Zbib, Free-Surface Effects in 3D Dislocation Dynamics: Formulation and Modeling, Journal of Engineering Materials and Technology. 124 (2002) 342.

[319] J. Narayan, J. Washburn, Stability of dislocation loops near a free surface, Journal of Applied Physics. 43 (1972) 4862.

[320] I. Vagera, Long range elastic interaction of prismatic dislocation loop with a grain boundary, Czech J Phys. 20 (1970) 702.

[321] I. Vagera, Long range force on a dislocation loop due to grain boundary, Czech J Phys. 20 (1970) 1278.

[322] H. Hosokawa, A.V. Desai, M.A. Haque, Plane stress fracture toughness of freestanding nanoscale thin films, Thin Solid Films. 516 (2008) 6444.
[323] P.J. Phillips, M. De Graef, L. Kovarik, A. Agrawal, W. Windl, M.J. Mills, Atomic-resolution defect contrast in low angle annular dark-field STEM, Ultramicroscopy. 116 (2012) 47.